

# Northumbria Research Link

Citation: Kumar, Rahul (2019) High sensitivity micro/nano singlemode-multimode-singlemode fibre sensors. Doctoral thesis, Northumbria University.

This version was downloaded from Northumbria Research Link:  
<http://nrl.northumbria.ac.uk/id/eprint/39984/>

Northumbria University has developed Northumbria Research Link (NRL) to enable users to access the University's research output. Copyright © and moral rights for items on NRL are retained by the individual author(s) and/or other copyright owners. Single copies of full items can be reproduced, displayed or performed, and given to third parties in any format or medium for personal research or study, educational, or not-for-profit purposes without prior permission or charge, provided the authors, title and full bibliographic details are given, as well as a hyperlink and/or URL to the original metadata page. The content must not be changed in any way. Full items must not be sold commercially in any format or medium without formal permission of the copyright holder. The full policy is available online: <http://nrl.northumbria.ac.uk/policies.html>

**High sensitivity micro/nano  
singlemode-multimode-singlemode  
fibre sensors**

**Rahul Kumar**

**PhD**

**2019**

# **High sensitivity micro/nano singlemode-multimode-singlemode fibre sensors**

Rahul Kumar

A thesis submitted in partial fulfilment of the  
requirement of University of Northumbria at  
Newcastle for the degree of

**Doctor of Philosophy**

Research undertaken in the Faculty of Engineering  
and Environmental Sciences



**Northumbria  
University**  
NEWCASTLE

March 2019

*In loving memory of my mother*

*To my father, brother and loving wife*

*With love and eternal appreciation*

## Abstract

Optical fibre interferometers have gained significant attention in the field of sensing, due to their advantages of high sensitivity, reliability, compact size, light weight, immunity to electromagnetic interference, environmental ruggedness and remote sensing capabilities. Among the interferometric sensors, singlemode – multimode – singlemode (SMS) fibre structures has advantages of easy and low cost fabrication and relative simplicity of integration with other optical devices. However, previous reported research in the SMS sensor has been limited to measurements of the traditional parameters such as temperature, strain, vibration and refractive index with limited sensitivity, which prevents further development of the sensing technique. In this thesis, temperature sensitivity enhancement and a new application in solid/liquid phase change detection have been firstly proposed and experimentally demonstrated based on the traditional SMS fibre structure; the traditional SMS fibre structure is then tapered and functionalised for magnetic field, humidity and biological sensing with ultrahigh sensitivity for human chorionic gonadotropin (hCG) detection. The key contributions of this thesis include

### *Modified SMS fibre for temperature sensing and phase transition monitoring of phase change materials*

Based on the modified SMS fibre structure, significant temperature sensitivity improvement (200 times over traditional SMS sensor) is experimentally demonstrated, by introducing a hollow core fibre filled with a polymer (refractive index 1.46), in the middle of the SMS structure, which constructed a new sensor of singlemode-multimode-polymer filled hollow core-multimode-singlemode fibre structure.

Solid-liquid phase change materials (PCMs) have been widely used in latent heat thermal storage systems for heat pumps, solar engineering, and spacecraft thermal control. A platinum-coated singlemode-multimode (SM) structure has been proposed as an optical fibre sensor (OFS) to monitor the phase transition of a phase change material (PCM). The sensor has been experimentally demonstrated to be able to detect the phase change point of different PCMs, including paraffin wax and two salt hydrates (S32 and S46) with advantages of simple operation and low cost.

### ***Tapered optical fibre sensor for magnetic field sensing***

A tapered singlemode – no-core fibre – singlemode (SNCS) fibre sensor (taper waist diameter of 8  $\mu\text{m}$ ) is proposed and experimentally demonstrated with a maximum sensitivity of 26,061 nm/RIU (refractive index unit), within the RI range of 1.4304 - 1.4320, which is over 10 times higher in sensitivity than that of a non-tapered SNCS structure. The tapered SNCS structure is then inserted into a glass tube (inner diameter of 1 mm) filled with magnetic fluid for measuring both magnetic field strength and direction. Experimentally a maximum sensitivity of 0.466 nm/mT has been achieved by using a tapered diameter of 10  $\mu\text{m}$  and 1.3% ferro-magnetic particles in magnetic fluid.

### ***Functionalised optical fibre for bio-sensing***

A high sensitivity label free human chorionic gonadotropin (hCG) is proposed and experimentally demonstrated with a sensitivity of 0.188 nm spectral shift for 0.05 mIU/mL hCG, based on the tapered SNCS fibre structure by coating an anti-hCG- $\beta$  antibody onto the fibre sensor to specifically capture the hCG hormone in the analyte such as urine sample of pregnant women. The sensitivity of the sensor can be improved by adding two different types of additional microspheres (1 and 0.3  $\mu\text{m}$  diameter) functionalised with anti-hCG- $\alpha$  antibody into the analyte, which will be captured by the hCG (bind by anti-hCG- $\beta$  antibody) on the fibre sensor. The sensitivity is enhanced to 0.273 nm spectral shift for 0.01 mIU/mL hCG, by adding anti-hCG- $\alpha$  antibody modified microspheres with 1  $\mu\text{m}$  diameter in the hCG samples. Further sensitivity improvement has been achieved with sensitivity of 0.984 nm spectral shift for 0.01 mIU/mL hCG, by enriching the hCG sample using immuno-magnetic separation. The proposed sensor system has detection limit as low as 0.0001 mIU/mL provided the optical spectrum analyser has a resolution of 0.01 nm.

## Acknowledgement

Firstly, I would like to express my sincere gratitude to my principal supervisor, Dr Qiang Wu, for his continuous support, motivation, guidance, and encouragement throughout my study at Northumbria University. I am very fortunate to have such a great supervisor with an excellent experience, who not only guided me through the technical phase, but also strongly advised me on being a good researcher and on how to be a person with an excellent personality. I am also grateful to my second supervisor, Dr Wai Pang Ng, for his help and continued support. My special thanks also extend to my external supervisors, Prof. Gerald Farrell and Prof. Yuliya Semenova, from the Technological University Dublin, Ireland, and my internal examiners, Dr Zhiwei Gao, Dr Hoa Le-Minh, and Dr Richard Fu, for their valuable suggestions and useful feedback.

The Northumbria University studentship has played a big role in my PhD study, and I would like to take this opportunity to express my gratitude to the Faculty of Engineering and Environmental Sciences, Northumbria University, for this support. Moreover, I would like to thank Prof. Xingdao He from Nanchang Hangkong University, China, for inviting and supervising me to do part of my PhD research work in his labs, and Dr Bin Liu and Dr Shengpeng Wan for guiding me throughout my visit. I would also like to thank Dr Yuankui Leng from Nanchang University, China, for guiding me with his expertise and providing me with the samples for my experiments on bio-sensing. My special thanks to Dr Jie Zeng, and Xuesong Fu for their hospitality during my visit to China.

Furthermore, I would like to convey my sincere acknowledgement to the members of the Optical Communications Research Group (OCRG) and Smart Sensors Research Group at the Department of Mathematics, Physics and Electrical Engineering, Northumbria University, for their help and support during my study. I would also like to extend my sincere gratitude to my publications' equal contributing authors Dr Guorui Zhou (Gerry), Dr Dejun Liu, Xixi Li and Han Wei for their contributions.

Finally, I would like to convey my sincere acknowledgement to my family including my mother who motivate me despite of her ill-health and sad demise during my PhD, my father who motivated me to pursue a carrier in academics and research, my wife for her

unconditional love and support, my brother and sister-in-law for their continuous support and encouragement, and my nephew and niece for bringing happiness to our family.

## **Declaration**

I declare that the work contained in this thesis has not been submitted for any other award and that it is all my own work. I also confirm that this work fully acknowledges opinions, ideas and contributions from the work of others. The ethical clearance for the research presented in this thesis has been approved. The approval has been sought and granted by the Faculty Research Ethics Committee on 09/12/2015.

I declare that the word count of this Thesis is 44,831

Name: **Rahul Kumar**

Signature:

Date:

# Table of Contents

<b>Abstract</b> .....	<b>i</b>
<b>Acknowledgement</b> .....	<b>iii</b>
<b>Declaration</b> .....	<b>v</b>
<b>List of Abbreviation</b> .....	<b>ix</b>
<b>List of Figures</b> .....	<b>xii</b>
<b>List of Tables</b> .....	<b>xviii</b>
<b>List of Publication</b> .....	<b>xx</b>
<b>CHAPTER 1 Introduction</b> .....	<b>1</b>
1.1 Background to the Research.....	2
1.2 Overview of OFSs .....	3
1.2.1 Intensity-modulated OFSs.....	3
1.2.2 Phase-modulated (Interferometric) fibre optic sensors .....	9
1.2.3 Spectrometric (wavelength-modulated) fibre sensors.....	12
1.2.4 Polarimetric fibre sensors.....	16
1.2.5 Other techniques.....	17
1.3 Problem statement and Motivation.....	19
1.4 Aim and objectives .....	22
1.5 Original contributions.....	23
1.6 Thesis Structure .....	24
<b>Chapter 2 Non-tapered Optical Fibre MMI Sensors</b> .....	<b>26</b>
2.1 Introduction .....	26
2.2 Principle of the SMS Fibre Sensor .....	26
2.2.1 Theory of light propagation in an SMS fibre structure .....	26
2.2.2 Multimode interference (MMI) and Self-imaging .....	29
2.2.3 Effect of temperature and strain on SMS fibre sensors.....	30

2.3	High Sensitivity Temperature Sensor Using Hollow-core Fibre Filled with Polymer .....	32
2.3.1	Sensor structure and experimental setup.....	32
2.4	An Optical Fibre Interferometer-based Breathing Sensor.....	37
2.5	Reflective SM Sensors for Monitoring Phase Transitions in PCMs .....	43
2.6	SMS Fibre-based Structure for RI Sensing .....	55
2.7	Effect of No-core Fibre Length and Diameter on RI Sensitivity .....	57
2.7.1	Sensor structure and experimental setup.....	57
2.7.2	Simulation results.....	59
2.7.3	Experimental results.....	61
2.8	Summary .....	63
<b>Chapter 3: Singlemode Tapered No-core Singlemode (STNCS) Fibre Sensor.....</b>		<b>66</b>
3.1	Introduction .....	66
3.2	Operating Principle of the STNCS Sensor .....	66
3.2.1	Tapered SNCS optical fibre structure .....	67
3.2.2	Method of fabrication.....	68
3.2.3	Tapered optical microfibres based on an SMS structure .....	69
3.3	RI Sensitivity .....	70
3.4	Temperature Dependence.....	73
3.5	Tapered Singlemode Small-core Fibre Sensor for Magnetic Field Sensing .....	74
3.5.1	Sensor fabrication and experimental setup .....	76
3.5.2	Effect of MF concentration .....	78
3.5.3	Effect of the taper waist diameter of TSCSMF.....	79
3.5.4	Sensitivity comparison .....	80
3.5.5	Effect of magnetic field orientation .....	80
3.6	Summary .....	82

<b>CHAPTER 4: Functionalised Singlemode Tapered No-core Singlemode (STNCS) Fibre Sensor for Humidity and Biochemical Sensing.....</b>	<b>84</b>
4.1 Introduction .....	84
4.2 Principle of Operation of the Functionalised Tapered Fibre .....	84
4.2.1 Host polymers suitable for optical fibres .....	86
4.3 STNCS Fibre Sensor Functionalised with Agarose Hydro-gel for Humidity Sensing .....	88
4.3.1 Sensor fabrication and experimental setup .....	89
4.3.2 Results and discussion .....	91
4.4 STNCS Fibre Sensor for Human Chorionic Gonadotropin (hCG) Hormone Detection .....	95
4.4.1 Sensor fabrication and experimental setup .....	98
4.4.2 Results and discussion .....	101
4.5 STNCS Optical Fibre Sensor for Oxygen Sensing .....	108
4.5.1 Sensor fabrication and experimental setup .....	110
4.5.2 Results and discussion .....	112
4.6 Summary .....	117
<b>CHAPTER 5: Conclusion and Future Work .....</b>	<b>120</b>
5.1 Introduction .....	120
5.2 Conclusion from the research .....	120
5.3 Future Work .....	126
<b>References .....</b>	<b>128</b>

## List of Abbreviation

<b>Ab</b>	Antibody
<b>Ag</b>	Antigen
<b>ASM</b>	Analyte sensitive material
<b>AuNPs</b>	Gold nano-particle
<b>BSA</b>	Bovine serum albumin
<b>DSC</b>	Differential scanning calorimetry
<b>DECC</b>	Department of energy and climate change
<b>DENV</b>	Dengue virus
<b>DI</b>	De-ionised
<b>DTA</b>	Differential thermal analysis
<b>ECIS</b>	Electrochemical immunosensor
<b>EDC</b>	1-ethyl-3-(3-dimethylaminopropyl) carbodiimide hydrochloride
<b>E-field</b>	Electric field
<b>EIS</b>	Enzyme immunosensor
<b>EMI</b>	Electromagnetic interference
<b>FBG</b>	Fibre brag grating
<b>FIB</b>	Focused ion beam
<b>FMPs</b>	Ferromagnetic particles
<b>FPI</b>	Fabry-Perot Interferometer
<b>FSH</b>	Follicle-stimulating hormone
<b>HBF</b>	High birefringent fibres
<b>HCF</b>	Hollow core fibre
<b>hCG</b>	Human chorionic gonadotropin
<b>IgG</b>	Immunoglobulin G
<b>IgM</b>	Immunoglobulin M
<b>IoT</b>	Internet of things
<b>IR</b>	Infra-red
<b>LH</b>	Luteinizing hormone
<b>LOD</b>	Limit of detection
<b>LPG</b>	Long period grating

<b>LSPR</b>	Localise surface plasmon resonance
<b>MB</b>	Methylene blue
<b>MF</b>	Magnetic fluid
<b>MI</b>	Michelson Interferometer
<b>MMF</b>	Multimode fibre
<b>MMI</b>	Multimode interference
<b>MMS</b>	Magnetic microsphere
<b>MRI</b>	Magnetic resonance imaging
<b>MZI</b>	Mach-Zehnder Interferometer
<b>NCF</b>	No-core fibre
<b>NHS</b>	N-hydroxysuccinimide
<b>NIR</b>	Near infrared
<b>OC</b>	Optical circulator
<b>OFS</b>	Optical fibre sensor
<b>OMFC</b>	Optical microfibre coupler
<b>OSA</b>	Optical spectrum analyser
<b>OSHA</b>	Occupational safety and health administration
<b>OVA</b>	Ovalbumin
<b>PB</b>	Phosphate buffer (without sodium chloride)
<b>PBS</b>	Phosphate buffer saline
<b>PCF</b>	Photonic crystal fibre
<b>PCIS</b>	Photochemical immunosensor
<b>PCM</b>	Phase change material
<b>PEO</b>	Polyethylene oxide
<b>PF</b>	Perfluorinated
<b>PMF</b>	Polarization maintaining fibres
<b>PMMA</b>	Polymethyl methacrylate
<b>POC</b>	Point of Care
<b>POF</b>	Plastic optical fibre
<b>ppm</b>	Part per million
<b>PSMS</b>	Polystyrene microsphere
<b>PVA</b>	Polyvinyl alcohol
<b>rGO</b>	Reduced graphene oxide

<b>RFI</b>	Radio frequency interference
<b>RH</b>	Relative humidity
<b>RI</b>	Refractive index
<b>RIU</b>	Refractive index unit
<b>RHU</b>	Relative humidity unit
<b>SCSMF</b>	Small-core singlemode fibre
<b>SDNCF</b>	Small diameter no-core fibre
<b>SEM</b>	Scanning electron microscope
<b>SI</b>	Sagnac interferometer
<b>SLD</b>	Super luminescent diode
<b>SLP</b>	Solid-liquid phase change
<b>SM</b>	Singlemode-multimode
<b>SMF</b>	Singlemode fibre
<b>SMHMS</b>	Singlemode-multimode-hollow core-multimode-singlemode fibre
<b>SMS</b>	Singlemode multimode singlemode fibre
<b>SNCS</b>	Singlemode no-core singlemode fibre
<b>SPR</b>	Surface plasmon resonance
<b>SPW</b>	Surface plasmon wave
<b>SRI</b>	Surrounding refractive index
<b>STMS</b>	Singlemode-tapered multimode-singlemode fibre
<b>STNCS</b>	Singlemode tapered no-core singlemode fibre
<b>STSCS</b>	Singlemode tapered small-core singlemode fibre
<b>SV</b>	Streptavidin
<b>TCM</b>	Thermochemical material
<b>TEOS</b>	Tetraethyl orthosilicate
<b>TFBG</b>	Tilted fibre bragg grating
<b>TOC</b>	Thermo-optic coefficient
<b>TSH</b>	Thyroid stimulating hormone

## List of Figures

<b>Figure 1.1.</b> Basic block diagram of an OFS system.....	3
<b>Figure 1.2.</b> Illustration of the bending loss mechanism .....	6
<b>Figure 1.3.</b> Illustration of (a) evanescent field trapped inside the cladding layer of a conventional optical fibre (b) evanescent field in a tapered optical fibre.....	6
<b>Figure 1.4.</b> Illustration of an all-fibre FPI.....	9
<b>Figure 1.5.</b> Basic configuration of the two-path fibre MZI.....	10
<b>Figure 1.6.</b> Basic configuration of the two path fibre MI.....	11
<b>Figure 1.7.</b> Basic configuration of an optical fibre SI.....	12
<b>Figure 1.8.</b> Illustration of a FBG .....	13
<b>Figure 1.9.</b> Schematic diagram of (a) LPG and (b) TFBG.....	14
<b>Figure 1.10.</b> Schematic diagram of a typical polarimetric fibre sensor .....	16
<b>Figure 1.11.</b> Kretschmann’s configuration for SPR.....	18
<b>Figure 1.12.</b> Classification of major OFSs considered for this research work: Level-1 represents classification based on spatial orientation, Level-2 represents classification based on the optical parameter used for detection and the major fabrication techniques combined, and Level 3 represents the major types of each classification. ....	19
<b>Figure 2.1.</b> Schematic diagram of the SMS fibre structure.....	27
<b>Figure 2.2.</b> Calculated spectral response of an SMS fibre structure, with an MMF length of 42.877 mm. ....	28
<b>Figure 2.3.</b> Simulation result showing the self-imaging property in an MMF with a core diameter of 105 $\mu\text{m}$ (reproduced from Q. Wang <i>et al.</i> JLT, vol. 26, no. 5, pp. 512–519, 2008) .....	29
<b>Figure 2.4.</b> (a) Simulation results showing the effect of change in a temperature, in temperature range 25 – 85 $^{\circ}\text{C}$ , on an SMS fibre structure with 10 cm length of MMF, and (b) comparison between the simulations and experimental results. ....	31
<b>Figure 2.5.</b> (a) Simulation results showing the effect of change in strain, from 0 – 3069 $\mu\epsilon$ , on an SMS fibre structure with 10 cm length of MMF, and (b) comparison between the simulations and experimental results. ....	31
<b>Figure 2.6.</b> Schematic diagram of a singlemode-multimode-hollow core-multimode-single mode fibre structure .....	33

<b>Figure 2.7.</b> Schematic diagram of the experimental setup used to measure the temperature sensitivity of the SMHMS structure.....	33
<b>Figure 2.8.</b> Spectral response for 10 mm of MMF and 10, 15 and 20 mm lengths of the polymer-filled HCF in the SMHMS structure. ....	35
<b>Figure 2.9.</b> Experimental results for the wavelength shift vs. change in temperature for the SMHMS structure with a 5mm MMF length and various HCF lengths.....	35
<b>Figure 2.10.</b> Temperature sensitivities for the sensors with two different MMF lengths as a function of different lengths (10, 15 and 20mm) of the polymer-filled HCF.....	36
<b>Figure 2.11.</b> Schematic diagram and a photograph of the real prototype of the oxygen mask with an embedded SMS structure. ....	38
<b>Figure 2.12.</b> Schematic diagram of the breath monitoring experimental setup. ....	39
<b>Figure 2.13.</b> Spectral responses of the SMS-based breath sensor during the inhalation and exhalation processes.....	40
<b>Figure 2.14.</b> Experimentally recorded breathing pattern and dynamic threshold in real-time (upper plot) and the corresponding breath analysis program’s response to a regular breathing pattern (lower plot).....	41
<b>Figure 2.15.</b> Experimentally recorded breathing pattern and dynamic threshold in real-time (upper plot) and the corresponding breath analysis program’s response to an irregular breathing pattern (lower plot).....	42
<b>Figure 2.16.</b> Experimentally recorded breathing pattern and dynamic threshold in real time (upper plot) and the corresponding breath analysis program’s response to an urgent breathing pattern (lower plot).....	42
<b>Figure 2.17.</b> Experimentally recorded breathing pattern and dynamic threshold in real time (upper plot) and the corresponding breath analysis program’s response to a slow breathing pattern (lower plot).....	43
<b>Figure 2.18.</b> Schematic diagram of the reflective SM optical fibre structure. ....	45
<b>Figure 2.19.</b> Schematic diagram of the experimental setup used for measuring the phase change ( $\delta\phi$ ) of PCM.....	46
<b>Figure 2.20.</b> Measured wavelength shift ( $\Delta\lambda$ ) vs. temperature ( $T$ ) for the platinum-coated SM structure with MMF length of: (a) 5 mm, and (b) 10 mm. Two sets of measurements were taken by heating and then cooling the paraffin wax over a temperature range of 30.0 °C – 70.0 °C.....	47

<b>Figure 2.21.</b> Comparison between the measured temperature ( $T$ ) and the wavelength shift ( $\Delta\lambda$ ) as a function of time ( $t$ ) for the paraffin wax over $30\text{ }^{\circ}\text{C} < T < 73\text{ }^{\circ}\text{C}$ for: (a) heating cycle, and (b) cooling cycle. The typical spectral response of the reflective SM sensor with a 5 mm long MMF during different phase states of the paraffin wax are also presented. ....	49
<b>Figure 2.22.</b> Comparison between the measured temperature ( $T$ ) and the wavelength shift ( $\Delta\lambda$ ) obtained using a reflective SM sensor with a 10 mm long MMF, as a function of time ( $t$ ) for the paraffin wax over a temperature range of $30.0\text{ }^{\circ}\text{C} < T < 73.0\text{ }^{\circ}\text{C}$ for: (a) heating, and (b) cooling cycles. ....	50
<b>Figure 2.23.</b> Measured wavelength shift ( $\Delta\lambda$ ) vs. temperature ( $T$ ) for the platinum coated SM structure with an MMF length of 5 mm for (a) SM46, and (b) SM32. ....	52
<b>Figure 2.24.</b> Comparison between the measured temperature ( $T$ ) and the wavelength shift ( $\Delta\lambda$ ) obtained using a reflective SM sensor with a 5 mm long MMF, as a function of time ( $t$ ) for (a) S46 and (b) S32 during the heating and cooling cycles. ....	53
<b>Figure 2.25.</b> Schematic diagram of a singlemode – no-core – singlemode optical fibre sensor .....	56
<b>Figure 2.26.</b> Schematic diagram of a singlemode – small core – singlemode optical fibre sensor .....	56
<b>Figure 2.27.</b> Schematic diagram of two main types of photonic crystal fibres (PCF) (a) index-guiding PCF and (b) photonic bandgap PCF. ....	57
<b>Figure 2.28.</b> Schematic diagram of the proposed fibre structure as a refractometer.....	58
<b>Figure 2.29.</b> Experimental setup used for RI sensing. ....	58
<b>Figure 2.30.</b> Simulated spectral response of the sensor at different surrounding RIs; and (b) dip wavelength shift vs. surrounding RI and its linear fit. ....	60
<b>Figure 2.31.</b> Simulated wavelength shift vs. surrounding RI for different lengths of the SDNCF: (a) $L = 12, 15,$ and $18\text{ mm}$ and $D = 55\text{ }\mu\text{m}$ ; (b) $L = 15, 20,$ and $25\text{ mm}$ and $D = 125\text{ }\mu\text{m}$ ; and (c) $D = 35, 45, 55,$ and $125\text{ }\mu\text{m}$ and $L = 15\text{ mm}$ . ....	60
<b>Figure 2.32.</b> Experimentally measured (a) spectral responses, and (b) wavelength shift of the RI sensor with $D = 55\text{ }\mu\text{m}$ in various RI liquids. ....	62
<b>Figure 2.33.</b> Measured wavelength shifts for RI sensors with $L = 15, 20,$ and $25\text{ mm}$ and $D = 125\text{ }\mu\text{m}$ in various RI liquids .....	62
<b>Figure 3.1.</b> Schematic diagram of a tapered SNCS fibre. ....	67
<b>Figure 3.2.</b> The experimental setup used for fabricating tapered optical fibres.....	69

<b>Figure 3.3.</b> Simulated (a-c) spectral response and (d-f) RI sensitivity of the STNCS OFS with 8 $\mu\text{m}$ taper waist diameter in the three RI ranges of 1.33, 1.37, and 1.41 respectively. ....	72
<b>Figure 3.4.</b> Experimentally observed RI sensitivity for the STNCS optical fibre sensor with 8 $\mu\text{m}$ taper waist diameter for the three RI ranges around (a) 1.33, (b) 1.37, and (c) 1.41 RI ranges .....	73
<b>Figure 3.5.</b> Temperature sensitivity of the STNC optical fibre with 6 $\mu\text{m}$ tapering diameter. ....	74
<b>Figure 3.6.</b> Schematic diagram of (a) the experimental setup, and (b) the tapered small-core singlemode optical fibre sensor surrounded by the magnetic fluid, for the purpose of magnetic field sensing.....	77
<b>Figure 3.7.</b> Examples of spectral responses observed while increasing the magnetic field around the TSCSMF fibre magnetic sensor with 10 $\mu\text{m}$ diameter surrounded by MF with (a) 0.39%, (b) 0.81%, and (c) 1.22% FMPs. ....	78
<b>Figure 3.8.</b> Wavelength shift caused due to the change in magnetic field strength for the TSCSMF of 10 $\mu\text{m}$ tapering diameter encapsulated in (a) 0.39% (b) 0.81% and (c) 1.2% FMPs in MF. ....	79
<b>Figure 3.9.</b> Wavelength shift vs magnetic field strength of TSCSMF with waist diameters of (a) 20 $\mu\text{m}$ (b) 15 $\mu\text{m}$ and (c) 10 $\mu\text{m}$ , surrounded with different concentrations (0.39, 0.81, 1.22 %FMPs) of MF. ....	79
<b>Figure 3.10.</b> Magnetic sensitivity comparison for the TSCSMFS optical fibre sensors with 10, 15, and 20 $\mu\text{m}$ diameters surrounded by 0.39, 0.81, and 1.22 %FMPs in the MF.....	80
<b>Figure 3.11.</b> (a) The experimental setup used for measuring the angular magnetic field dependence in the X-Y plane; and (b) wavelength shift from $\lambda_0$ when the rotation angle changes from $0^\circ$ to $360^\circ$ in the X-Y plane. ....	81
<b>Figure 3.12.</b> Schematic of the experimental setup used for measurements of the angular field dependence in (a) the X-Z, and (b) the Y-Z plane; (c) Experimentally measured wavelength shift from $\lambda_0$ versus angle from $0^\circ$ to $360^\circ$ in the X-Z and Y-Z planes for different magnetic field strength values. ....	82
<b>Figure 4.1.</b> Schematic demonstration of (a) labelled and (b) label-free bio-sensing. ....	85
<b>Figure 4.2.</b> Schematic demonstration of the two major methods used for chemical sensing: (a) the molecular imprinting method, and (b) the reagent entrapment in the polymer matrix. ....	86

<b>Figure 4.3.</b> Schematic of the three most common methods for immobilising the ASM in a host polymer matrix. In (a), the ASM molecules (blue dots) are homogeneously distributed in the host polymer (orange). In (b), the ASM molecules are adsorbed on the surface of micro or nanoparticles (green), which are then incorporated into the host polymer. In (c), the ASM molecules are first homogeneously distributed in micro or nanoparticles (red), which are then incorporated into the host polymer.....	88
<b>Figure 4.4.</b> (a) Schematic diagram of the STNCS optical fibre coated with agarose hydro-gel. (b) SEM image of the STNCS taper waist cross-section after coating, and (c) the bend radii measured using optical microscope. ....	90
<b>Figure 4.5.</b> Schematic diagram of the experimental setup used for measuring humidity. ...	91
<b>Figure 4.6.</b> Spectral response of (a) the straight STNCS optical fibre RH sensor, and (b) the loop STNCS optical fibre sensor. ....	92
<b>Figure 4.7.</b> Wavelength shift versus RH for the straight STNCS and loop STNCS with 0, 0.045, 0.101, and 0.198 $\mu\text{m}$ hydro-gel coating thicknesses, over (a) complete range of 35 – 85 %RH (b) linear range of 35 – 70 %RH. ....	92
<b>Figure 4.8.</b> Comparison of the RH sensitivities of the straight STNCS and the STNCS loop. ....	93
<b>Figure 4.9.</b> (a) Response and recovery times for the STNCS loop, (b) comparison of the response and recovery times of the straight STNCS and STNCS loop OFSs with 0.045, 0.101, and 0.198 $\mu\text{m}$ hydro-gel coating thickness. ....	94
<b>Figure 4.10.</b> Schematic diagram of (a) the STNCS optical fibre structure, and (b) the RI change caused by the bonding of hCG and anti-hCG- $\alpha$ Ab modified MMSs on the fibre surface, immobilised with anti-hCG- $\beta$ Ab. ....	98
<b>Figure 4.11.</b> Stability of STNCS in PBS. ....	99
<b>Figure 4.12.</b> (a) The surface modification and Ab immobilisation procedure. (b) The experimental setup for hCG detection. (c) The functionalized fibre sensor used for hCG detection and sensitivity enhancement using MMSs. (d) SEM images for the STNCS waist cross-section, functionalised fibre after hCG detection, and the anti hCG- $\alpha$ modified MMSs binding on the fibre surface. ....	100
<b>Figure 4.13.</b> Spectral response from STNCS fibre sensor modified with 16 $\mu\text{g}/\text{mL}$ of capture Ab concentration, to detect (a) 0.05 mIU/mL (b) 5 mIU/mL and (c) 500 mIU/mL of hCG concentration in urine sample .....	102

<b>Figure 4.14.</b> Investigation of the effect of capture Ab concentrations on the STNCS fibre surface for detecting entire range from 0.05 – 5000 mIU/mL of the hCG in urine samples .....	103
<b>Figure 4.15.</b> (a) Standard curve and repeatability test, and (b) selectivity test for the STNCS optical fibre sensor immobilised with 16µg/mL of capture Ab. ....	103
<b>Figure 4.16.</b> Comparison of the two-step and direct incubation processes of functionalised STNCS fibre with hCG and MMSs. ....	105
<b>Figure 4.17.</b> Sensitivity improvement for the 0.01, 0.05, and 0.25 mIU/mL concentrations of hCG obtained by adding MMSs with 300 nm and 1 µm diameters, and by the enrichment process.....	106
<b>Figure 4.18.</b> Schematic diagram of functionalized STNCS optical fibre sensor; Inset SEM images of coated STNCS. ....	111
<b>Figure 4.19.</b> Schematic diagram of the experimental set-up.....	112
<b>Figure 4.20.</b> Intensity variations of the STNCS optical fibre sensor with 2 µm taper waist diameter and 0.86 µm coating thickness of MB sol-gel for different concentrations of oxygen: (a) with respect to wavelength and (b) with respect to time. ....	113
<b>Figure 4.21.</b> The change in intensity as a function of different oxygen concentrations for 2 and 4 µm taper waist diameters of STNCS OFS, coated with 0.39, 0.69, and 0.89 µm layer thickness of MB sol-gel; and un-tapered 125 µm of SNCS optical fibre sensor coated with 0.86 µm coating thickness of MB sol-gel. ....	114
<b>Figure 4.22.</b> Effect of coating thickness and diameter of the STNCS OFS on sensitivity. ....	115
<b>Figure 4.23.</b> Selectivity test for MB-Sol gel coated STNCS optical fibre sensor with a 2 µm taper waist diameter and a coating thickness of 0.86 µm. ....	116
<b>Figure 4.24.</b> Repeatability test for the STNCS OFS with a 2 µm taper waist diameter and a coating thickness of 0.86 µm. ....	116

## List of Tables

<b>Table 2.1.</b> Summary of parameters used in the simulation model of SMS fibre structure	.28
<b>Table 2.2.</b> Summary of SMHMS fibre structure parameters and specifications of components used in the experimental setup, for temperature sensing	.....34
<b>Table 2.3.</b> Comparison of the change in average sensitivity as a function of increasing lengths of MMF and polymer-filled HCF in the SMHMS structure	.....36
<b>Table 2.4.</b> Summary of SMS fibre structure parameters and specifications of components used in the experimental setup, for breath rate monitoring	.....39
<b>Table 2.5.</b> Summary of reflective SM fibre structure parameters and specifications of components used to build the experimental setup, for phase change monitoring	.....46
<b>Table 2.6.</b> Measured temperature ( $T$ ) for different phase states of the paraffin wax for the sensor with 5 and 10 mm long MMFs	.....51
<b>Table 2.7.</b> Measured temperature ( $T$ ) values for different phase states of S46 and S32 using the SM sensor with a 5 mm long MMF	.....54
<b>Table 2.8.</b> Summary of reflective SDNCF fibre structure parameters and specifications of components used to build the experimental setup, for RI measurement	.....59
<b>Table 3.1.</b> Summary of parameters used in the simulation model of tapered SNCS OFS structure	.....71
<b>Table 3.2.</b> Comparison between the RI sensitivities of different fibre replacements of MMF in the STMS OFS structure	.....73
<b>Table 3.3.</b> Summary of the TSCSMF fibre structure parameters and specifications of components used in the experimental setup, for magnetic field sensing	.....77
<b>Table 3.4.</b> Sensitivity values for the TSCSMF optical fibre sensors of 10, 15, and 20 $\mu\text{m}$ diameters surrounded by 0.39, 0.81, and 1.22 %FMPs in the MF	.....80
<b>Table 4.1.</b> Summary of the STNCS OFS parameters coated with hydrogel and specifications of components used in the experimental setup, for humidity sensing	.....91
<b>Table 4.2.</b> RH sensitivities of the straight and loop STNCS with 0, 0.045, 0.101, and 0.198 $\mu\text{m}$ hydro-gel coating thicknesses	.....93
<b>Table 4.3.</b> Response and recovery times for the straight STNCS and loop STNCS OFSs coated with 0.045, 0.101, and 0.198 $\mu\text{m}$ thick layers of hydro-gel	.....94

<b>Table 4.4.</b> Summary of the STNCS OFS and MMSs parameters, functionalised with hCG- $\beta$ and hCG- $\alpha$ Abs respectively, and specifications of components used in the experimental setup, for detecting hCG. ....	101
<b>Table 4.5.</b> Experimentally recoded values of wavelength shift observed for 0.01, 0.05, and 0.25 mIU/mL concentration of hCG for the three methods described above. ....	107
<b>Table 4.6.</b> Summary of the STNCS OFS parameters coated with MB sol-gel, and specifications of components used in the experimental setup, for oxygen sensing. ....	112
<b>Table 4.7.</b> Experimentally measured sensitivities for all STNCS optical fibre sensors with different coating layers of MB sol-gel. ....	115

## List of Publication

### Journal Publication

- [1] **R. Kumar**, W. Han, D. Liu, *et al.*, “Optical fibre sensors for monitoring phase transitions in phase changing materials,” **Smart Materials and Structures**, vol. 27, no 10, pp. 105021, 2018.
- [2] G. Zhou, **R. Kumar\***, Q. Wu, *et al.*, “A simple all-fibre comb filter based on the combined effect of multimode interference and Mach-Zehnder interferometer,” **Scientific reports**, vol. 8, no. 1, pp. 11803, 2018. (\*equal contribution)
- [3] G. Zhou, Q. Wu, **R. Kumar\***, *et al.* “High sensitivity refractometer based on reflective SMF-small diameter no-core fibre structure”, **Sensors**, vol. 17, pp. 1415, 2017. (\*equal contribution).
- [4] X. Li, D. Liu, **R. Kumar\***, *et al.* “A simple optical fibre interferometer based breathing sensor,” **Measurement Science and Technology**, vol. 28, pp. 035105, 2017. (\*equal contribution).
- [5] D. Liu, **R. Kumar**, F. Wei, *et al.*, “High sensitivity optical fibre sensors for simultaneous measurement of methanol and ethanol”, **Sensors and Actuators B: Chemical**, vol. 271, pp. 1-8, 2018.
- [6] D. Liu, **R. Kumar**, F. Wei, *et al.*, “Highly sensitive twist sensor based on partial silver coated hollow core fibre structure”, **Journal of Lightwave Technology**, vol. 36, no. 17, pp. 3672-3677, 2018.
- [7] L. Niu, G. Zhou, X. Miao, X. Yuan, **R. Kumar**, *et al.*, “Micro/Nanofibre with Hollow Silica Nanoparticles Thin-Film for Airborne Molecular Contaminants Real-Time Sensing,” **Advances in Condensed Matter Physics 2018**, vol. 11, pp. 1-6, 2018.
- [8] D. Liu, Q. Wu, C. Mei, J. Yuan, X. Xin, A. Mallik, F. Wei, W. Han, **R. Kumar** *et al.*, “Hollow Core Fibre Based Interferometer for High Temperature (1000 °C) Measurement”, **Journal of Lightwave Technology**, vol. 36, no. 9, pp. 1583-1590, 2018.

## **Conference Publication**

[1] **R. Kumar**, W. Han, D. Liu, *et al.*, “Singlemode-multimode-singlemode fibre structure for phase transition monitoring in phase changing materials.” **Journal of Physics: Conference Series**, vol. 1065, no 25, pp. 252024, 2018.

[2] **R. Kumar**, D. Liu, JH. Yuan, *et al.*, “Tapered no-core optical fibre for oxygen sensing”, in 11th International Symposium on Communication Systems, Networks, and Digital Signal Processing (**CSNDSP**), Budapest, 2018.

[3] **R. Kumar**, W. P. Ng, Y. Q. Fu, *et al.*, “High sensitivity temperature sensor based on a polymer filled hollow core optical fibre interferometer”, in 25th International Conference on Optical Fibre Sensors (**OFS-25**), Jeju, Korea, vol. 10323, pp.1-4, 2017.

# CHAPTER 1 Introduction

Optical fibre devices have attracted significant research interest since the development of low loss optical fibre in the 1960s [1]. Since then, optical fibre devices have been thoroughly investigated in many fields ranging from optical sensing to optical communication due to their exceptional properties including compact size, wide bandwidth, and immunity to electromagnetic interference (EMI). Of the various application areas relevant to optical fibre devices, sensing is of special importance since it is the prerequisite in almost every technology, starting from automation and entertainment to transportation and medical and environmental monitoring. Furthermore, the recent advances in nano-technology have made the realisation of miniature sensors with high sensitivity and remote sensing capability a realistic possibility.

The first few sensing experiments using optical fibres were conducted in the early 1970s and involved the demonstration of acoustic waves interaction with an optical fibre that was sensitive enough to develop an optical fibre microphone [2] and an optical fibre strain sensor to measure strains of less than  $0.4 \mu\epsilon$  (micro-strain) [3]. Since then, the field of optical fibre sensors (OFSs) has continued to progress and develop enormously. Currently, optical fibres utilising distributed fibre sensing technology are installed in bridges and dams for structural monitoring of such facilities. Furthermore, OFSs are now an integral part of the wings of airplanes and wind turbines to monitor the wear and tear due to the stress exerted on the structure. In addition, OFS technology has provided novel solutions for real time monitoring applications, where electronic sensors are either hindered by the EMI or are impractical and hazardous to use, such as in oil wells, gas pipelines and nuclear and thermal power plants. In the field of biomedical diagnosis, the current requirement is miniature sensors for real-time diagnosis of biomolecules, for which optical fibre have such capability. Furthermore, traditional surgery is almost being redefined by the use of optical fibres, where scalpels are getting replaced by low loss optical fibres to transmit laser energy for laparoscopy. Optical fibres have also revolutionised the field of biomedical imaging after the introduction of the endoscopy procedure.

This chapter introduces the fundamentals of optical fibre sensing and presents an overview of the major categories of fibre sensors to form the base for the rest of the chapters in this thesis.

## 1.1 Background to the Research

A sensor is a device that is used to measure any physical, chemical or biological property of the measurand and respond with a feedback in terms of an alternative form of energy such as an electrical, acoustic or optical signal which can then be processed, transmitted, and correlated to the change in property of the measurand. In this context, an optical fibre sensor can be defined as a means through which physical, chemical, or biological measurand interacts with the light guided through an optical fibre to produce a modulated optical signal with information related to the measured parameter [4]. The basic concept of this fibre optic sensing system is demonstrated in Figure 1.1, where the light guided through an optical fibre is modulated due to its interaction with the external parameter or measurand. The modulated signal is then carried to the detector, which extracts the measurand information from the modulated optical signal. Depending on the type of the fibre sensor and its operating principle, the sensor system operates either in transmission mode, where the sensor has an individual input and output port, or in reflection mode, where the output signal from the sensor is reflected back to the input port for detection.

Due to negligible losses in optical fibres, the earliest OFSs were extrinsic and used the optical fibre only to carry the light to the actual sensing site. An optical fibre proximity probe was patented in 1967 to measure minute rotations by analysing the amount of reflected light from the surface positioned near the fibre probe [5]. Davies and Kingsley [6] in 1974 showed the effect of mechanical tension over a short section of fibre which phase modulated the optical signal. This proved to be the stepping stone for developing fibre-based intrinsic transducers.

OFSs have all the merits for a desirable sensor such as being lightweight and having low power consumption, high sensitivity and bandwidth, multiplexing capability and multifunctional sensing potential. OFSs have significant advantages over traditional electronic sensors such as immunity to EMI, electrical non-conductivity, environmental ruggedness, resistance to humidity and chemical corrosions, easy structural integration and remote operation capability. Even though OFSs have many advantages over their electrical counterparts, they have some limitations and disadvantages such as their high initial set-up cost, long term stability, relatively low transduction efficiency and system complexity. However, in the near future, as more research, commercialisation, and standardisation efforts are performed, it is expected that some of these current limitations will be addressed.

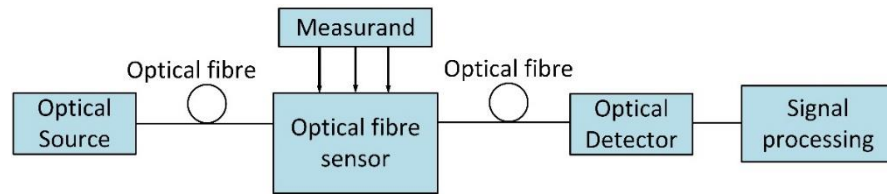


**Figure 1.1.** Basic block diagram of an OFS system.

## 1.2 Overview of OFSs

To date, several different approaches have been used to categorise OFSs. However, it is difficult to categorise all the possible types of fibre sensors due to the scale and rate of development of new sensing schemes. Depending on the light property that is modified by the measurand, OFSs are mainly classified into four main categories:

- Intensity-modulated sensors
- Phase-modulated (interferometric) sensors
- Polarization-modulated (polarimetric) sensors
- Wavelength-modulated (spectrometric) sensors

A summary of the major classifications of OFSs with a view to this research work is discussed in this section and is graphically illustrated in Figure 1.12 at the end of this section. Based on spatial sensing resolution, OFSs can be broadly classified into three types, namely point, quasi-distribute and distributed OFSs. A point sensor is used to measure the desired parameter only at a discrete point. However, with spatial multiplexing, such a sensor has potential to be used to analyse multiple points and parameters over a broader area and is classified as a quasi-distributed sensor. On the other hand, distributed fibre sensors utilise phenomena such as Rayleigh, Raman and Brillouin scattering in the fibre to provide spatial and temporal information of the measurand along any point on a single fibre over a broad area. This research work is dedicated to developing a point sensor. Therefore, in the further discussion to follow, we focus on the point sensors in the four-major classifications mentioned earlier.

### 1.2.1 Intensity-modulated OFSs

Intensity-modulated sensors are one of the earliest OFSs in which the intensity of the guided light is modulated either to detect mechanical perturbation on the sensor, or a property of the

surrounding medium due to the absorption of light. The advantages of intensity-modulated OFSs include the ease of fabrication and their simple detection system and signal processing requirements. However, intensity changes can be introduced due to other undesirable sources such as optical fibre bending, splice misalignment, and source power fluctuation, which makes intensity-modulated optical fibre sensing platforms unreliable. One solution for this problem is intensity referencing, where a fraction of the input light is used for monitoring the input power fluctuation. Two of the common intensity-modulated OFSs are fibre bend sensors and evanescent wave sensors.

(i) Fibre bend sensors

Bending of optical fibres found their early application in mechanical systems to determine the displacement, rotation, alignment, and bending angle of the system. Over the years, fibre bend sensors have been configured for measuring physical parameters such as pressure, temperature, and refractive index (RI). An illustration of the bending loss mechanism is shown in Figure 1.2. Depending on the scale of fibre bend, effects associated with bending in multimode fibres (MMFs) and singlemode fibres (SMFs) are classified into micro bend and macro bends.

**Micro bending** occurs in a MMF, where the mechanical perturbations cause the redistribution of light power among the multiple modes in the fibre. With the increase in severity of mechanical perturbations or bending, more light is coupled into the radiating modes and is therefore lost. Therefore, the light intensity is proportional to the bending radius, and micro-bend losses are observed if the fibre is bend beyond the critical bending radius ( $R < R_c$ ) given by the following equation [7]:

$$R_c = \frac{2\pi a}{(2\Delta n)^{1/2}} \quad 1.1$$

where  $a$  is the core radius, and  $\Delta n$  is the difference in core and cladding refractive index (RI). These sensors suffer from modal sensitivity and high insertion loss and are not as sensitive as the interferometric sensors.

An SMF is generally used for **Macro bending** OFSs with a relatively large bend diameter ( $R \geq R_c$ ). The power loss in the core of the SMF is due to a uniform bend yielding two forms of loss: a pure bend loss and a transition loss [8]. The pure bend loss results from the guidance loss at the outer portion of the fibre core, where the phase velocity of the fundamental modes become equal to the speed of light in the cladding, which leads to leaking

light from the core into the cladding at the bend. Transition loss arises due to the change in mode field characteristics whenever there is a change in curvature. The mode profile in the straight fibre shifts radially outward at the bend, which couples some of the power from the guided mode to the radiating mode whenever there is a change of curvature.

Macro and micro bend sensors can be used in similar applications. For instance, Wang *et al.* in [9] demonstrated a displacement sensor with a resolution of sub-50 nm displacement based on a high bend loss SMF (1060XP, Nufern) with a bend diameter of 15 mm, using a ratio metric measurement system. An SMF-MMF-SMF (SMS) based curvature sensor was demonstrated by Gong *et al.* with a maximum wavelength-curvature sensitivity of  $-10.38 \text{ nm/m}^{-1}$  and an intensity-curvature sensitivity of  $-130.37 \text{ dB/m}^{-1}$  [10]. In 2013, Wang *et al.* introduced 37 mm length of SMF between two SMF-MMF fibre structures to excite cladding modes and make the fibre sensor structure sensitive to RI. A maximum curvature sensitivity of  $-14.40 \pm 0.02 \text{ nm/m}^{-1}$  was achieved, with a temperature cross-sensitivity of  $4.354 \times 10^{-3} \text{ m}^{-1}/^{\circ}\text{C}$  [11]. Recently, Wang *et al.* introduced a 45 mm length of a seven-core fibre (7CF) in between two SMF-MMF fibre structures to enhance the temperature sensitivity to  $55.81 \text{ pm}/^{\circ}\text{C}$ , where the maximum curvature sensitivity was  $31.54 \text{ nm/m}^{-1}$  over the curvature range of  $0.45 - 1.01 \text{ m}^{-1}$  [12]. A fibre Bragg grating (FBG) with a grating period of  $1.0739 \text{ }\mu\text{m}$  and 15 mm length was demonstrated in [13] with a curvature sensitivity of  $18.90 \text{ }\mu\text{W/m}^{-1}$  within a small curvature range of  $0.0 - 1.2 \text{ m}^{-1}$ , a resolution of  $0.0054 \text{ m}^{-1}$  and no temperature cross-sensitivity. In [14], a long period grating (LPG) inscribed with two cascaded gratings with  $6^{\circ}$  tilt opposite to each other was demonstrated, with a curvature sensitivity of  $+15.2825 \text{ nm/m}^{-1}$  and  $-15.4935 \text{ nm/m}^{-1}$  for bending along the +Y-axis and -Y-axis, respectively, and a temperature cross-sensitivity of  $0.0406 \text{ nm}/^{\circ}\text{C}$  and  $0.0286 \text{ nm}/^{\circ}\text{C}$  for the two spectral dips. A comparison between a straight and a micro-bend tapered no-core fibre sensor is experimentally demonstrated in Chapter 4 of this thesis for a humidity sensing application.

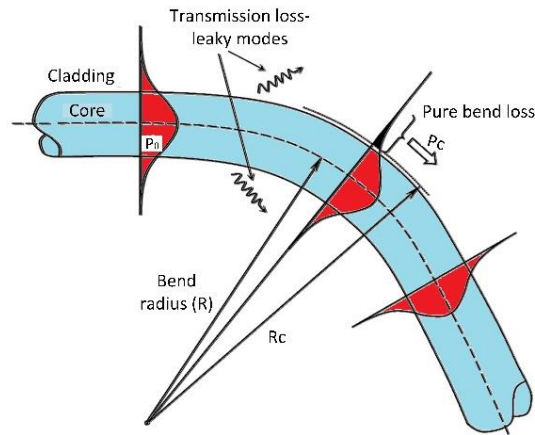


**Figure 1.2.** Illustration of the bending loss mechanism

(ii) Evanescent field-based sensors

In a conventional optical fibre, light propagates by means of total internal reflection (TIR) inside the fibre's core. However, for light reflecting at the core-cladding interface, a portion of the electromagnetic field extends into the cladding layer, as shown in Figure 1.3 (a). This extended field is called the evanescent field. The power within the evanescent field decays exponentially with distance from the core, and the penetration depth up to which the evanescent field extends into the surrounding medium is calculated using the following equation [15]:

$$d_p = \frac{\lambda}{2\pi\sqrt{n_{co}^2 \sin^2 \theta - n_{cl}^2}} \quad 1.2$$

where  $d_p$  is called the penetration depth,  $n_{co}$  and  $n_{cl}$  are the RI's of the core and cladding, respectively,  $\theta$  is the angle of reflection of the light at core-cladding interface, and  $\lambda$  is the wavelength of the light source.

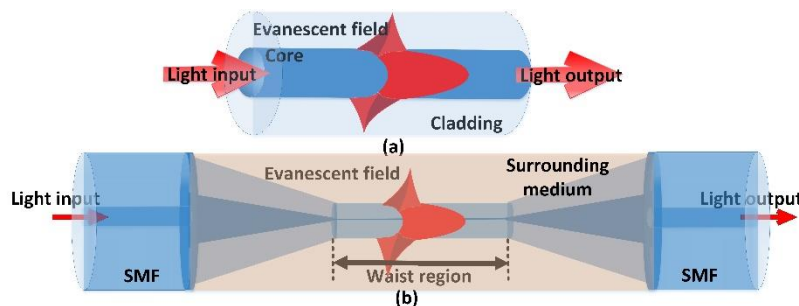


**Figure 1.3.** Illustration of (a) evanescent field trapped inside the cladding layer of a conventional optical fibre (b) evanescent field in a tapered optical fibre.

In a conventional optical fibre, the thickness of the cladding layer is sufficient to trap this evanescent field within the fibre structure. However, if the cladding layer is either removed or its thickness is reduced to  $\sim 1 \mu\text{m}$ , the evanescent field can be exposed to the fibre's surrounding, which is the basis of the concept behind evanescent field fibre sensors. These sensors perform the sensing function by utilising the interaction between the evanescent field and the local environment surrounding the fibre surface, as shown in Figure 1.3 (b). The evanescent field within the fibre can be exposed by reducing the cladding layer through side polishing the optical fibre. For example, three different polishing depths and bend radii in a plastic optical fibre were investigated for RI sensing in [16]. In [17], a side polished U-shaped plastic optical fibre (POF) with a step index profile was used to measure the transmitted power in glycerine solution of 1.33 – 1.44 RI range, demonstrating a maximum sensitivity of 817 %/RIU (refractive index unit) when the curvature radius, polishing depth and length were 2 mm, 400  $\mu\text{m}$ , and 10 mm, respectively. A side polished SMS fibre structure was demonstrated in [18] with a maximum RI sensitivity of 1190 nm/RIU (which is comparable with the chemical etching process) within an RI range of 1.43-1.45 for a polishing depth of 20.6  $\mu\text{m}$ . In [19], the temperature sensitivity of a side-polished singlemode fibre was demonstrated to be 0.5 dB/ $^{\circ}\text{C}$ , where the fibre had an initial curvature radius of 2.25 cm and was dipped in commercial grade vegetable oil, which exhibits RI variation with temperature. A side polished FBG was demonstrated in [20] with a maximum RI sensitivity of 300 nm/RIU at RI  $\sim 1.455$  and a Bragg wavelength of 980 nm. Furthermore, it can be calculated that this sensitivity can be improved to 340 nm/RIU for a Bragg wavelength of 1290 nm. A temperature cross-sensitivity of 10.9 pm/K was also monitored by another FBG inscribed in the same fibre. Such side polishing or chemical etching of the cladding layer is also popular for bio and chemical sensing, as demonstrated in [21] for DNA detection by depositing poly-L-lysine (PLL) on the polished surface between two LPG gratings with a period of 600  $\mu\text{m}$ . The RI sensitivity of the sensor was 909.1 nm/RIU, and a spectral shift of 1.82 nm was demonstrated after 65 minutes of interaction with a single strain DNA. In [22], a side polished POF with a polished length of 2 cm and depth of 60  $\mu\text{m}$  was coated with graphene and polyaniline nanocomposite and was used for ammonia sensing with a maximum sensitivity of 132.8 a.u./ $\text{NH}_3\%$  (a.u.- arbitrary unit).

Micro and nano fibres, which are fabricated by heating and stretching the conventional optical fibre to reduce its diameter to few micrometres or even nanometres, are another typical evanescent field-based sensor technology. Such a fibre sensor has the advantage of

providing a smooth and lossless connection to optical components. In addition, the taper profile can be precisely controlled by controlling the pulling function [23]. This makes microfibres and nano-fibres exhibit remarkable optical and mechanical properties, including large evanescent fields, strong optical confinement, flexibility, configurability, and robustness [24]. For instance, a tapered SMF was demonstrated in [25] with a maximum RI sensitivity of 1545.355 nm/RIU with a taper waist diameter and waist length of 15  $\mu\text{m}$  and 10 mm, respectively, within an RI range of 1.3325 – 1.3377. This sensor was further demonstrated for gelatine detection with a highest sensitivity of 2.4214 nm/%W/V (weight per volume). Tapered SMFs have also been used for pressure measurement, where in [26], a sensitivity of 0.008 dB/mBAR was achieved within a pressure range of 0-1265 mBAR. The maximum RI sensitivity of a tapered SMS fibre sensor was demonstrated in [27] to be 1913 nm/RIU for RI  $\sim$ 1.44, where a taper waist diameter and length of 30  $\mu\text{m}$  and 150  $\mu\text{m}$  were used, respectively. The coupling coefficient between two weakly fused SMFs in an optical microfibre coupler (OMFC) is affected by the surrounding RI, as demonstrated in [28], where a maximum RI sensitivity of 39541.7 nm/RIU was achieved at a low ambient RI of 1.3334, using a taper diameter of 1.4  $\mu\text{m}$ . Another weakly coupled multicore tapered fibre was demonstrated in [29] for measuring temperatures of up to 1000  $^{\circ}\text{C}$  with a sensitivity of 36.8 pm/ $^{\circ}\text{C}$ . In [30], inscribing of a grating with a period of 1061 nm on the uniform waist of a tapered MMF with 3.5  $\mu\text{m}$  diameter was demonstrated, resulting in a force sensitivity of 1900 nm/N.

Evanescent field-based sensors are very versatile since the change in the spectral response arising from the evanescent field can be amplified (by reducing the taper waist diameter) or detected in conjunction with various other sensing mechanism. The various sensing mechanism, depending on the analyte and the application of the sensor include observing changes in the output power due to RI changes, evanescent field absorption, fluorescence, surface plasmon resonance (SPR) and whispering-gallery modes. Furthermore, evanescent field-based sensors have the advantage of surface specific detection. The limited penetration depth of the evanescent wave spatially separates the surface bounded molecules from other interferers that may be present in the bulk solution. It is due to these advantages and the flexibility of micro/tapered fibres that make them one of the most popular form of OFSs. Evanescent field-based sensors are demonstrated for sensitivity enhancement using a tapered no-core fibre sensor in Chapter 3 of this thesis.

### 1.2.2 Phase-modulated (Interferometric) fibre optic sensors

Phase-modulated sensors are also known as interferometric sensors. This type of sensor is based on detecting the phase difference of the coherent light travelling along two different paths either in the same or different fibres. Such interferometric sensors are highly sensitive, have a simple structure, and are one of the most popular types of OFSs. Generally, they are based on one of the following four configurations:

#### (i) Fabry-Perot Interferometer (FPI)

Structurally, FPI consist of a cavity between two reflecting surfaces placed parallel to each other. Figure 1.4 presents an illustration of a typical optical fibre-based FPI. As shown in the figure, the light beams reflect at the two interfaces between air and fibre, forming a FP cavity to produce a stable interference pattern. The phase difference between the reflected light beams is given by the following equation:

$$\delta = \frac{2\pi}{\lambda} n2L \quad 1.3$$

From the above equation, it is obvious that the phase difference or the interference pattern depends on the length ( $L$ ) and the RI ( $n$ ) of the cavity. By measuring the phase difference, a fibre FPI can be used for sensing various environmental parameters including temperature, pressure, and RI measurements. For example, in [31], a 2.1 mm length of photonic crystal fibre (PCF) was fusion-spliced between two SMFs to create a FPI cavity to sense both pressure and temperature within the cavity, achieving an average pressure sensitivity of -5.8 pm/MPa in the pressure range of 0 – 40 MPa, and an average temperature sensitivity of 13.7 pm/°C in the temperature range of 25 – 70 °C. The temperature sensitivity of such a structure can be enhanced by using a FPI cavity made with high thermo-optic coefficient materials, where, for instance, Zhang *et al.* proposed to connect a 125 µm inner diameter ceramic ferrule and using it as the sensing cavity; while the other end of ferrule was sealed with optical glue of 1.52 RIU. The sensor achieved a maximum temperature sensitivity of 67.35 nm/°C for the sensing cavity lengths of 77.59 µm [32].

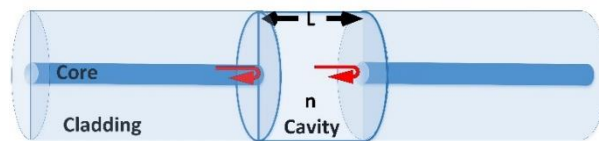


**Figure 1.4.** Illustration of an all-fibre FPI.

## (ii) Mach-Zehnder Interferometer (MZI)

The early MZI configurations consisted of two separate optical fibre paths called the reference and signal arms, where only the signal arm was exposed to external perturbations. Two standard optical fibre couplers were used to split the input light from the source into the two arms and then recombine them at the detector, as shown in Figure 1.5. The phase variations in the sensing arm due to external perturbations such as temperature, pressure, or strain can be determined by calculating the phase difference between the reference and sensing signals. More recently, research and development efforts have been successful in making MZIs more compact and efficient by considering two or more separate light paths within the same fibre as a means of measuring the phase shift. Such an in-line MZI employs the interference between the multiple modes propagating via different paths in the same fibre. Examples of implementation of this scheme include an SMS-based OFS, which was demonstrated in [33] with a temperature sensitivity of  $-9.98 \text{ pm}/^\circ\text{C}/\text{cm}$  and strain sensitivity of  $9 \text{ pm}/\mu\epsilon$  using a Corning (F01GI62NCG01) MMF, while in [34], a small-core SMF section spliced between two standard SMFs coated with polyethylene oxide was used to develop a humidity sensor with a maximum relative humidity sensitivity of  $430 \text{ nm}/\text{RHU}$  (relative humidity unit). In addition, an RI sensor based on three cascaded SMF tapers was demonstrated in [35], achieving an RI sensitivity of  $28.6 \text{ nm}/\text{RIU}$ . Due to their structural simplicity, in-line MZIs form the foundation of this research, where un-tapered multimode interferometry based MZIs are discussed in detail in Chapter 2 of this thesis.

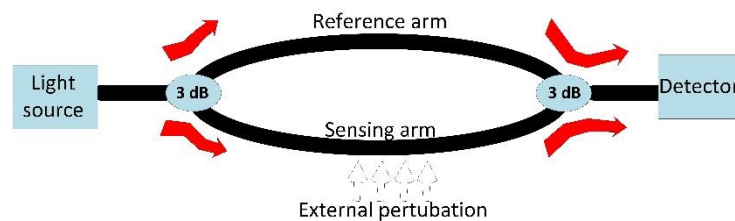
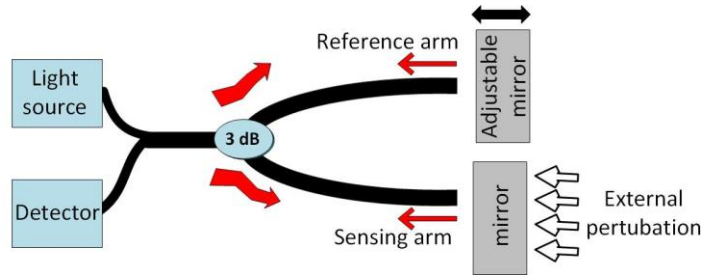


Figure 1.5. Basic configuration of the two-path fibre MZI.

## (iii) Michelson Interferometer (MI)

The MI configuration is similar to the MZI configuration and can be considered as half of an MZI. The major difference between MIs and MZIs is that the interference in MZIs is produced by transmitted beams, while in MIs, it is produced by reflected beams. A schematic diagram of a typical MI is shown in Figure 1.6, where the light beam in both the reference and signal arms are reflected by placing a mirror at the end of each arm, and the same fibre

coupler is used to split and recombine the light beam. The circulator isolates the reflected light from the transmitted light, which is then used to identify the phase change at the detector. Such a reflection-type configuration has the advantages of compactness and ease of installation. For in-line fibre MIs, the reflection is generally created by coating a thin metal layer at the end-face of the fibre. For example, in [36], Mathew *et al.* demonstrated a reflective SMF-PCF sensor with a humidity sensitivity of  $\sim 24$  pm/%RH for relative humidity  $> 70\%$ . The maximum RI sensitivity of a reflective SMF-coreless fibre sensor was demonstrated in [37] to be 1467.59 nm/RIU within the RI range of 1.364 – 1.397 RIU, where a 5 mm length of 24  $\mu\text{m}$  diameter fibre was used. In [38], one end of an SMF-thin core fibre was turned into a circular arc and coated with carbon nanotubes to form an MI with a maximum RI sensitivity of 178.88 dB/RIU within the RI range of 1.334 – 1.371.



**Figure 1.6.** Basic configuration of the two path fibre MI.

#### (iv) Sagnac interferometer (SI)

In a typical optical fibre SI shown in Figure 1.7, the input light is split into two parts by a 3 dB fibre coupler, resulting in propagation in opposite directions. The two counter propagating light beams re-combine at the same coupler after propagating an identical path. To introduce an optical path difference, a birefringent fibre section is added in the loop, which works as the sensing element in this SI structure. The interference at the output occurs between the beams propagating along the slow and fast axis of the birefringent fibre, and the phase difference between the two beams is given by the following equation:

$$\delta = \frac{2\pi}{\lambda} BL \quad 1.4$$

where  $B = |n_f - n_s|$  is the birefringence coefficient of the sensing fibre,  $L$  is the length of birefringent fibre, and  $n_f$  and  $n_s$  are the effective indices of the fast and slow modes, respectively [39]. For a certain wavelength ( $\lambda$ ), the phase difference is proportional to the birefringence coefficient. Therefore, high birefringent fibres (HBFs) or polarization

maintaining fibres (PMFs) are preferred for achieving high phase sensitivity. Examples of implementation of SIs include a Sagnac loop configuration in OMFC, implemented by simply joining the two output ports, where a maximum RI sensitivity of 3617 nm/RIU was achieved within the RI range of 1.33 – 1.41 [40]. A Sagnac loop formed by connecting the two ends of a 3 dB coupler using a 12.3 cm of highly birefringent PCF with two asymmetric cores was demonstrated in [41] for rotation, strain, and temperature sensing, with a maximum sensitivity of  $7.88 \times 10^{-3}$  rad/°,  $5.47 \times 10^{-5}$  rad/ $\mu\epsilon$  and  $5.58 \times 10^{-4}$  rad/°C in the ranges of 140 ° – 220 °, 0 – 3000  $\mu\epsilon$  and 25 – 145 °C, respectively. Magnetic field measurement based on SI with a sensitivity of -488 pm/mT was demonstrated in [42] using an OMFC with 2.6  $\mu\text{m}$  taper waist diameter surrounded with magnetic fluid, where the SI configuration was achieved by connecting a 20 cm long PMF between the two output ports.

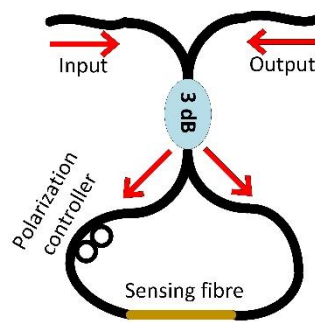


Figure 1.7. Basic configuration of an optical fibre SI.

### 1.2.3 Spectrometric (wavelength-modulated) fibre sensors

Spectrometric fibre sensors, also known as wavelength-modulated fibre sensors, display a change in the optical wavelength (spectral modulation) of the propagating light due to an external perturbation. Some common spectrometric fibre sensors are Bragg grating sensors, fluorescence sensors, and blackbody sensors.

#### (i) Fibre Bragg grating (FBG)

FBGs are one of the most widely used spectrometric sensors and are fabricated by inscribing periodic RI changes within the fibre core [43], as shown in Figure 1.8. Due to these periodic RI modulations in the fibre core (usually an SMF's core), the forward propagating core mode is reflected and coupled into a backward propagating core mode. The reflected Bragg wavelength ( $\lambda_B$ ) depends on the effective RI of the grating ( $n_e$ ) and the grating period ( $\Lambda$ ) according to the following equation:

$$\lambda_B = 2n_e\Lambda$$

1. 5

The changes in  $\Lambda$  and  $n_e$  due to strain and temperature on the FBG have been utilised for sensing various physical parameters. However, the major disadvantage of traditional FBGs is their cross-sensitivity, which makes it difficult to distinguish between the effects of strain and temperature. Therefore, various methods have been suggested for simultaneous measurement of the two parameters, such as inscribing the grating at the splice point of a Corning SMF-28 and an Er/Yb doped fibre, producing two Bragg wavelengths due to the average RI difference of 0.00391 between the two fibres. This method was used in [44] for simultaneous measurement of strain and temperature, with a maximum sensitivity of 1.05 pm/ $\mu\epsilon$  and 10.6 pm/ $^\circ\text{C}$ , respectively. Another scheme involved the use of two FBGs bound to a cantilever as a diaphragm-cantilever type FBG pressure sensor, with a maximum sensitivity of 339.956 pm/MPa [45]. Due to the positioning of the two FBGs on either side of the cantilever, the temperature induced error was as low as 0.93% between 5 – 70  $^\circ\text{C}$ . Due to their strain sensitivity, FBGs have also been demonstrated for vibration sensing [46] and other related applications [47].

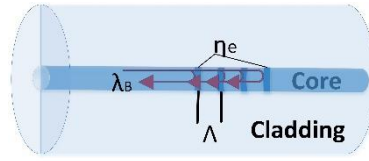


**Figure 1.8.** Illustration of a FBG

Depending on the distance and angle of gratings, LPGs and tilted fibre Bragg gratings (TFBGs) are the two most popular fibre grating based OFSs. In LPGs, the typical grating period is between 100  $\mu\text{m}$  to 1 mm. LPGs promote coupling between the forward propagating core mode and the co-propagating cladding mode, as shown in Figure 1.9 (a). Therefore, LPGs can be used to identify the surrounding RI by measuring the transmission of light. The phase matching between the forward propagating core mode and the co-propagating cladding mode is achieved at a wavelength  $\lambda = [n_{eff}(\lambda) - n_{clad}^i(\lambda)]\Lambda$ , where  $n_{eff}$  is the effective RI of the propagating core mode at a wavelength  $\lambda$ ,  $n_{clad}^i$  is the effective RI of the  $i^{th}$  cladding mode, and  $\Lambda$  is the grating period of the LPG. Therefore, LPGs can be used to make an in-line MZI fibre sensor, where depending on the grating period ( $\Lambda$ ), the temperature and strain sensitivity of the LPG is tuned. For  $\Lambda > 100 \mu\text{m}$ , core modes couple

to lower order cladding modes and are influenced by material effect, which makes the LPG highly sensitive to temperature. Examples of such LPGs include that reported in [48], where an LPG was fabricated in a standard telecom optical fibre achieving a temperature sensitivity of  $0.03 \text{ nm}/^\circ\text{C} - 0.1 \text{ nm}/^\circ\text{C}$ . Another demonstration involved making an LPG in a photosensitive B-Ge co-doped optical fibre, resulting in a sensitivity of  $2.75 \text{ nm}/^\circ\text{C}$  [48]. For  $\Lambda < 100 \mu\text{m}$ , the core modes couple to higher order cladding mode, where in such a case, the material effect is in-significant, and as such, the LPG can be made insensitive to temperature. In this configuration, an LPG with a period of  $40 \mu\text{m}$  was demonstrated in [49] with a temperature sensitivity of  $1.8 \text{ pm}/^\circ\text{C}$ , and recoating the LPG with a negative thermo-optic coefficient material resulted in reducing the temperature sensitivity to  $0.7 \text{ pm}/100^\circ\text{C}$  [50]. For LPG with  $\Lambda > 100 \mu\text{m}$ , the material contribution is negative and the waveguide contribution is positive, which means a low strain sensitivity can be achieved. For example, an LPG with  $\Lambda = 340 \mu\text{m}$  written in a corning flex core fibre was demonstrated in [49] with a strain sensitivity of  $0.04 \text{ pm}/\mu\epsilon$ . For  $\Lambda < 100 \mu\text{m}$ , both the material and waveguide contributions are negative, hence, a large strain sensitivity can be achieved, such as that achieved in [49], where a strain sensitivity of  $-2.2 \text{ pm}/\mu\epsilon$  was demonstrated for an LPG with  $\Lambda = 40 \mu\text{m}$ . RI sensitivity of LPGs arises from the dependence of the phase matching condition upon the effective RI of the cladding modes, which in turn depends on the RI of the cladding and surrounding medium. The RI sensitivity increases as the surrounding RI (SRI) approaches the cladding RI, where a maximum RI sensitivity is achieved near the cladding RI ( $\sim 1.4$ ). When  $\text{SRI} = \text{cladding RI}$  (exactly equal), the cladding appears to be of an infinite extent and supports no discrete modes, and when  $\text{SRI} > \text{cladding RI}$ , no guided modes are supported by the fibre, and hence, no spectral response is observed in this case. Based on this, an ultrahigh temperature sensitivity of  $1900 \text{ nm}/^\circ\text{C}$  was demonstrated in [51] over a  $1^\circ\text{C}$  range using Cargile oil whose  $\text{RI} \neq \text{cladding RI}$ .

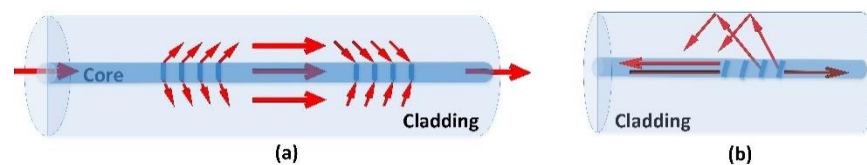


**Figure 1.9.** Schematic diagram of (a) LPG and (b) TFBG

In TFBGs, the grating planes are tilted relative to the fibre axis, which results in coupling light from the core mode to (1) a subset of the large number of modes that can be guided by

the (much larger) cladding of the fibre; (2) leaky modes of the cladding; and (3) highly directional light beams radiating out of the fibre. Due to the tilt angle ( $\theta$ ) of the grating plane, the grating period is modified as  $\Lambda_g = \frac{\Lambda}{\cos \theta}$ , and therefore, the Bragg wavelength is modified as  $\lambda_B = 2n_e \frac{\Lambda}{\cos \theta}$ . Due to the tilt angle, part of the forward propagating core mode will be coupled into the counter propagating cladding mode, as shown in Figure 1.9 (b). Therefore, the resonance wavelength of the cladding mode is  $\lambda = [n_{eff}(\lambda) - n_{clad}^i(\lambda)]\Lambda_g$ , where the symbols have the same meaning as those explained for the LPG. Introducing a parallel double angle grating of 2.2° and 3.8°, a maximum RI sensitivity of 1023.1 nm/RIU was demonstrated in [52] within the RI range of 1.4401 – 1.4570. In addition, a TFBG of 5 mm length and 1.5° tilt inscribed in boron-germanium co-doped optical fibre core was used to demonstrate a strain sensitivity of 0.8 pm/ $\mu\epsilon$  and a temperature sensitivity of 6 pm/°C [53].

## (ii) Fluorescent-based fibre sensors

Fluorescent based sensors are widely used for physical and chemical sensing to measure temperature, humidity and viscosity. The two most common configurations are the end tip sensor and the blackbody cavity types. In a blackbody sensor configuration, the blackbody cavity placed at the end of an optical fibre starts to glow as the temperature of the cavity rises, thus acting like a light source. Therefore, using a detector and a narrow band filter, the profile of the blackbody curve can be determined. These sensors are capable of measuring temperature variations in the range of few degrees centigrade under intense radio frequency fields, and have been commercialised as an optical fibre thermometer [54]. Examples of this type of sensors include a fluorescent sensor based on a tapered SMF used to capture the fluorescence from an excited pH indicator, with a detection range of 3-9 pH [55]. Fluorescence-based OFSs are also popular for bio-chemical sensing, where, for instance, oxygen sensing using an un-cladded POF coated with Tris (4, 7-diphenyl-1, 10-phenanthroline) ruthenium (II) dichloride (Ru(dpp)3Cl2) and platinum octaethylporphyrin was demonstrated in [56], with a maximum sensitivity of 14 counts/%O<sub>2</sub> for an 8 mm coating length and a 160 mm/min withdrawal rate. TiO<sub>2</sub> composite nanoparticles functionalised with Nafion as a label were used in [57] to demonstrate human chorionic gonadotropin (hCG) detection with a low limit of detection (LOD) of 0.07 mIU/mL. However, in general, the fluorescence produced is typically in the visible spectrum of light, and as such, these sensors suffer from interference from the ambient light. Furthermore, another disadvantage of this type of sensors is the limited life time of the fluorescence material.

### 1.2.4 Polarimetric fibre sensors

The polarization state of the light propagating in a birefringent fibre changes because of the difference in the phase velocity of the two polarization components. The polarization properties of the light are affected by the stress, strain, pressure and temperature of the fibre. Therefore, the polarimetric sensor identifies these physical properties by detecting the change in polarization state of the output light relative to the input light. A symmetric deformation effect or temperature variations in a SMF affect the propagation constant ( $\beta$ ) for every mode due to the changes in fibre length ( $L$ ) and the RI of the core and cladding. The influence of longitudinal strain ( $\epsilon$ ) or temperature ( $T$ ) on the phase difference of an SMF polarimetric sensor is given by the following equation [58]:

$$\frac{\delta(\Delta\phi)}{\delta X} = \Delta\beta \frac{\partial L}{\partial X} + L \frac{\partial(\Delta\beta)}{\partial X} \quad 1.6$$

where  $X$  stands for temperature, pressure or strain.

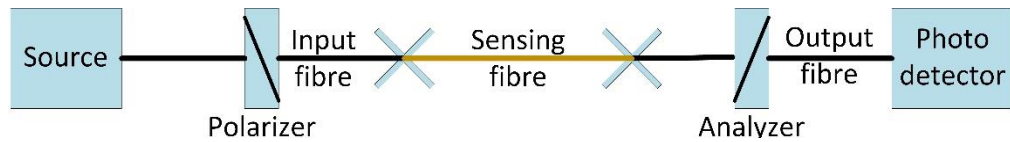


**Figure 1.10.** Schematic diagram of a typical polarimetric fibre sensor

An intensity-based optical fibre polarimetric sensor using a polarization analyser arrangement is shown in Figure 1.10. The input light from the source is linearly polarized at  $45^\circ$  to the principal axis of the birefringent fibre, so that both polarization modes are equally excited in the fibre sensor. The polarization state at the output is converted to intensity by using a polarization analyser, oriented at  $90^\circ$  with respect to the input polarization state. Therefore, any change in polarization state can be observed as a change in intensity due to the external perturbation via  $I_s(\lambda) = \frac{I_0}{2} [1 + \cos(\Delta\phi)]$ , at a wavelength  $\lambda$ . The phase difference between the two orthogonal polarizations can also be extracted using an experimental setup consisting of a tuneable laser source and a polarimeter/polarization control system.

Typically, high-birefringent optical fibres such as bow tie, panda, elliptical core and polarization maintaining PCF fibres, are used to develop polarimetric sensors for various applications. For example, a bow-tie optical fibre was used for structural monitoring in [59], where a change in intensity occurs as a result of an increase in the number of cracks or the

crack length in the structure. A polarization maintaining PCF embedded in carbon-epoxy, E glass-epoxy, and E glass-unsaturated polyester resin composite materials was also demonstrated in [60], with thermal elongation induced strains of  $3.648 \times 10^{-5} \text{ } \epsilon/\text{ }^\circ\text{C}$ ,  $1.52 \times 10^{-5} \text{ } \epsilon/\text{ }^\circ\text{C}$ , and  $2.42 \times 10^{-5} \text{ } \epsilon/\text{ }^\circ\text{C}$ , respectively. In [61], a polarimetric optical fibre pressure sensor using a polarization-diversity loop with 8 cm long tapered panda fibre and a FBG spliced with an PMF was demonstrated, achieving a sensitivity of  $-27.70 \text{ nm/MPa}$  in the measurement range of  $0 - 0.5 \text{ MPa}$ .

### 1.2.5 Other techniques

Several other techniques, either utilised in conjunction with previous interferometers or individually, are also used to develop OFSs for various applications. Two of the major techniques used extensively are discussed in this section.

#### (i) Surface plasmon resonance (SPR) technique

For the metal-dielectric configuration shown in Figure 1.11, a resonance occurs when the incident light at the metal-dielectric interface has a momentum matching those of free electrons in the metal. Due to this resonance, the light energy gets absorbed and the electrons start oscillating to generate surface plasmon waves (SPWs). The SPWs propagate at the interface between the metal and dielectric surface. However, if the thickness of the metal layer ( $d$ ) is small, or, for nano-scaled metallic structures such as metallic nanoparticles or nanorods, a localised SPR (LSPR) is formed on the metal surface.

The S and P polarizations refer to the plane in which the electric field (E-field) of the light is oscillating. The S-polarized light refers to the case where the E-field is parallel to the glass-metal interface, and therefore does not contribute to exciting SPWs. However, P-polarized light, in which the E-field is perpendicular to the interface, excites SPRs. The reflectance ( $R$ ) of a P-polarized light beam, based on the three-layer (glass (3) – metal film (1) – medium (2)) Kretschmann's configuration shown in Figure 1.11, can be calculated using Fresnel's theory as follows [62]:

$$R = \left| \frac{[r_{31} + r_{12} \exp(2iK_{z1}d)]}{[1 + r_{31} + r_{12} \exp(2iK_{z1}d)]} \right|^2 \quad 1.7$$

where  $r_{31} = \frac{Z_3 - Z_1}{Z_3 + Z_1}$ ,  $r_{12} = \frac{Z_1 - Z_2}{Z_1 + Z_2}$ ,  $Z_i = \frac{\varepsilon_i}{k_{zi}}$ ,  $k_{zi} = [\varepsilon_i(\omega/c)^2 - k_{x3}^2]^{0.5}$  for  $i = 1, 2, 3$ ,  $k_{x3} = \varepsilon_3^{0.5} \frac{\omega}{c} \sin\theta$ ,  $n_i = \sqrt{\varepsilon_i}$ ,  $n_i$  ( $i = 1, 2, 3$ ) is the refractive index of the  $i$ -th medium,  $d$  is the metal layer's thickness,  $\omega$  is the incident photon frequency,  $\varepsilon_i$  is the permittivity of the  $i$ -th medium, and  $\theta$  is the incident ray angle. The SPR technique is generally used in conjunction with an evanescent field sensor such as a tapered fibre, tilted FBG, or LPG. For example, in [63], a tapered SMF with a taper waist diameter and length of 48  $\mu\text{m}$  and 1.25 mm, respectively, was coated with gold (Au) nano particles of  $24 \pm 3$  nm diameter to excite SPWs. This sensor was demonstrated with an RI sensitivity of 51 nm/RIU within the RI range of 1.333 – 1.403, as well as for anti-DNP antibody (Ab) detection with a limit of detection of  $1.06 \times 10^{-9}$  g/mL (4.8 pM) [63]. In [64], SPWs were excited using an tilted FBG with an Au layer to achieve a RI sensitivity of 200 nm/RIU within the RI range of 1.332 – 1.357. Furthermore, the sensitivity was enhanced to 500 nm/RIU by adding another germanium oxide layer with a total thickness of 415 nm. Another demonstration involved the use of a 7 mm long single-mode birefringent polymer D-shape fibre with a core made of PMMA/PS copolymer, which was coated with 40 nm of Au layer to demonstrate an RI sensitivity of  $\sim 2800$  nm/RIU at RI  $\sim 1.410$  [65]. In an SPR-based OFS, the coupling of evanescent field with surface plasmons strongly depends on the wavelength, fibre parameters, probe geometry, and the metal layer properties.

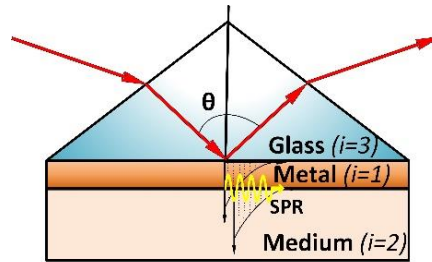


**Figure 1.11.** Kretschmann's configuration for SPR.

## (ii) Micromachining technique

In the last two decades, advances in microfabrication techniques such as laser drilling, micro milling, and focused ion-beam (FIB) have led to the development of a variety of novel fibre sensor structures for different applications. However, the development of such fibre sensor structures requires high precision equipment, which increases the initial setup cost and complexity. Examples of utilisation of microfabrication techniques include that reported in [66], where a tapered SMS fibre sensor was cut using FIB to obtain a flat end-face with  $\sim 2.9$

$\mu\text{m}$  diameter, and was then coated with a thin layer of gold to increase reflectance. The sensor demonstrated a RI sensitivity of 265 nm/RIU within the RI range of 1.33 – 1.40. An FP-FBG composite structure was also reported in [67], where it was fabricated by creating two micro-holes of 35  $\mu\text{m}$  length, realising a sensor with an RI and temperature sensitivity of 1120.799 nm/RIU and  $-0.165 \text{ nm}/^\circ\text{C}$  for the 2<sup>nd</sup> FPI, and 1128.190 nm/RIU and  $-0.175 \text{ nm}/^\circ\text{C}$  for the 1<sup>st</sup> FPI in the FBG.

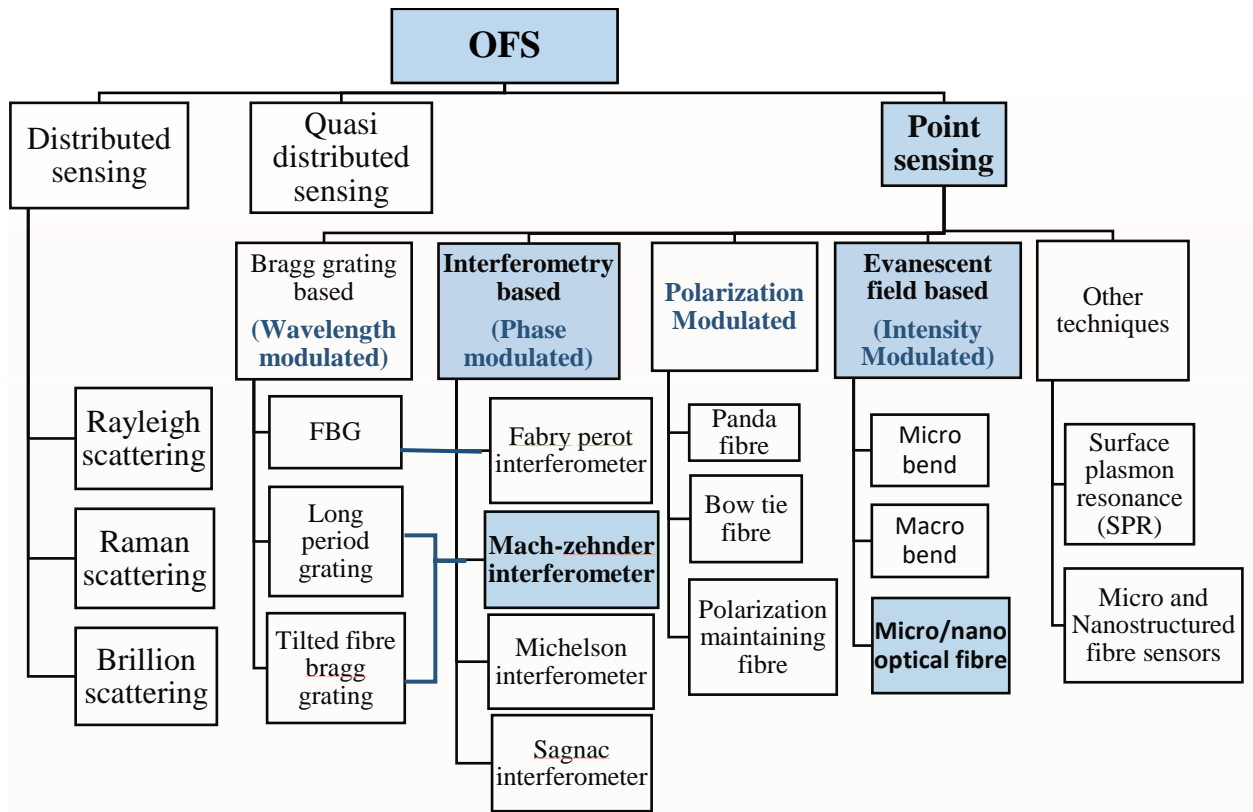


**Figure 1.12.** Classification of major OFSs considered for this research work: Level-1 represents classification based on spatial orientation, Level-2 represents classification based on the optical parameter used for detection and the major fabrication techniques combined, and Level 3 represents the major types of each classification.

### 1.3 Problem statement and Motivation

Sensors play a vital role in the fields of metrology, automation and healthcare, and have become an integral part of almost every system, especially with the growing expansion of the internet of things (IoT). It is estimated that the current global sensor market will rise from its worth of \$7.51 billion in 2016 to \$27.38 billion by 2022 [68]. However, in many applications, robust, highly sensitive, durable sensors are still required, as their design and implementation remain a challenge for existing sensor technologies. The aim of this research

is to address such a challenge by designing and demonstrating a new generation of optical fibre-based sensors that are suitable for a variety of applications.

Attention towards the use of optical fibres for sensing chemical, biological, and physical parameters was first drawn in the 1980s [4]. Since then, the field of optical fibre-based sensors have experienced massive development due to their advantages of high sensitivity, small size, environmental ruggedness, immunity to EMI, and high temperature resistance. In this research, these advantages are utilised to demonstrate the following array of challenging sensing applications:

**Monitoring phase change materials (PCMs):** According to the Department of Energy & Climate Change (DECC), in 2014, the majority of heat energy usage in the domestic and service sectors was for space heating (77% and 72%, respectively). Energy consumption reduction under the current climate change conditions is a major challenge in buildings design, where excessive energy consumption creates an economic and environmental burden.

Improving thermal performance of buildings through the use of PCM, which maintain the temperature of the heating system over a long time, is a promising strategy for reducing buildings' energy consumption [69]. However, such PCMs require replacement after a few years of use due to the incongruous melting and phase separation that occur due to the cyclic melting and solidification in the heat storage and heat release processes, respectively. As such, a suitable sensing technology that could be easily imbedded into PCMs to monitor their phase states is required to provide continuous monitoring of such PCMs and make them a viable technology for reducing buildings' energy consumption. The electronic sensors are mostly unsuitable for such applications, because they are relatively larger in size and are inefficient at high temperature and in corrosive environment.

The MMF section in the traditional SMS fibre sensor is extremely sensitive to micro/macro bending. Therefore, the changes in its spectral response can be calibrated to detect the phase state of PCMs (based on the spectral changes due to the micro bending of the MMF section during the phase change of PCMs). In this thesis, we intend to develop a new optical fibre sensor for detecting phase state changes of PCMs based on an SMS fibre structure.

**Monitoring breathing state:** Biosensors that are immune to EMI and radio frequency interference (RFI) are required for environments such as hospital settings, where, for

instance, monitoring patients' conditions, such as breathing state, during MRI scans is currently challenging since the use of the EMI- and RFI-susceptible electronic transducers is generally both unreliable and hazardous to the patient.

To address this problem, we proposed to use a bend SMS fibre sensor to monitor breathing states in such high EMI environments, as the spectral response of sensor can be calibrated to detect the respiration rate of patients (based on the intensity changes due to the macro bending of MMF section that take place as a result of the breathing action).

**Monitoring oxygen levels:** Non-electronic sensors that are capable of operating in hazardous environments are currently required for applications such as real-time monitoring of air quality in high temperature and corrosive environmental conditions, and monitoring oxygen levels in confined spaces like coal mines and electrically hazardous spaces like oil and gas rigs and nuclear power plants. Such sensors must be durable, provide immunity to EMI, and offer high temperature resistance.

To develop an OFS for bio-chemical sensing applications such as monitoring of oxygen and humidity levels and detecting biomarkers such as pH [70], antibodies [71], and antigen [72] related to specific diseases, the traditional SMS fibre sensor is considered unsuitable due to the lack of light-environment interaction. This is because of the presence of a cladding layer in conventional optical fibres, which encapsulates the evanescent field produced at the core-cladding interface within the cladding layer. In the past, removing the cladding layer of an optical fibre by chemical etching or side polishing [18] was proposed for making a fibre sensor sensitive to the surrounding RI. However, such techniques introduce surface roughness and make the sensor response unstable, while also compromising the mechanical strength of the sensors' structure. With the advancement in optical fibre fabrication technology and availability of speciality optical fibres, the simplest solution to achieve the aforementioned aim is to use a coreless or no-core fibre (NCF), which can provide an easily accessible evanescent field without the need for etching the cladding layer. Furthermore, the RI sensitivity of the SMF-NCF-SMF OFS can be improved by increasing the evanescent field interaction with its surrounding, which can be achieved by reducing the NCF diameter (i.e. tapering the optical fibre), as explained in Section 1.2.1. These two methods pave the way for creating highly sensitive sensors that can detect minute changes in the surrounding RI, and can therefore be utilised to detect oxygen levels in electrically hazardous or corrosive environments.

**Real-time detection of pathogens:** It is estimated that around 13 million GP appointments are missed by patients each year [73]. Therefore, biosensors that can offer real-time detection of diseases and can be used in hospital settings are of great importance, both in the developed part of the world, where people intend to monitor their health timely, or in developing countries with limited healthcare facilities.

Silica fibre sensors are chemically inert with no specificity towards any biological analytes, and they are mainly sensitive to their surrounding RI changes. Therefore, to develop an OFS-based bio-chemical sensor, the bio/chemical analytes should introduce a RI change in the fibre sensor's surface. Therefore, functionalising the fibre sensor with a chemical or biological agent, which can capture and interact with the analyte to change the RI of the functional layer is a key step to the development of a bio-chemical sensor. One of the key motivations of this PhD thesis is to develop an optical fibre sensor functionalisation technique and apply such a sensor for Point-Of-Care (POC) applications, such as for real-time detection of hCG level in a urine sample, for pregnancy and tumour diagnosis.

#### **1.4 Aim and objectives**

**Research aim:** The aim of this thesis is to develop highly sensitive OFSs for the detection and quantification of different physical parameters and bio-chemical analytes.

**Objectives:** The specific objectives of this thesis are:

- (a) During the initial stage of this research work, to develop an in-depth understanding of the interferometric OFSs and investigate the traditional SMS fibre sensor for monitoring physical parameters, such as temperature and pressure.
- (b) To develop a novel high sensitivity optical fibre sensor for monitoring phase state of PCMs and respiration rate of patients during MRI.
- (c) To extend the application of the SMS fibre sensor by introducing and improving the RI sensitivity of the fibre structure. To realise this objective, as opposed to using the conventional method of removing the cladding layer to improve the light-environment interaction, a commercially available single layer optical fibre, such as no-core fibre (NCF), is investigated as a means of introducing RI sensitivity.
- (d) To develop a reliable fibre tapering technology for fabrication of the tapered SMS sensors.

- (e) To demonstrate the suitability of using high RI sensitivity tapered SMS sensor for magnetic sensing.
- (f) To investigate various surface functionalisation techniques for the proposed OFSs in order to develop a robust, highly sensitive bio-chemical sensor, and to demonstrate its suitability for real-life applications, such as for detecting oxygen levels in confined spaces and for detecting hCG levels in urine samples.

## 1.5 Original contributions

This thesis introduces several original contributions to knowledge that can be summarised as follows:

- **High sensitivity SMS based temperature sensor:** The temperature sensitivity of the traditional SMS fibre sensor is low due to the low thermo-optic coefficient of silica. Introducing a hollow core fibre filled with high thermo-optic coefficient polymer between two SM fibre structures was utilised to improve the temperature sensitivity by over 200 times. The results demonstrated no influence of the MMF fibre length and diameter; however, the temperature sensitivity was shown to improve with increasing the polymer-filled hollow core fibre's length.
- **SMS breath state sensor:** The traditional SMS fibre sensor was utilised to develop a breath sensor for detecting different breathing states. In principle, the sensor monitors the changes in intensity due to the macro bending introduced in the MMF section as a result of the breathing action.
- **SMS sensor for PCM phase change monitoring:** A reflective version of the SMS fibre sensors was utilised to determine the phase change point of a phase change material. This sensor works by utilising the micro bending introduced in the MMF section during the phase change of PCMs. The length of the MMF section of the sensor was optimised, and the fibre sensor was demonstrated to determine the phase change point of paraffin wax and two other slat hydrates.
- **Tapered SMS sensor for magnetic field measurement:** Singlemode tapered small core singlemode (STSCS) OFSs encapsulated in different concentrations of magnetic

fluid were demonstrated for magnetic sensing. Different taper diameters of the small core and different concentrations of the magnetic fluid were experimentally investigated. The results demonstrated a maximum sensitivity of 0.466 nm/mT for a tapered diameter of 10  $\mu\text{m}$  encapsulated in a 1.3% magnetic fluid concentration. The influence of the magnetic field orientation on the optical fibre magnetic sensor was also investigated.

- **Tapered SMS sensor for RH monitoring:** An STNCS OFS functionalised with agarose hydro-gel was experimentally demonstrated for humidity sensing. Different tapering diameters of the NCF and different coating thicknesses of agarose hydro-gel were experimentally investigated. The maximum RH sensitivity of 0.029 nm/RH achieved was within a broad RH range of 35 – 75 %RH. Introducing a bend of 4.7 cm radius to the functionalised sensor was shown to improve the sensitivity to 0.042 nm/RH over the same RH range.
- **Surface modified tapered SMS for bio-chemical sensing:** A tapered no-core fibre sensor functionalised with methylene blue (MB) captured in a sol-gel matrix was demonstrated for oxygen sensing. The effect of the tapering diameter and coating thickness was investigated. A maximum sensitivity of 0.19 dB/O<sub>2</sub>% with good repeatability and selectivity were experimentally demonstrated for the proposed sensor. Subsequently, an ultrasensitive hCG sensor was proposed and investigated using a surface immobilised STNCS fibre sensor. The sensitivity of the sensor was improved by adding additional surface modified magnetic microspheres (MMSs) which will specifically bind with hCG samples. The sensitivity was further improved to a maximum of 98.4 nm/mIU/mL by enriching the hCG-MMSs sample with magnetic field.

## 1.6 Thesis Structure

This thesis is focused on the research work dedicated to OFSs based on fibre structures with multimode interference (MMI). The organisation of this thesis includes literature reviews, original contributions, conclusions, and future work, which are divided into five chapters as follows.

After a brief introduction including an overall review of the major types of OFSs in Chapter 1, Chapter 2 introduces non-tapered OFSs based on MMI. The traditional SMS fibre sensor is proposed and investigated both experimentally and theoretically, which is then demonstrated for monitoring different breathing states. Furthermore, a novel high temperature sensitivity sensor is developed and experimentally demonstrated by introducing a hollow core fibre filled with high thermo-optic coefficient polymer between two SMFs. A new fibre sensor using a reflective SM sensor for detecting the phase change point in a PCM is also demonstrated in this chapter.

Chapter 3 provides an overview of tapered OFSs by introducing their principle of operation and method of fabrication. The RI sensitivity and temperature dependence of the STNCS are investigated before proposing it for bio-chemical sensing. A STSCS fibre sensor is demonstrated for magnetic sensing, and the sensor fabrication and experimental setup used to conduct the experiment are also discussed in this chapter.

Chapter 4 focuses on the method to functionalise the STNCS fibre sensor for different bio-chemical sensing applications. Firstly, a humidity sensor was developed and experimentally investigated by coating a thin layer of humidity sensitive material agarose hydro-gel onto the STNCS fibre sensor. Secondly, an optical fibre oxygen sensor was experimentally investigated using MB entrapped in sol-gel matrix to capture and react with the oxygen in its surrounding, and lastly, a novel ultrasensitive hCG sensor is reported using anti-hCG- $\beta$  antibody functionalised STNCS fibre sensor.

Finally, Chapter 5 summarizes the key results and achievements, draws the conclusions from this thesis and presents a brief overview of potential future research work and directions.

## **Chapter 2 Non-tapered Optical Fibre MMI Sensors**

### **2.1 Introduction**

Fibre-optic devices based on multimode interference (MMI), exhibiting a convergence and divergence of a number of modes in a multimode fibre (MMF) and waveguides, have been an area of active research over the past few decades due to their low cost, ease of fabrication and the freedom they offer in tailoring the output spectrum. MMI-based devices in the field of communications have been used to develop a range of integrated optical devices, including modulators, power splitters, optical switches, directional couplers, band-pass filters, and fibre lenses for telecommunication networks [33]. Optical fibre sensors (OFSs) based on MMI are susceptible to external perturbations, hence, the effect of temperature and strain as external perturbations has been explored in the past using singlemode – multimode - singlemode (SMS) optical fibre structures to develop strain and temperature sensors [33]. This chapter firstly presented an overview of different OFSs based on MMI, which forms the base of this research work. Then a novel high sensitivity temperature sensor is proposed and demonstrated by introducing a hollow core fibre (HCF) filled with a high thermo-optic coefficient (TOC) polymer in the middle of two singlemode fibres. Based on the high sensitivity to bend for the SMS fibre structure, a novel fibre sensor used for breath state and phase change point monitoring has been proposed and investigated respectively.

### **2.2 Principle of the SMS Fibre Sensor**

#### **2.2.1 Theory of light propagation in an SMS fibre structure**

The SMS fibre structure comprises of a short section of an MMF with length  $L$ , sandwiched between input and output singlemode fibres (SMFs), as shown in Figure 2.1. The MMF section in our discussions has a step-index profile. For the purpose of theoretical analysis, the SMF and MMF are assumed to be perfectly aligned and there is no reflection at their interface, which occurs in practice due to the small refractive index (RI) difference between the SMF and MMF.

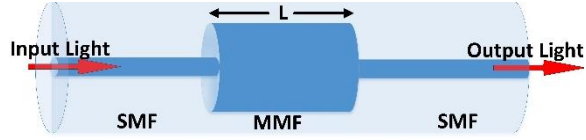


**Figure 2.1.** Schematic diagram of the SMS fibre structure

Considering the circular symmetry of the fundamental mode in the SMF, the input light is assumed to have a field distribution of  $E(r, 0)$ . When light is launched in the MMF, the input field is decomposed into multiple eigen-modes  $\{LP_{nm}\}$  in the MMF. Due to the circular symmetry of the input field and the ideal alignment assumed above, only  $LP_{0m}$  modes can be excited (which has been addressed in [74]). Furthermore,  $F_m(r)$  is used to denote the field profile of the  $m^{th}$  eigen-mode in the MMF, which is normalized as  $\int_0^\infty |E(r, 0)|^2 r dr = \int_0^\infty |F_m(r)|^2 r dr$ , where,  $m = 1, 2 \dots M$  are the number of guided modes in the MMF. Neglecting the small radiation from the MMF, the field at the interface between the input SMF and MMF can be expressed as follows:

$$E(r, 0) = \sum_{m=1}^M c_m F_m(r) \quad 2.1$$

where  $c_m$  is the excitation coefficient of each mode, which can be calculated by the overlap integral between  $E(r, 0)$  and  $F_m(r)$ :

$$c_m = \frac{\int_0^\infty E(r, 0) F_m(r) r dr}{\int_0^\infty F_m(r) F_m(r) r dr} \quad 2.2$$

The number of  $LP_{0m}$  modes excited in the MMF is  $M \approx V/\pi$  ( $V = \left\{\frac{2\pi}{\lambda}\right\} a \sqrt{n_{co}^2 n_{cl}^2}$ ), where  $a$  is the radius of the MMF core,  $n_{co}$  and  $n_{cl}$  are the refractive indices of the core and cladding of the MMF, respectively, and  $\lambda$  is the wavelength of propagating light.

As the light propagates in the MMF section, the field equation at a propagation distance  $z$  can be calculated using the following equation:

$$E(r, z) = \sum_{m=1}^M c_m F_m(r) \exp(i\beta_m z) \quad 2.3$$

where  $\beta_m$  is the propagation constant of the  $m^{th}$  eigen-mode in the MMF.

The field at the output SMF is calculated by the overlap integral between the light fields in the MMF and the fundamental mode of the output SMF. Since the output SMF has the same fibre parameters as the input SMF, and considering the orthogonal relationship between the eigen-modes of the MMF, the coupling loss can be calculated via the following equation:

$$L_s(z) = 10 \log_{10} \left| \sum_{m=1}^M c_m^2 \exp(i\beta_m z) \right|^2 \quad 2.4$$

Based on the above calculations, a MATLAB® simulation model was developed, and an example of spectral response of a typical SMS fibre structure is shown in Figure 2.2. In the simulation, an MMF with a length of 42.877 mm and core radius of 52.5 μm were considered, and the RIs of the core and cladding were 1.4446 and 1.4271, respectively. The core diameter of SMF (SMF28) considered was 8.2 μm, with 1.4504 and 1.4447 as the RIs of the core and cladding, respectively. Table 2.1 summarises the value of parameters used in the simulation.

**Table 2.1.** Summary of parameters used in the simulation model of SMS fibre structure

Optical fibre type	Parameter
MMF (Thorlabs-AFS 105/125Y)	Core Dia. = 105 μm Cladding Dia. = 125 μm Length = 42.87 mm RI of core = 1.4446 RI of cladding = 1.4271
SMF (Thorlabs-SMF-28)	Core Dia. = 8.2 μm Cladding Dia. = 125 μm RI of core = 1.4504 RI of cladding = 1.4447

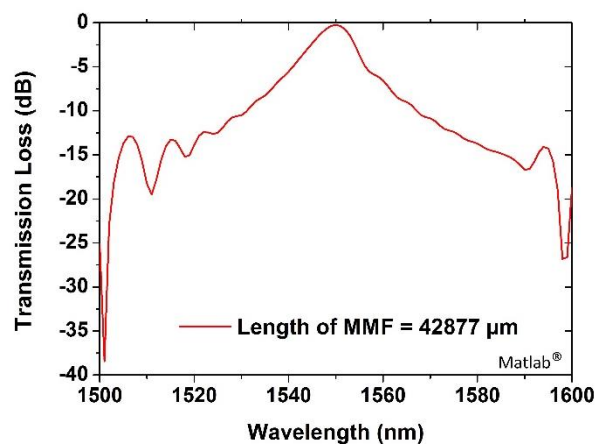


**Figure 2.2.** Calculated spectral response of an SMS fibre structure, with an MMF length of 42.877 mm.

### 2.2.2 Multimode interference (MMI) and Self-imaging

The peaks and dips in the spectral response presented in Figure 2.2 are due to the interference between the multiple modes propagating in the MMF. The fundamental mode in the input SMF excites multiple modes upon entering the MMF section. These multiple modes take different propagation paths, with different propagation constants along the MMF section and interfere at the output SMF. For a particular wavelength, if majority of the modes are in-phase and a constructive interference occurs at the output SMF, a higher intensity value (peak) is observed in the output transmission spectrum. Similarly, a lower intensity value (dip) is observed for the wavelength if the multiple modes are out of phase and a destructive interference occurs at the output SMF. For a particular MMF, these transmission losses due to MMI in the SMS fibre structure depend on the MMF length and the wavelength.

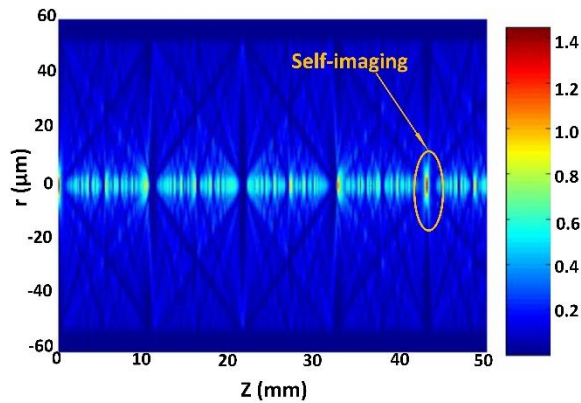


**Figure 2.3.** Simulation result showing the self-imaging property in an MMF with a core diameter of 105  $\mu\text{m}$  (reproduced from Q. Wang *et al.* JLT, vol. 26, no. 5, pp. 512–519, 2008)

Self-imaging can be defined as a property of multimode waveguides by which an input field profile is reproduced due to constructive interference to form single or multiple images of the singlemode input field at periodic intervals along the propagation direction of the MMF [75]. The calculated spectral response for the MMF with a length  $z = 42.877$  mm shown in Figure 2.2 has minimum losses ( $\sim 0$  dB) at 1550 nm. This theoretically implies that, after propagating a distance  $z$  in the MMF, the MMI pattern will be a replica of the input ( $z = 0$ ) without any losses. Therefore for a 1550 nm wavelength, 42.877 mm length of the particular MMF is the self-imaging distance. Figure 2.3 shows a simulation example of the light intensity distribution along the MMF with a core diameter of 105  $\mu\text{m}$  [74]. At a distance of 42.87 mm from the entry point, it is found that the light intensity distribution replicates the light distribution at the entry point of the MMF section. This is the so-called self-imaging distance.

### 2.2.3 Effect of temperature and strain on SMS fibre sensors

The MMI in the SMS fibre structure is easily influenced by the strain and temperature applied on the fibre structure. This fact has been utilised to develop SMS fibre-based strain and temperature sensors. The major influence of temperature is the change of RI of both the core and the cladding. However, changes in the core diameter and fibre length also occur due to thermal expansion, which are taken into account in the developed simulation model. Similarly, when a strain is applied on the SMS fibre structure, there is an obvious change in the fibre length and core diameter due to stretching of the optical fibre. In addition, a negligible variation in the RIs of the core and the cladding occurs due to the photo-elasticity of the dielectric material under the applied strain.

The temperature and strain dependence of the RI can be expressed using the following equations 2.5 (a) and (b), respectively

$$n_i(T) = n_{0i} + \left( \frac{dn_{0i}}{dT} \right) (T - T_0) \quad 2.5 (a)$$

$$n_i(\varepsilon) = n_{0i} - \frac{n_i^3}{2} [p_{12} - \sigma(p_{11} + p_{12})] \varepsilon \quad 2.5 (b)$$

where  $n_{0i}$  represents the initial RI (at room temperature  $T_0$  and no-strain condition), and the subscript “ $i$ ” signifies the core or cladding region. The value of the thermo-optic coefficient  $\frac{dn}{dT}$  for fused silica is known to be  $1.06 \times 10^{-5} / ^\circ\text{C}$ . Also, the strain–optic coefficients  $p_{11}$  and  $p_{12}$  are 0.12 and 0.27, respectively, and the Poisson ratio  $\sigma = 0.17$  for fused silica.

Changes in the MMF length and core radius with temperature and strain can be calculated by the following equations

$$\Delta l = \alpha l \Delta T + l \varepsilon \quad 2.6$$

$$\Delta a_i = \alpha a_{0i} \Delta T - \sigma a_{0i} \varepsilon \quad 2.7$$

Here  $\alpha$  is the thermal expansion coefficient, whose value is  $\alpha = 5.0 \times 10^{-7} / ^\circ\text{C}$  for fused silica [33], and  $l$  and  $a_i$  are the initial MMF length and core/cladding radius, respectively.

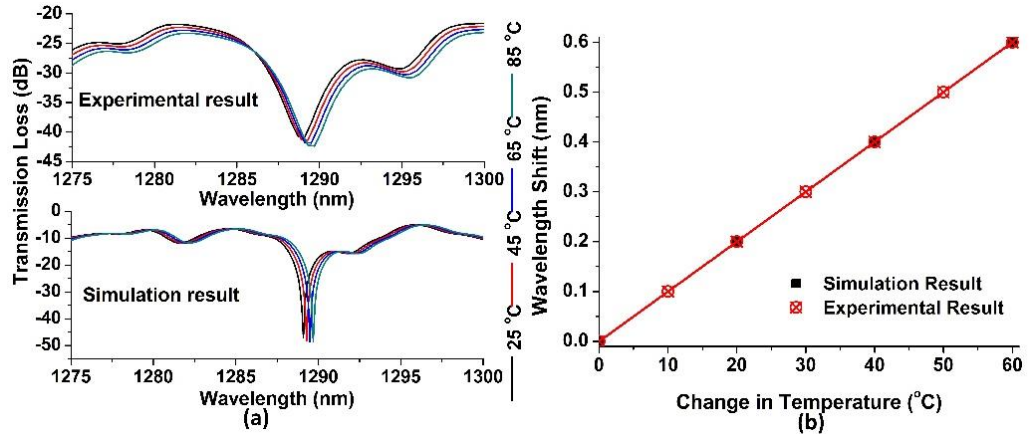


**Figure 2.4.** (a) Simulation results showing the effect of change in a temperature, in temperature range 25 – 85 °C, on an SMS fibre structure with 10 cm length of MMF, and (b) comparison between the simulations and experimental results.

Figure 2.4 shows the experimental and simulations results for an SMS-based sensor over a temperature range from 25 to 85 °C. In the simulations, the parameters of SMF28 and AFS105/125Y were used for the SMF and MMF, respectively. The length of the MMF used in the experiment was around 10 cm, and that considered in the simulations was 9.8725 cm to match the spectral responses. The calculated and experimentally observed spectral responses, over a temperature range from 25 to 85 °C, are shown in Figure 2.4 (a). The comparison of simulated and experimentally achieved sensitivities is presented in Figure 2.4 (b), which shows a similar temperature sensitivity of 10 pm/°C. During simulations as well as experimentation, only the effect of temperature on the MMF section were considered. The silica optical fibre has a well-defined temperature coefficient, which helps in accurately calculating the temperature effect.

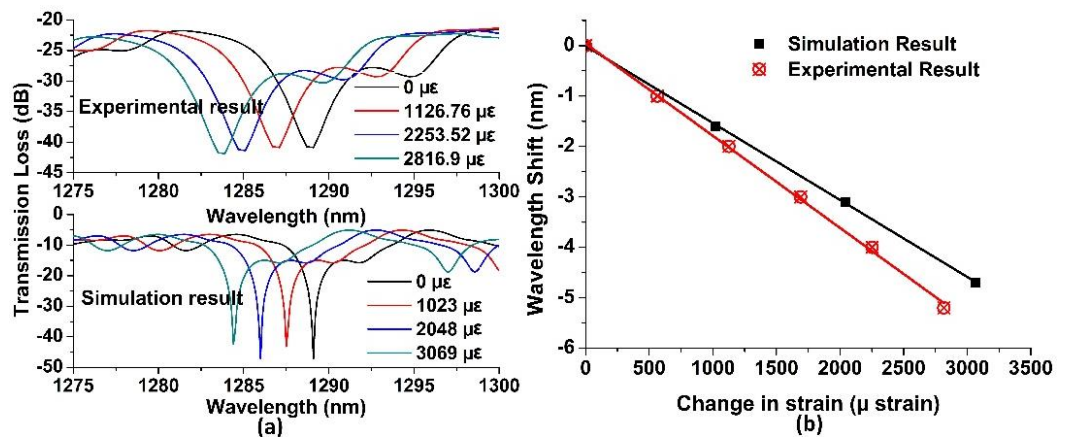


**Figure 2.5.** (a) Simulation results showing the effect of change in strain, from 0 – 3069 µε, on an SMS fibre structure with 10 cm length of MMF, and (b) comparison between the simulations and experimental results.

Figure 2.5 (a) shows the strain induced spectral responses and wavelength shifts as obtained from the numerical simulations and experimental demonstrations. The length of the MMF used in the experiment was around 10 cm and that considered in the simulation was 9.87 cm, which was done to match the simulated and experimental spectral responses. Strains in the range from 0 – 3000  $\mu\epsilon$  (micro-strain) were applied. As shown in Figure 2.5 (b), the simulated strain sensitivity was 1.56 pm/ $\mu\epsilon$ , which is very close to the measured strain sensitivity of 1.77 pm/ $\mu\epsilon$ .

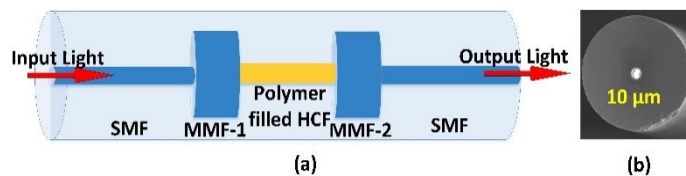
### **2.3 High Sensitivity Temperature Sensor Using Hollow-core Fibre Filled with Polymer**

Temperature sensors have a wide range of applications in both industry and research, which often require high sensitivity and accuracy. OFSs provide the advantages of high sensitivity, wide dynamic range, multiplexing capability, remote sensing capability, immunity to electromagnetic interference (EMI), and the capability to operate in harsh environments. Different types of OFS structures such as those based on gratings [76], FPIs, special fibres [77], and D-shaped PCFs [78] have already been described as temperature sensors in the previous discussions, in Chapter 1. Since the optical fibre is normally made of silica which has low TOC (typically  $1.06 \times 10^{-5} /^\circ\text{C}$ ), the traditional silica fibre sensor has relatively low temperature sensitivity. To improve the temperature sensitivity, polymer coated fibre sensors have been proposed, which utilise polymer materials having a TOC higher than that of silica. For example, an improved sensitivity of 255.4 pm/ $^\circ\text{C}$  has been demonstrated for the fibre Bragg grating (FBG) sensor, which is more than four times higher than that of a conventional uncoated FBG sensor [79]. In this section, we proposed a novel high sensitivity temperature sensor by using a polymer-filled hollow core fibre sandwiched between two SMF-MMF (SM) fibre structures. Since the polymer material has a much higher thermo-optic coefficient ( $-1.83 \times 10^{-4} /^\circ\text{C}$ ) [80] compared to that of silica ( $1.06 \times 10^{-5} /^\circ\text{C}$ ), a high temperature sensitivity was experimentally demonstrated.

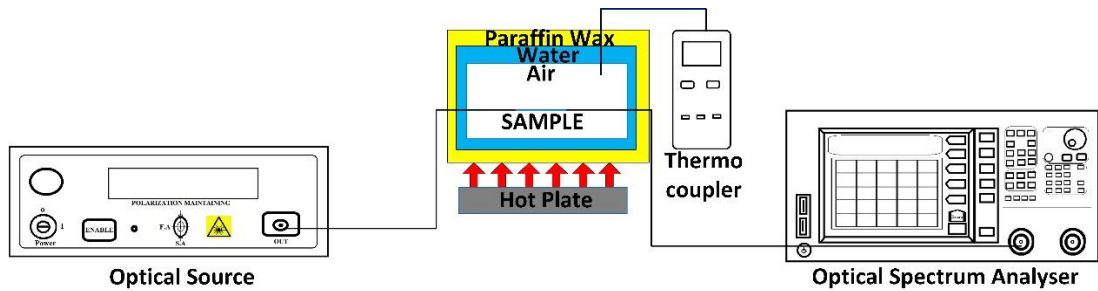
#### **2.3.1 Sensor structure and experimental setup**

Figure 2.6 shows a schematic diagram of the proposed SMF-MMF-HCF-MMF-SMF (SMHMS) interferometer-based fibre structure. When light is injected into the input MMF

(MMF-1) through an input SMF, multiple modes are excited and propagate across the MMF-1 section. At the interface between MMF-1 and HCF, these modes will excite multiple modes in the polymer-filled HCF section, which are highly dependent on the core RI of the HCF [81]. These modes propagate separately and interfere with each other and will be coupled to the output MMF (MMF-2), and eventually be coupled to the output SMF, resulting in a transmission spectrum with characteristic interference dips. In the experiments, the SMF (SMF-28, Thorlabs) was fusion-spliced to a short section (lengths of 5 mm and 10 mm were both used) of a conventional MMF with a 105/125  $\mu\text{m}$  core/cladding diameter (AFS105/125Y, Thorlabs) to form an SM fibre structure. The HCF has 10  $\mu\text{m}$  air core diameter and 125  $\mu\text{m}$  cladding diameter, where the air core was filled with Norland Adhesive (NOA-84) polymer. The polymer has an RI of 1.46 and a high TOC ( $-1.83 \times 10^{-4} / ^\circ\text{C}$ ) compared to that of silica ( $1.06 \times 10^{-5} / ^\circ\text{C}$ ). After curing the NOA-84, a short section of the NOA-84-filled HCF was fusion-spliced between the two SM structures.



**Figure 2.6.** Schematic diagram of a singlemode-multimode-hollow core-multimode-single mode fibre structure



**Figure 2.7.** Schematic diagram of the experimental setup used to measure the temperature sensitivity of the SMHMS structure.

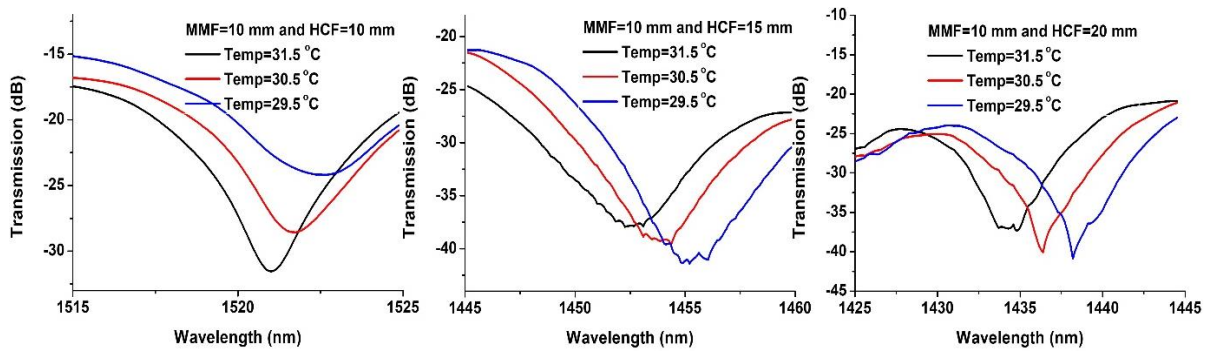
Figure 2.7 shows the schematic diagram of the experimental setup used for measuring the temperature response of the sensor. In the experiments, both MMF-1 and MMF-2 had similar lengths and same core diameters. Two different lengths of 5 mm and 10 mm for the two MMFs and three different lengths (10 mm, 15 mm and 20 mm) of the HCF were used to investigate the influence of the MMF and HCF lengths on the sensitivity of the temperature

sensor. Table 2.2 summarises the parameters of the fibre structure and the specifications of the components used to build the experimental setup.

**Table 2.2.** Summary of SMHMS fibre structure parameters and specifications of components used in the experimental setup, for temperature sensing.

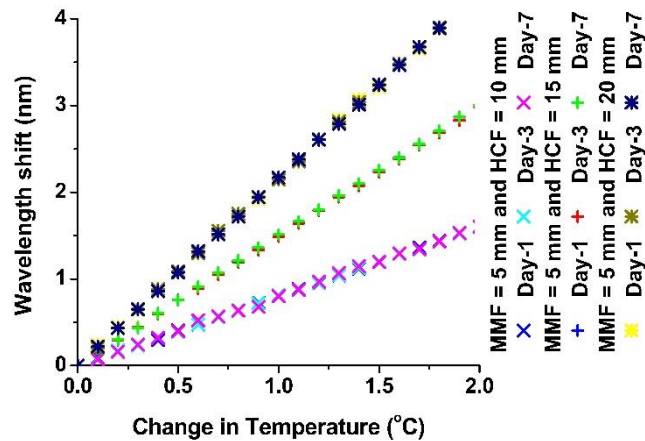
	<b>Fibre Type</b>	<b>Parameter</b>
<b>Fibre Structure</b>	MMF (Thorlabs-AFS 105/125Y)	Core diameter = 105 $\mu\text{m}$ Cladding diameter = 125 $\mu\text{m}$ Length = 5 and 10 mm
	SMF (Thorlabs-SMF-28)	Core diameter = 8.2 $\mu\text{m}$ Cladding diameter = 125 $\mu\text{m}$
	HCF	Core diameter = 10 $\mu\text{m}$ Cladding diameter = 125 $\mu\text{m}$ Length = 10, 15 and 20 mm
	Norland Adhesive (NOA-84)	RI = 1.46 TOC = $-1.83 \times 10^{-4} \text{ } ^\circ\text{C}$
	<b>Components</b>	<b>Specifications</b>
<b>Experimental setup</b>	Optical source (Thorlabs SLD S5FC1550S-A2)	Centre wavelength = 1550 nm Output power = 2.5 mW Bandwidth = 90 nm
	Thermocouple (RS 206-3738)	Temperature range = $-50 - 1300 \text{ } ^\circ\text{C}$ Resolution = 0.1 $^\circ\text{C}$
	Optical spectrum analyzer (Yokogawa AQ6370D)	Wavelength range = 600 -1700 nm Accuracy = $\pm 0.01 \text{ nm}$ Resolution = 0.02 nm

Figure 2.8 shows the spectral responses for three SMHMS structures with a fixed length of the MMFs (10 mm), and variable lengths of polymer-filled HCF (10, 15 and 20 mm). It can be observed that as the temperature increases, the spectral responses shift towards shorter wavelengths monotonically for all the three samples. A similar response was observed for the SMHMS structures with a 5 mm length of the MMF and three different lengths of 10, 15, and 20 mm of the polymer-filled HCF. Figure 2.8 also shows that a longer HCF length (HCF=20 mm) causes a larger blue shift in the dip wavelength compared to those caused by shorter HCF lengths (HCF=10 and 15 mm). Note that, since the spectral dips were noisy, 3 dB analysis of the spectral dip was applied to identify the dip wavelength in the spectral responses.



**Figure 2.8.** Spectral response for 10 mm of MMF and 10, 15 and 20 mm lengths of the polymer-filled HCF in the SMHMS structure.

Figure 2.9 shows the wavelength shifts vs. change in temperature for the three SMHMS fibre structures. As can be seen from Figure 2.9, for a fixed length of MMF, the longer the HCF length, the higher the temperature sensitivity achieved. The maximum sensitivity achieved in the experiments was 2.16 nm/°C for the polymer-filled HCF with a 20 mm length, which is 2.7 times (0.79 nm/°C) of that with 10 mm HCF length. The repeatability of all the six SMHMS fibre structures was also investigated by comparing the initial measurements on day one with those carried out on the 3rd and 7th days after the fabrication of the sensors. Figure 2.9 also shows that the sensors have good repeatability and stability where the wavelength shifts measured on the 1<sup>st</sup>, 3<sup>rd</sup> and 7<sup>th</sup> days after fabrication are almost the same.



**Figure 2.9.** Experimental results for the wavelength shift vs. change in temperature for the SMHMS structure with a 5mm MMF length and various HCF lengths.

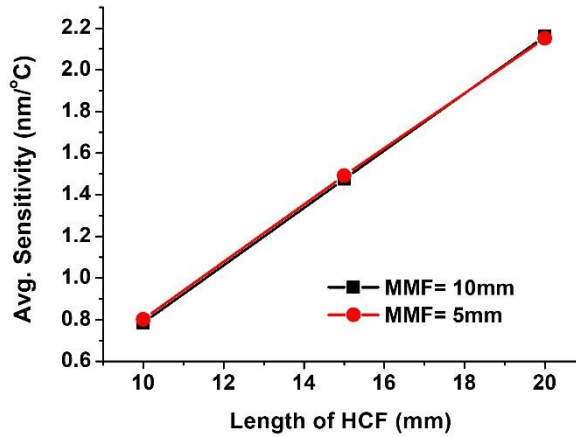


**Figure 2.10.** Temperature sensitivities for the sensors with two different MMF lengths as a function of different lengths (10, 15 and 20mm) of the polymer-filled HCF.

Figure 2.10 shows the influence of both the MMF and HCF lengths on the temperature sensitivity of the sensors. The individual sensitivity values of the sensors with different lengths of MMFs and polymer-filled HCF are listed in Table 2.3. It can be observed that the length of the MMF section has limited influence on temperature sensitivity of the SMHMS fibre structure. However, the length of HCF has significant influence on the sensor's temperature sensitivity where a sensor with a longer length of HCF has a higher temperature sensitivity, and a maximum temperature sensitivity of 2.16 nm/°C was achieved with a 20 mm length of polymer-filled HCF.

**Table 2.3.** Comparison of the change in average sensitivity as a function of increasing lengths of MMF and polymer-filled HCF in the SMHMS structure.

Length of polymer filled HCF (mm)	Temperature Sensitivity (nm/°C)	
	Length of MMF-1 & MMF-2 (5 mm)	Length of MMF-1 & MMF-2 (10 mm)
10	0.80	0.79
15	1.49	1.47
20	2.15	2.16

In conclusion, a highly-sensitive temperature sensor based on a polymer-filled HCF interferometer was proposed and investigated in this section. Experimentally, a maximum temperature sensitivity of 2.16 nm/°C was demonstrated, which is 200 times higher than that of a traditional SMS temperature sensor. The length of the MMF section was found to have a negligible influence on the temperature sensitivity of the sensor.

## 2.4 An Optical Fibre Interferometer-based Breathing Sensor

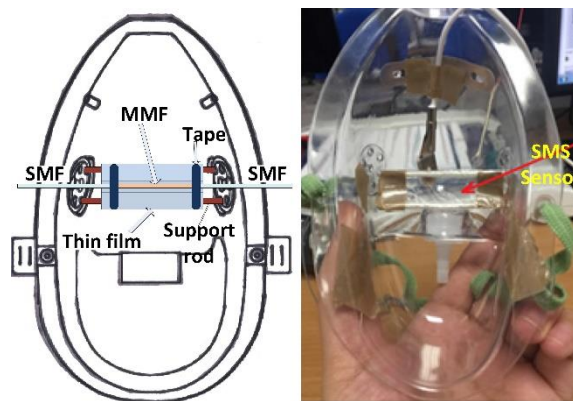
Breathing rate is defined as the frequency of breaths taken within a certain amount of time. The typical breathing rate for a healthy adult at rest is between 12 and 20 breaths per minute. It is recognised as one of the most important human vital signs to assess the physiological state, as a lot of valuable information related to cardiac, neurological, and pulmonary conditions can be obtained by analysing breathing data [82]. For example, patients' heart and lung condition can be identified by monitoring breathing state of the patient.

There are various methods for conducting breathing state measurements such as monitoring the air exhaled through the nose and mouth, or the external movement of the thoracic cavity/chest. Based on different working principles, a number of breath state sensors have been proposed, such as sensors utilising humidity or temperature measurements, and capnometers and spirometers to monitor breathing behaviour [83]. To date, most of the commercialised breath measurement devices are based on electronic sensors, which can be easily influenced by local electric/magnetic fields due to the presence of metallic parts or electrically conductive wires. Consequently, electronic breathing sensors are not suitable for applications associated with strong electric/magnetic environments [84], such as in a magnetic resonance imaging (MRI) system. However, in many practical situations, it is important to monitor the respiratory rate and apnoea during the use of MRI.

In this thesis, a simple, cost effective breathing state sensor is proposed based on an SMS fibre structure, which monitors the power variations of the input light intensity (instead of the wavelength shift monitored by FBG sensors [85] for which an expensive interrogation system is required), showing a fast and good response to different types of breathing conditions (regular, irregular, slow and rapid breathing states). The proposed breath sensor does not require any chemical/physical coating on the fibre sensor surface (and hence has a long life-time) and is mechanically robust.

In the proposed SMS fibre structure (schematically shown in Figure 2.1), light entering from the input SMF into the MMF (which typically has a step-index profile) excites multiple modes propagating along the MMF section. The field in the MMF section will be distributed symmetrically with respect to the fibre axis due to the symmetrical RI profile. However, if the MMF is bent, the RI profile is no longer symmetric, and as such, even a minor bend within the MMF section will introduce significant power variations at the output of the SMS fibre structure [86]. If such an SMS sensor is embedded within a flexible membrane

positioned near the patient's mouth, the breathing process will introduce macro bends to the SMS structure, and hence will result in light power variations at the output of the SMS fibre structure. By monitoring the light power variation, the breathing state can be measured. In our experiments, a short section of a multimode fibre (AFS105/125Y with a core diameter of 105  $\mu\text{m}$  and cladding diameter of 125  $\mu\text{m}$ ) with a length of approximately 20 mm was fusion-spliced between two singlemode fibres (SMF-28) and attached to a thin plastic film within an oxygen mask, as shown in Figure 2.11. The SMS fibre was straight and fixed on a plastic film which was wrapped around two thin support rods. The distance between the SMS-based breathing sensor and the patient's nose was set to approximately 50 mm, and can be adjusted in real-life applications depending on the condition of the patient. When the patient is breathing, the air flowing from their nose/mouth will induce pressure on the thin plastic film, and hence will bend the SMS sensor, resulting in power variations at the output of the sensor.



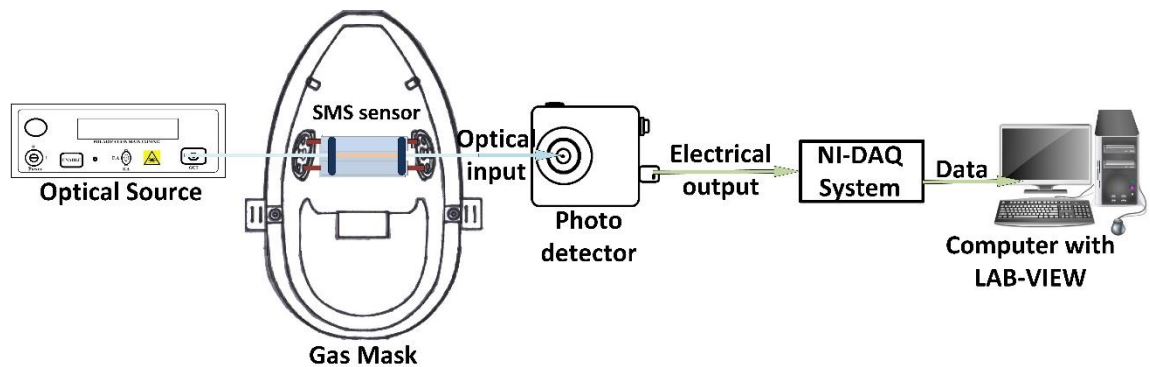
**Figure 2.11.** Schematic diagram and a photograph of the real prototype of the oxygen mask with an embedded SMS structure.

Figure 2.12 illustrates the schematic diagram of the experimental setup used for breath state monitoring. The broadband optical source (Thorlabs S5FC 1550P) used in the experiment is a super-luminescent diode with a central wavelength of 1550 nm. Light transmitted through the SMS structure is converted into an electrical signal by a photo-detector, acquired with a data acquisition system (NI-ELVIS II), and then analysed using a program based on a LabVIEW software. Table 2.4 summarises the parameters of the fibre structure and the specifications of the components used to build the experimental setup, for breath rate monitoring.

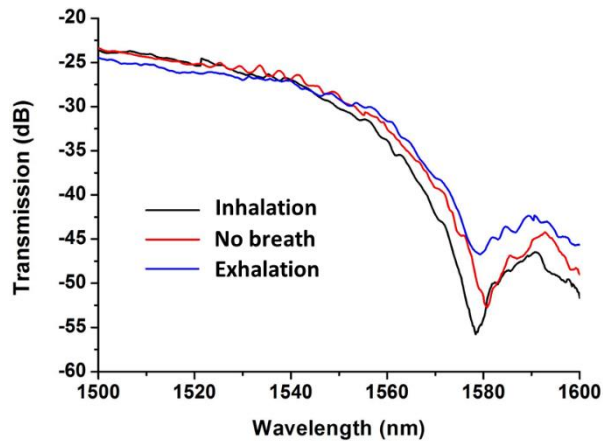
**Table 2.4.** Summary of SMS fibre structure parameters and specifications of components used in the experimental setup, for breath rate monitoring.

	<b>Fibre Type</b>	<b>Parameter</b>
<b>Fibre Structure</b>	MMF (Thorlabs-AFS 105/125Y)	Core diameter = 105 $\mu\text{m}$ Cladding diameter = 125 $\mu\text{m}$ Length = 5 and 10 mm
	SMF (Thorlabs-SMF-28)	Core diameter = 8.2 $\mu\text{m}$ Cladding diameter = 125 $\mu\text{m}$
	<b>Components</b>	<b>Specifications</b>
<b>Experimental setup</b>	Optical source (Thorlabs SLD S5FC1550S-A2)	Centre wavelength = 1550 nm Output power = 2.5 mW Bandwidth = 90 nm
	Photodetector (Thorlabs PDA 10CS-EC)	Wavelength range = 900 – 1700 nm Band width = 17 MHz Gain = 0 – 70 dB
	NI-DAQ System (NI ELVIS II)	Sample rate = 100 MS/s Resolution = 14 bit Bandwidth = 50 MHz

Figure 2.13 illustrates the transmission spectral response during the inhalation and exhalation process. The inhalation and exhalation cycles result in different forces on the plastic film, which in turn induces different bend radii in the SMS fibre structure (due to the different forces applied to the plastic film), and hence different spectral responses are recorded at the photodetector.

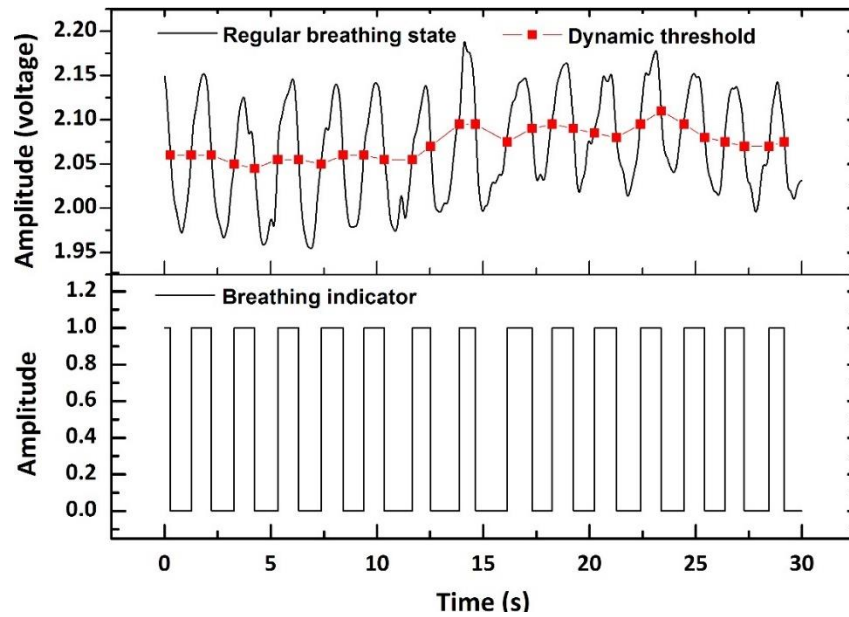


**Figure 2.12.** Schematic diagram of the breath monitoring experimental setup.



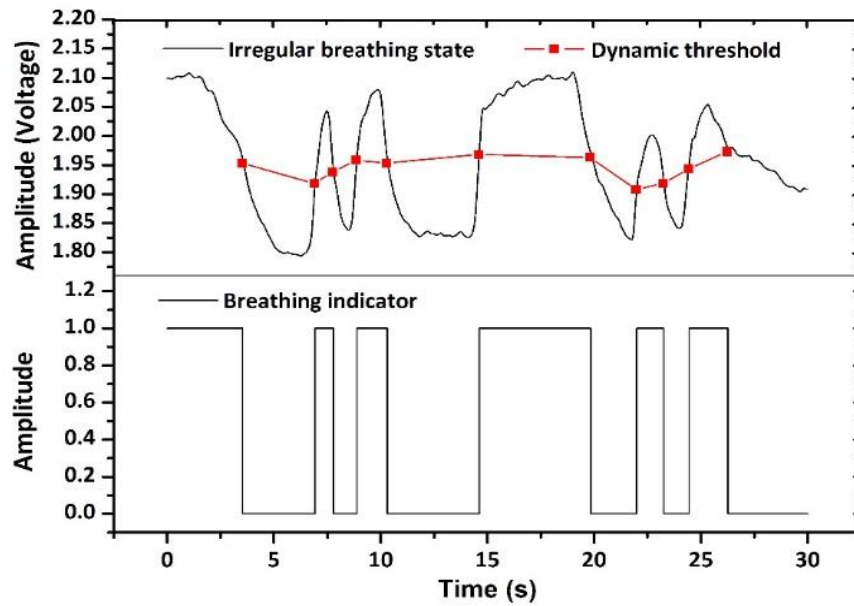
**Figure 2.13.** Spectral responses of the SMS-based breath sensor during the inhalation and exhalation processes.

Figure 2.14 illustrates the breath pattern for a regular breath state tested during a 30 seconds period. The upper plot shows the voltage change (representing the transmitted power variations detected by the photodetector) corresponding to the real time breathing response. During the exhale cycle, the airflow from the patient's nose introduces a bend to the SMS sensor, resulting in power variations transmitted to the photodetector. Therefore, the valleys and peaks of the photodetector's response in Figure 2.14 represent the inhalation and exhalation cycles, respectively. It is noted that due to the fact that the SMS sensor itself is bound to a thin plastic film, it is difficult to ensure that it is attached in a perfectly straight position. In addition, the power detected by the photodetector does not remain constant due to the inevitable environmental fluctuations from airflow, vibrations, and the incomplete recovery of the plastic film shape. It is hence impossible to set a fixed value as the threshold for determining either the inhalation or exhalation states. However, this problem can be solved by setting a dynamic threshold as an average value of all adjacent peak and valley pairs, as shown in Figure 2.14 with a red spot line plot. The lower plot in Figure 2.14 is the breathing cycle indicator, calculated from the breathing pattern in the upper plot using the dynamic threshold. In the experiment, a value lower than the threshold was defined as breathing state '0', which corresponds to an inhalation, while a value higher than the threshold was defined as breathing state '1', which corresponds to an exhalation. It is clear from the Figure 2.14 that the SMS fibre structure-based breathing sensor can be easily used for monitoring a regular breathing process.



**Figure 2.14.** Experimentally recorded breathing pattern and dynamic threshold in real-time (upper plot) and the corresponding breath analysis program’s response to a regular breathing pattern (lower plot).  
 (\* Experimental setup designed by Dejun Liu and Rahul Kumar, readings taken by Xixi Li, Northumbria University.)

In order to demonstrate that the proposed breathing sensor system is capable of monitoring various breathing states in real-time, three more breathing behaviours were tested, and the corresponding breathing patterns are shown in Figure 2.15, Figure 2.16 and Figure 2.17, which represent irregular, urgent and slow breathing states, respectively. From the figures, one can see that the proposed sensor can easily distinguish between the aforementioned different types of breathing conditions.



**Figure 2.15.** Experimentally recorded breathing pattern and dynamic threshold in real-time (upper plot) and the corresponding breath analysis program's response to an irregular breathing pattern (lower plot).  
 (\* Experimental setup designed by Dejun Liu and Rahul Kumar, readings taken by Xixi Li, Northumbria University.)

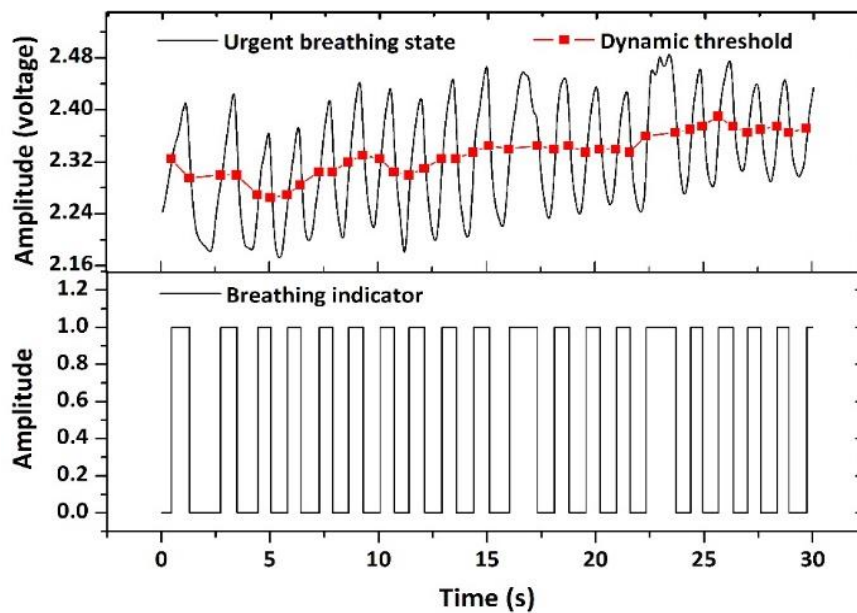


**Figure 2.16.** Experimentally recorded breathing pattern and dynamic threshold in real time (upper plot) and the corresponding breath analysis program's response to an urgent breathing pattern (lower plot).  
 (\* Experimental setup designed by Dejun Liu and Rahul Kumar, readings taken by Xixi Li, Northumbria University.)

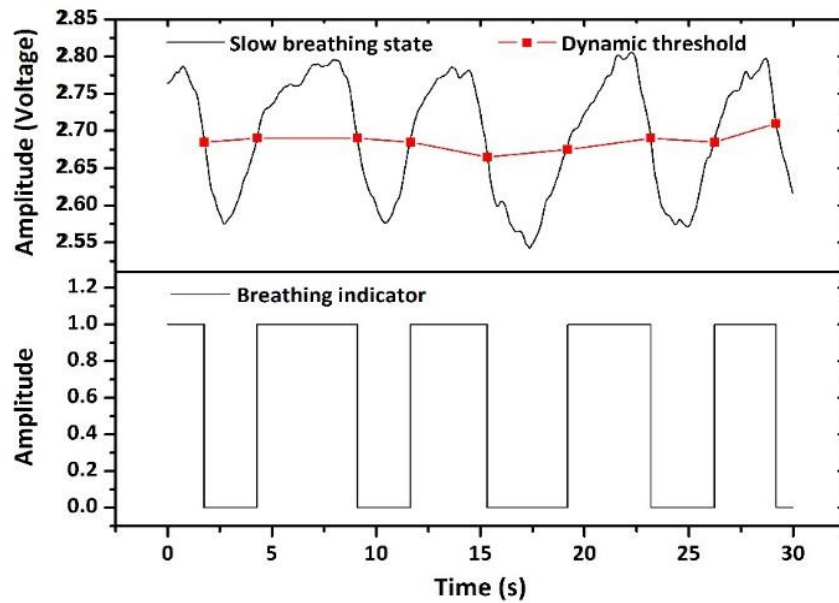


**Figure 2.17.** Experimentally recorded breathing pattern and dynamic threshold in real time (upper plot) and the corresponding breath analysis program’s response to a slow breathing pattern (lower plot).  
 (\* Experimental setup designed by Dejun Liu and Rahul Kumar, readings taken by Xixi Li, Northumbria University.)

In conclusion, a simple SMS fibre structure-based breathing sensor was proposed and experimentally investigated. By detecting the transmitted optical power variations due to fibre bending resulting from inhalation and exhalation cycles, patients’ breathing states can be monitored in real-time. The proposed sensor can help to easily distinguish between the different types of breathing conditions, ranging from regular and irregular breathing to urgent and slow breathing patterns. The sensor features advantages of easy fabrication, low cost, fast response, and potentially good resistance to environmental contamination.

## 2.5 Reflective SM Sensors for Monitoring Phase Transitions in PCMs

Solid-liquid PCMs have been widely used in latent heat thermal storage systems for heat pumps [87, 88], solar engineering [89], and spacecraft thermal control [90]. A simple and common application of PCMs can be seen in thermally insulated water bottles, where the PCM surrounded by water melts and is used to store the heat from the hot water. The stored heat is then released back to the water at a slower rate, as the PCM solidifies to maintain the desired water temperature over a longer period of time than would be the case if a simple insulator was used instead of a PCM. There are a large number of PCMs, which melt and solidify over a wide range of temperatures, and which are attractive for a wide number of applications [91]. The practical realisation of an efficient PCM-based thermal energy

management system requires an in-depth understanding of the PCM behavior during the melting and solidification stages. Solidification can occur below the expected phase transition temperature, a phenomenon referred to as under-cooling [91]. Temperature measurements are widely used to measure the amount of stored thermal energy in PCMs. However, in many cases, at the solid-liquid phase (SLP) change state, most materials have the same temperature but different energy levels. For example, at 0 °C, 1 gram of liquid water has 333.55 Joules more energy than that of solid ice. Therefore, sole dependency on temperature measurements may lead to an incorrect estimation of the stored energy in the PCM, particularly in a large PCM-based energy storage system. To address this issue, several techniques such as Differential Scanning Calorimetry (DSC) [92] and Differential Thermal Analysis (DTA) [93] have been proposed to estimate the phase state of PCMs. However, these techniques suffer the disadvantage of high cost and complex operation. For example, DSC requires a trained technician to carry out measurements as well as high cost equipment, such as a specialised furnace and sensors with star shaped arrangement of thermocouple. It is hence necessary to develop a new technique to monitor the SLP change by determining the start and end points of phase changes, a measurement which cannot be undertaken by traditional temperature sensors. One possible option is the use of OFS technology.

Among the various OFSs available, the SMS fibre sensor is very sensitive to even minor bending forces applied to it [94]. In a PCM, at the SLP change point, small local variations in the state of the material surrounding the fibre will result in slightly different forces being applied to different locations on the SMS fibre sensor, since these local variations occur on a spatial scale similar in size to the dimensions of the SMS sensor. The result is that micro bends occur along the length of the SMS sensor, which in turn lead to a significant wavelength shift ( $\Delta\lambda$ ) in the output spectrum of the SMS fibre sensor. In this experimental investigation, the SMS fibre-based sensor structure is proposed and demonstrated as a better and more accurate means to monitor the phase change ( $\delta\phi$ ) of a PCM between solid and liquid states. The well-known PCM, paraffin wax (327204 Aldrich), having a melting point between 53 °C - 57 °C, was used as the host material to test and optimise the proposed sensor because of its low cost and commercial availability. The optimised sensor was then further investigated to identify the phase states of two common PCMs of salt hydrates, namely S32 and S46 [90], which have phase change temperatures of 32 °C and 46 °C, respectively. In

future, the proposed sensor can be used as a cheaper alternative for real-time phase state monitoring of other PCMs in thermal energy storage systems.

In our research, two reflective SM fibre sensors with different MMF lengths of 5 mm and 10 mm were fabricated in order to investigate the influence of the MMF length on the measurement accuracy when monitoring the  $\delta\phi$  point of the PCM, as shown in Figure 2.18. The reflective SM structure was fabricated by fusion-splicing a short length of MMF (AFS105/125Y) with a conventional SMF (SMF28) and coating the MMF end with a thin layer of platinum (10 nm thickness). Note that, in principle, both the reflective and the conventional SMS fibres have the same transmission principle. Light propagates along the SMF and upon entering the MMF will excite multiple modes within its core. Since the MMF end is coated with a platinum coating, the propagating light will be reflected into the MMF fibre and subsequently coupled back into the SMF. The interference between the multiple modes within the MMF results in transmission dips in the output spectral response, which depend on the surrounding environment (i.e., local temperature ( $T$ ), longitudinal strain ( $\varepsilon$ ) and the fibre bending).

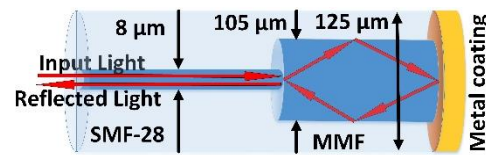


**Figure 2.18.** Schematic diagram of the reflective SM optical fibre structure.

The schematic diagram of the experimental setup used for measuring  $\delta\phi$  of the PCM is shown in Figure 2.19. A glass rod was used to fix both the OFS and a thermocouple as close as possible ( $< 2$  mm apart), with the rod and attachments then immersed in a beaker containing 250 mL of PCM. A broadband light source (SLD1005S) was used to launch light into the optical sensor via an optical circulator (OC). The reflected light from the sensor was observed with an optical spectrum analyser (OSA, Yokogawa AQ6370D) via the OC in order to analyse its spectral response. The OSA was programmed to automatically record the dip wavelength (maximum dip) every 2 minutes over a wide wavelength range from 1450 nm to 1650 nm. A thermocouple (RS 206-3738, K type, Accuracy  $\pm 0.2\%$  reading error  $+1$  °C) was used as a temperature reference from which the temperature readings were recorded every 2 minutes to correlate with the readings from the OSA. The heating and cooling conditions were maintained the same by using a water bath to gradually increase or

decrease the temperature. In addition, while heating the hot plate, the temperature was set to a level so that the time required to heat the PCM from its solid state to the liquid state was the same as that required to cool the PCM back to its solid state. Table 2.5 summarises the parameters of the reflective SM fibre structure and the components used to build the experimental setup for phase change measurement.

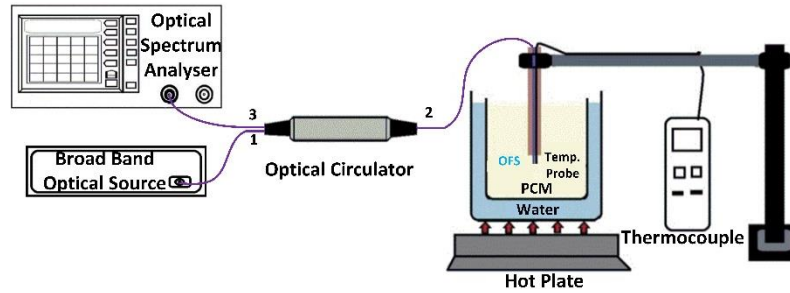


**Figure 2.19.** Schematic diagram of the experimental setup used for measuring the phase change ( $\delta\phi$ ) of PCM.

**Table 2.5.** Summary of reflective SM fibre structure parameters and specifications of components used to build the experimental setup, for phase change monitoring.

	<b>Fibre Type</b>	<b>Parameter</b>
<b>Fibre Structure</b>	MMF (Thorlabs-AFS 105/125Y)	Core diameter = 105 $\mu\text{m}$ Cladding diameter = 125 $\mu\text{m}$ Length = 5 and 10 mm
	SMF (Thorlabs-SMF-28)	Core diameter = 8.2 $\mu\text{m}$ Cladding diameter = 125 $\mu\text{m}$
	Metal coating (EMS 150R Plus rotary pumped coater)	Coating thickness = 10 nm Sputtering target/Metal used = Platinum (Pt)
	<b>Components</b>	<b>Specifications</b>
<b>Experimental setup</b>	Optical source (Thorlabs SLD S5FC1550S-A2)	Centre wavelength = 1550 nm Output power = 2.5 mW Bandwidth = 90 nm
	Optical circulator (Thorlabs- 6015-3-APC)	Wavelength range = 1525 – 1610 nm Insertion Loss = 0.8 dB Isolation > 40 dB Directivity (1→3) > 50 dB
	Thermocouple (RS 206-3738)	Temperature range = -50 – 1300 $^{\circ}\text{C}$ Resolution = 0.1 $^{\circ}\text{C}$
	Optical spectrum analyzer (Yokogawa AQ6370D)	Wavelength range = 600 -1700 nm Accuracy = $\pm$ 0.01 nm Resolution = 0.02 nm

### 2.5.1 Paraffin wax as a phase change material

Figure 2.20 (a) and (b) show the measured  $\Delta\lambda$  as a function of temperature (30.0  $^{\circ}\text{C}$  - 70.0  $^{\circ}\text{C}$ ) for the platinum-coated SM fibre structures with 5 mm and 10 mm long MMFs, respectively. Note that, to validate the reliability and repeatability of the proposed sensor,

two sets of measurements were carried out. The temperature  $T$  of the paraffin wax was measured with the thermocouple.

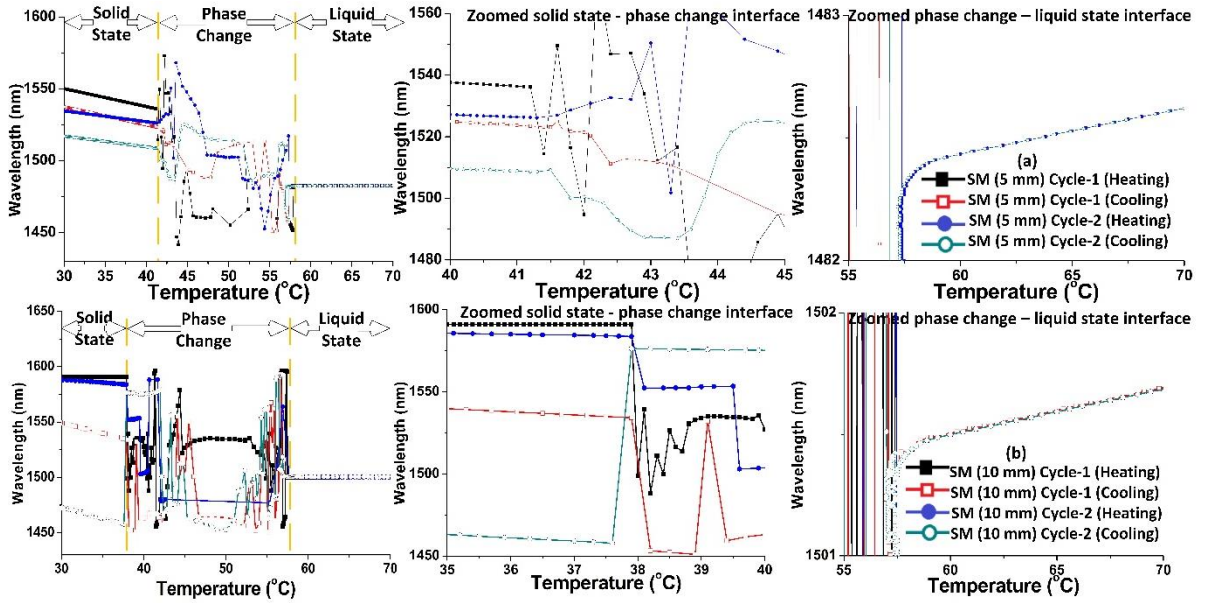


**Figure 2.20.** Measured wavelength shift ( $\Delta\lambda$ ) vs. temperature ( $T$ ) for the platinum-coated SM structure with MMF length of: (a) 5 mm, and (b) 10 mm. Two sets of measurements were taken by heating and then cooling the paraffin wax over a temperature range of 30.0 °C – 70.0 °C.

As shown in Figure 2.20 (a), there are two temperature ranges, namely 30.0 °C <  $T$  < 41.5 °C and 57.7 °C <  $T$  < 70.0 °C, where the paraffin wax is in solid and liquid states, respectively, and where the wavelength responses are fairly linear but with different slopes. The results indicate that the shift in the spectral dip within the aforementioned temperature range of 30.0 °C <  $T$  < 41.5 °C is mainly due to the temperature-induced strain on the sensor immersed in solid and liquid paraffin wax, while the spectral dip variation within temperature range of 57.7 °C <  $T$  < 70.0 °C is because of the temperature induced RI changes for both fibre sensor and paraffin wax. Of most interest is the temperature range 41.5 °C <  $T$  < 57.7 °C, where both solid and liquid states exist simultaneously, and where the stress applied along the length of the fibre sensor is not uniform, which in turn induces random micro-bends in the SM fibre sensor, thus resulting in a random wavelength shift with temperature. Note that the abrupt nature of the changes in the spectral wavelength is likely due to the random lateral force applied to the sensor by the solid-liquid mixed phase states of the wax, which leads to an abrupt micro-bending state at a random position and a random radius along the MMF section of the fibre sensor.

Figure 2.20 (a) also shows a good agreement in terms of the temperature range within which the phase change takes place for both cycles 1 and 2 (i.e., heating and cooling  $T$ ), as well as a similar response for each cycle. Note that, for all the measurements taken at  $T > 57.7$  °C, the wavelength profiles are the same. This is due to the fact that the wax is in the liquid state and the forces acting upon the sensor are small and homogenous, resulting in the absence of micro bending of the SM fibre sensor. However, for  $T < 41.5$  °C, the wax is in a solid state, resulting in micro bending of the sensor. Note that the micro bending state appears again when the wax cools down from the liquid to the solid phase state, thus resulting in a different but linear  $\Delta\lambda$  as a function of  $T$  (i.e., for all four sets of measurements for  $T < 41.5$  °C). For  $T < 41.5$  °C, the wax is completely solidified, and hence the temperature-induced micro bending in the SM fibre sensor is relatively small, thus resulting in a linear wavelength response. Similar changes in the wavelength with temperature are also observed for the reflective SM structure with a 10 mm long MMF (see Figure 2.20 (b)). The primary difference between the responses observed for the sensors with 5 and 10 mm long MMFs is in the temperature range where random fluctuations of the wavelength are clearly observed (i.e., indicating the  $\delta\phi$  of the paraffin wax), which are 41.5 °C – 57.7 °C and 37.8 °C – 57.7 °C for the 5 mm and 10 mm long MMFs, respectively. This is because the sensor's area immersed into the wax is larger because of the longer MMF, resulting in a higher temperature difference  $\Delta T$  across the MMF section compared with the shorter length MMF, since the temperature distribution in the wax is not uniform. Note that a higher  $\Delta T$  along the sensor's length will introduce more micro bending in the MMF section, thus resulting in random  $\Delta\lambda$  changes over a much larger temperature range read by the thermocouple, which is not desirable. The purpose of the sensor is to monitor  $\delta\phi$  at a single point without influence of other points in the wax. The undesired temperature influence from the adjoining layers of the wax for the shorter length MMF (i.e., 5 mm) sensor is rather small in comparison with the longer length MMF (i.e., 10 mm) sensor. Therefore, one can conclude that the sensor with a 5 mm long MMF offers improved measurement accuracy within the phase change state ( $41.5$  °C  $< T < 57.7$  °C) compared to that of 10 mm MMF sensor.

Figure 2.21 shows the measured  $T$  and the wavelength shift as a function of time for the paraffin wax within the temperature range  $30.0$  °C  $< T < 73.0$  °C for both, the heating and cooling cycles. Also depicted are the typical spectral responses for the reflective SM sensor with a 5 mm long MMF. As shown in Figure 2.21 (a), during the continuous heating process,  $T$  increases linearly for up to  $t = 120$  minutes, and then changes rapidly for the next 43

minutes, reaching a steady state value of  $\sim 57.7$  °C at  $t = 163$  minutes. Following this,  $T$  continues to increase in a linear manner. The first rise in  $T$  is due to the solid wax transferring heat with a relatively low thermal conductivity, which results in a significant  $\Delta T$  between the bottom of the wax (located near the heat source) and the measured point. After 120 minutes, the wax enters the phase change state, where both liquid and solid coexist, which significantly increases the thermal conductivity and consequently the abrupt changes in temperature. The constant  $T$  during  $163 < t < 273$  minutes is due to the liquid and solid in the container having the same  $T$ , where the additional heat energy absorbed by the wax is used to change the phase state from solid to liquid rather than alter the temperature. Beyond  $t > 273$  minutes, all wax changes from solid to liquid, and the absorbed heat begins to increase the wax's temperature. The spectral response of the reflective SM sensor with the 5 mm long MMF displays a random spectral pattern with no linear relationship in terms of the spectral width, intensity, or number of spectral dips with the changes in  $T$ , for  $121 < t < 174$  minutes and  $41.4$  °C  $< T < 57.7$  °C. This is because of the aforementioned paraffin wax-induced random micro-bending state of the SM sensor due to the simultaneous existence of solid and liquid phase states of the wax in the SM sensor area. Figure 2.21 (b) shows the opposite response for both  $T$  and  $\Delta\lambda$  to that of Figure 2.21 (a) for the case when the paraffin wax is cooling. The random spectral response within the time range  $156 < t < 205$  minutes is consistent with the simultaneous existence of solid and liquid phase states over the temperature range  $41.5$  °C  $< T < 57.7$  °C for the cooling cycle.

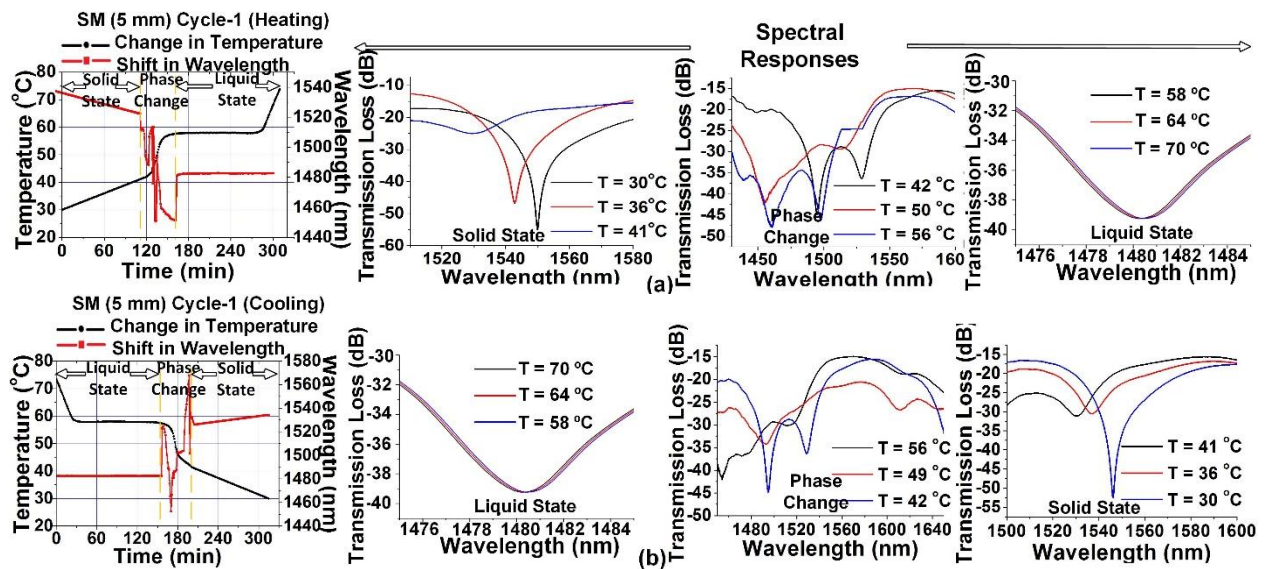


**Figure 2.21.** Comparison between the measured temperature ( $T$ ) and the wavelength shift ( $\Delta\lambda$ ) as a function of time ( $t$ ) for the paraffin wax over  $30$  °C  $< T < 73$  °C for: (a) heating cycle, and (b) cooling cycle. The typical spectral response of the reflective SM sensor with a 5 mm long MMF during different phase states of the paraffin wax are also presented.

Figure 2.22 shows the measured temperature and the wavelength shift observed using a reflective SM sensor with a 10 mm long MMF, as a function of time for the paraffin wax within the temperature range  $30.0\text{ }^{\circ}\text{C} < T < 73.0\text{ }^{\circ}\text{C}$ , for both, the heating and cooling cycles. Both the time and temperature follow the same relationship as that explained above for the reflective SM sensor with a 5 mm long MMF. However, the spectral response of the reflective SM sensor with a 10 mm long MMF displays a random wavelength variation in a wider temperature range ( $37.8\text{ }^{\circ}\text{C} < T < 57.7\text{ }^{\circ}\text{C}$ ) for  $80 < t < 172$  minutes while heating the paraffin wax, when compared to the reflective SM with 5 mm long MMF. This is because, during the heating and cooling process, the temperature distribution within the paraffin wax sample is not uniform. The longer length (10 mm) MMF is exposed to a larger area within the paraffin wax, resulting in larger temperature variations along the 10 mm MMF section compared to that of 5 mm MMF. However, the reference thermocouple only measures temperature at one point, resulting in a recorded random wavelength variation within a wider temperature range. The random spectral response within the time range of  $156 < t < 250$  minutes suggests the simultaneous existence of solid and liquid phase states at  $37.9\text{ }^{\circ}\text{C} < T < 57.6\text{ }^{\circ}\text{C}$  while cooling the paraffin wax.

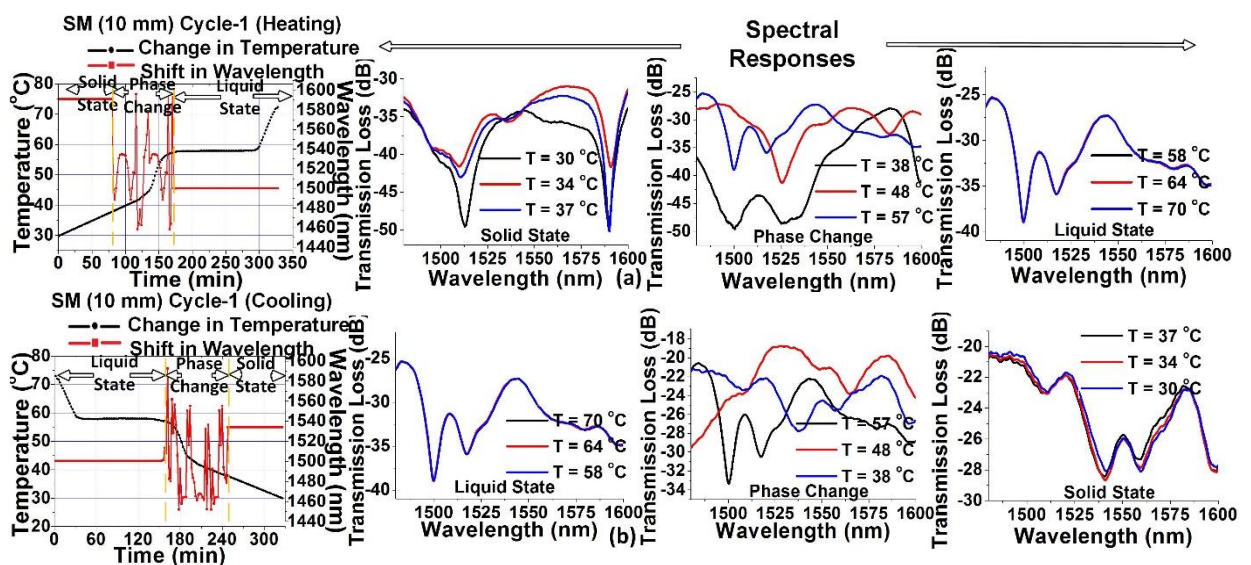


**Figure 2.22.** Comparison between the measured temperature ( $T$ ) and the wavelength shift ( $\Delta\lambda$ ) obtained using a reflective SM sensor with a 10 mm long MMF, as a function of time ( $t$ ) for the paraffin wax over a temperature range of  $30.0\text{ }^{\circ}\text{C} < T < 73.0\text{ }^{\circ}\text{C}$  for: (a) heating, and (b) cooling cycles.

It should be noted in Figure 2.21 and Figure 2.22 that the time required for the phase change, measured using thermocouple (constant  $T$  region represented by black square) is longer than that measured using reflective SM sensor (random wavelength variation represented by red

dots). This is because, the temperature of the paraffin wax (entire 250 mL) measured using thermocouple will remain stable until the phase of entire paraffin wax changes. However, the phase state of the wax layer closer to the hot plate will change before the top layer, therefore as desired from a point sensor, the reflective SM sensor measures the phase state of the wax layer surrounding it, as explained previously. Hence suggesting, only temperature information of PCM is insufficient for precise measurement of its phase state. A range of measured  $T$  values for different phase states of the paraffin wax for the two cycles of heating and cooling, corresponding to the sensor with 5 mm-long MMF and 10 mm long MMF are given in Table 2.6.

**Table 2.6.** Measured temperature ( $T$ ) for different phase states of the paraffin wax for the sensor with 5 and 10 mm long MMFs.

Phase	Temperature (°C)							
	5 mm of MMF				10 mm of MMF			
	Cycle – 1		Cycle – 2		Cycle-1		Cycle - 2	
	Heating	Cooling	Heating	Cooling	Heating	Cooling	Heating	Cooling
<b>Solid</b>	30 – 41.4	30 – 41.5	30 – 41.3	30 – 41.5	30 – 37.8	30 – 37.9	30 – 37.9	30 – 37.6
$\delta\phi$	41.4 - 57.7	41.5 – 57.7	41.3 – 57.7	41.5 – 57.8	37.8 - 57.7	37.9 – 57.6	37.9 – 57.7	37.6 – 57.7
<b>Liquid</b>	57.7 – 70.0	57.7 – 70.0	57.7 – 70	57.8 – 70	57.7 – 70	57.6 – 70.0	57.7 – 70.0	57.1 – 70.0

From the data presented in Table 2.6, one can clearly conclude that the start and end points of the phase change are 41.5 °C and 57.7 °C, respectively, for the 5 mm-long MMF sensor, which is smaller than that for 10 mm-long MMF sensor (37.8 °C and 57.7 °C), showing a better measurement accuracy for the shorter MMF sensor. The complete melting point of paraffin wax (57.7 °C) as observed from the proposed sensor matches the melting point of paraffin wax described in its data sheet.

The reflective SM sensor with 5 mm long MMF was further investigated as a means to measure the  $\delta\phi$  of two salt hydrates, S32 and S46, functioning as PCMs. The experimental investigation for these PCMs was carried out using the same experimental setup described above.

## 2.5.2 Salt hydrates S32 and S46 as PCMs

Salt is basically acid-base molecules, which are created when acid-anion and base-cation combine to form a crystalline structure. Salt hydrates are formed when water molecules are incorporated into the crystalline structure of the salt. Salt hydrates are the most commonly used thermochemical material (TCM) [95], in which the heat is stored by performing a reversible endothermic  $\leftrightarrow$  exothermic reaction ( $Salt \cdot nH_2O + heat \leftrightarrow Salt + nH_2O$ ) to change its phase state over a narrow temperature range. In this analysis, two salt hydrates, S32 and S46 (PCM products ltd) [90], were used as PCM samples, which have nominal phase state transition temperatures of 32 °C and 46 °C, respectively. Figure 2.23 (a) and (b) show the measured  $\Delta\lambda$  as a function of  $T$  of the reflective SM fibre structure with 5 mm long MMF, for S46 and S32 PCMs, respectively.

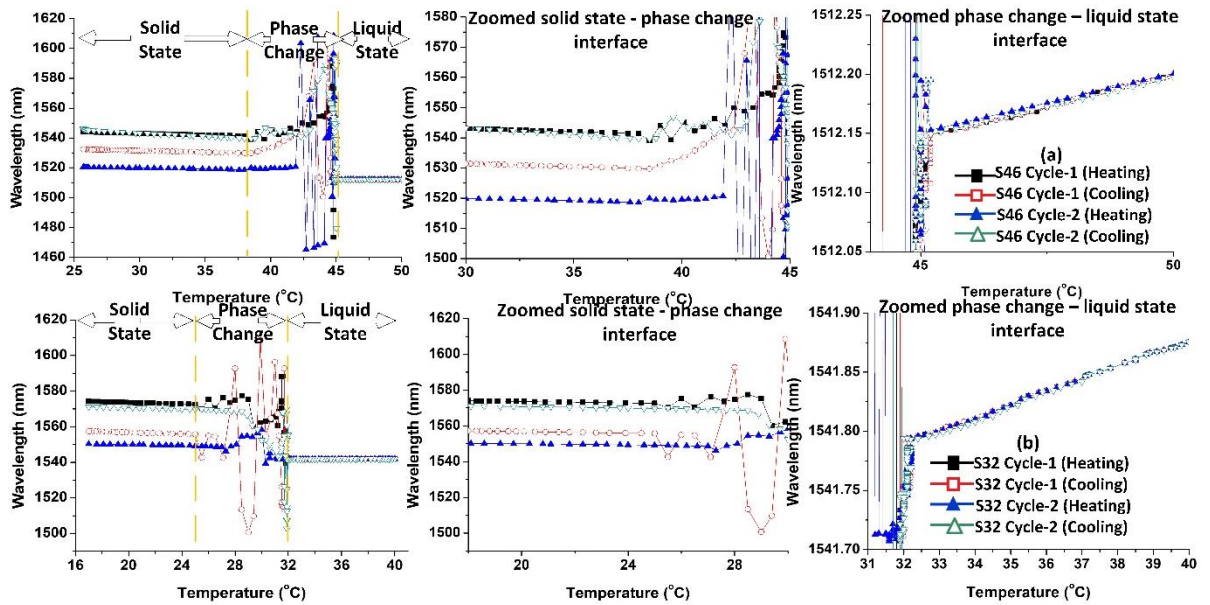


**Figure 2.23.** Measured wavelength shift ( $\Delta\lambda$ ) vs. temperature ( $T$ ) for the platinum coated SM structure with an MMF length of 5 mm for (a) SM46, and (b) SM32.

As can be seen in Figure 2.23 (a), the phase state of the S46 PCM changes between 38.5 °C – 45.9 °C, which is indicated by the random wavelength shift as a response to random micro-bends in the SM sensor during the phase change, similar to those observed in the paraffin wax. For  $T < 38.5$  °C and  $T > 45.9$  °C, the S46 PCM is in solid and liquid states, respectively. Figure 2.23 (b) shows the changes in the phase state of S32 PCM, occurring between 25.5 °C – 32.1 °C, as indicated by the random spectral wavelength shift during the measurement. For  $T < 25.5$  °C and  $T > 32.1$  °C, the S32 PCM is in solid and liquid states, respectively.

These experimental results suggest the suitability of the proposed sensor to identify the phase change of PCMs over a wide temperature range.

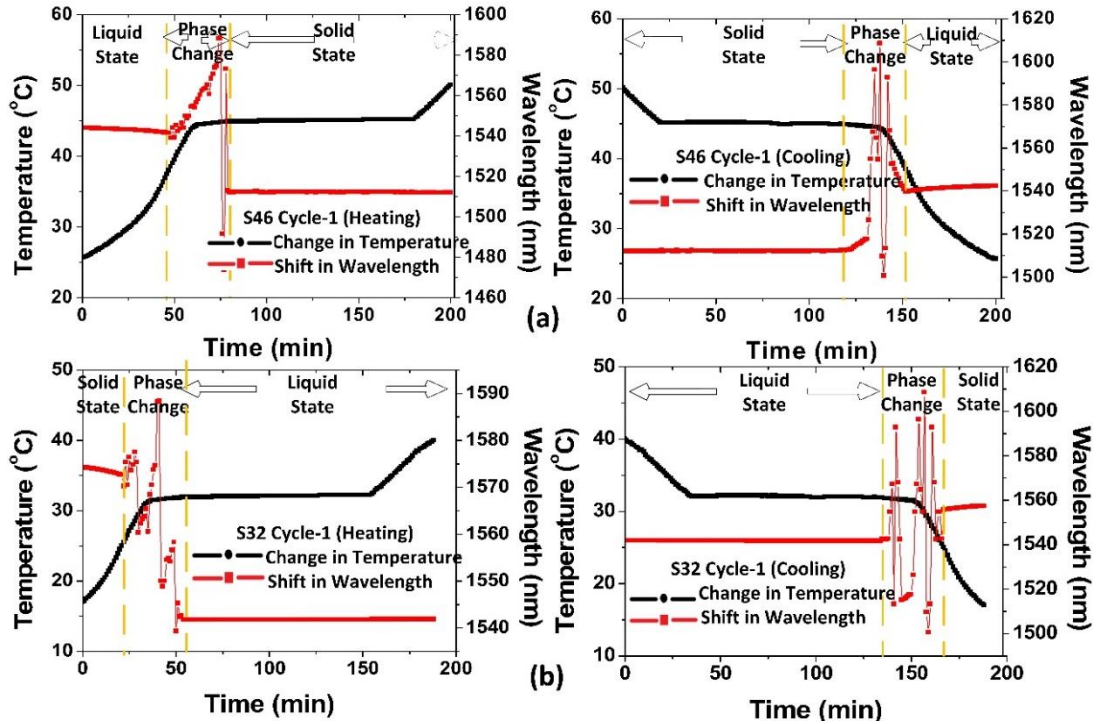


**Figure 2.24.** Comparison between the measured temperature ( $T$ ) and the wavelength shift ( $\Delta\lambda$ ) obtained using a reflective SM sensor with a 5 mm long MMF, as a function of time ( $t$ ) for (a) S46 and (b) S32 during the heating and cooling cycles.

Figure 2.24 (a) shows the measured temperature and the wavelength shift as a function of time for S46 within  $26.0\text{ }^{\circ}\text{C} < T < 50.0\text{ }^{\circ}\text{C}$  during the heating and cooling cycles. Both the time and temperature follow a similar relationship to that observed for paraffin wax, except for the  $T$  and  $t$  ranges for different phase states. The two temperature ranges where the spectral response of the reflective SM sensor with a 5 mm long MMF is fairly linear (i.e.,  $26.0\text{ }^{\circ}\text{C} < T < 38\text{ }^{\circ}\text{C}$  and  $46.1\text{ }^{\circ}\text{C} < T < 60.0\text{ }^{\circ}\text{C}$ ) indicate that the S46 is in solid and liquid states, respectively. The spectral response has a random wavelength variation in the temperature range  $38.5\text{ }^{\circ}\text{C} < T < 45.9\text{ }^{\circ}\text{C}$  at time range  $47 < t < 81$  minutes while heating the S46. During the cooling process of S46, the random wavelength variation is observed in the same temperature range of  $38.5\text{ }^{\circ}\text{C} < T < 45.9\text{ }^{\circ}\text{C}$  at time range  $121 < t < 152$  minutes. The random spectral response within the time range of  $47 < t < 81$  minutes (heating) and  $121 < t < 152$  minutes (cooling) suggests the simultaneous existence of both solid and liquid phase states at the temperature range between  $38.5\text{ }^{\circ}\text{C} < T < 45.9\text{ }^{\circ}\text{C}$ .

Figure 2.24 (b) shows similar results for the S32 PCM, except for the difference in  $T$  and  $t$  ranges. The spectral response of the reflective SM sensor experiences a random wavelength shift in the temperature range of  $25.5\text{ }^{\circ}\text{C} < T < 32.1\text{ }^{\circ}\text{C}$  during the process of both heating and cooling the S32 PCM, which indicates that solid and liquid phase states exist simultaneously in the temperature range between  $25\text{ }^{\circ}\text{C} < T < 32.1\text{ }^{\circ}\text{C}$  while heating and cooling the S32 PCM. The temperature ranges measured for different phase states of S46 and S32 using an optimised SM sensor with 5 mm long MMF are summarised in Table 2.7.

**Table 2.7.** Measured temperature ( $T$ ) values for different phase states of S46 and S32 using the SM sensor with a 5 mm long MMF.

Phase	Temperature ( $^{\circ}\text{C}$ )							
	S46				S32			
	Cycle - 1		Cycle - 2		Cycle-1		Cycle - 2	
	Heating	Cooling	Heating	Cooling	Heating	Cooling	Heating	Cooling
<b>Solid</b>	26 – 38	26 – 38	26 – 38	26 – 38	17 – 25	17 – 25	17 – 25	17 – 25
$\delta\phi$	38.5 – 45.9	38.5 – 45.9	38.5 – 45.9	38.5 – 45.9	25.5 – 32.1	25.5 – 32.1	25.5 – 32	25.5 – 32
<b>Liquid</b>	46.1 – 50	46.1 – 50	46.1 – 50	46.1 – 50	32.2 – 40	32.2 – 40	32.1 – 40	32.2 – 40

In conclusion, a reflective SM structure was proposed in this section as an OFS to monitor the phase transition of PCMs. During the phase change of the PCM, both solid and liquid states exist simultaneously, which results in random lateral forces applied onto the SM structure, thus introducing an abrupt micro-bending in the sensor. The micro-bending of the reflective SM sensor introduces an abrupt wavelength shift in the spectral response of the sensor. Based on the aforementioned principle, the influence of MMF length on the phase transition measurement was carried out using paraffin wax, which has a phase transition temperature range of  $41.5\text{ }^{\circ}\text{C} - 57.7\text{ }^{\circ}\text{C}$ , as the PCM. The initial experimental results demonstrated that a sensor with a shorter length of MMF (5 mm) offered improved measurement accuracy compared to that with the longer length MMF (10 mm). The reflective SM sensor with 5 mm MMF length was further investigated to identify the phase states of two salt hydrates (S32 and S46) with a nominal phase transition temperatures of  $32\text{ }^{\circ}\text{C}$  and  $46\text{ }^{\circ}\text{C}$ , respectively, suggesting the suitability of the proposed sensor for monitoring the phase states of any PCM, over a wide temperature range.

## 2.6 SMS Fibre-based Structure for RI Sensing

The traditional SMS fibre structure cannot be used for the measurement of the surrounding RI of the sensor. This is because the thickness of the cladding layer of an MMF is normally large, and as such, the evanescent field at the core-cladding interface is entrapped within the cladding layer and has no contact with the surrounding medium. To expose the evanescent field and make it interact with the surrounding environment, several effective fibre optic processing techniques based on modifying the traditional SMS fibre structure have been reported, which include etching the cladding layer [18], tapering the MMF section [27], or replacing the MMF with special optical fibres discussed further in this section. Etching the cladding layer, either chemically or mechanically, to expose the evanescent field to its surrounding medium introduces surface roughness, which makes the output response unstable and the sensor unreliable. On the other hand, tapering the MMF into a bi-conical shaped microfibre with a smaller diameter (typically  $< 10 \mu\text{m}$ ) to increase the evanescent field interaction with its surrounding medium is an alternative technique to introduce and improve RI sensitivity, and is discussed in detail in the next chapter. Replacing the MMF with a special optical fibre such as a no-core fibre (NCF), a small-core singlemode fibre (SCSMF), a photonic crystal fibre (PCF), or a hollow-core fibre (HCF) is another method of introducing RI sensitivity in an SMS based fibre structure. These special optical fibres are structurally modified in comparison with the traditional optical fibres, and an overview of a few of them is provided in the following discussion.

A no-core optical fibre (NCF 125) shown in Figure 2.25, is typically a silica cylinder of 125  $\mu\text{m}$  in diameter of constant RI (i.e. a single layered optical fibre). When considering light propagation inside the optical fibre, the entire fibre is considered as the core, and the surrounding medium as the cladding layer. This results in light reflection directly at the no-core – surrounding medium interface, thus allowing the evanescent field to interact with the surrounding medium. A simple singlemode – no-core – singlemode (SNCS) OFS was experimentally demonstrated in [96] with an RI sensitivity of 227.14 nm/RIU (refractive index unit) in the RI range from 1.300 to 1.430, and 7,792.85 nm/RIU in the RI range from 1.440 to 1.454. Fukano *et al.* demonstrated a high RI resolution of  $8.1 \times 10^{-6}$  using MMI in a structure composed of a no-core fibre sandwiched between two SCSMFs [97]. A coreless fibre (or NCF)-based structure has also been widely reported for humidity sensing [98], temperature sensing [99], and curvature sensing [100].

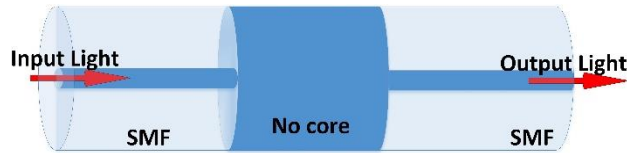


**Figure 2.25.** Schematic diagram of a singlemode – no-core – singlemode optical fibre sensor

Another replacement to the MMF which makes the SMS-based sensor structure sensitive to its surrounding RI is the SCSMF, whose core diameter is typically in the range of few nanometers. The core diameter mismatch between the SMF28 and the SCSMF, as shown in Figure 2.26, excites cladding modes within the SCSMF, thus generating evanescent field at the cladding-surrounding medium interface. Q. Wu *et al.* provided a comprehensive theoretical analysis for the SMF28–SCSMF–SMF28 structure and experimentally demonstrated a maximum sensitivity of 1808 nm/RIU for a surrounding RI range from 1.324 to 1.431 [101].

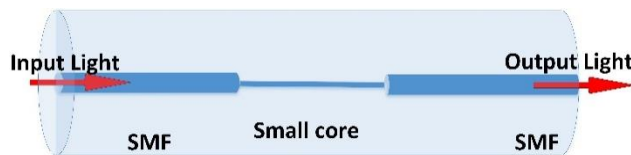


**Figure 2.26.** Schematic diagram of a singlemode – small core – singlemode optical fibre sensor

PCFs, also known as a micro-structured optical fibres, are relatively new type of fibres that were first reported in 1996 by Knight *et al.* [102]. Depending on the light guidance mechanism, PCFs can be classified as either index-guiding PCFs or photonic bandgap PCFs. An index-guiding PCF has a solid core surrounded by a micro-structured cladding, as shown in Figure 2.27 (a). Due to the presence of air holes in the cladding, the effective RI in the core is higher than that in the cladding, and the light is guided by the same mechanism as in a conventional optical fibre. The second type of PCFs is known as the hollow core PCF (HC-PCF), shown in Figure 2.27 (b). The light propagates through the lower RI fibre core by the photonic bandgap effect, allowing light guidance based on the proper design of micro-structured cladding. It should be noted that only a specific range of wavelengths which do not fall within the photonic crystal's stop bands can be efficiently confined in the core and propagate along the HC-PCF. In [103], Wang *et al.* presented an RI sensor based on an SMF-PCF-SMF structure with completely collapsed air holes. The sensor, with 5 cm length of PCF, was experimentally demonstrated to achieve a maximum RI sensitivity of 326 nm/RIU within the RI range of 1.403-1.422. Furthermore, Wang *et al.* in [104] demonstrated an RI

sensitivity of 224.2 nm/RIU for a directly spliced SMF-PCF-SMF OFS, with a PCF length of 4 cm.

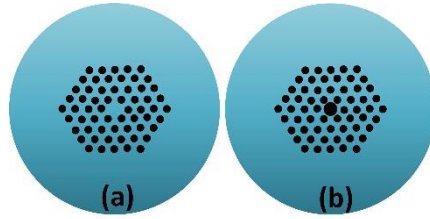


**Figure 2.27.** Schematic diagram of two main types of photonic crystal fibres (PCF) (a) index-guiding PCF and (b) photonic bandgap PCF.

In a multicore fibre, the light is guided along multiple cores. If the cores in a multicore fibre are close enough, modes transmitted in each of the cores can evanescently couple. This superposition of individual modes are known as super-modes. Zhang *et al.* demonstrated an RI sensor based on a twin core fibre with a novel T-shaped taper, achieving an RI sensitivity of 240.22 nm/RIU at 1580 nm for an RI range from 1.3388 – 1.3909 [105].

HCFs have an air-core in a silica cladding, which is mostly used as a means to incorporate an air-gap micro cavity within the fibre to form a Fabry-Perot interferometer (FPI) for sensing. For example, an HCF based FPI structure was demonstrated by Liu *et al.* in [106], achieving an RI sensitivity of 155.6 nm/RIU within the RI range of 1.33 – 1.39.

## 2.7 Effect of No-core Fibre Length and Diameter on RI Sensitivity

A high sensitivity RI sensor based on a reflective single mode small diameter no-core fibre structure is investigated in the following discussion. In this structure, a small diameter no-core fibre (SDNCF) used as a sensor probe was fusion-spliced to the end face of a traditional SMF, and the end face of the SDNCF was coated with a thin film of gold to provide light reflection. The influence of SDNCF diameter and length on the RI sensitivity of the sensor was investigated experimentally as well as through simulations.

### 2.7.1 Sensor structure and experimental setup

The schematic configuration of the proposed fibre refractometer is shown in Figure 2.28. It can be observed that the surrounding liquid effectively acts as the “cladding” of the SDNCF. When the input light carried by the SMF enters the SDNCF, multiple modes are excited,

which propagate within the SDNCF. The multiple modes of the SDNCF are eventually reflected by the end face of the SDNCF and are coupled back to the input SMF, which also acts as the output fibre of the sensor. For the experimental investigation, the fibre refractometer was fabricated by manually aligning SDNCFs of different lengths and diameters along a standard SMF (SMF28) before fusion-splicing. The fusion arc time and power were adjusted to ensure a low loss splice between the SMF and the SDNCF.

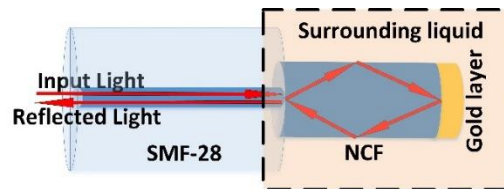


**Figure 2.28.** Schematic diagram of the proposed fibre structure as a refractometer

Figure 2.29 shows the schematic diagram of the experimental setup used for RI sensing. Light from a super luminescent diode (SLD) source (Thorlabs S5FC1005S) with a wavelength range of 1450 – 1650 nm was launched into Port 1 of a circulator, while Port 2 of the circulator was connected to the fibre refractometer. An OSA (Yokogawa AQ6370C) connected to Port 3 of the circulator was used to measure the output spectral response of the fibre refractometer. The fibre structure was fully immersed into an RI liquid sample. All measurements were carried out at room temperature.

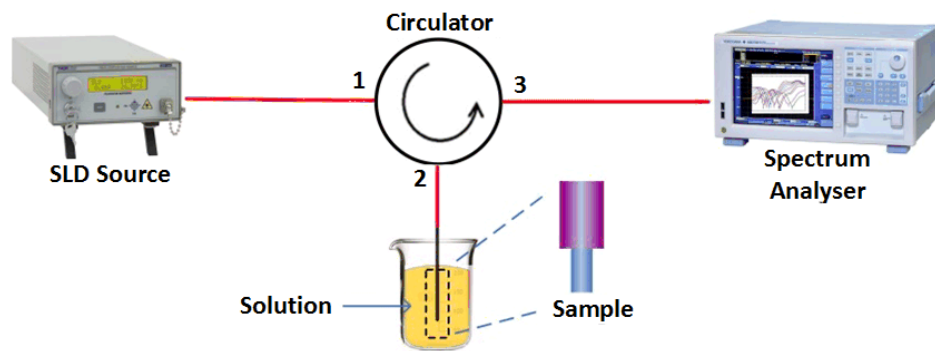


**Figure 2.29.** Experimental setup used for RI sensing.

Table 2.8 summarises the parameters of SMF and SDNCF used to fabricate the sensor structure, also presented are the specifications of the components used to build the experimental setup for RI sensing.

**Table 2.8.** Summary of reflective SDNCF fibre structure parameters and specifications of components used to build the experimental setup, for RI measurement.

	<b>Fibre Type</b>	<b>Parameter</b>
<b>Fibre Structure</b>	SDNCF (POF Corporation, Taiwan)	SDNCF diameter = 55 and 125 $\mu\text{m}$ SDNCF length = 15, 20, 25 mm
	SMF (Thorlabs-SMF-28)	Core diameter = 8.2 $\mu\text{m}$ Cladding diameter = 125 $\mu\text{m}$
	Metal coating (EMS 150R Plus rotary pumped coater)	Coating thickness = 10 nm Sputtering target/Metal used = Gold (Au)
	<b>Components</b>	<b>Specifications</b>
<b>Experimental setup</b>	Optical source (Thorlabs SLD S5FC1550S-A2)	Centre wavelength = 1550 nm Output power = 2.5 mW Bandwidth = 90 nm
	Optical circulator (Thorlabs- 6015-3-APC)	Wavelength range = 1525 – 1610 nm Insertion Loss = 0.8 dB Isolation > 40 dB Directivity (1→3) > 50 dB
	Optical spectrum analyzer (Yokogawa AQ6370D)	Wavelength range = 600 -1700 nm Accuracy = $\pm 0.01$ nm Resolution = 0.02 nm

### 2.7.2 Simulation results

If the SMF and SDNCF are ideally aligned, the input field at the interface between SMF and SDNCF is circularly symmetric, and only  $LP_{0m}$  modes will be excited in the SDNCF when light travels from the SMF to the SDNCF. Since the proposed reflective SMF – SDNCF is similar in principle to the SMS fibre sensor, the field equation at the end surface of the SDNCF is calculated in a similar manner as given by Equations 2.1 – 2.3, where the entire radius of the SDNCF is considered as the core radius. When the light is reflected back by the end-face of the SDNCF, an additional reflection coefficient  $\Gamma_m$  is introduced to the field  $E(r, z)$ , and the field at the output (which is the same as the input port) of the SDNCF is calculated by the following equation:

$$E'(r, 0) = \sum_{m=1}^M \Gamma_m E(r, z) \exp(j\beta_m z) \quad 2.8$$

where  $\Gamma_m$  is the reflectivity of the end-face of the SDNCF for each mode. The output power of the structure  $P_{out}(z)$  can thus be expressed as:

$$P_{out}(z) = \frac{|\int_0^\infty E'(r, z) E(r, 0) r dr|^2}{\int_0^\infty |E(r, z)|^2 r dr \int_0^\infty |E(r, 0)|^2 r dr} \quad 2.9$$

When the RI of the surrounding liquid changes, the effective RI of the SDNCF cladding changes correspondingly, and hence the excitation coefficient  $c_m$  of each modes changes, ultimately leading to a change in the optical output of the fibre structure in the above equation.

Based on the above analysis, numerical simulations were carried out, and the simulated spectral responses to surrounding liquids with various RIs are shown in Figure 2.30 (a). In the simulations, the RIs of the core and cladding of the SMF were 1.4504 and 1.4447 respectively. The core diameter of the SMF was 8.2  $\mu\text{m}$ , while an SDNCF of 55  $\mu\text{m}$  diameter, RI of 1.4504, and length of 15 mm was simulated. Since there is a gold layer on the end-face, to simplify the simulation, a reflection coefficient of  $\Gamma = 1$  was assumed. Figure 2.30 (a) shows that, as the surrounding RI increases, the spectral dip of the sensor shifts to longer wavelengths monotonically. The dip wavelength vs. the surrounding RI is plotted in Figure 2.30 (b), which shows a good linear fit (with correlation coefficient of  $R^2 = 0.988$ ) and a slope of 349.5 nm/RIU.

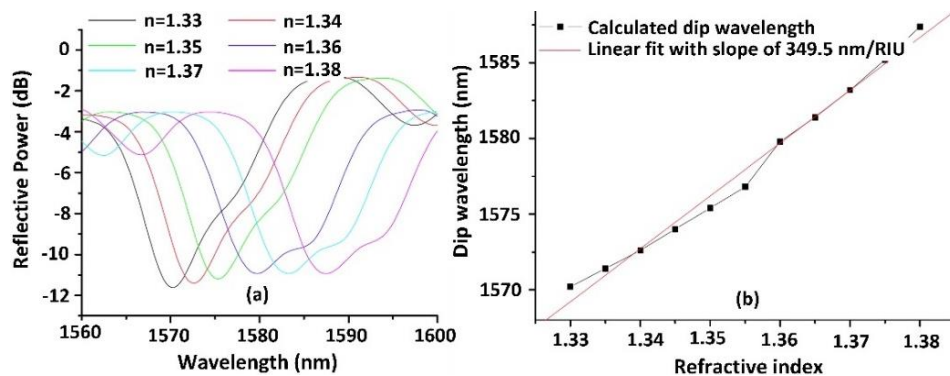


**Figure 2.30.** Simulated spectral response of the sensor at different surrounding RIs; and (b) dip wavelength shift vs. surrounding RI and its linear fit.

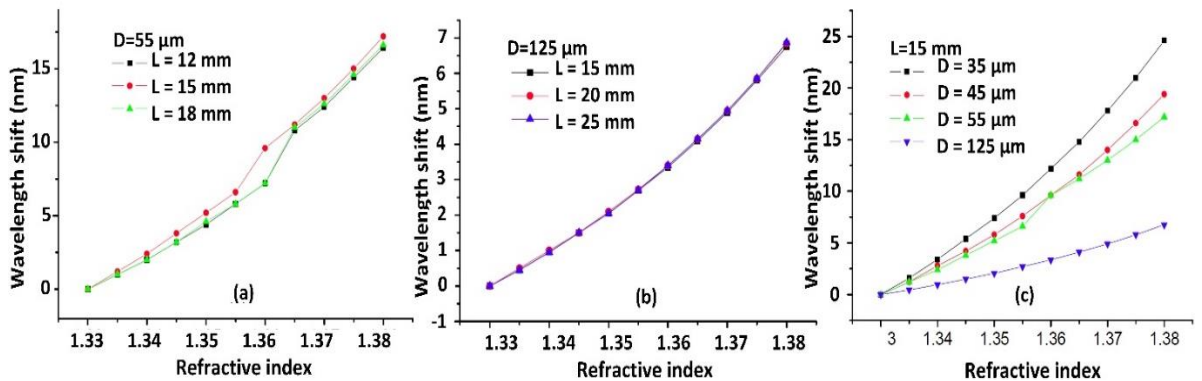
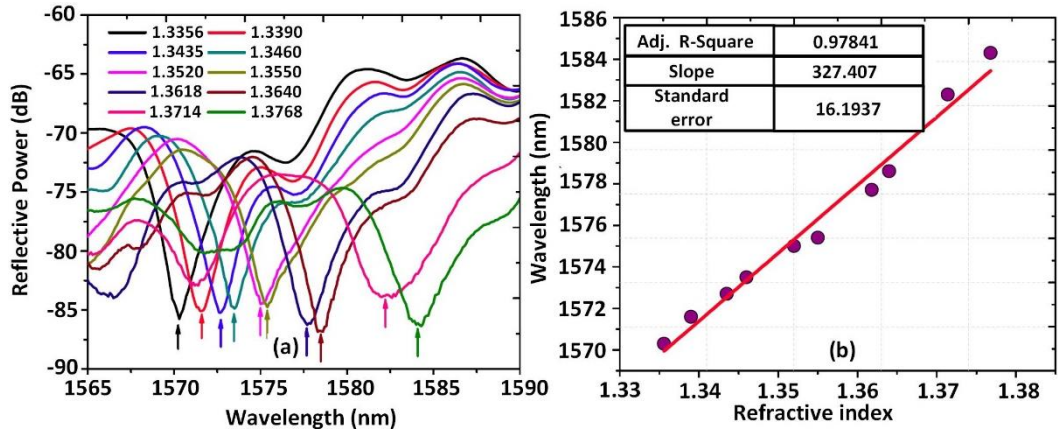


**Figure 2.31.** Simulated wavelength shift vs. surrounding RI for different lengths of the SDNCF: (a) L = 12, 15, and 18 mm and D = 55  $\mu\text{m}$ ; (b) L = 15, 20, and 25 mm and D = 125  $\mu\text{m}$ ; and (c) D = 35, 45, 55, and 125  $\mu\text{m}$  and L = 15 mm.

It can be seen from Figure 2.31 (a) and (b) that, for both diameters of  $D = 55 \mu\text{m}$  and  $125 \mu\text{m}$ , the length of the SDNCF has a limited influence on the RI sensitivity. The RI sensitivities for the SDNCF with  $D = 55 \mu\text{m}$  are 336, 349.5, and 340.7 nm/RIU corresponding to the three lengths of 12, 15, and 18 mm, respectively. Similarly, for the NCF with  $D = 125 \mu\text{m}$ , the RI sensitivities are 133.6, 134.7 and 135.7 nm/RIU corresponding to the three lengths of 15, 20 and 25 mm, respectively. The influence of the diameter of the SDNCF on RI sensitivity is illustrated in Figure 2.31 (c). It is easy to see that, for smaller diameters of SDNCF, the wavelength shift is larger, resulting in achieving higher RI sensitivities with smaller diameters of SDNCF. For the SDNCF with a diameter of  $35 \mu\text{m}$ , the estimated sensitivity is as high as 486 nm/RIU, which is a significant improvement compared to that of the  $125 \mu\text{m}$  diameter SDNCF sensor.

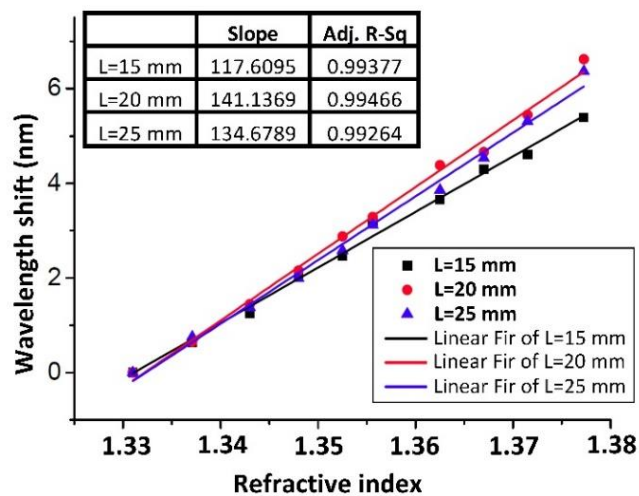
### 2.7.3 Experimental results

Figure 2.32 (a) shows the measured spectral responses of the sensor in various RI liquids, which are comparable with the simulated spectral response shown in Figure 2.30 (a). These RI liquids were made with different concentrations of sugar solution, which were calibrated using an Abbe refractometer (Kruess AR4D). The RIs of the RI liquids in the experiment were in the range of 1.33 –1.38. As can be seen in Figure 2.32 (a), the spectral response shifts monotonically towards longer wavelengths as the RI increases. Furthermore, Figure 2.32 (b) plots the wavelength shift of the spectral dip versus the change in RI of the surrounding medium. The figure indicates that the wavelength shift in the sensor's spectral response exhibits good linearity with the increase in RI. The RI sensitivity of the fibre sensor was measured to be 327 nm/RIU, which is very close to the simulated value of 349.5 nm/RIU, indicating that the developed simulation model is reliable.



**Figure 2.32.** Experimentally measured (a) spectral responses, and (b) wavelength shift of the RI sensor with  $D = 55 \mu\text{m}$  in various RI liquids.

To investigate the influence of SDNCF length experimentally, three sensors with different SDNCF lengths of 15, 20, and 25 mm and a diameter of  $125 \mu\text{m}$  were fabricated and experimentally investigated. Figure 2.33 shows that the three sensors with lengths of 15, 20, and 25 mm have RI sensitivities of 117.6, 141.1, 134.7 nm/RIU respectively, confirming that the length of the SDNCF has a very limited influence on the RI sensitivity of the sensor. The experimental results are also in good agreement with the simulated value of  $\sim 134$  nm/RIU. The results also show that the RI sensor with the larger SDNCF diameter ( $125 \mu\text{m}$ ) has a lower sensitivity (maximum 141 nm/RIU) in comparison with the smaller SDNC diameter of  $55 \mu\text{m}$  ( $\sim 327$  nm/RIU). Therefore, it can be concluded that the RI sensitivity of the NCF can be increased by reducing the fibre diameter, while the fibre length has a negligible influence on the RI sensitivity.



**Figure 2.33.** Measured wavelength shifts for RI sensors with  $L = 15, 20,$  and  $25$  mm and  $D = 125 \mu\text{m}$  in various RI liquids

In conclusion, a reflective SDNCF-based SMS fibre structure was proposed for RI sensing. Both the simulations and experimental results showed that the wavelength shift of the proposed refractometer exhibits a good linear relationship with an increase in the RI of the liquid under test. The simulation results showed that the length of the SDNCF has a limited influence on the RI sensitivity of the refractometer, but the diameter of SDNCF does have a significant influence on the RI sensitivity. The calculated maximum sensitivity for the RI sensor was 486 nm/RIU in the RI range from 1.33 to 1.38 for the SDNCF with a diameter of 35  $\mu\text{m}$ . The measured experimental sensitivity of the fibre refractometer with an SDNCF diameter of 55  $\mu\text{m}$  was 327 nm/RIU, which agrees well with the simulation result of 349.5 nm/RIU. The proposed refractometer has the advantages of being an endpoint sensor, which demonstrates a high sensitivity combined with a simple structure and easy fabrication. If an even smaller diameter of commercial NCF was used to replace the current 55  $\mu\text{m}$  fibre, the sensitivity of the refractometer can be further improved. The proposed fibre structure with an appropriate coating could have a wide range of applications, such as the detection of bio or chemical analytes, magnetic field and humidity measurements.

## 2.8 Summary

In this chapter, OFSs based on MMI were discussed in detail. The traditional SMS fibre structure was considered to explain the working principle of MMI-based sensors. External perturbations, such as strain and temperature, affecting the MMF section of the traditional SMS fibre structure influence the MMI pattern, which was exploited to demonstrate strain and temperature sensors, both theoretically and experimentally. A novel SMS based temperature sensor, with a temperature sensitivity over 200 times higher than traditional SMS sensor is experimentally demonstrated in this chapter. The lower temperature sensitivity of the traditional SMS fibre sensor due to the low TOC of silica ( $1.06 \times 10^{-5} / ^\circ\text{C}$ ) was improved by introducing a polymer-filled HCF with a higher TOC ( $-1.83 \times 10^{-4} / ^\circ\text{C}$ ) in the middle of the SMS structure.

In addition, a new breath sensor based on an SMS fibre structure was experimentally demonstrated to determine different types of breathing conditions (such as regular and irregular breath states) by detecting the power variations due to the macro bending applied to the SMS section by each inhalation and exhalation process. The proposed SMS-based breath sensor offers the advantages of easy fabrication, low cost, fast response, potentially

good resistance to environmental contamination, and the ability to monitor different breathing states in strong electro-magnetic interference environments (such as during an MRI or a CT scan).

Furthermore, an innovative method of determining phase change point of PCMs was demonstrated in this chapter. The micro bending introduced in a reflective SM structure due to random lateral forces during the phase change of PCMs was experimentally exploited in determining the phase states of paraffin wax (with phase transition temperature range of 41.5 °C – 57.7 °C) and two other salt hydrates, namely S32 (with a nominal phase transition temperature of 32 °C) and S46 (with a nominal phase transition temperature of 46 °C), suggesting the suitability of such a reflective SM sensor for monitoring the phase state of PCMs over a wide temperature range.

The sensitivity towards the RI of surrounding media is important in developing sensors for various applications, and is a requirement in this research work for developing a bio-chemical sensor. Therefore, methods to improve the RI sensitivity of the traditional SMS structure were discussed, and a reflective SDNCF based on an SMS fibre structure was demonstrated for RI sensing. The investigation of the effect of the length and diameter of the SDNCF on RI sensitivity suggested that SDNCF with a smaller diameter has higher RI sensitivity, while SDNCF length of the sensor has no significant influence on RI sensitivity. The calculated maximum RI sensitivity of the sensor was 486 nm/RIU in the RI range from 1.33 to 1.38 for the SDNCF with a diameter of 35 µm. The experimentally measured sensitivity of the fibre refractometer with an SDNCF diameter of 55 µm was 327 nm/RIU, which agrees well with the simulation result of 349.5 nm/RIU, hence suggesting that the RI sensitivity of the structure can be further improved by using a smaller diameter of NCF. The proposed OFS, with an appropriate coating, can have a wide range of applications, such as the detection of bio or chemical analytes, magnetic field detection, and humidity monitoring.

The fabrication cost for each of the SMS based fibre structures demonstrated in this chapter for different sensing application is very low (~ £10). However, the wavelength-based demodulation technique (optical spectrum analyser) used for measuring the wavelength shift corresponding to the change in parameter under observation, is expensive (~ £30,000). As observed from the experimental results demonstrated in this chapter, when the parameter under observation changes, the intensity value (at a specific wavelength) also changes along with the corresponding wavelength shift. Therefore, for practical systems the cheaper

alternative for designing a demodulation technique can use intensity-based analysis, in which the broadband optical source can be replaced by an IR-LED (~ £50) as a light source, and photodetector (~ £50) along with data acquisition system (~ £100) for computer interfacing, can be used for analysing the intensity changes in the sensor output. Hence, reducing the effective cost (< £300) for implementing OFSs in practical system, which can be further reduced in bulk production.

## **Chapter 3: Singlemode Tapered No-core Singlemode (STNCS) Fibre Sensor**

### **3.1 Introduction**

In this chapter, the traditional singlemode–multimode–singlemode (SMS) fibre sensor is made sensitive towards surrounding refractive index (RI) by replacing the multimode fibre (MMF) section with a coreless or no-core fibre (NCF). This single-layered NCF allows the evanescent field to directly interact with its surrounding without the need for removing the cladding layer to expose the evanescent field, as in the case of conventional fibres. The study of the NCF in the previous chapter suggested that smaller diameter NCFs have larger evanescent fields and hence higher RI sensitivity. Hence, the NCF diameter is reduced by tapering the fibre down to a few micrometres to increase the RI sensitivity.

This chapter begins by presenting an overview of the optical guidance properties in a tapered optical microfibre, followed by its fabrication process, and lastly its new sensing application for magnetic field measurement.

### **3.2 Operating Principle of the STNCS Sensor**

A singlemode – no-core – singlemode (SNCS) optical fibre sensor (OFS) is fabricated by replacing the MMF with an NCF in the SMS optical fibre structure. The guidance of light in an NCF can be intuitively understood by considering the entire fibre as its core and the surrounding medium as its “cladding”. Due to the absence of cladding layer, the evanescent field, which in general is produced and entrapped at the core-cladding interface, is now generated at the NCF-surrounding interface. This enables the evanescent field to directly interact with the fibre’s surroundings, thus making the SNCS OFS inherently sensitive to its surrounding RI (SRI). The amount of evanescent field around the fibre surface can be increased by reducing the fibre diameter, for example by tapering the NC section in the SNCS OFS to an STNCS OFS, the SRI sensitivity can be enhanced significantly (from 135 nm/RIU to 1046.34 nm/RIU for RI range around 1.33). In the case of STNCS, the diameter of the taper waist is reduced to a few micrometres ( $< 10 \mu\text{m}$ ), which allows for a significant portion of optical power (in the form of evanescent field) to propagate outside of the microfibre. It is necessary for the surrounding medium (“cladding”) to have a RI value lower

than that of the microfibre (typically  $< 1.44$ ), so that an adequate level of light confinement is achieved for its propagation along the microfibre.

### 3.2.1 Tapered SNCS optical fibre structure

In general, the conventional optical fibre is tapered by heating a section of the fibre at a temperature high enough to soften the silica fibre ( $\sim 1100\text{ }^\circ\text{C}$ ) and stretch it into a biconically-tapered shape. This bi-conical shape of the tapered optical fibre, shown schematically in Figure 3.1, can be divided into three main parts to understand the propagation of light in such a structure. The central part, with the smallest diameter, is called the taper waist. The two sections on both sides of the taper waist, between the taper waist and the uniform untapered fibre, are called the transition regions. Out of all the three sections, the taper waist is the most sensitive section, where significant amount of evanescent field interacts with the surrounding medium. Based on the shape of the transition region, tapered optical fibres can be divided into adiabatic and non-adiabatic types. For an adiabatically tapered fibre, the taper angle that exists along the transition region is so small that the majority of the optical power is confined within the core, and the coupling between the fundamental mode and the higher order modes is negligible. From an intuitive perspective, the taper angles are so small (shallow) for an adiabatic taper that the propagating mode sees a straight fibre [107]. However, if the taper angle of the transition region is large (abrupt) enough so that the core mode does not support propagation without coupling of power into the higher order modes, then such a tapered fibre can be considered as non-adiabatic. The energy transfer from the fundamental mode to the higher order modes is dependent on the rate of change of fibre diameter with distance along the fibre, which also determines the transmission loss. Therefore, the shape of the transition region plays an important role in controlling the light propagation, coupling between modes, and transmission losses, and as such, controlling its shape is important. To minimise the mode coupling, and hence the power loss, an adiabatic taper is preferred and is therefore considered in this thesis.

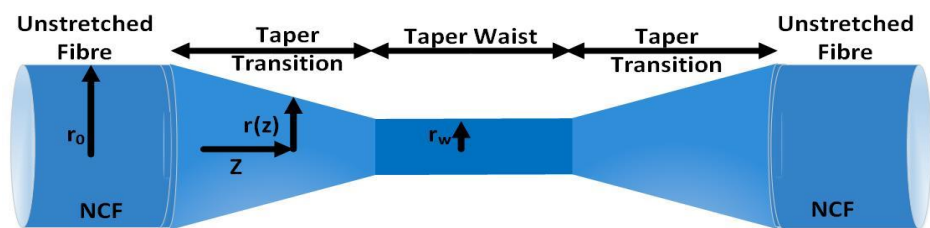


**Figure 3.1.** Schematic diagram of a tapered SNCS fibre.

Birks *et al.* developed a theory to control and fabricate different transition profiles in a tapered optical fibre structure [23]. Based on the conservation of mass, the model assumes the volume of the fibre to be constant during the tapering process. Furthermore, the length of the uniform taper waist region is always equal to the length of softened fibre, which is also equal to the total effective heating length  $L$ . The following equation holds under these conditions:

$$\frac{dr_w}{dx} = -\frac{r_w}{2L} \quad 3.1$$

where  $r_w$  is the radius of tapered fibre waist and  $x$  is the elongation of the fibre while tapering. During fabrication,  $L$  can be kept constant or varying while tapering the fibre. A constant  $L$  value (as used in our experiments) is used to fabricate a taper which has a relatively shallow transition regions with decaying exponential profile, and can therefore be approximately considered as an adiabatic taper. With a constant  $L$  and given original radius of the fibre  $r_0$ , the final taper waist radius of the tapered fibre  $r_w$  is expressed as:

$$r_w(x) = r_0 e^{-x/2L} \quad 3.2$$

Furthermore, the profile of the transition region can be expressed as:

$$r(z) = r_0 e^{-z/L} \quad 3.3$$

### 3.2.2 Method of fabrication

Tapered microfibres are fabricated using the micro-heater brushing technique [108], where the micro-heater (heat source) brushes over the fibre surface, adiabatically heating a section of conventional optical fibre while stretching it. In general, a standard fibre tapering process can be described as follows: The optical fibre is prepared for tapering by stripping off the buffer coating from a short section (3 – 4 cm) of the fibre; the stripped fibre is then cleaned and fixed onto two translation stages; the bare fibre section is then placed into a high-temperature heating source (micro-heater) and the temperature inside the micro heater should be high enough (usually around 1100 °C) to sufficiently soften the silica fibre into a viscoelastic state; the two translation stages then slowly move outward in the opposite direction to stretch the fibre and form it into a designed taper shape with the desired diameter.

A schematic diagram of the fibre tapering setup used in this research work is shown in Figure 3.2. The setup consists of two major parts:

(1) The heating source, which is a ceramic micro-heater (CMH-7019, NTT-AT). The micro-heater is mounted on a 3-dimensional translation stage to precisely control the position of the micro-heater relative to the fibre. The temperature inside the micro-heater is precisely controlled by a high precision DC current power supply.

(2) Pulling rigs, which are two computer-controlled linear motorised translation stages (XLSQ150A- E01, Zaber) are used to stretch the heated fibre. The tapering motion is controlled by a program written in C#, which precisely controls the tapering process. By setting parameters such as the original fibre diameter, required taper waist diameter, and heater bruising length in the program, a microfibre with the desired profile and taper waist diameter is fabricated.

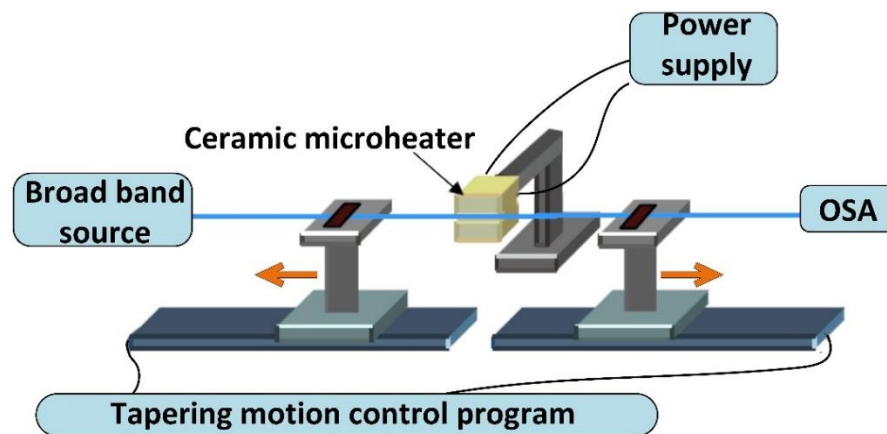


Figure 3.2. The experimental setup used for fabricating tapered optical fibres.

### 3.2.3 Tapered optical microfibres based on an SMS structure

Research on tapered optical fibre structures with diameters smaller than those of standard optical fibres date back to the 1970s [109]. Typical taper diameters ranging from several to tens of micro-meters are fabricated and used for different applications. Applications in optical filtering [110], amplification [111], and super continuum generation [112] have been proposed for optical communications, based on tapered optical fibres. Some work has also been carried out to explore the potential of tapered optical fibres for sensing, using the evanescent field [113] or the bending effects in the tapers [114]. In 1999, Moar *et al.* directly measured the evanescent fields of tapered optical fibres using scanning near-field optical microscopy, which provided the base for developing sensors using tapered optical fibres

[115]. In the early 2000, optical fibres with even smaller diameters in the subwavelength range, also known as nano-fibres, were demonstrated with extremely high RI sensitivity [116]. However, their experimental realisation is difficult due to the poor mechanical stability and difficulties in manipulation of such nano-fibres. Therefore, the major experimental explorations in the past were focused on using optical micro-fibres.

Similar to the different configurations of traditional SMS fibre structures discussed previously in Chapter 2, various replacements of the tapered MMF section in the SMF-tapered MMF-SMF (STMS) with other fibres have been demonstrated in the past, such as no-core fibres, small core SMFs, and other special fibres like photonic crystal fibres (PCF) and the multi-core fibres. The traditional STMS fibre was first proposed in 2011 by Wang *et al.* [75], demonstrating an RI sensitivity of 24.69 nm/RIU within the RI range of 1.333 – 1.382, with a maximum RI sensitivity of 1913 nm/RIU, achieved around the near-cladding RI of  $\sim 1.4$ . Multiple tapers on the same fibre can enhance the RI sensitivity further, but at the cost of an increased fabrication complexity and poor structural strength. For example, a multi tapered SMS fibre structure with up to eight tapers was demonstrated in [117] with an RI sensitivity of 261.9 nm/RIU in the RI range of 1.3333-1.3737. Replacing the MMF section with a small core SMF (SCSMF) to fabricate an SMF-tapered small core SMF-SMF (STSCS) fibre structure has also been investigated, and a maximum RI sensitivity of 19,212.5 nm/RIU was achieved in [118] within the RI range of 1.4304 to 1.4320. The use of a PCF has also been demonstrated, where for instance, a tapered multicore fibre was used in [119] to demonstrate a RI sensitivity of 171.2 nm/RIU within the RI range of 1.3448 – 1.3774. A hollow core fibre (HCF) with an improved RI sensitivity of 214.97 nm/RIU within the RI range of 1.333-1.379 was also demonstrated by forming an up-taper at the two splice points, and a concave cone in the HCF [120]. Another tapered hollow core PCF was demonstrated in [121] with a maximum RI sensitivity of 1426.70 nm/RIU within the RI range of 1.3917 – 1.4204. In our investigation, presented in Section 3.3, the maximum RI sensitivity observed by tapering the no-core fibre is 26,061 nm/RIU within the RI range of 1.402 – 1.421.

### **3.3 RI Sensitivity**

RI is an important physical parameter, and sensing it is considered to be the foundation for sensing various other parameters. For example, magnetic fields can be detected using an RI

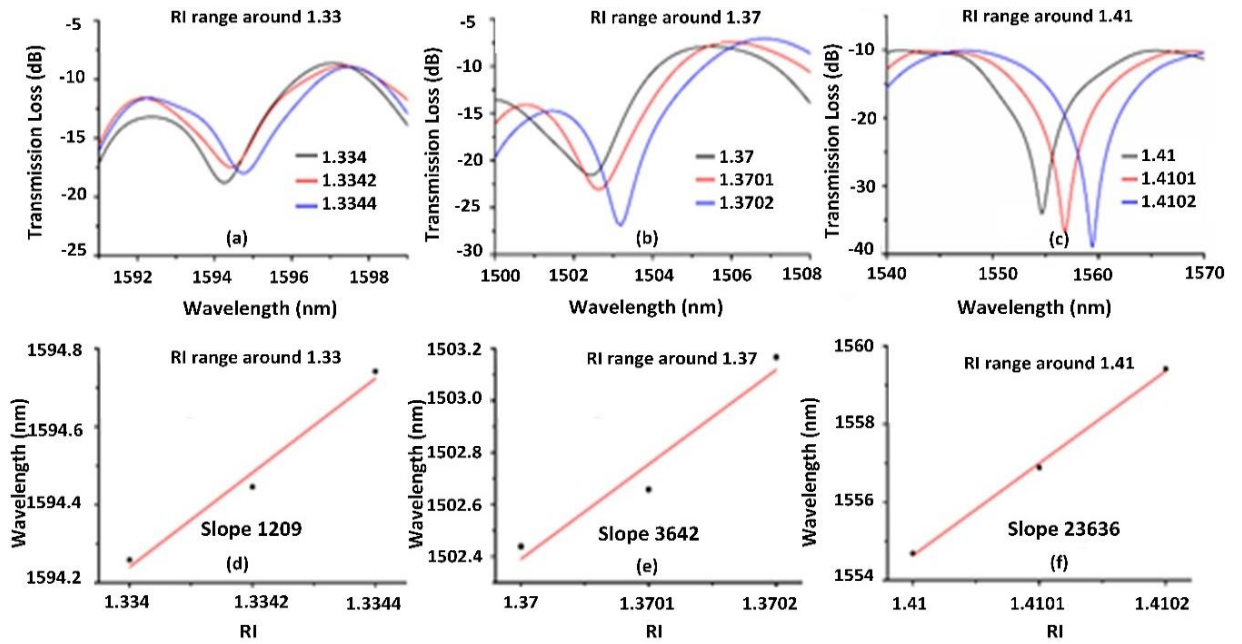
fibre sensor by measuring the change of RI surrounding the fibre sensor due to the alignment of magnetic particles around the sensor surface.

Figure 3.3 shows simulation results for the spectral response and RI sensitivity of the tapered NCF structure. Since the tapered NCF diameter in the transition region (Figure 3.1) changes continuously, the traditional mode transmission method [122] isn't suitable to simulate the RI sensitivity. In this case, beam propagation method (BPM) with 2D model is used to investigate the RI sensitivity of the structure. In the simulation, the RI of tapered no-core fibre is 1.4428 with taper waist of 8  $\mu\text{m}$ , the length of the tapered no-core fibre section is 10 mm and each of the taper transition sections have a length of 7 mm. The SMF has core and cladding diameter of 9 and 125  $\mu\text{m}$ , and the corresponding RI of 1.4507 and 1.4428 respectively. The parameter used in the simulation is summarised in Table 3.1.

**Table 3.1.** Summary of parameters used in the simulation model of tapered SNCS OFS structure.

Optical fibre type	Parameter
NCF	RI of taper NCF = 1.4428 Taper waist diameter = 8 $\mu\text{m}$ Waist length = 10 mm Transition length = 7 mm
SMF	Core Dia. = 9 $\mu\text{m}$ Cladding Dia. = 125 $\mu\text{m}$ RI of core = 1.4504 RI of cladding = 1.4428

As shown in Figure 3.3 (a-c), the spectral dip shifts monotonically towards longer wavelengths as the SRI increases. Furthermore, the wavelength shift observed in all the three RI ranges of 1.33, 1.37 and 1.41 are different, and appear to increase exponentially as the SRI (1.41) approaches the RI of the NCF (1.44). The RI sensitivities of the STNCS OFS observed in Figure 3.3 (d-f) are 1,209, 3,642 and 23,636 nm/RIU for the three RI ranges of 1.33-1.3344, 1.37-1.3702 and 1.41-1.4102 respectively.



**Figure 3.3.** Simulated (a-c) spectral response and (d-f) RI sensitivity of the STNCS OFS with 8  $\mu\text{m}$  taper waist diameter in the three RI ranges of 1.33, 1.37, and 1.41 respectively.  
 (\* Simulated in RSoft BeamPROP™ by Dr. Bin Liu, Jiangxi Engineering Laboratory for Optoelectronics Testing Technology, Nanchang Hangkong University, Jiangxi, Peoples R China.)

Figure 3.4 shows the summarized wavelength shift versus RI responses measured for the three RI ranges mentioned above. The RI sensitivities observed were 1,046, 3,780 and 26,061 nm/RIU for the RI ranges of 1.333 – 1.338, 1.372 – 1.375, and 1.413 – 1.415, respectively. The linear correlative coefficient  $R^2$  for all the three RI ranges was greater than 0.9, which indicates a good linear relationship between the wavelength shift and the RI changes over a small RI range. As estimated from the simulation model the RI sensitivity increases exponentially when the SRI approaches the NCF RI therefore, the maximum sensitivity of 26,061 nm/RIU was observed within the RI range of 1.413 – 1.415. Assuming the resolution of OSA is 0.01 nm, the STNCS OFS has a significantly high RI resolution of  $3.837 \times 10^{-7}$ , therefore suggesting that the STNCS OFS is a suitable sensing platform for developing a bio-chemical sensor.

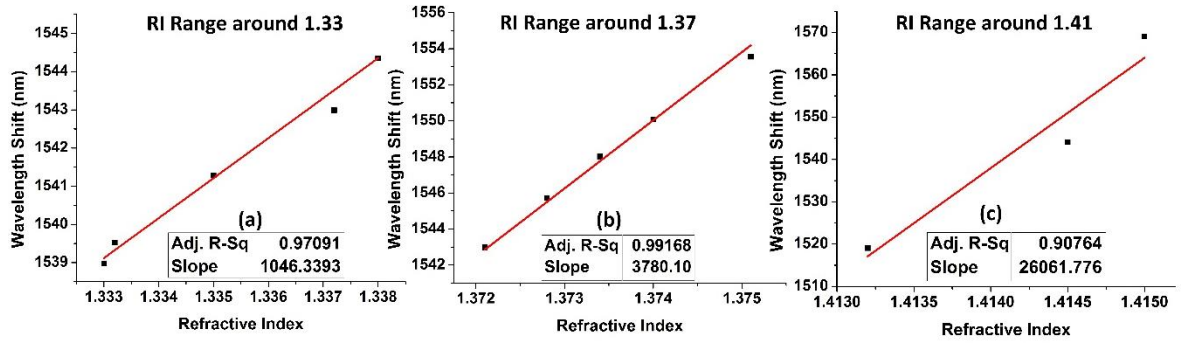


**Figure 3.4.** Experimentally observed RI sensitivity for the STNCS optical fibre sensor with 8  $\mu\text{m}$  taper waist diameter for the three RI ranges around (a) 1.33, (b) 1.37, and (c) 1.41 RI ranges

To date, many types of RI sensors based on different configurations and types of optical fibres have been reported for bio-chemical sensing. A comparison of different replacements for the MMF in the STMS fibre structure with other fibres is given in Table 3.2, with a view to compare their RI sensitivities and investigate the suitability of the STNCS OFS for bio-chemical sensing applications.

**Table 3.2.** Comparison between the RI sensitivities of different fibre replacements of MMF in the STMS OFS structure

Fibre replacement in STMS fibre structure	Taper waist diameter ( $\mu\text{m}$ )	RI Range	Sensitivity (nm/RIU)	RI range Max. sensitivity	Ref
Multimode fibre	30	1.33 – 1.44	487	~ 1.44 1,913 nm/RIU	[27]
Small core fibre	12.5	1.3405 – 1.3463	1,198.3	1.430-1.432 1,9212.5 nm/RIU	[118]
Hollow core fibre	38	1.333 – 1.379	214.9		[120]
Multicore PCF	75.9	1.3448 – 1.3774	171.2		[119]
Hollow core PCF	65	1.3327-1.3634	334.03	1.392-1.420 1,426.70 nm/RIU	[121]
No-core fibre	8	1.333 – 1.338	1,046	1.413-1.415 26,061 nm/RIU	In our work

### 3.4 Temperature Dependence

It is well known that the RI of any medium is temperature dependent, therefore, it is important to measure the influence of temperature on the spectral response of the STNCS OFS before using it for the measurement of other parameters. Figure 3.5 shows the temperature sensitivity of an STNCS OFS with 6  $\mu\text{m}$  waist diameter. It can be observed that when the temperature is increased from 30  $^{\circ}\text{C}$  to 120  $^{\circ}\text{C}$ , the spectral dip shifts towards longer wavelengths with an average slope of 0.041 nm/ $^{\circ}\text{C}$ . The spectral response also shows a decrease in the transmission

loss as the temperature increases, with a rate of 0.05 dB/°C. The results suggest a limited influence of temperature on the STNCS OFS response.

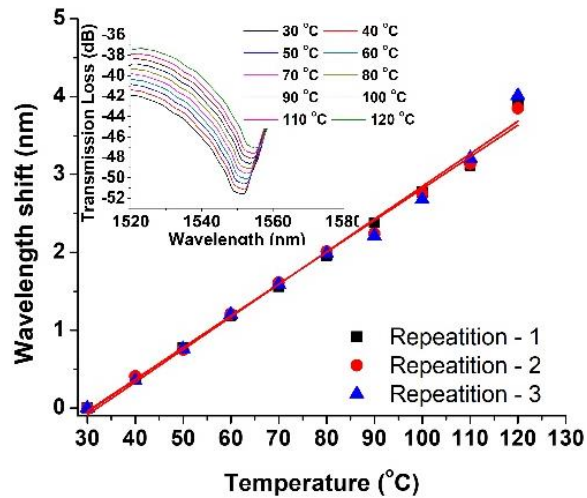


Figure 3.5. Temperature sensitivity of the STNC optical fibre with 6 µm tapering diameter.

### 3.5 Tapered Singlemode Small-core Fibre Sensor for Magnetic Field Sensing

Optical fibre magnetic field sensors based on magnetic fluids (MFs) have gained significant research interest recently due to the magneto-optic properties of MFs, such as field dependent RI, optical birefringence, and transmission [123, 124]. MFs are highly stable colloidal suspensions of ferromagnetic nano-particles distributed evenly throughout a volume either in water or oil to form the most widely used water and oil based MFs. Several magnetic field sensors have been developed by combining optical fibres with magnetically susceptible fluids, either embedded in a polymer matrix or in an aqueous solution around the optical fibre. Magnetic sensors based on cladding etched fibre Bragg gratings (FBGs) [125] and tilted FBGs [126] interacting with MF have already been reported. However, due to the low interaction between the fundamental core mode and the higher order cladding modes, such sensors have limited sensitivities as low as 10 pm/mT. A Sagnac interferometer magnetic field sensor incorporating a free-space MF film with the use of two collimators has been reported, which has a higher sensitivity of ~ 0.167 nm/mT but a more complex structure [127].

Microfibre-based magnetic field sensors show higher magnetic field sensitivity than that of a traditional fibre sensor due to their higher RI sensitivity. For instance, Zeng *et al.* proposed an optical microfibre mode interferometer coated with an MF, and demonstrated a sensitivity

of -0.293 nm/mT [128]. In addition, Deng *et al.* reported in [129] a magnetic field sensor with a sensitivity of 0.162 nm/mT, composed of an asymmetric taper with a waist diameter of 45  $\mu\text{m}$  immersed in an MF. Luo *et al.* reported another magnetic field sensor using an optical micro fibre coupler (OMFC) surrounded with an MF and demonstrated a sensitivity of 1.918 nm/mT in a narrow range of weak magnetic fields of up to 30 mT [130]. Wei *et al.* demonstrated in [42] a highly sensitive magnetic field sensor with a sensitivity of - 0.488 nm/mT using an OMFC combined with an MF in a Sagnac loop formed using a polarization maintaining fibre within the magnetic field range from 0 to 200 mT. Other optical fibre hetero-structures and special fibre structures have also been proposed in combination with MFs for magnetic field sensing, such as the SMF–HCF–SMF optical fibre structure immersed in MF, which was demonstrated in [131] with a sensitivity of -1.7 nm/mT. A fibre spherical structure (bulb) on a singlemode fibre coated with an MF [132], a D-shaped fibre structure immersed in an MF [133], and peanut-shaped structure cascaded with a long period grating [134] have also been demonstrated for magnetic sensing.

MFs are stable colloidal solutions which can maintain a homogeneous state perennially. In the absence of magnetic field, the ferromagnetic particles (FMPs) are distributed randomly in the carrier medium. When the magnetic field is applied to the MF, the FMPs undergo Brown and N’eel relaxation [135], which makes the magnetic particles agglomerate to form a chain along the direction of the applied magnetic field. In 2002, Yang *et al.* [136] successfully measured the RI of an MF under different magnetic field intensities using the total reflection technique. The RI dependence of the MF ( $n_{MF}$ ) on the magnetic field intensity  $H$  and the temperature  $T$  are attributed to the chain or column formation and can be given by the Langevin function, expressed as follows [137]:

$$n_{MF} = [n_s - n_0] \left[ \coth \left( \alpha \frac{H - H_{c,n}}{T} \right) - \frac{T}{\alpha(H - H_{c,n})} \right] + n_0 \quad \text{for } H > H_{c,n} \quad 3.4$$

where  $H_{c,n}$  is the critical magnetic field strength under which the RI of the MF starts to change,  $n_0$  is the RI of the MF under fields lower than  $H_{c,n}$ ,  $n_s$  denotes the saturated value of the RI for the MF, and  $\alpha$  is a fitting parameter.

In this section, a high sensitivity tapered small core singlemode (TSCSMF) [118] OFS encapsulated in MF is proposed and demonstrated for magnetic field detection. The effect of the SCSMF tapering diameter and FMP concentration in the MF on the sensor sensitivity

is experimentally demonstrated. The influence of orientation of magnetic field on the sensor's response is also investigated experimentally in this section.

### **3.5.1 Sensor fabrication and experimental setup**

The small core singlemode optical fibre (SM-450, Thorlabs) has a core diameter smaller than that of SMF28. Therefore, the SMF28–SCSMF–SMF28 sensor structure operating at longer wavelengths supports higher order cladding modes due to core diameter mismatch. In this experiment, the SCSMF section of an SMF28–SCSMF–SMF28 structure was tapered by the conventional heat-pull technique as described above, to fabricate the TSCSMF OFS structure. TSCSMFs with three tapering diameters of 10, 15 and 20  $\mu\text{m}$  were fabricated to investigate the influence of the taper waist diameter on the sensitivity of the sensor. The fabricated TSCSMF was encapsulated in a glass capillary tube, which was filled with the desired concentration of the MF, and both ends were sealed by using sealing-wax. The schematic diagram of the fabricated sensor is shown in Figure 3.6 (b), where an oil-based MF with 10 nm average particle size of FMPs was used in this experiment. The original concentration of the MF contains, by volume, 5% FMPs, 10% surfactant/dispersant and 85% carrier [138], which was diluted to three different concentrations of 1.2%, 0.8% and 0.4% of FMPs respectively, to investigate the influence of MF concentration on magnetic field sensitivity.

A schematic diagram of the experimental setup used for testing the magnetic sensors is shown in Figure 3.6 (a). The set-up consists of an electro-magnet, whose magnetic field strength can be controlled by changing the value of current flowing through its coils using a DC power supply. A gauss meter was used to measure the actual value of magnetic field strength as a reference, the probe of which was fixed in the middle between the electro magnet close to the TSCSMF ( $\sim 1$  mm apart). The taper waist region of the TSCSMF was positioned in the middle of the magnetic poles, where the density of magnetic field is maximum. A broad band optical source (SLD1005S) was used to launch the light into the OFS, whose other end was connected to the OSA to analyse the spectral response from the sensor.

In the absence of a magnetic field, the FMPs are distributed randomly around the TSCSMF sensor. When an external magnetic field is applied, the FMPs orient themselves along the magnetic field lines applied to the sensor as shown in Figure 3.6 (b). This alignment of FMPs

around the TSCSMF increases the RI around the fibre sensor. With the increase in strength of magnetic field, more FMPs from the MF gets aligned along the magnetic field, which further increases the RI around the fibre sensor. When the external magnetic field is removed, the FMPs return to their initial random alignment again. Table 3.3 summarises the parameters of the fibre structure and the specifications of the components used to build the experimental setup, for magnetic field sensing.

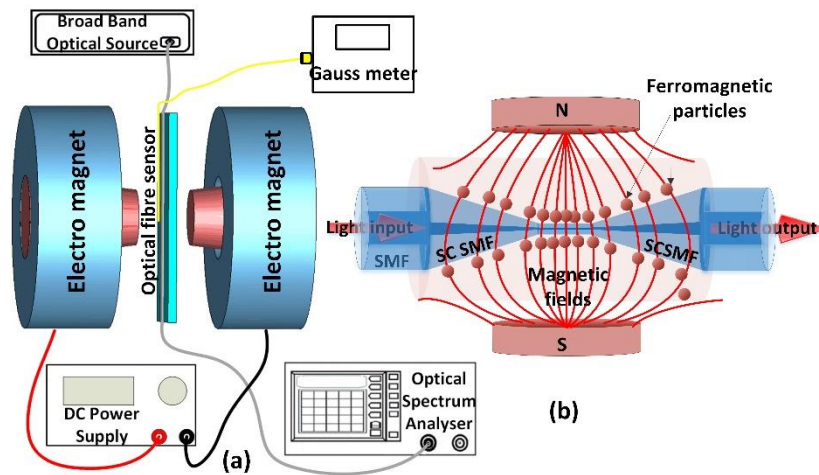


**Figure 3.6.** Schematic diagram of (a) the experimental setup, and (b) the tapered small-core singlemode optical fibre sensor surrounded by the magnetic fluid, for the purpose of magnetic field sensing.

**Table 3.3.** Summary of the TSCSMF fibre structure parameters and specifications of components used in the experimental setup, for magnetic field sensing.

	<b>Fibre Type</b>	<b>Parameter</b>
<b>Fibre Structure</b>	TSCSMF (Thorlabs-SM450)	Taper waist diameter ~ 10, 15 and 20 $\mu\text{m}$ Waist length ~ 10 mm Transition length ~ 10 mm
	SMF (Thorlabs-SMF-28)	Core diameter = 8.2 $\mu\text{m}$ Cladding diameter = 125 $\mu\text{m}$
	Magnetic Fluid (eMAGNETS-FF25)	FMP size = 10 nm FMPs concentration = 5% by volume
	<b>Components</b>	<b>Specifications</b>
<b>Experimental setup</b>	Optical source (Thorlabs SLD S5FC1550S-A2)	Centre wavelength = 1550 nm Output power = 2.5 mW Bandwidth = 90 nm
	Gauss meter (Weite Magnetic Technology Ltd. WT10A)	Measuring Range = 0 – 200 mT Resolution = 0.1 mT
	Electro magnets (Newport Instruments)	Made of magnetically soft iron, with a coil of insulated copper strip wound in an annular recess inside it
	DC Power supply (RS components Ltd. EL302RT))	Output voltage = 0 – 30 V Output Current = 2 A Power Rating = 130 W
	Optical spectrum analyzer (Yokogawa AQ6370D)	Wavelength range = 600 -1700 nm Accuracy = $\pm 0.01$ nm Resolution = 0.02 nm

### 3.5.2 Effect of MF concentration

The spectral response observed for the TSCSMF with 10  $\mu\text{m}$  tapered waist diameter, encapsulated in MF containing (a) 0.39%, (b) 0.81%, and (c) 1.22% FMPs, is shown in Figure 3.7. It can be observed that, with an increase in magnetic field strength, the spectral dip shifts monotonically towards longer wavelengths. This is because of the increase of the RI of the MF around the fibre sensor, due to the increase in the number of FMP alignments around the fibre sensor, as explained above. The TSCSMF encapsulated in a higher concentration of the MF shows a larger spectral shift for the same strength of magnetic field. This is because, higher concentrations of MF contain more FMPs, thus for the same value of magnetic field strength, larger number of FMPs will align near the TSCSMF OFS, introducing larger RI variations surrounding the sensor. It should be noted that the 3 dB dip wavelength analysis was considered to calculate the average position of the spectral dip, as the spectral responses were noisy.

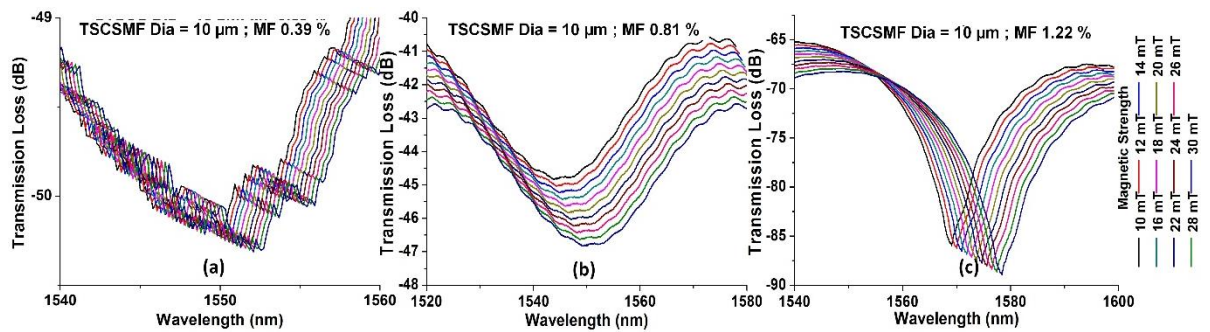


**Figure 3.7.** Examples of spectral responses observed while increasing the magnetic field around the TSCSMF fibre magnetic sensor with 10  $\mu\text{m}$  diameter surrounded by MF with (a) 0.39%, (b) 0.81%, and (c) 1.22% FMPs.

The wavelength shift versus magnetic field strength is shown in Figure 3.8 (a-c). As explained previously, for the same taper waist diameter of the TSCSMF, the sensitivity to magnetic field increases with the increase of the concentration of the MF. Each reading was taken 2 minutes after applying the magnetic field to the sensor to make sure the spectral response stabilised, which could reduce the hysteresis effect and allow the FMP to release the residual magnetisation. It can also be observed that the wavelength shift for a change in magnetic field strength remains almost the same while increasing and decreasing the magnetic field strength, which demonstrates good reversibility of the proposed sensor.

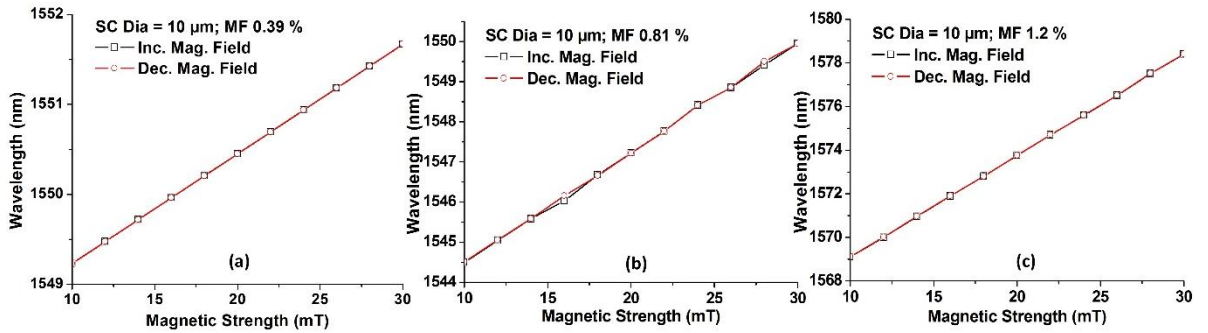


**Figure 3.8.** Wavelength shift caused due to the change in magnetic field strength for the TSCSMF of 10  $\mu\text{m}$  tapering diameter encapsulated in (a) 0.39% (b) 0.81% and (c) 1.2% FMPs in MF.

### 3.5.3 Effect of the taper waist diameter of TSCSMF

The influence of taper waist diameter was investigated. To do so, nine sensors were fabricated using TSCSMF with waist diameters of (a) 20  $\mu\text{m}$ , (b) 15  $\mu\text{m}$  and (c) 10  $\mu\text{m}$ , surrounded with MF of three different concentrations (0.39, 0.81 and 1.2 %FMPs). Figure 3.9 shows the wavelength shift as a function of magnetic field strength for all nine fabricated sensors. It can be observed that the wavelength shifts show good linearity with the increase in the magnetic field strength for all the fabricated sensors. The rate of wavelength shift, which is the sensitivity of the fabricated TSCSMF OFS, increases as the taper waist diameter of the TSCSMF decreases from 20  $\mu\text{m}$  to 10  $\mu\text{m}$ . This is because, for a smaller tapering diameter, more evanescent field interacts with the surrounding medium, which increases the RI sensitivity of the TSCSMF fibre sensor. Figure 3.9 also shows that the sensitivity to the magnetic field strength increases as the FMPs concentration increases, for all the three taper waist diameters

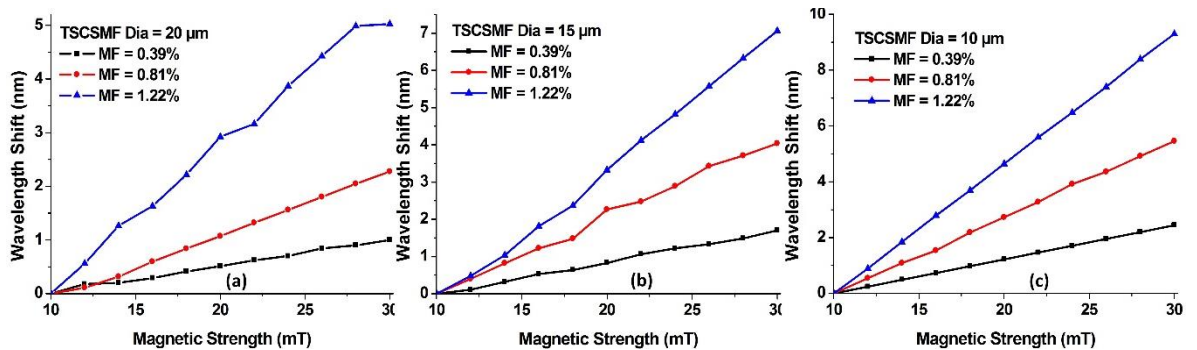


**Figure 3.9.** Wavelength shift vs magnetic field strength of TSCSMF with waist diameters of (a) 20  $\mu\text{m}$  (b) 15  $\mu\text{m}$  and (c) 10  $\mu\text{m}$ , surrounded with different concentrations (0.39, 0.81, 1.22 %FMPs) of MF.

### 3.5.4 Sensitivity comparison

Figure 3.10 shows the relationship between the sensitivity of the sensor, taper waist diameter and FMP concentration. The maximum observed sensitivity was 0.46 nm/mT for the TSCSMF with 10  $\mu\text{m}$  taper waist diameter, surrounded by the MF with 1.22% concentration of FMPs. The minimum sensitivity observed was 0.049 nm/mT where the TSCSMF has a taper waist diameter of 20  $\mu\text{m}$  and 0.39% FMPs in the MF. The highest set of magnetic field sensitivity using the three concentrations of FMPs (0.39, 0.81, 1.22 % FMPS) was achieved for the TSCSMF with 10  $\mu\text{m}$  taper waist diameter, which confirms that the sensor with smaller taper waist diameter has larger sensitivity. Table 3.4 summarises the numerical values of the sensitivities recorded for all nine fabricated sensors with different TSCSMF waist diameters encapsulated in different MF concentrations.

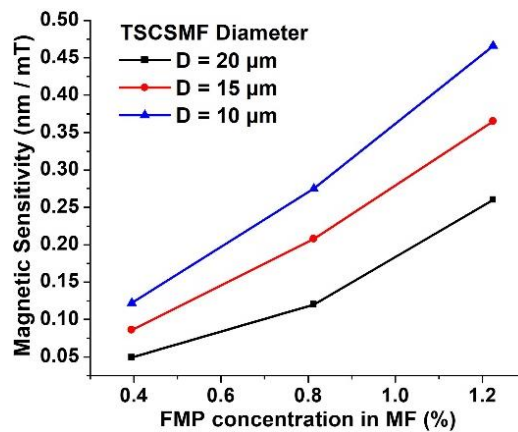


**Figure 3.10.** Magnetic sensitivity comparison for the TSCSMFS optical fibre sensors with 10, 15, and 20  $\mu\text{m}$  diameters surrounded by 0.39, 0.81, and 1.22 %FMPs in the MF.

**Table 3.4.** Sensitivity values for the TSCSMF optical fibre sensors of 10, 15, and 20  $\mu\text{m}$  diameters surrounded by 0.39, 0.81, and 1.22 %FMPs in the MF.

Amount of FMPs in the MF (%)	Sensitivity (nm/mT)		
	TSCSMF dia. = 20 $\mu\text{m}$	TSCSMF dia. = 15 $\mu\text{m}$	TSCSMF dia. = 10 $\mu\text{m}$
1.22	0.26	0.365	0.466
0.81	0.12	0.208	0.275
0.39	0.049	0.086	0.122

### 3.5.5 Effect of magnetic field orientation

The dependence of the magnetic field orientation on the performance of the TSCSMF based magnetic sensor was also examined using the fibre sensor with 10  $\mu\text{m}$  taper waist diameter and a 1.22% concentration of FMPs in the MF. For this purpose, a separate experimental set-up was used, consisting of two permanent magnets of 20 mT, which created a parallel

and homogeneous magnetic field between them. A 360° rotating platform was used to hold the two magnets at a fixed and equal distance from each other, around the stationary fibre sensor. The orientation of the magnetic field applied to the sensor was changed by rotating the platform with 5° steps in the planes X-Y, X-Z and Y-Z, as shown in Figure 3.11 and Figure 3.12. The rotation angle  $\alpha$  is defined as the clockwise angle between the normal line of the magnetic field and the direction of the TSCSMF axis, where  $\alpha = 0^\circ$  refers to the case when magnetic field axis is normal to the fibre axis, while  $\alpha = 90^\circ$  refers to the case when magnetic field axis is parallel to the fibre axis.

A schematic diagram of the experimental setup is shown in Figure 3.11 (a), where a permanent magnet with 20 mT magnetic field strength was rotated around the Z axis. The permanent magnets used had a cross section area smaller than the sensing area of the TSCSMF. Initially, when the TSCSMF optical fibre magnetic sensor was placed at the centre between the two magnets, the spectral dip was observed to shift slowly from its initial position towards a longer wavelength, before reaching a stable value after 2 minutes. This initial drift is because the magnetic field created by the permanent magnets has maximum strength at the centre of the TSCSMF, which attracts the FMPs in the MF towards the centre of TSCSMF, causing a small change in the RI. Once the concentration of FMPs around the TSCSMF within the magnetic field cross-section becomes stable, no further changes in the RI occur while rotating the magnetic field direction in the X-Y plane. The results of this experiment (after the spectral dip stabilises) are shown in Figure 3.11 (b). In this configuration, the magnetic field direction is perpendicular to the TSCSMF axis at all time, so the particle density along the TSCSMF does not change, and neither does the RI. Therefore, the wavelength does not shift as the magnetic field is rotated in the X-Y plane.

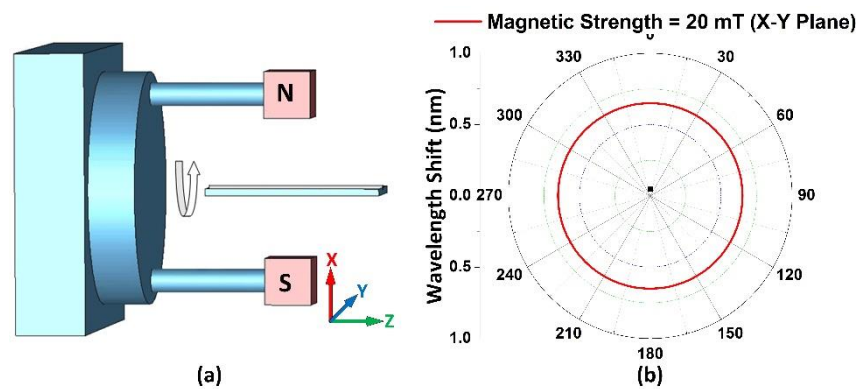


**Figure 3.11.** (a) The experimental setup used for measuring the angular magnetic field dependence in the X-Y plane; and (b) wavelength shift from  $\lambda_0$  when the rotation angle changes from  $0^\circ$  to  $360^\circ$  in the X-Y plane.

The results for the experiments when the permanent magnets are rotated around X-Z and Y-Z planes are shown in Figure 3.12 (c). When the magnetic field is applied around the TSCSMF fibre sensor encapsulated in the MF, the FMPs gather around the surface of the capillary tube forming a multi-particle chain. Furthermore, their density around the TSCSMF becomes non-homogeneous and asymmetric with respect to the fibre axis. When the magnetic field direction is rotated in the X-Z or Y-Z planes, the chain's direction and the FMP density around the TSCSMF rotate accordingly, which affects the RI of the MF surrounding the TSCSMF and ultimately the spectral response of the sensor. The maximum wavelength shift was observed when  $\alpha$  is set to  $0^\circ$  (i.e. magnetic field axis was parallel to the TSCSMF axis), while the minimum wavelength shift was observed when  $\alpha$  was set to  $90^\circ$  (i.e. magnetic field axis was perpendicular to the TSCSMF axis). The maximum wavelength shift in the X-Z plane was greater than that in the Y-Z plane due to the tapered shape of the TSCSMF.

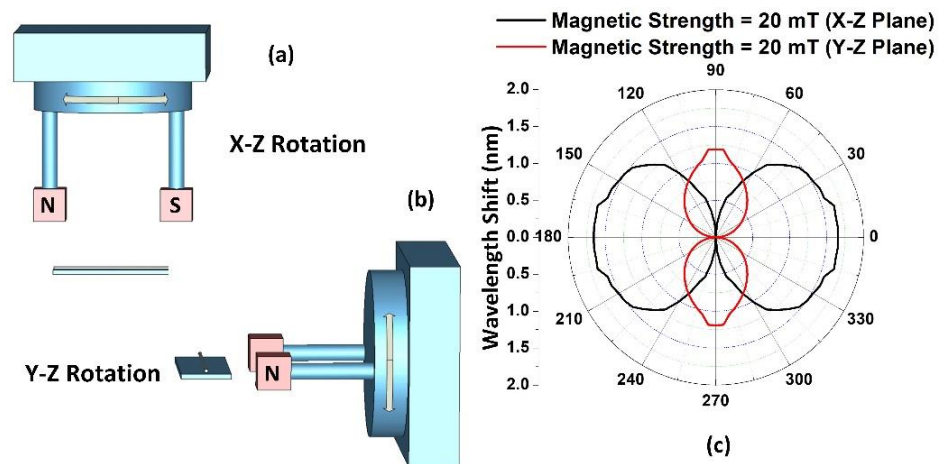


**Figure 3.12.** Schematic of the experimental setup used for measurements of the angular field dependence in (a) the X-Z, and (b) the Y-Z plane; (c) Experimentally measured wavelength shift from  $\lambda_0$  versus angle from  $0^\circ$  to  $360^\circ$  in the X-Z and Y-Z planes for different magnetic field strength values.

### 3.6 Summary

In this chapter, the technique of tapering the conventional optical fibre was adopted for increasing the RI sensitivity and the background of tapered microfibre sensors was discussed. The STNCS OFS, fabricated by tapering a NCF, was utilized as a sensing platform for a variety of applications, one of which is the detection of RI variations surrounding the fibre sensor. The maximum RI sensitivity demonstrated was 26,061 nm/RIU within the RI range of 1.402 – 1.421 which has a taper waist diameter of 8  $\mu\text{m}$ . This RI sensitivity is higher than the previously proposed tapered SMS-based OFSs used for bio-

chemical sensing. Therefore, the STNCS OFS can be considered as a suitable sensor platform for developing a bio-chemical sensor.

A high sensitivity magnetic field sensor was proposed and investigated based on the TSCSMF OFS which was encapsulated in an MF. The magnetic sensitivity of this sensor was investigated by studying the effect of the taper waist diameter of the TSCSMF and the concentration of the MF surrounding it. The magnetic sensor demonstrated reversible results, with a maximum sensitivity of 0.46 nm/mT for a TSCSMF with 10  $\mu\text{m}$  taper waist diameter, encapsulated in 1.22% FMPs in the MF. The effect of magnetic field orientation along X-Y, X-Z and Y-Z was also investigated for developing a vector magnetic field sensor. The fabrication cost of the TSCSMF OFS is very low ( $\sim$  £10) and the cost of MF used in this experiment is  $\sim$  £10. As suggested in the summary of Chapter 2 (Section 2.8), the overall cost of implementing OFS in practical system can be reduced by using intensity-based analysis (i.e. using photo-detector and data acquisition system to measure intensity changes corresponding to magnetic field variation), instead of wavelength-based analysis demonstrated in this chapter. Therefore, reducing the effective cost ( $<$  £300) for implementing TSCSMF OFS in practical system, for magnetic field sensing, which can be further reduced in bulk production.

# **CHAPTER 4: Functionalised Singlemode Tapered No-core Singlemode (STNCS) Fibre Sensor for Humidity and Biochemical Sensing**

## **4.1 Introduction**

This chapter presents an overview of the functionalisation process by which a capture layer on the fibre surface is immobilised to develop and demonstrate an optical fibre sensor (OFS) for bio-chemical sensing applications. The fibre sensor without surface modification can only detect refractive index (RI) variations, which won't have specific binding with the target substances and hence cannot be used for bio-chemical sensing. To realize the function of detecting bio-chemical analytes, it is required to deposit specific capture layer on the fibre sensor surface to interact with the bio or chemical analyte, where the fibre sensor acts as a sensor platform for detecting the RI variations due to the capture of bio-chemical analytes by the deposited capture layer. The capture layer deposited on the fibre sensor surface could be a polymer matrix, which will trap the analyte, or contain compounds which react with a specific analyte in the entrapped sample, or may be a bio-molecule which bonds with the analyte. In this chapter, based on the STNCS fibre sensor, different specific capture layers were functionalised on the sensor for different applications including humidity, oxygen, and human chorionic gonadotropin (hCG) detection. The working principle of the functionalised tapered fibre sensor is also explained in the first part of this chapter, before demonstrating its application for bio-chemical sensing. A wide range of host polymers suitable for capturing the desired analyte are available, therefore, a brief description of such polymers is also included in this chapter.

## **4.2 Principle of Operation of the Functionalised Tapered Fibre**

There are two types of biosensors, namely labelled and label-free sensors. The labelled bio-sensing technique is shown in Figure 4.1 (a), requires a secondary antibody (Ab) usually with a florescent label to bind with the primary Ab of interest via the Ab-Ag (antibody-antigen) interaction. The fibre beneath the capture layer is only used to carry the fluorescence produced for detection. The second method, known as label-free detection and is shown in Figure 4.1 (b), does not require a secondary Ab. The label-free detection techniques, in

conjunction with highly sensitive OFSs, are gaining popularity due to their fabrication simplicity, which makes them suitable for real-time sensing. Therefore, in this chapter, a label-free STNCS OFS-based immunosensor is discussed in detail and demonstrated for real-time detection of hCG. Furthermore, secondary Ab immobilised on a non-fluorescent magnetic microsphere is demonstrated as a new method for improving sensitivity of the hCG immunosensor.

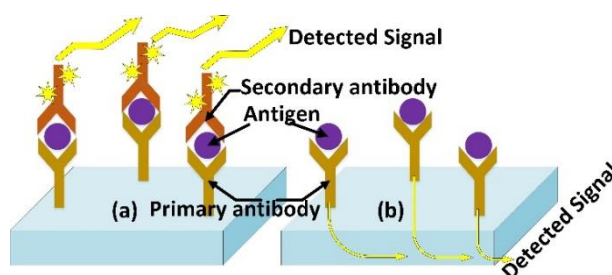


**Figure 4.1.** Schematic demonstration of (a) labelled and (b) label-free bio-sensing.

There are two major techniques used for developing optical fibre-based chemical sensors, which require immobilising a host polymer matrix on the fibre surface. The first method, shown in Figure 4.2 (a), involves molecularly imprinting the polymer surface, described generally as follows:

- i) The particles of similar size as the analyte (called template) are entrapped in the polymer matrix by evenly mixing the template particles in the polymer solution.
- ii) The template entrapped polymer solution is then coated on the sensor surface, which is then cured by heating it in an oven for a specific time under constant temperature and pressure (heat curing).
- iii) After curing the polymer, the template particles are washed out using a solvent, hence creating cavity on the polymer surface, which is used to capture the actual analyte.

The molecularly-imprinted polymer is in general suitable for larger particle sizes, such as particulate matter from a vehicular exhaust [139], but have poor repeatability and lifetime. This is because, the general method of re-using molecularly-imprinted sensors involves washing the captured analyte with a solvent, which may also dissolve the polymer and de-shape the imprinted cavity. The second method, shown in Figure 4.2 (b), involves entrapping a reagent in the polymer matrix, and is described generally as follows:

- i) A chemical reagent which can react specifically with the target to change its optical properties (like RI, absorption or fluorescence) is chosen, and entrapped in the polymer matrix by evenly mixing the reagent in a polymer solution.
- ii) The reagent entrapped polymer solution is then coated on the sensor surface, which is then cured by the heat curing process described above.
- iii) After curing the polymer, the functionalised sensor can be used directly for detecting the analyte.

This second functionalisation method is more reliable and has shown better repeatability and longer lifetime. Therefore, in this chapter, a STNCS fibre sensor, with methylene blue (MB) entrapped in sol-gel matrix, is used to capture and interact with the oxygen present in its surrounding, and is demonstrated for oxygen sensing.

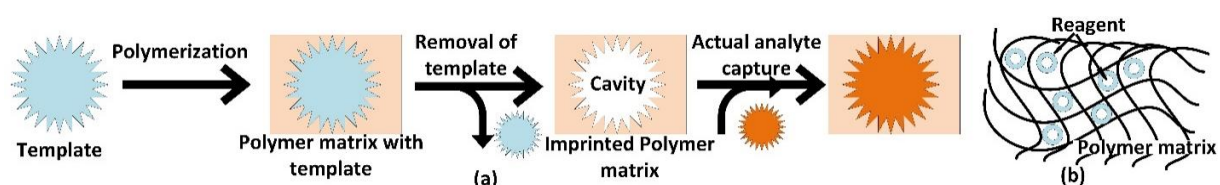


**Figure 4.2.** Schematic demonstration of the two major methods used for chemical sensing: (a) the molecular imprinting method, and (b) the reagent entrapment in the polymer matrix.

#### 4.2.1 Host polymers suitable for optical fibres

The host polymer apart from entrapping the reagent, functions as (i) a solid support for the fibre sensor and (ii) a filter that allows certain permeability to the desired analyte, while rejecting other species in the sample. The incorporation of the fibre sensor into the host polymer has several additional beneficial effects such as: (a) the host polymer provides a constant micro-environment and protects the fibre sensor from potential interferents, (b) quenching constants can be adjusted by the proper choice of materials, and (c) the interaction of the fibre sensor with the sample materials is prevented. There are several requirements for the matrix to be a viable host for the fibre sensors, which are:

- The analyte-sensitive material (ASM) and the matrices are to be compatible in terms of solubility, so that the ASM entrapped in the matrix remain inside without leaching or aggregation.
- The matrix must be optically transparent, possess good adhesion to a conceivable mechanical support, and should be easy to handle.

- The matrix's permeability and diffusion rate for the analyte should match the specific needs of the sensor with respect to the quench-ability and response time.
- The polymer is expected to possess good long-term stability and should not degrade.
- The host should not significantly alter the photo-physical properties (such as spectra or decay times) of the OFS.
- If used in vivo, biocompatibility should be warranted [140].

The methods used for entrapping the ASM in an analyte-permeable host polymer can be divided into three main subgroups, which are schematically shown in Figure 4.3. In Method A, the ASM is homogeneously dissolved in a polymer solvent, which is then functionalised on the fibre surface using the dip coating method. This method is easy and therefore is the most popular method. However, this method doesn't work if the ASM does not covalently bond or dissolve in the polymer solution. Therefore, Method B, which is generally used for a charged ASM, involves the adsorption of the charged ASM on the surface of particles (such as alumina, silica, or porous glass beads) by means of electrostatic interaction. These ASM adsorbed micro-particles are then incorporated into a host matrix such as silicone rubber or polystyrene. For example, the demonstrations involving phosphorescent dyes on silica [141] and ionic ruthenium probes on silica particles [142] used this method for developing an oxygen sensor. It should be noted, that unlike in Method A, the bulk polymers need not be a solvent for the ASM in Method B (in fact, they should not be at all). In Method C, rather than the adsorption of the ASM on the particles' surface, the ASM is first dissolved in a solvent along with micro/nanoparticles. These particles, coated with ASM, are then incorporated in a host polymer matrix, which is functionalised on the fibre surface for sensing the desired analyte. This approach is generally used to increase the area of surface interaction, and is suitable for multiple-analyte sensing by incorporating particles functionalised with the ASMs sensitive towards different analytes. It is obvious from these considerations that the selection of a favourable matrix is a key to a successful sensor design.

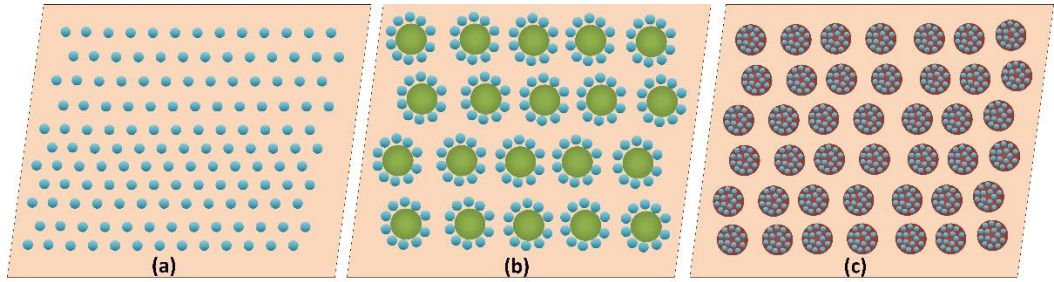


**Figure 4.3.** Schematic of the three most common methods for immobilising the ASM in a host polymer matrix. In (a), the ASM molecules (blue dots) are homogeneously distributed in the host polymer (orange). In (b), the ASM molecules are adsorbed on the surface of micro or nanoparticles (green), which are then incorporated into the host polymer. In (c), the ASM molecules are first homogeneously distributed in micro or nanoparticles (red), which are then incorporated into the host polymer.

### 4.3 STNCS Fibre Sensor Functionalised with Agarose Hydro-gel for Humidity Sensing

Humidity is the amount of water vapour contained in the air. The measurement of humidity level is useful in many fields, such as in meteorological services, chemical and food processing industries, civil engineering, air-conditioning, horticulture, electronic processing, paper and textile production. Electronic humidity sensors are unsuitable for applications in electromagnetic or corrosive environmental conditions. In this context, OFSs provide advantages of small size, low weight, immunity to electromagnetic interference, corrosion resistance, and the potential for remote sensing, over their electronic counterparts.

In recent years, different optical fibre structures based on multimode interference (MMI) have been demonstrated for relative humidity (RH) measurement. For example, a side-polished multimode fibre (MMF) with a polishing depth and length of 40  $\mu\text{m}$  and 36 mm, respectively, was coated three times with gelatine material to achieve a maximum sensitivity of 0.14 dB/%RH within the RH range of 40 – 90 %, and a fast response time of 1000 milliseconds [143]. A small-core singlemode fibre (SCSMF) (core diameter  $\sim$  1.15  $\mu\text{m}$ ) functionalised with poly ethylene oxide (PEOS) (with coating thickness  $<$  1  $\mu\text{m}$ ) was demonstrated with a maximum RH sensitivity of 430 nm/%RH within the RH range of 80 – 83 % [34]. Furthermore, a tapered SCSMF with 12.5  $\mu\text{m}$  taper waist diameter was demonstrated for RH sensing without any functionalisation, achieving a maximum RH sensitivity of 18.3 nm/%RH in the RH range from 90.4% to 94.5% [118]. A no-core fibre coated with agarose hydro-gel was also demonstrated with an RH sensitivity of -149 pm/%RH within the RH range of 30 – 75 %, where the response and recovery time of the sensor were recorded to be 4.8 and 7.1 seconds, respectively [144]. Another example

involved the use of a 4 cm long photonic crystal fibre (PCF) (NKT Photonics LMA-10) fusion-spliced between two singlemode fibres (SMFs) and coated with a polyvinyl alcohol (PVA) film of  $\sim 8 \mu\text{m}$  thickness to demonstrate RH sensing with a sensitivity of  $40 \text{ pm}/\% \text{RH}$  within the RH range of 20 – 90 %, with good repeatability and low temperature dependence [145]. A Fabry-Perot interferometer (FPI)-based RH sensor was also demonstrated by fusion-splicing an 8.4 cm long hollow-core fibre (HCF) with a  $70 \mu\text{m}$  inner diameter between two standard SMFs. The HCF was coated with a reduced graphene oxide (rGO) to form a FP resonator in the cladding layer. The RH sensor was demonstrated to achieve a sensitivity of  $0.22 \text{ dB}/\% \text{RH}$  within the RH range of 60 – 90 %, and a response and recovery time of 5.2 and 8.1 seconds, respectively [146]. Moreover, a 25 mm long LPG with a grating period of  $400 \mu\text{m}$ , coated with graphene oxide, was demonstrated for RH sensing with an RH sensitivity of  $0.15 \text{ dB}/\% \text{RH}$  within the RH range of 60 – 95 % [147].

Most optical fibre RH sensors discussed above are based on a hygroscopic polymer material, which can absorb the surrounding humidity. There are variety of hygroscopic materials, among which agarose hydro-gel is widely used for RH monitoring due to its advantages of low cost and convenient fabrication [148].

In this section, an agarose hydro-gel coated STNCS OFS is demonstrated for RH sensing. The thickness of the coating layer is investigated to achieve an RH sensitivity of  $0.0295 \text{ nm}/\% \text{RH}$  within the linear RH range of 35 – 70 %RH using a STNCS with  $4 \mu\text{m}$  taper waist diameter, coated with a  $0.198 \mu\text{m}$  thick hydro-gel. The RH sensitivity is increased to a maximum of  $0.04107 \text{ nm}/\% \text{RH}$  by bending the OFS in form of a loop with a radius of  $\sim 4.7 \text{ cm}$ , without affecting the linearity over the same RH range. The effect of coating thickness on the response and recovery times is also investigated for the loop STNCS sensors.

#### **4.3.1 Sensor fabrication and experimental setup**

In this experiment, the previously proposed STNCS OFS with a waist diameter of  $4 \mu\text{m}$  was used as a sensing platform for the development of the RH sensor. The STNCS was then functionalised with an agarose solution, prepared by dissolving 1 wt.% (weight-percent) agarose in de-ionised (DI) water at  $65 \text{ }^\circ\text{C}$ . The dip coating technique was then used to apply the layers of agarose on the OFS surface. When the agarose solution on the STNCS surface dried out, the resulting hydro-gel coating on the STNCS OFS formed a 3-dimensional mesh of channels held together by hydrogen bonds. The Agar of which the hydro-gel is made of

is insoluble in cold water, but swells considerably after absorbing as much as twenty times its own weight of water [149]. Therefore, when the coating is exposed to moisture, it swells up by absorbing the moisture from its surrounding, which in turn changes the RI of the coating layer surrounding the OFS. The evanescent field in the waist region of the STNCS OFS is sensitive to the surrounding RI, and as such, this change in the RI of the hydro-gel influences the output spectral response of the sensor, which can be calibrated to develop an optical fibre humidity sensor.

A schematic diagram of the STNCS OFS coated with agarose hydro-gel is shown in Figure 4.4 (a). The influence of the coating thickness on the fibre surface was investigated by coating the STNCS OFS with different thicknesses (0.04, 0.10, and 0.19  $\mu\text{m}$ ) of agarose hydro-gel. These sensors were then bent to a radius of  $\sim 4.7$  cm to compare their sensitivity over that of straight sensors.

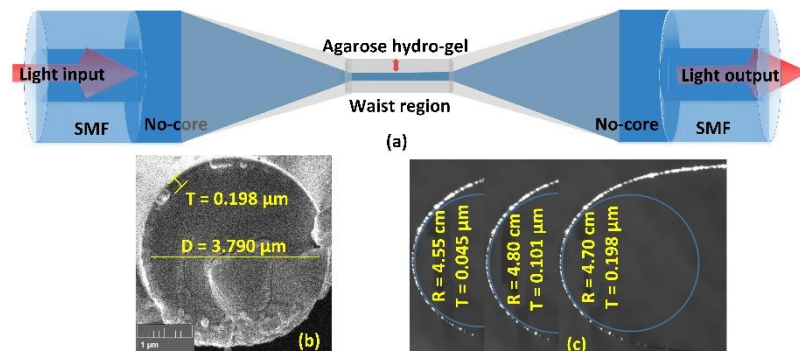


**Figure 4.4.** (a) Schematic diagram of the STNCS optical fibre coated with agarose hydro-gel. (b) SEM image of the STNCS taper waist cross-section after coating, and (c) the bend radii measured using optical microscope.

The thickness of the hydro-gel coating layer (T) and the taper waist diameter of the STNCS OFS (D) were measured using scanning electron microscope (SEM), as shown in Figure 4.4 (b), while the bending radius (R) of the loop STNCS was measured using an optical microscope, as shown in Figure 4.4 (c).

The RH response for all six-fabricated sensors (i.e. STNCS and loop STNCS with three different coating thicknesses) is measured in a humidity-controlled chamber. The RH of the air-tight gas chamber was controlled by changing the ratio of dry and moist air in the mixer, based on the current humidity level of the chamber. The humidity level in the chamber was measured using a calibrating sensor. The schematic diagram of the experimental setup is shown in Figure 4.5. This system can maintain the RH level within the chamber to better than 1% RH from 10% to 100% RH for normal ambient conditions. The temperature of the

chamber was also monitored and maintained within a range of  $\pm 0.5$  °C. A broadband light source (SLD1005S) was used to launch the light into the OFS, and the output light from the sensor was observed with an optical spectrum analyser (OSA, Yokogawa AQ6370D) to analyse its output spectral response. Table 4.1 summarises the parameter of STNCS OFS coated with hydrogel, and specifications of the components used to build the experimental setup used for humidity sensing.

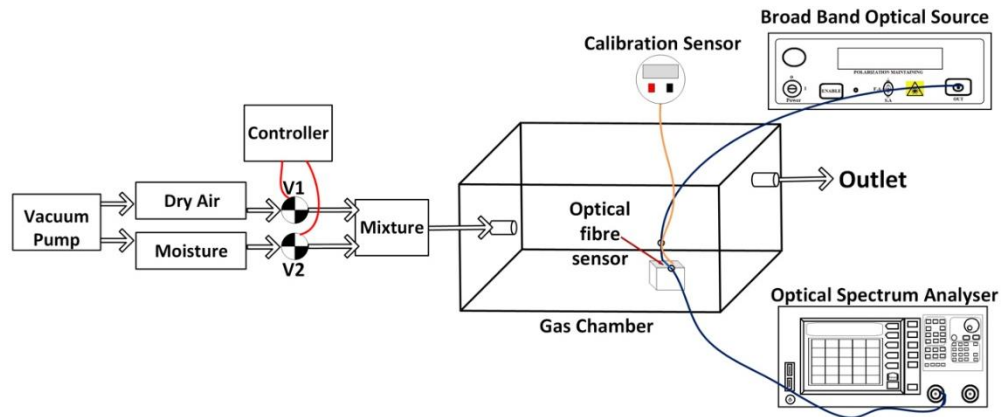


**Figure 4.5.** Schematic diagram of the experimental setup used for measuring humidity.

**Table 4.1.** Summary of the STNCS OFS parameters coated with hydrogel and specifications of components used in the experimental setup, for humidity sensing.

	<b>Fibre Type</b>	<b>Parameter</b>
<b>Fibre Structure</b>	STNCS (POF Corporation Ltd.-NCF125)	Taper waist diameter $\sim 4$ $\mu\text{m}$ Waist length $\sim 10$ mm Transition length $\sim 10$ mm Bend radius $\sim 4.7$ cm
	SMF (Thorlabs-SMF-28)	Core diameter = $8.2$ $\mu\text{m}$ Cladding diameter = $125$ $\mu\text{m}$
	Agarose hydro-gel (Sigma-Aldrich, UK)	Coating thickness $\sim 0.04, 0.10,$ and $0.19$ $\mu\text{m}$
	<b>Components</b>	<b>Specifications</b>
<b>Experimental setup</b>	Optical source (Thorlabs SLD S5FC1550S-A2)	Centre wavelength = $1550$ nm Output power = $2.5$ mW Bandwidth = $90$ nm
	Calibration sensor (RS components Ltd.)	Temperature range = $-40 - 125$ °C Temperature resolution = $0.1$ °C Humidity resolution = $0.1$ %RH
	Optical spectrum analyzer (Yokogawa AQ6370D)	Wavelength range = $600 - 1700$ nm Accuracy = $\pm 0.01$ nm Resolution = $0.02$ nm

### 4.3.2 Results and discussion

As shown in Figure 4.6 (a), when the RH in the chamber is increased from  $35 - 85$  %RH, the spectral dip of the STNCS OFS shifts monotonically towards longer wavelengths. This is because the absorption of moisture by the hydro-gel will introduce RI change of the

coating on the OFS, resulting in the change of spectral response of the sensor. It can also be observed from Figure 4.6 (b) that, upon bending the STNCS OFS with 4  $\mu\text{m}$  taper waist diameter and 0.198  $\mu\text{m}$  coating thickness, the spectral dip exhibits a larger wavelength shift for the same value of RH.

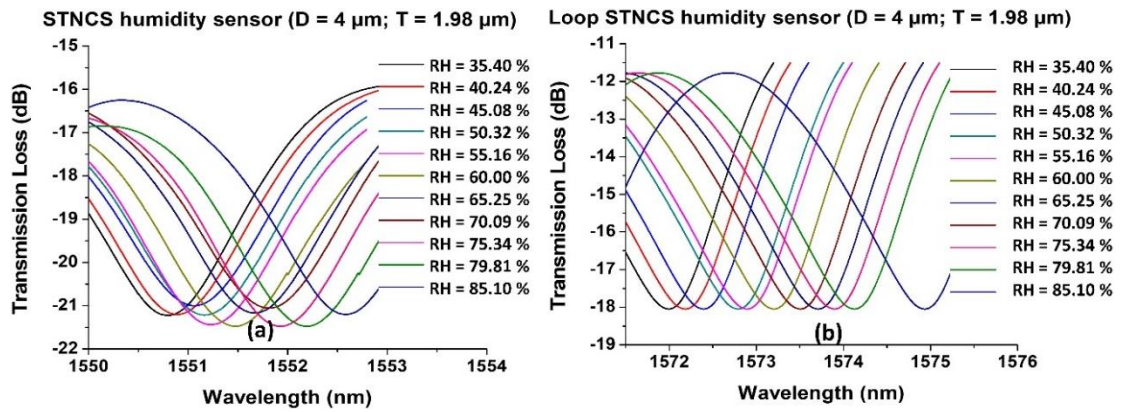


**Figure 4.6.** Spectral response of (a) the straight STNCS optical fibre RH sensor, and (b) the loop STNCS optical fibre sensor.

Figure 4.7 (a) shows that an increase in the coating layer thickness results in an increase in the RH sensitivity of the sensor. However, for larger coating thicknesses, the wavelength shifts nonlinearly as the RH increases. Therefore, in our further discussion, we will consider only the linear response (correlation coefficient ( $R^2$ ) > 0.9) of the proposed RH sensor, over a small RH range of 35 – 70 %, as shown in Figure 4.7 (b).

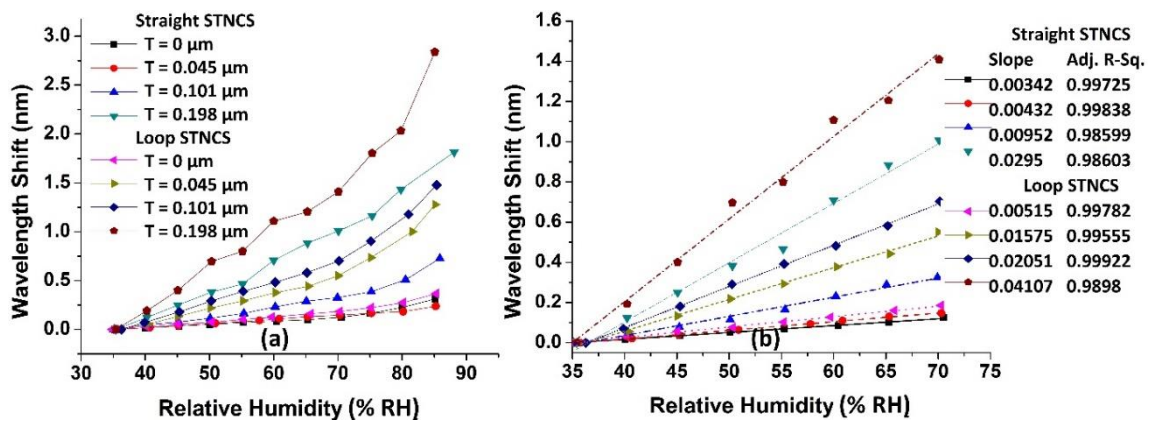


**Figure 4.7.** Wavelength shift versus RH for the straight STNCS and loop STNCS with 0, 0.045, 0.101, and 0.198  $\mu\text{m}$  hydro-gel coating thicknesses, over (a) complete range of 35 – 85 %RH (b) linear range of 35 – 70 %RH.

The influence of bending the STNCS OFS around the waist region on the RI sensitivity of the sensor was investigated. The experimental results of the bent tapered no-core section of the STNCS OFS with a bend radius  $R \approx 4.7$  cm for the same coating thickness of hydro-gel,

are shown in Figure 4.7. The RH sensitivities of the straight STNCS and STNCS loop without hydro-gel coating were also tested as a reference, which were observed to be 0.03 and 0.05 nm/%RH, respectively, indicating that the bend applied to the STNCS improved the RH sensitivity of the sensor. It should be noted that the R values of the STNCS loops were measured before using them for RH sensing, hence ensuring that all three STNCS loops had a similar value of R. The sensitivity of the straight and loop STNCS OFSs coated with different layer thicknesses of the hydro-gel are presented in Table 4.2.

**Table 4.2.** RH sensitivities of the straight and loop STNCS with 0, 0.045, 0.101, and 0.198  $\mu\text{m}$  hydro-gel coating thicknesses

Hydro-gel coating thickness ( $\mu\text{m}$ )	RH sensitivity of straight STNCS OFS with $D = 4 \mu\text{m}$ and $R = 0 \text{ cm}$ (nm/%RH)	RH sensitivity of Loop STNCS OFS with $D = 4 \mu\text{m}$ and $R \approx 4.7 \text{ cm}$ (nm/%RH)
0	0.00342	0.00515
0.045	0.00432	0.01575
0.101	0.00952	0.02051
0.198	0.0295	0.04107

Figure 4.8 compares the RH sensitivity of all six fabricated sensors tested above, three of which are straight STNCS, and the other three are loop STNCS OFSs. The results show a 0.11 nm improvement in sensitivity when the STNCS optical fibre sensor is bent with  $R \approx 4.7 \text{ cm}$  to form an STNCS loop. In this experiment, the maximum sensitivity achieved was 0.04 nm/%RH within the linear RH range of 35 – 70 %RH using an STNCS loop with  $R \approx 4.7 \text{ cm}$  and  $D \approx 4 \mu\text{m}$ , coated with a hydro-gel with  $T = 0.198 \mu\text{m}$ .

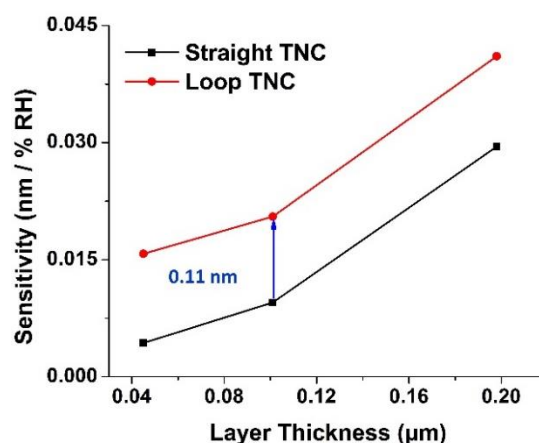


**Figure 4.8.** Comparison of the RH sensitivities of the straight STNCS and the STNCS loop.

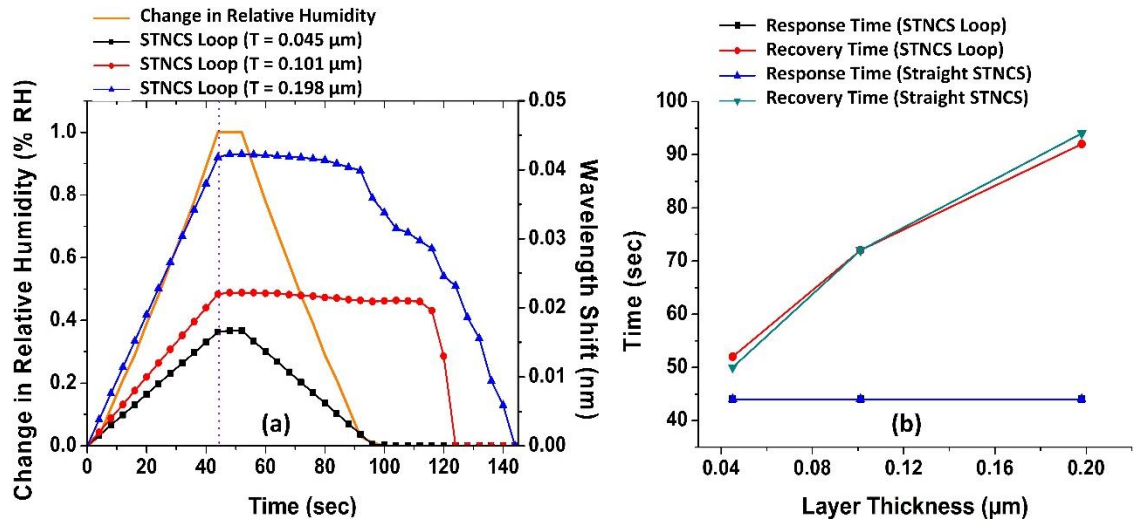


**Figure 4.9.** (a) Response and recovery times for the STNCS loop, (b) comparison of the response and recovery times of the straight STNCS and STNCS loop OFSs with 0.045, 0.101, and 0.198  $\mu\text{m}$  hydro-gel coating thickness.

The response and recovery times (which are the times taken by the sensor to respond to a unity increase or decrease in %RH, respectively) for all the six STNCS optical fibre RH sensors were tested by changing the RH of the humidity chamber by unity (1% RH), and observing the time required for the spectral dip to stabilise. The response time (time taken for the spectral response to stabilise when RH is increased by 1%) for all the sensors was recorded to be around 44 seconds. However, as observed from Figure 4.9 (a), an increase in T results in an increase in the recovery time, which is because a thicker layer requires more time to dry. The response and recovery times for the straight and loop STNCS OFSs coated with 0.045, 0.101, and 0.198  $\mu\text{m}$  thick layers of hydro-gel are presented in Table 4.3. It should be noted that, temperature measurements were also taken, which under room condition do not vary more than  $\pm 0.5$   $^{\circ}\text{C}$ . Therefore, the humidity readings were taken with negligible influence of temperature cross-sensitivity.

**Table 4.3.** Response and recovery times for the straight STNCS and loop STNCS OFSs coated with 0.045, 0.101, and 0.198  $\mu\text{m}$  thick layers of hydro-gel.

Layer Thickness ( $\mu\text{m}$ )	Response Time (STNCS Loop) (sec)	Recovery Time (STNCS Loop) (sec)	Response Time (Straight STNCS) (sec)	Recovery Time (Straight STNCS) (sec)
0.045	44	52	44	50
0.101	44	72	44	72
0.198	44	92	44	94

In conclusion, a RH sensor using an STNCS OFS functionalised with hydro-gel was proposed and experimentally demonstrated. The investigation of the different coating thicknesses suggests, that the thicker the coating thickness, the higher is the sensitivity; thinner coatings have relatively lower sensitivity but shorter recovery times. A maximum RH sensitivity of 0.029 nm/%RH has been achieved within the linear sensing range of 35 – 70 %RH using an STNCS OFS with  $D = 4 \mu\text{m}$ , functionalised with a hydro-gel of thickness  $T = 0.198 \mu\text{m}$ . The sensitivity within this linear sensing range (35 – 75 %RH) was improved to 0.041 nm/%RH by bending the above OFS with  $R = 4.7 \text{ cm}$ . The response and the recovery times of the proposed RH sensor were measured to be 44 and 92 seconds, respectively.

#### **4.4 STNCS Fibre Sensor for Human Chorionic Gonadotropin (hCG) Hormone Detection**

Human chorionic gonadotropin (hCG) is a glycoprotein secreted by the placental trophoblast cells after implantation. It simulates the corpus luteum in the ovary to produce progesterone, which maintains the lining of the uterus during the first week of pregnancy [150]. hCG is a heterodimer composed of two different  $\alpha$ - and  $\beta$ - subunits combined by noncovalent bonds, where the  $\beta$  subunit is the most important diagnostic marker for pregnancy and tumors due to it being unique to hCG, while the  $\alpha$ -subunit is identical to luteinizing hormone, follicle-stimulating hormone and thyroid-stimulating hormone (TSH) [151]. The hCG level in a urine sample of a pregnant woman is an important parameter for determining pregnancy and its related disorders. In practice, an hCG level  $> 5 \text{ mIU/mL}$  is considered positive for pregnancy. However, the current pregnancy test strip has a relatively low detection threshold of  $10 \text{ mIU/mL}$ , which can only be reached after 2 weeks of conception [152-154]. hCG can also be an indicator for tumors, where elevated levels of hCG are reported in patients diagnosed with tumors [155, 156], and it is therefore important to monitor hCG levels when assessing the recovery of patients receiving chemotherapy [157]. When the concentration of hCG in blood serum reaches  $15\text{-}150 \text{ mIU/mL}$ , it is almost certain that a gonadal tumor or testicular seminoma is diagnosed [158]. In addition, the detection of hCG is important in sports medicine, as it is abused either to conceal the use of anabolic steroids, or to increase the production of testosterone by athletes, and is therefore banned by the World Anti-doping Agency [159]. Normally, hCG concentration in the human body is very low ( $0.02 \text{ mIU/mL}$ )

[160], and hence a highly sensitive hCG sensor is required to detect low concentrations of hCG.

The current hCG detection technique utilises immune recognition based on the high binding affinity between anti-hCG- $\alpha$  or - $\beta$  antibodies (Ab) and the hCG antigen (Ag). This Ab-Ag interaction has led to the development of various immunosensors for hCG detection, such as the *Enzyme immunosensor* (EIS), *Electrochemical immunosensor* (ECIS) and *Photochemical immunosensor* (PCIS) which detect the changes in electrical signal, when hCG from the sample binds with the hCG-Ab immobilized on the electrode surface. EIS is one of the earliest methods for determining hCG concentration, which combines the amplification of enzyme-catalyzed reaction with the specificity of the Ab-Ag affinity reaction. EIS has a relatively low sensitivity of 0.4 mIU/mL, and is only suitable for qualitative and semi-qualitative determination of hCG [161]. Santandrew *et al.* proposed in [162] an amperometric immunosensor consisting of a conducting graphite-methacrylate matrix functionalised with anti-hCG- $\beta$  Ab, with an hCG limit of detection (LOD) of 2.6 mIU/mL. The LOD was improved to as low as 0.00036 mIU/mL in [163], but at the cost of the increased complexity associated with depositing a carbon nanotubes film on the electrodes to increase conductivity of such electronic sensors. PCIS is another type of immunosensors used for hCG detection, which require a secondary Ab linked with the reagent to produce fluorescence. Since the intensity of fluorescence is normally very weak, this type of sensors often suffers from background interference (ambient light). An example of PCIS was demonstrated by L. Mao *et al.* in [57] with a low LOD of 0.07 mIU/mL using TiO<sub>2</sub> composite nanoparticles functionalised by Nafion as label. *Surface plasmon resonance* (SPR)-based immunosensors are another method for direct and rapid detection of bio samples. An SPR immunosensor with good specificity and selectivity but relatively low hCG LOD of 100 mIU/mL was demonstrated by M.Piliarik *et al.* in [164].

Due to the advantages of compact size, immunity to electromagnetic interference, and remote sensing capability [165], optical fibre sensors have attracted wide research interests in many areas such as automotive, chemical industry, aircraft, and medical diagnosis [166]. Numerous optical fibre-based sensor structures have been demonstrated as biosensors. For example, an LPG sensor was demonstrated for streptavidin (SV) and immunoglobulin M (IgM) detection by depositing three layers of silica matrix (PAH/SiNPs) imbedded with gold nanoparticles and immobilised with the corresponding Abs, achieving a sensitivity of 3.88 and 11 nm/(ng/mm<sup>2</sup>) for SV and IgM detection, respectively [167]. A tapered MMF (taper

waist diameter of 10  $\mu\text{m}$  and length of 10 mm) functionalised with Dengue virus (DENV) NS1 glycoprotein was demonstrated for anti-DENV NS1 IgG Ab detection, with a sensitivity of  $7 \times 10^{-6}$  a.u/pg/mL [168]. In addition, an evanescent field sensor based on an MZI was demonstrated for DNA detection in [169]. The interferometric sensor based on a core-offset fusion-spliced SMF (core offset of 62.5  $\mu\text{m}$  and a sensing length of 195  $\mu\text{m}$ ) was immobilised with staphylococcal protein A and goat anti-human IgG, and was demonstrated for detecting human IgG with a LOD of 47 ng/mL [170]. Special fibres such as tapered PCFs functionalised with biotin were also demonstrated as immunosensors for the detection of SV in [171]. A dual-core OFS was also demonstrated for IgG detection and demonstrated a LOD of 4  $\mu\text{g/mL}$  for a 1 hour measurement [172]. Among the different types of OFSs, interferometric sensors based on singlemode-multimode-singlemode (SMS) fibre sensors [122] have attracted a wide research interest in recent years, as they have the advantages of a simple fabrication process and low cost, while exhibiting high RI sensitivity [118, 173].

In this section, an ultrasensitive microfibre interferometer biosensor is proposed for ultralow hCG concentration detection. The fibre sensor structure used for this study is a singlemode-tapered no-core-singlemode (STNCS) optical fibre sensor, which generates an easily accessible evanescent field around its tapered waist region. The fibre sensor was functionalised by immobilising anti-hCG- $\beta$  Ab on the fibre sensor surface, specifically around the tapered waist region, and was then demonstrated to detect an hCG sample with concentration as low as 0.05 mIU/mL. To further improve the sensitivity of the sensor, magnetic microspheres (MMSs) immobilised by anti-hCG- $\alpha$  Ab were added to the hCG analyte, which effectively increase the RI (because of the large size of MMSs) due to the capture of hCG samples. Experimentally, the sensor can detect hCG concentrations  $< 0.01$  mIU/mL by adding the surface modified MMSs and enriched hCG samples.

#### 4.4.1 Sensor fabrication and experimental setup

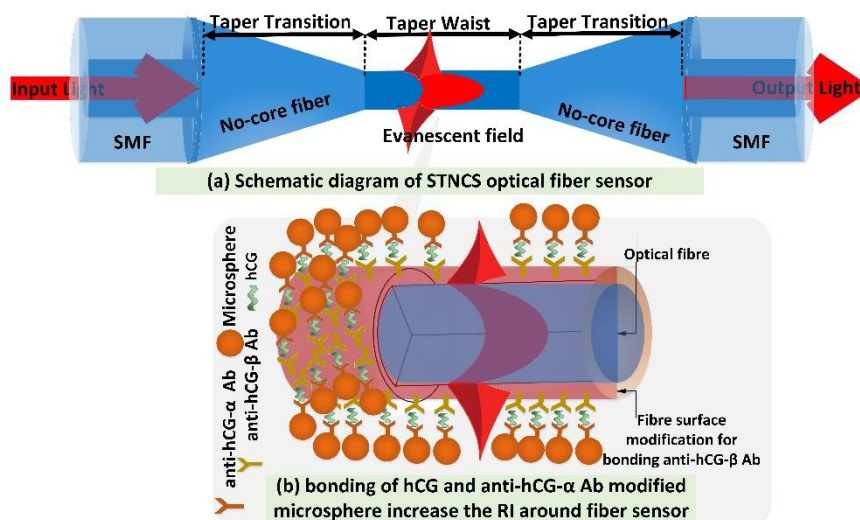


**Figure 4.10.** Schematic diagram of (a) the STNCS optical fibre structure, and (b) the RI change caused by the bonding of hCG and anti-hCG- $\alpha$  Ab modified MMSs on the fibre surface, immobilised with anti-hCG- $\beta$  Ab.

A schematic diagram of the microfibre interferometer is shown in Figure 4.10 (a). As the light is incident from the SMF into the no-core fibre (NCF), multiple modes are excited, which propagate within the NCF section. When the NCF is tapered to small diameters, the percentage of evanescent field transmitted around the NCF surface increases significantly, which results in the increase of RI sensitivity of the fibre sensor, which is the basis for hCG detection in this experiment. An STNCS OFS with 8  $\mu\text{m}$  taper waist diameter was used as the sensor base in the experiments, and was functionalised by immobilising the fibre surface with an hCG capture layer (anti-hCG- $\beta$  Ab), where the bonding of the analyte (hCG and anti-hCG- $\alpha$  Ab modified MMSs) results in an increase in RI, and so the structure can be used as an optical fibre biosensor for hCG detection, as shown in Figure 4.10 (b).

##### Initial test before surface modification

In principle, the proposed optical fibre sensor detects hCG concentrations based on the RI changes induced when the hCG in the urine sample adheres onto the modified fibre surface, due to the Ab-Ag interaction. Therefore, knowledge about the RI sensitivity of the STNCS optical fibre sensor is necessary, specifically in the RI range of 1.33, which is the RI of most of the buffer solutions used in our experiment. As demonstrated in Figure 3.4 (a-c) of Chapter 3, the RI sensitivities of the STNCS optical fibre with an 8  $\mu\text{m}$  taper waist diameter

are 1046.34, 3780.10, and 26,061.77 nm/RIU for the RI ranges around 1.33, 1.37 and 1.4, respectively.

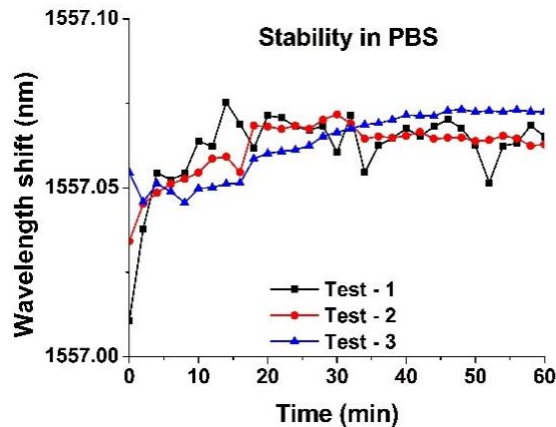


Figure 4.11. Stability of STNCS in PBS.

In the experiment, the stability of the OFSs' spectral response in phosphate buffer saline (PBS) is desired, because it will be used extensively to prepare different concentrations of hCG sample and also for washing the OFS during the bio-sensing experiment. As shown in Figure 4.11, three rounds of stability tests were carried out, showing a relatively stable and repeatable spectral response with an average spectral variation of  $\pm 0.05$  nm over a 60 minutes duration. The key wavelength shift was observed in the first 5 minutes, which is possibly due to the stress applied by the initial PBS flow around the sensor.

The developed STNCS sensor was then functionalised by immobilising anti-hCG- $\beta$  Ab as capture Ab on the fibre sensor surface, which binds specifically with hCG. When the hCG binds with the anti-hCG- $\beta$  Ab, both the RI and thickness of the STNCS sensor change, resulting in the wavelength shift of the sensor. Once the wavelength shift is calibrated, the concentration of hCG can be determined.

The schematic for the fibre surface modification and immobilisation procedure is shown in Figure 4.12 (a), and can be described as follows [174]:

- i) The fibre surface was treated with 5% silane reagent (3- (Triethoxysilyl) propylsuccinic anhydride) in ethanol for 2 ~ 4 hours at room temperature to attach the carboxyl groups on the surface.
- ii) After washing the fibre sensor with ethanol and PB (phosphate buffer without sodium chloride) (pH = 6.0), the fibre surface was treated with freshly prepared EDC (1-ethyl-3-(3-dimethylaminopropyl) carbodiimide hydrochloride) and NHS (N-hydroxysuccinimide) solution for 1 hour. This step results in coupling an activated

succinimide ester (obtained from EDC and NHS reaction) to which the capture antibody can easily attach.

- iii) The fibre surface was immediately treated with capture antibody in PBS (phosphate buffer saline) for 4 hours.
- iv) The fibre sensor was then immersed into 1% BSA (Bovine serum albumin) for 2 hours at room temperature to block the excess NHS ester and the uncovered gaps of fibre sensor, thus suppressing unspecified biofouling.
- v) Finally, the fibre sensor was washed with PBS buffer before using it to detect the hCG sample.

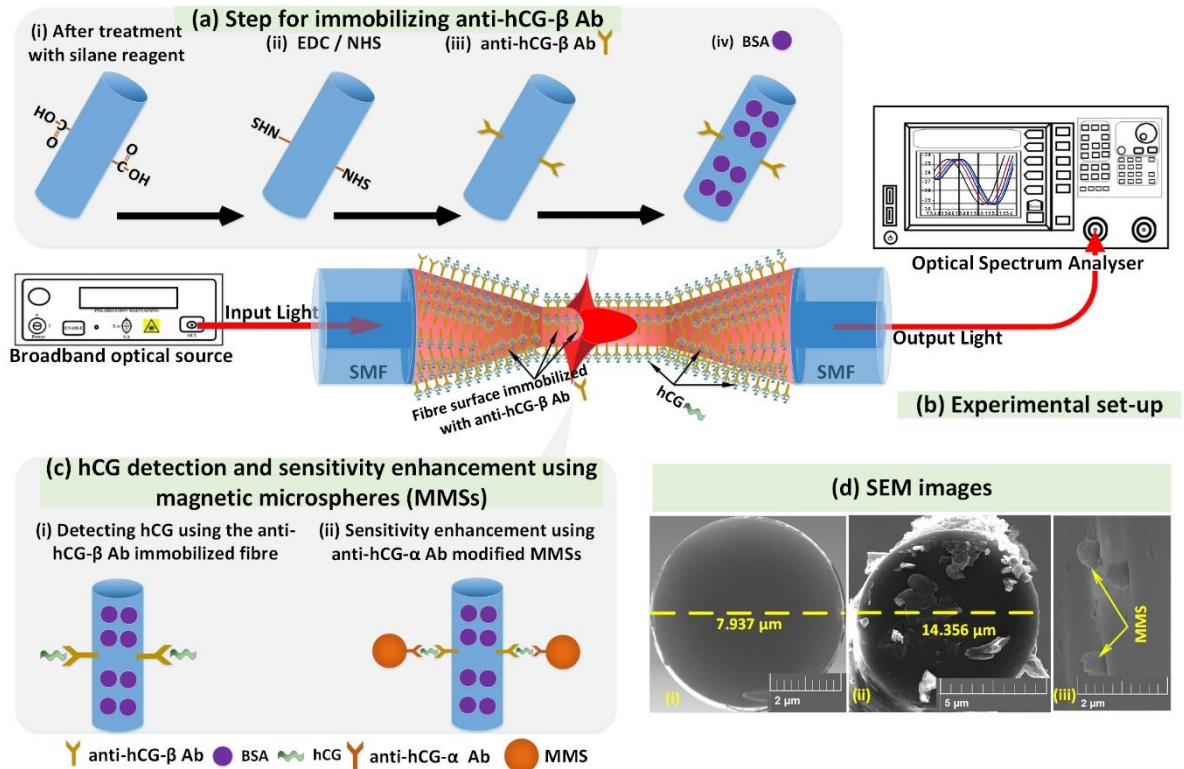


**Figure 4.12.** (a) The surface modification and Ab immobilisation procedure. (b) The experimental setup for hCG detection. (c) The functionalized fibre sensor used for hCG detection and sensitivity enhancement using MMSs. (d) SEM images for the STNCS waist cross-section, functionalised fibre after hCG detection, and the anti hCG-α modified MMSs binding on the fibre surface.

The experimental setup shown in Figure 4.12 (b) consists of a broadband light source (SLD1005S) and an optical spectral analyser (OSA, Yokogawa AQ6370D). The light supplied by the broadband source was launched into the functionalised STNCS fibre sensor, which was placed in a microchannel of volume  $\sim 400 \mu\text{L}$ , and the output light from the sensor was detected by the OSA. The channel ( $400 \mu\text{L}$ ) was then filled with hCG samples of different concentrations. The capture antibody on the fibre surface creates a covalent bond with the hCG present in the urine sample, thus adhering onto the fibre surface, as shown in Figure 4.12 (c-i). The scanning electron microscope (SEM) images of the (i) STNCS waist

cross-section, (ii) the modified STNCS fibre after hCG detection, and (iii) the bonding of the anti-hCG- $\alpha$  Ab modified MMSs on the fibre surface are shown in Figure 4.12 (d).

In this experiment, six different concentrations of hCG (0.05, 0.5, 5, 50, 500, 500 mIU/mL) were prepared by diluting the stock urine samples (17,857 mIU/mL hCG) of pregnant women in PBS. The response of the fibre sensor in different concentrations of hCG was observed by adding each of the hCG samples, starting from the lowest (0.05 mIU/mL) all the way to the highest (500 mIU/mL) hCG concentration in the above concentration series. After each observation, and before introducing the next concentration of hCG, PBS was added in the channel for 10 minutes to wash the un-bonded hCG due to deposition. This washing step was important to eliminate the influence of the un-bonded or loosely bonded hCG. Table 4.4 summarises the parameters of STNCS OFS and the MMSs and specifications of components used in the experimental setup for hCG detection.

**Table 4.4.** Summary of the STNCS OFS and MMSs parameters, functionalised with hCG- $\beta$  and hCG- $\alpha$  Abs respectively, and specifications of components used in the experimental setup, for detecting hCG.

	<b>Fibre Type</b>	<b>Parameter</b>
<b>Fibre Structure</b>	STNCS (POF Corporation Ltd.-NCF125)	Taper waist diameter ~ 8 $\mu$ m Waist length ~ 10 mm Transition length ~ 10 mm Functionalised with hCG- $\beta$ Ab
	SMF (Thorlabs-SMF-28)	Core diameter = 8.2 $\mu$ m Cladding diameter = 125 $\mu$ m
	MMSs	Diameter = 300 nm & 1 $\mu$ m Functionalised with hCG- $\alpha$ Ab
	<b>Components</b>	<b>Specifications</b>
<b>Experimental setup</b>	Optical source (Thorlabs SLD S5FC1550S-A2)	Centre wavelength = 1550 nm Output power = 2.5 mW Bandwidth = 90 nm
	Channel	Volume = 400 $\mu$ L Material = Glass
	Optical spectrum analyzer (Yokogawa AQ6370D)	Wavelength range = 600 -1700 nm Accuracy = $\pm$ 0.01 nm Resolution = 0.02 nm

#### 4.4.2 Results and discussion

##### Investigation of capture layer concentration

The influence of capture Ab concentration on the performance of the sensor was firstly studied using four STNCS fibre sensors immobilised with different concentrations of capture Ab (4, 8, 16 and 32  $\mu$ g/mL) to detect 0.05, 0.5, 5, 50, 500, 5000 mIU/mL of hCG sample. Figure 4.13 shows the output spectral response of the STNCS fibre sensor, modified with 16  $\mu$ g/mL of capture Ab, for different concentrations (0.05, 5, and 500 mIU/mL) of hCG. It can be observed that when the hCG in the urine sample adheres on to the modified fibre surface,

the spectral dip shifts towards longer wavelengths. In addition, an increase in the hCG concentration results in shifting the spectral dip by a larger value. Note that the spectral shift was observed during the initial 20 minutes, after which the spectral response stabilised. This observation suggests that the hCG in the urine sample takes about 20 minutes to adhere on to the modified fibre surface. In other words, either the saturation of bonding sites on the capture layer, or the exhaustion of hCG in the urine sample occurs within the first 20 minutes. The maximum spectral shift observed was during the initial 10 minutes of changing the hCG concentration, which suggests that the maximum adhesion of hCG occurs during the first 10 minutes, and the spectral tend to stabilise in the next 10 minutes.

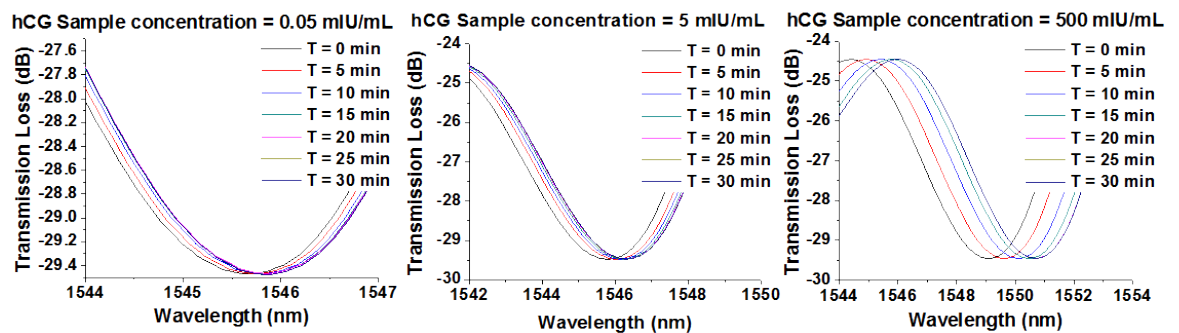


**Figure 4.13.** Spectral response from STNCS fibre sensor modified with 16 µg/mL of capture Ab concentration, to detect (a) 0.05 mIU/mL (b) 5 mIU/mL and (c) 500 mIU/mL of hCG concentration in urine sample

Figure 4.14 shows the wavelength shift vs. time for the four STNCS fibre sensors immobilised with four different capture Ab concentrations (4, 8, 16, and 32 µg/mL) to detect different concentrations of hCG samples (0.05, 0.5, 5, 50, 500, 5000 mIU/mL). It can be seen that the capture Ab dosages of 4 and 8 µg/mL were insufficient to detect higher concentrations (50 and 500 mIU/mL) of hCG, and were exhausted by the lower concentrations of hCG in the desired range (0.05 – 5000 mIU/mL). The capture Ab dosage of 16 µg/mL was observed to be suitable for detecting the desired range from 0.05 – 500 mIU/mL of the hCG sample. The total spectral shift observed was 5.22 nm for this range. Increasing the capture Ab dosage to 32 µg/mL did not show any significant improvement, with a total spectral shift of 5.18 nm observed for the desired range. Therefore, in our further experiments, an STNCS optical fibre immobilised with 16 µg/mL of capture Ab was used.

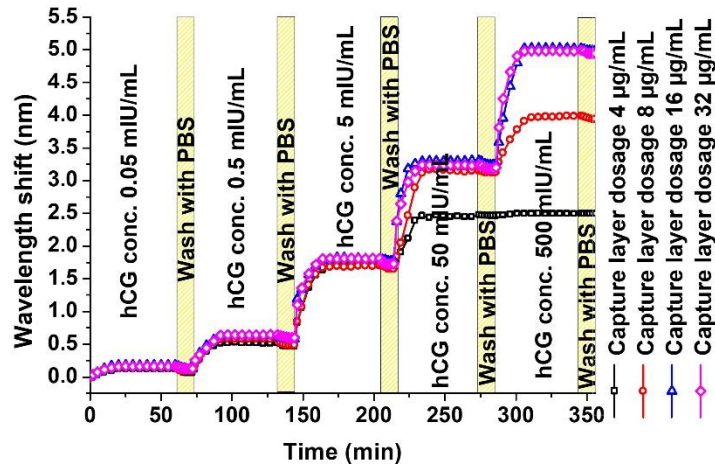


**Figure 4.14.** Investigation of the effect of capture Ab concentrations on the STNCS fibre surface for detecting entire range from 0.05 – 5000 mIU/mL of the hCG in urine samples

The repeatability of the proposed sensor was tested by observing the wavelength shift for each of the five concentrations in the range of 0.05 – 500 mIU/mL of hCG using three different STNCS optical fibre sensors immobilised with 16 µg/mL of capture Ab, and the results are shown in Figure 4.15 (a). The average wavelength shift observed during each repetition was  $0.18 \pm 0.01$ ,  $0.69 \pm 0.01$ ,  $1.91 \pm 0.04$ ,  $3.44 \pm 0.03$ , and  $5.22 \pm 0.02$  nm for 0.05, 0.5, 5, 50, 500 mIU/mL of hCG, respectively. Based on these values, a standard curve fitting can be achieved as described in Equation 4.1. By measuring the wavelength shift  $y$ , the hCG concentration  $x$  can thus be calculated by solving Equation 4.1:

$$y = \frac{6.884 \times x^{0.471}}{6.047 + x^{0.471}} \quad 4.1$$

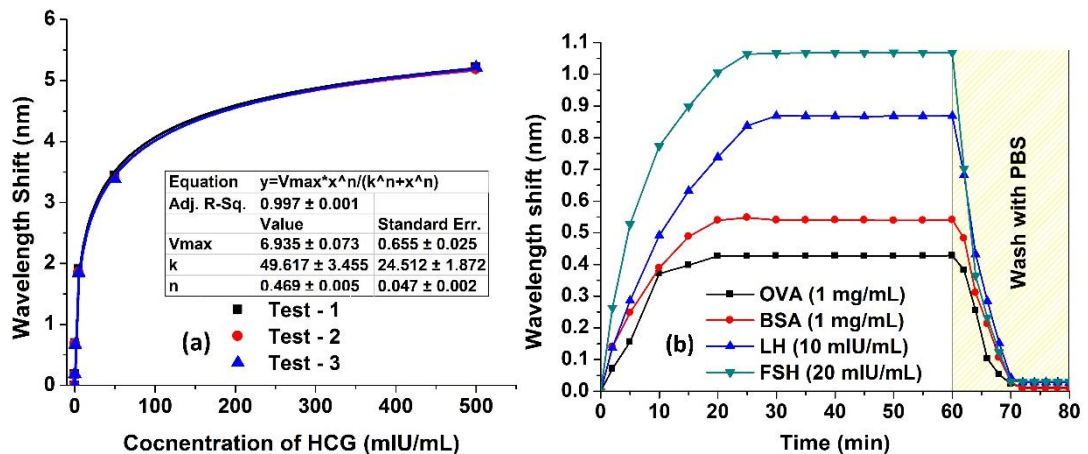


**Figure 4.15.** (a) Standard curve and repeatability test, and (b) selectivity test for the STNCS optical fibre sensor immobilised with 16µg/mL of capture Ab.

To test the selectivity of the proposed sensor, four different nonspecific analytes were tested by four different STNCS optical fibre sensors immobilised with 16  $\mu\text{g/mL}$  of capture Ab. Figure 4.15 (b) shows the wavelength shift when 1 mg/mL of ovalbumin (OVA), 1mg/mL of bovine serum albumin (BSA), 10 mIU/mL of Luteinizing hormone (LH), and 20 mIU/mL of Follicle-stimulating hormone (FSH) were introduced separately to the four fibre sensors. As shown in Figure 4.15 (b), during the initial 25 minutes, the spectral dip of all the four fibre sensor shifts by around 0.43, 0.54, 0.86 and 1.06 nm for OVA, BSA, LH and FSH, respectively, and then stabilises. When the reading of wavelength was stable, the fibre sensors were washed with PBS for 20 minutes, and the spectral wavelength was observed to shift back to almost the same value of the initial wavelength, with only 0.013, 0.010, 0.028, 0.030 nm wavelength deviations for OVA, BSA, LH and FSH, respectively. This result indicates that the large wavelength shift observed is due to the deposition of the nonspecific analyte onto the fibre surface, which can be washed by PBS. Furthermore, the above results demonstrate the good selectivity of the proposed sensor towards hCG.

#### **Sensitivity improvement by adding functionalised magnetic microspheres (MMSs) to the hCG samples**

The initial experiment demonstrated that the sensor can detect hCG with concentrations as low as 0.05 mIU/mL, where a sensitivity as high as 3.76 nm/mIU/mL was recorded. To further improve the sensitivity of the fibre sensor, the use of MMSs functionalised with anti-hCG- $\alpha$  Ab is proposed, which will bind with the analyte hCG captured by the anti-hCG- $\beta$  Ab on the fibre surface to introduce an additional increase in the effective RI and thickness of the fibre coating. Figure 4.12 shows the schematic diagram of the scheme, demonstrating the addition of MMSs functionalised with anti-hCG- $\alpha$  Ab to the sensing system. As shown in Figure 4.12 (c-i), when the hCG is captured by anti-hCG- $\beta$  Ab, additional MMSs functionalised with anti-hCG- $\alpha$  Ab will be added to the microchannel, where the MMSs will be bonded to the hCG on the fibre sensor surface, as shown in Figure 4.12 (c-ii). Since the size of MMS is significantly larger than that of hCG, the MMSs attached to the fibre sensor surface will introduce significant changes in the effective RI and thickness of the fibre sensor section, which will introduce a significant wavelength shift for the sensor, resulting in an improvement in the sensor sensitivity.

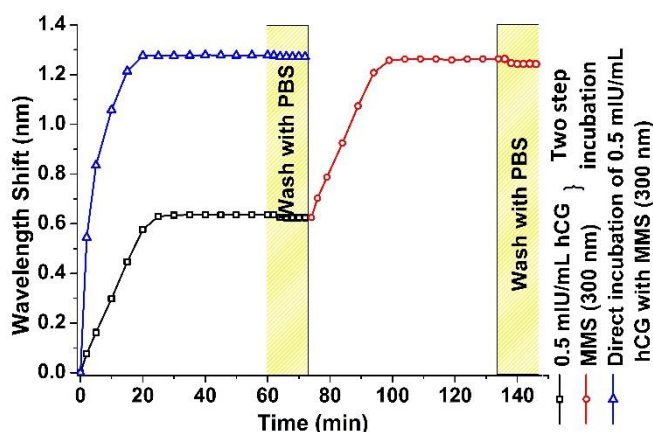


**Figure 4.16.** Comparison of the two-step and direct incubation processes of functionalised STNCS fibre with hCG and MMSs.

The effect of adding anti-hCG- $\alpha$  Ab modified MMSs is demonstrated in Figure 4.16, where the MMSs used in the experiment were polystyrene microspheres encapsulated with Fe<sub>3</sub>O<sub>4</sub> nanoparticles (PSMS, concentration 0.04  $\mu$ g/mL and 300 nm diameter). As shown in Figure 4.16, if there are no MMSs added to the system, the wavelength shift observed for 0.5 mIU/mL hCG is 0.62 nm (black square), which can be amplified to 1.268 nm (red circle) by adding the functionalised MMSs into the microchannel. This additional spectral shift is due to the bonding of anti-hCG- $\alpha$  Ab modified MMSs with the hCG sample captured on the fibre surface, as shown in Figure 4.12 (c-ii). The above hCG measurement included a two-step process: (1) using the anti-hCG- $\beta$  Ab modified fibre sensor to detect hCG; and (2) immersing the fibre sensor after step 1 into an anti-hCG- $\alpha$  Ab modified MMS liquid to enable binding between the captured hCG and the anti-hCG- $\alpha$  Ab modified MMSs. The above two-step process was compared with the direct hCG incubation process, where the anti-hCG- $\alpha$  Ab modified MMSs was directly mixed in the hCG sample, and added into the microchannel to perform the test. It can be observed from Figure 4.16 that the direct incubation of the hCG-MMS mixture introduces a wavelength shift of 1.271 nm (blue triangle) for 0.5 mIU/mL of hCG sample, which is similar to the 1.268 nm shift achieved using the two step incubation process. Since the direct process is simpler than the two-step process, the direct incubation process was used in the subsequent experiments.

The influence of MMSs' diameter on the sensor sensitivity was investigated by using MMSs (PEMS encapsulated with Fe<sub>3</sub>O<sub>4</sub> nanoparticles) of 300 nm and 1  $\mu$ m diameters, where the anti-hCG- $\alpha$  Ab was attached onto the two MMSs. In the experiments, the concentration of both the MMSs was 0.4  $\mu$ g/mL. Two identical STNCS sensors immobilised with 16  $\mu$ g/mL

of capture Ab were used to test the influence of the MMS-hCG samples, one for 300 nm MMS, and one for 1  $\mu$ m MMS. Figure 4.17 shows the wavelength shift of the fibre sensor immersed into the anti-hCG- $\alpha$  Ab modified MMSs (with 300 nm and 1  $\mu$ m diameters), in different hCG concentrations. As shown in Figure 4.17, wavelength shifts of 0.12, 0.57 and 0.95 nm for the MMSs of 300 nm diameter were experimentally observed for 0.01, 0.05, 0.25 mIU/mL concentrations of hCG, respectively. When the particle size of the MMSs was increased to 1  $\mu$ m diameter, the wavelength shift was observed to increase to 0.27, 1.27, and 2.17 nm for the same hCG concentration of 0.01, 0.05, 0.25 mIU/mL, respectively, which indicates more than 2 times higher sensitivity compared to that of 300 nm MMSs. The maximum sensitivity achieved in the experiments was 27 nm/mIU/mL, which was achieved by adding anti-hCG- $\alpha$  Ab modified MMSs with 1  $\mu$ m diameter into the 0.01 mIU/mL hCG samples.

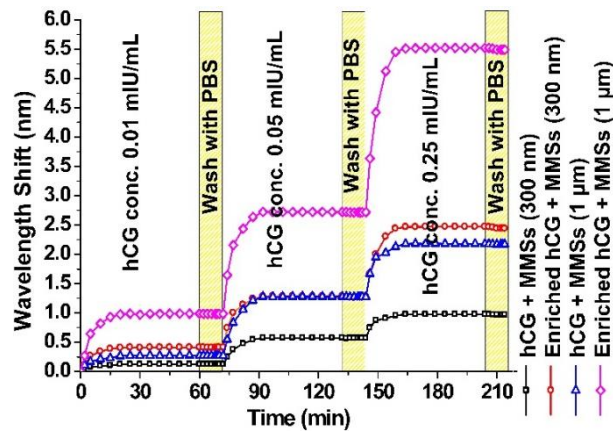


**Figure 4.17.** Sensitivity improvement for the 0.01, 0.05, and 0.25 mIU/mL concentrations of hCG obtained by adding MMSs with 300 nm and 1  $\mu$ m diameters, and by the enrichment process.

The sensitivity can be further improved by the enrichment of hCG samples. The enrichment process can be described as follows.

The enrichment efficiency of hCG in the previous sample was improved by immunomagnetic separation, which is a conventional laboratory method to efficiently isolate the hCG in the urine sample, or their dilution series in PBS [175]. In our experiments, three hCG samples (2 mL) with concentrations of 0.01, 0.05 and 0.25 mIU/mL were incubated with anti-hCG- $\alpha$  Ab modified MMSs with diameter of 300 nm or 1  $\mu$ m (0.4  $\mu$ g/mL) in a tube for 10 minutes. The tube was then put on a magnetic separator for 2 minutes for immunomagnetic separation, followed by removal of supernatant. The MMSs captured with

hCG, left in the tube was re-suspended in 400  $\mu\text{L}$  of PBS and applied to the fibre sensor for measurements.

The effect of enrichment can be observed in Figure 4.17. The three enriched hCG samples with 300 nm diameter MMSs showed a wavelength shift of 0.41, 1.26, and 2.44 nm for hCG concentrations of 0.01, 0.05 and 0.25 mIU/mL, respectively, whereas the enriched hCG samples with 1  $\mu\text{m}$  diameter PEMS showed a wavelength shift of 0.98, 2.71, 5.49 nm for the same hCG concentrations of 0.01, 0.05 and 0.25 mIU/mL, respectively. The results therefore show that the sensitivity is further improved to 98 nm/mIU/mL by enriching the 0.01 mIU/mL hCG with 1  $\mu\text{m}$  diameter MMSs.

Table 4.5 summarises the wavelength shift observed by the three methods explored above (using the STNCS OFS with hCG only, adding surface modified MMSs, and enrichment of samples).

**Table 4.5.** Experimentally recoded values of wavelength shift observed for 0.01, 0.05, and 0.25 mIU/mL concentration of hCG for the three methods described above.

hCG concentrat (mIU/mL)	Wavelength shift				
	(nm)				
	hCG only	hCG + MMSs (300 nm)	Enriched hCG + MMSs (300 nm)	hCG + MMSs (1 $\mu\text{m}$ )	Enriched hCG + MMSs (1 $\mu\text{m}$ )
0.01	-	0.121	0.409	0.273	0.984
0.05	0.188	0.569	1.263	1.273	2.715
0.25	0.361	0.952	2.439	2.170	5.4929

As shown in Table 4.5, when the concentration of hCG is 0.05 mIU/mL, 6.7 and 14 times improvements can be obtained by adding 1  $\mu\text{m}$  diameter MMSs and enriching the hCG samples, respectively, compared to the use of hCG only. When the hCG concentration is 0.01 mIU/mL, the fibre sensor cannot detect hCG directly. However, when the hCG is combined with surface modified MMSs, the sensor can detect hCG with concentrations as low as 0.01 mIU/mL, where 0.121 nm and 0.273 nm wavelength shifts are obtained for the MMSs with 300 nm and 1  $\mu\text{m}$  diameter, respectively. The wavelength shift can be further improved to 0.984 nm when the hCG sample (combined with MMSs of 1  $\mu\text{m}$  diameter) is enriched. Assuming the resolution of OSA is 0.01 nm, the LOD of the fibre sensor could be as low as 0.0001 mIU/mL, which is the lowest detection limit reported to date.

## 4.5 STNCS Optical Fibre Sensor for Oxygen Sensing

Fresh air usually contains 23.5% oxygen, and a concentration of less than 19.5% has been defined by the Occupational Safety and Health Administration (OSHA) as an oxygen deficient condition [140]. Therefore, maintaining appropriate oxygen concentration is of great importance, especially in confined spaces like coal mines and submarines. Low blood oxygen level in humans can cause symptoms like shortness of breath, dizziness, confusion and lack of coordination. Furthermore, detection and quantification of oxygen concentrations is not only a necessity to sustain all forms of life on earth, but is also useful in the field of bio-chemistry, medicine, and various industrial applications [176]. Developing highly-efficient sensors for accurately measuring oxygen concentrations is of considerable importance, and significant efforts have been devoted to this task. Considering the range of applications for oxygen sensors, several schemes have been developed, such as semiconducting resistive type sensors that work at high temperatures, and Clark electrodes for detecting oxygen in solutions [177]. However, these sensors have a relatively long response time. This problem can be resolved by using optical sensors, which are based on the fluorescence measurements of luminophores. These sensors are compact and provide immunity to electromagnetic interferences (EMI), therefore making them ideal for applications where non-optical based sensors cannot be used. In addition, these types of sensors offer multiplexing capabilities and implementation in distributed and quasi-distributed sensor networks (as part of the “internet of things”), as well as operability over longer transmission distance in harsh indoor and outdoor environments. In fluorescence-based fibre sensors, the luminance produced by the interaction between a fluorescent material and oxygen is transmitted into the fibre and is collected by the detector. This type of sensor has a low signal to noise ratio due to the weak fluorescence signal superimposed to the transmission light [178]. This issue can be further resolved by directly coating the fluorescent material onto the optical fibre.

Many optical fibre structures have already been proposed for gas sensing, offering the advantages of good precision, accuracy, ease of miniaturisation, and continuous remote sensing specifically for gaseous environments, where physical monitoring is not possible, such as in the measurement of oxygen in power plants [179]. For example, an optical microfibre coupler (OMFC) with a 3  $\mu\text{m}$  taper waist diameter coated with 90 nm coating thickness of sol-gel was demonstrated in [180] for ammonia gas concentration, with a sensitivity of 2.23 nm/ppm (part-per million). The resolution of the sensor was 5 ppb, and

the response and recovery times were ~ 50 and 35 seconds, respectively. Another sol-gel coated tapered SCSMF with 13.5  $\mu\text{m}$  taper waist diameter and thicker (249 nm) sol-gel coating was demonstrated to improve the sensitivity to 2.47 nm/ppm for ammonia gas concentration; where the resolution of the sensor was 4 ppb, while the response and recovery times were less than 2 and 5 minutes, respectively [181]. In addition, an OMFC with a taper waist diameter of 1.9  $\mu\text{m}$  coated with Nile red in sol-gel matrix was demonstrated for the simultaneous measurement of methanol and ethanol concentrations, with a sensitivity of -0.130 nm/ppm and -0.036 nm/ppm, respectively [173].

Most fibre-based sensors used for oxygen monitoring are coated with an oxygen-sensitive fluorescent dye, which interacts with the oxygen in the form of absorbance, reflection (transmission), or luminescence of visible light [182]. For example, Tris (2,2'-bipyridyl) dichlororuthenium(II) hexahydrate and Tris(bipyridine) ruthenium(II) chloride were coated in [183] on a D-shaped LPG with a polishing depth of 41.87  $\mu\text{m}$ , and were used to demonstrate a sensitivity of 1.54%/V (volt) and 9.62%/V, respectively. The coating thickness for both ruthenium complexes were 625 nm and produced a fluorescence at 610 nm. Another ruthenium complex (Ru(II) complex), which produced fluorescence at 591 nm, was demonstrated for oxygen sensing by coating it on a tapered polymer optical fibre (initial diameter = 1 mm) with a taper waist diameter in the range of 400 – 600  $\mu\text{m}$  [184]. The fluorescence produced by most of the dye is in the visible wavelength range, which limits the practicality of such sensors due to the interference from the ambient light. Such fluorescent sensors are also unsuitable for use in biological environments, as the visible wavelength of light is often attenuated by the biological matter. This fact led to the development of near-infrared (NIR) luminescent compounds such as platinum (II) ring-fused chlorine [185], and ring-fused 5,15-diphenylchlorins [186] for bio-sensing applications, which provide deeper penetration of the NIR light into the bio samples for determining their oxygen intake [187].

In this section, a chromogenic (colour change) approach is considered for the detection and quantification of oxygen, based on the evanescent field absorption in the near infrared (NIR) region. Absorptiometric OFSs, such as the one demonstrated in this section, use chemical compounds (such as Methylene Blue and Indigo) that either undergo a chromogenic reaction with oxygen, or where oxygen causes a colour shift, such as in the hemoglobin–oxyhemoglobin system [188]. Methylene blue (MB) [189] is widely used dye as a redox indicator, exhibiting a colour change from its reduced state to the oxidized state. In the

experiment reported in this section, MB is selected as the sensing material, and is immobilised on the singlemode-tapered no-core-singlemode (STNCS) OFS using the sol-gel processing technique. The colour change of MB is closely related to the concentration of oxygen [189], which in turn influences the absorption of the evanescent field of the STNCS OFS. Therefore, it can be utilised to detect and quantify oxygen concentrations. Most optical oxygen sensors, such as the ones described above, use optical fibres as waveguides to carry the fluorescence (visible wavelength) emitted by the fluorescent dye coated on the fibres. In contrast, the proposed MB coated STNCS optical fibre oxygen sensor operates in the NIR wavelength and utilises a chromogenic (colour change) approach. Therefore, the proposed sensor can be used for detection and quantification of oxygen concentrations in an environment with few interfering factors.

#### **4.5.1 Sensor fabrication and experimental setup**

##### **Methylene Blue (MB) sol-gel preparation and sensor functionalisation**

In this experiment, the STNCS OFS is fabricated by tapering the no-core section in a singlemode – no-core – singlemode (SNCS) OFS down to smaller diameters of 2 and 4  $\mu\text{m}$ . The coating layer for oxygen sensing was prepared by entrapping methylene blue ( $\text{C}_{16}\text{H}_{18}\text{ClN}_3\text{S}\cdot 3\text{H}_2\text{O}$ ) in sol-gel, which is an optically transparent glass-like material formed by hydrolysis and polymerization of metal alkoxides or metalorganic compounds at the room temperature. The porous matrix of sol-gel, formed by the three-dimension network of  $\text{SiO}_2$ , allows the oxygen to penetrate the polymer and interact with the dissolved MB [140]. The fabrication procedure of the MB sol-gel film is outlined below.

1. A 0.006 gm of methylene blue was dissolved in 3 mL ethanol and sonicated for 20 minutes.
2. A 1 mL DI water was acidified by adding 30  $\mu\text{L}$  of HCL (0.04 mol/ V).
3. A 4.5 ml of tetraethyl orthosilicate (TEOS) was mixed with 5.5 mL of ethanol by stirring it for 20 minutes.
4. The acidified water prepared in the Step 2 was added to the above solution in the Step 3, and stirred continuously for 20 minutes.
5. A 1 mL of the methylene blue solution prepared in the Step 1 was added to the above solution (Step 4) and stirred for another 20 minutes.

6. The above solution was ready to be used for coating of the STNCS optical fibre structure.

The STNCS was then coated by the prepared MB sol-gel solution in the Step 6 above, by using the dip coating method. Three different coating thickness (i.e., 0.86, 0.69 and 0.39  $\mu\text{m}$ ) of MB sol-gel is coated on the two STNCSs' with taper waist diameters of 2 and 4  $\mu\text{m}$  fabricated above.

Figure 4.18 shows a schematic diagram of the coated STNCS OFS structure. An un-tapered (125- $\mu\text{m}$ ) SNCS OFS is also coated with 0.86  $\mu\text{m}$  of MB sol-gel for comparison purposes. The SEM images of the coated fibre are depicted in Figure 4.18 (inset).

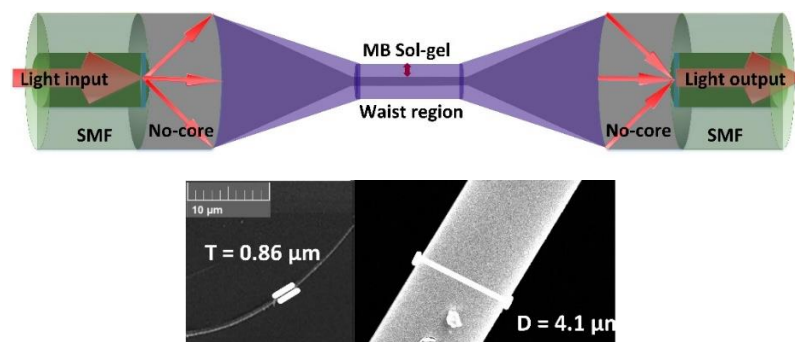


**Figure 4.18.** Schematic diagram of functionalized STNCS optical fibre sensor; Inset SEM images of coated STNCS.

### Experimental Set-up

A schematic diagram of the experimental set-up used for characterising the proposed sensing system is shown in Figure 4.19. An airtight box with a volume of 1 litre was used as a gas chamber. The gas chamber had two inlets and a single outlet to allow the flow of oxygen (test gas) and nitrogen (carrier gas) through the chamber. The concentration of oxygen in the gas chamber was controlled by changing the flow rate of oxygen using a gas flow controller. To eliminate the gas flow induced fluctuations to the OFS, the flow controller was initially switched on allowing the gas (nitrogen + oxygen mixture) to flow in the chamber for 2 minutes. Thereafter, the inlet and the outlet valves were closed to create a steady-state environment with the desired concentration of oxygen in the chamber. The measurements were taken every 1 minute for a duration of 10 minutes using an OSA. A broadband optical source with a stable output power in the NIR region of 800-1150 nm was used to launch light into the OFS. Table 4.6 summarises the parameter of STNCS OFS coated with MB sol-

gel and specifications of the components used for building the experimental setup, for oxygen sensing.

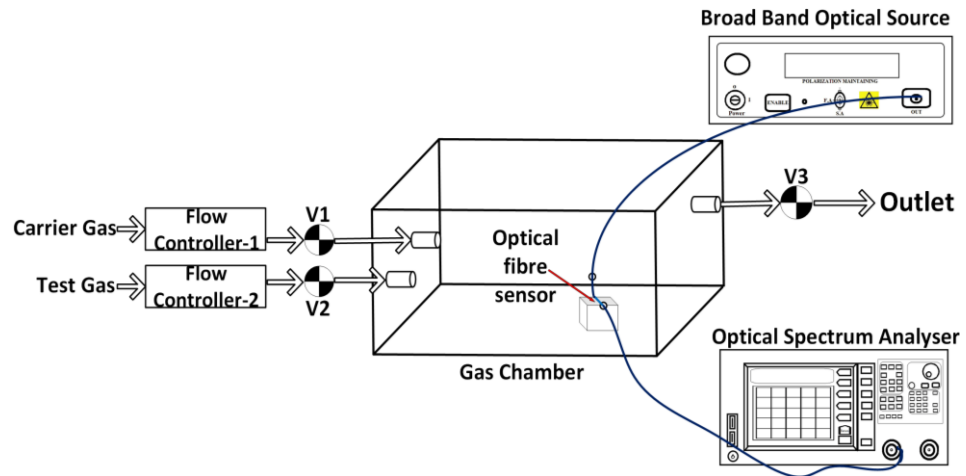


**Figure 4.19.** Schematic diagram of the experimental set-up.

**Table 4.6.** Summary of the STNCS OFS parameters coated with MB sol-gel, and specifications of components used in the experimental setup, for oxygen sensing.

	<b>Fibre Type</b>	<b>Parameter</b>
<b>Fibre Structure</b>	STNCS (POF Corporation Ltd.-NCF125)	Taper waist diameter ~ 2, 4 and 125 $\mu\text{m}$ Waist length ~ 10 mm Transition length ~ 10 mm
	SMF (Thorlabs-SMF-28)	Core diameter = 8.2 $\mu\text{m}$ Cladding diameter = 125 $\mu\text{m}$
	Methylene Blue (Sigma-Aldrich, UK)	Coating thickness ~ 0.39, 0.69, and 0.86 $\mu\text{m}$
	<b>Components</b>	<b>Specifications</b>
<b>Experimental setup</b>	Optical source (Thorlabs SLD S5FC1550S-A2)	Centre wavelength = 1550 nm Output power = 2.5 mW Bandwidth = 90 nm
	Flow controller (RS components Ltd.)	Minimum flow rate = 0.4 L/min Maximum flow rate = 5 L/min
	Optical spectrum analyzer (Yokogawa AQ6370D)	Wavelength range = 600 -1700 nm Accuracy = $\pm 0.01$ nm Resolution = 0.02 nm

#### 4.5.2 Results and discussion

The NIR spectrum (800-1150 nm) was observed for all seven fabricated sensors, and 993.5 nm was selected for the experiment because (i) MB presents better absorption at shorter wavelengths, and (ii) the available peak wavelength is around 993.5 nm, which makes it easier to monitor the intensity variation using an OSA. For the STNCS OFS with 2  $\mu\text{m}$  tapering diameter and 0.86  $\mu\text{m}$  coating thickness of MB sol-gel, a decrease in the output intensity with an increase in oxygen concentration was observed, as shown in Figure 4.20.

The oxygen concentration was increased step-wise from 0% to 37.5% of volume concentration. The OSA was programmed to automatically record the light intensity at the 935.5 nm wavelength (i.e., the peak wavelength) after every 1 minute, for the entire duration of 10 minutes (including 2 minutes of gas flow and 8 minutes of steady state analysis) for each step, as shown in Figure 4.20. The decrease in the light intensity with the increase in oxygen concentration is due to the evanescent field absorption by the MB sol-gel layer, as explained before. The spectral response of the STNCS OFS with 2  $\mu\text{m}$  taper waist diameter and 0.86  $\mu\text{m}$  coating thickness of MB sol-gel, over a wavelength range of 2 nm (a central wavelength of 993.5 nm) for the mentioned oxygen concentrations is illustrated in Figure 4.20 (a). In each step, the random intensity variation occurring in the first 2 minutes is due to the dynamic environment inside the gas chamber, as a result of gas flow. However, as can be observed, the sensor displays a stable response when the inlet and outlet valves are closed. Figure 4.20 (b) shows a maximum response time of 4 minutes for the STNCS OFS with 2  $\mu\text{m}$  taper waist diameter and 0.86  $\mu\text{m}$  coating thickness of MB sol-gel. The response time excludes the 2 minutes of dynamic state in the gas chamber while the oxygen was flowing in. A similar response time was observed for the other six sensors.

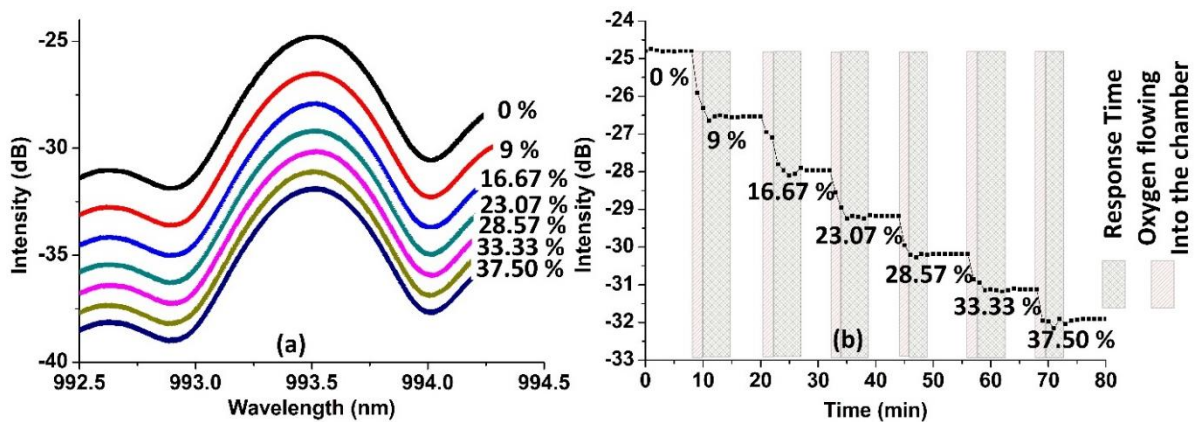


**Figure 4.20.** Intensity variations of the STNCS optical fibre sensor with 2  $\mu\text{m}$  taper waist diameter and 0.86  $\mu\text{m}$  coating thickness of MB sol-gel for different concentrations of oxygen: (a) with respect to wavelength and (b) with respect to time.

### Effect of taper waist diameter and coating thickness

Figure 4.21 shows the changes in the intensity for all seven sensor structures as a function of different oxygen concentrations (from 0% - 37.5% increase in oxygen concentration by volume). It can be observed from Figure 4.21 that all sensors display linear profiles, and that for the 0.86  $\mu\text{m}$  coating thickness of MB sol-gel coating, there is a significant improvement in oxygen sensitivity when the optical fibre sensor's diameter is reduced from 125  $\mu\text{m}$  to 2

$\mu\text{m}$ . This is because smaller tapering diameters allow more evanescent field in the taper waist region, hence increasing the absorption by the MB sol-gel layer.

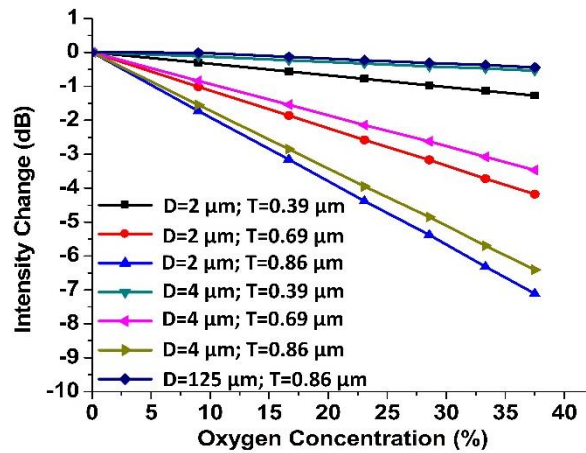


**Figure 4.21.** The change in intensity as a function of different oxygen concentrations for 2 and 4  $\mu\text{m}$  taper waist diameters of STNCS OFS, coated with 0.39, 0.69, and 0.89  $\mu\text{m}$  layer thickness of MB sol-gel; and untapered 125  $\mu\text{m}$  of SNCS optical fibre sensor coated with 0.86  $\mu\text{m}$  coating thickness of MB sol-gel.

However, the STNCS OFSs with 2 and 4  $\mu\text{m}$  taper waist diameters have similar sensitivity for the same coating thickness, thus suggesting no further improvement in oxygen sensitivity below a tapering diameter of 2  $\mu\text{m}$ . This is because the MB sol-gel attains an absorption saturation for that level of oxygen concentration. The absorption of the evanescent field also increases by increasing the number of coating layers, hence improving the oxygen sensitivity. The sensitivities for all six sensors were calculated by finding the slope of the line through linearly fitting the experimental data, and are presented in Figure 4.21. The layer thickness of the MB sol-gel was measured using SEM. The predicted values of sensitivity as a function of the coating thickness for a range of fibre sensor diameters are plotted in Figure 4.22. As shown, for the fibre sensor diameter of 2  $\mu\text{m}$ , the sensitivity linearly increases with the coating thickness, thus demonstrating the potential of the MB sol-gel coating thickness to increase the sensitivity of oxygen measurement. In the experiment, the STNCS OFS with a taper waist diameter of 2  $\mu\text{m}$  and MB sol-gel coating thickness of 0.86  $\mu\text{m}$  exhibited a maximum sensitivity of 0.189 dB/O<sub>2</sub>% within the oxygen volume concentration range of 0 - 37.5 %. The sensitivity value for all seven OFS is presented in Table 4.7, with the view to show the effect of the NCF diameter and MB sol-gel coating thickness on sensitivity.

**Table 4.7.** Experimentally measured sensitivities for all STNCS optical fibre sensors with different coating layers of MB sol-gel.

Layer thickness ( $\mu\text{m}$ )	Taper waist dia. of STNCS OFS	Sensitivity (dB / O <sub>2</sub> %)
0.86	2	0.189
0.69		0.112
0.39		0.034
0.86	4	0.171
0.69		0.092
0.39		0.014
0.86	125	0.013

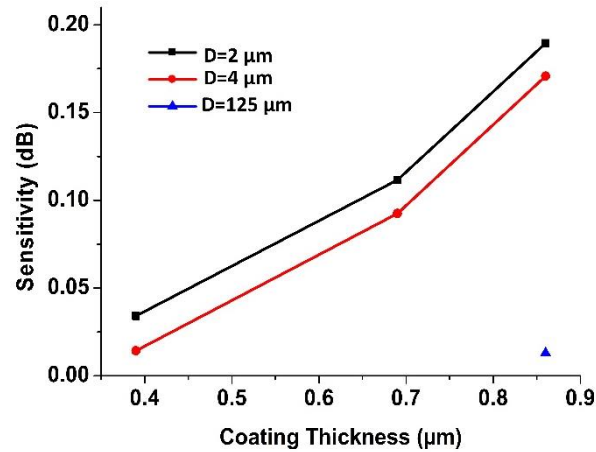


**Figure 4.22.** Effect of coating thickness and diameter of the STNCS OFS on sensitivity.

### Selectivity

The STNCS OFS with a taper waist diameter of 2  $\mu\text{m}$  and 0.86  $\mu\text{m}$  coating layer thickness of MB sol-gel was tested for its selectivity towards oxygen by introducing argon and ethanol in the gas chamber, instead of oxygen. Introducing argon and ethanol with concentration volume of 9% into the gas chamber did not introduce a significant change in intensity, as compared with the intensity change introduced by the same concentration of oxygen, as can be observed in Figure 4.23. Therefore, it can be concluded that the proposed sensor exhibits good selectivity towards oxygen.

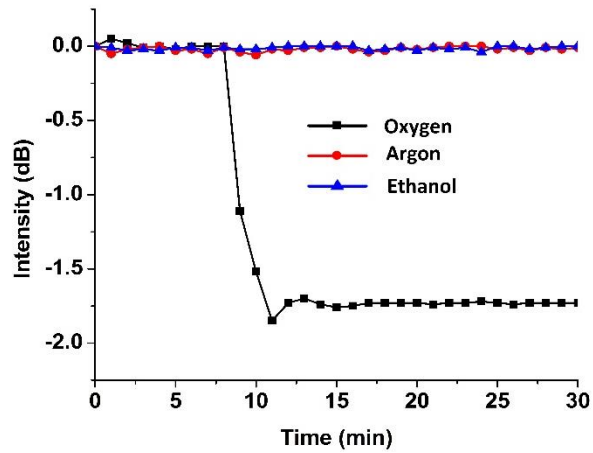


**Figure 4.23.** Selectivity test for MB-Sol gel coated STNCS optical fibre sensor with a 2  $\mu\text{m}$  taper waist diameter and a coating thickness of 0.86  $\mu\text{m}$ .

### Repeatability

The STNCS OFS with a taper waist diameter of 2  $\mu\text{m}$  and 0.86  $\mu\text{m}$  coating layer thickness of MB sol-gel was left in ambient conditions for a period of 7 days, and was tested again for the same range of oxygen concentrations. Figure 4.24 demonstrate a good repeatability for the proposed STNCS optical fibre oxygen sensor.

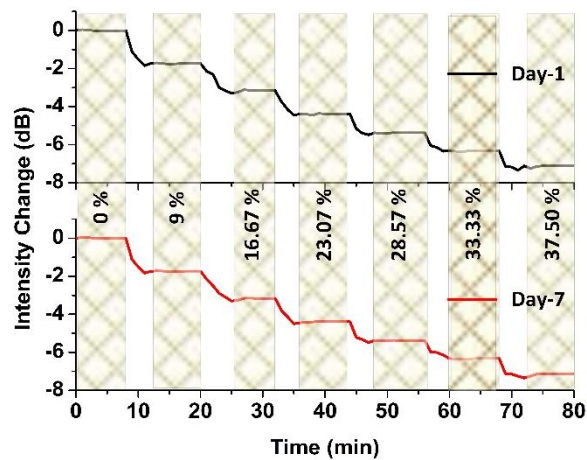


**Figure 4.24.** Repeatability test for the STNCS OFS with a 2  $\mu\text{m}$  taper waist diameter and a coating thickness of 0.86  $\mu\text{m}$ .

In conclusion, this section experimentally demonstrated a STNCS OFS functionalised with MB sol-gel for oxygen sensing. A maximum sensitivity of 0.189 dB/O<sub>2</sub>% was achieved for the STNCS with a 2  $\mu\text{m}$  diameter functionalised with 0.86  $\mu\text{m}$  layer thickness of MB sol-gel. The proposed sensor had a response time of 4 minutes in the steady-state environment with good selectivity towards oxygen, and presented repeatable results even after 7 days of fabricating the sensor. Since the proposed sensor utilises the chromogenic approach and operates in the NIR wavelength region, it is expected to encounter minimal influence from

the ambient light, and can therefore be used for applications where visible light is attenuated, such as for measuring oxygen concentrations in bio-molecules.

## 4.6 Summary

In this chapter, the principle of functionalised tapered optical microfibres was discussed, followed by an experimental demonstration of the previously proposed STNCS optical fibre sensing platform with three different coating layers on its surface. Firstly, agarose hydro-gel, which simply absorbs moisture from its surroundings to change its RI, was coated on the STNCS OFS to develop an RH sensor. Secondly, a label-free bio sensor was demonstrated for hCG detection through functionalising the STNCS OFS by immobilising anti-hCG- $\beta$  Ab as capture Ab on the fibre surface. Thirdly, MB sol-gel, which captures and interacts with the oxygen from its surrounding, was coated on the STNCS OFS to develop an oxygen sensor. This therefore demonstrated the suitability of the proposed STNCS OFS for bio and chemical sensing applications. The key accomplishments reported in this chapter can be summarised as follows.

An STNCS OFS coated with agarose hydro-gel was proposed as an RH sensor. The influence of the coating layer thickness of hydro-gel and the STNCS OFS taper waist diameter were investigated, where a maximum RH sensitivity of 0.0295 nm/%RH was achieved using an STNCS with a taper waist diameter of 4  $\mu$ m, coated with 0.198  $\mu$ m thickness of hydro-gel. This sensitivity was further enhanced by bending the taper waist region in the STNCS to form a STNCS loop with a 4.7 cm radius of curvature. The maximum linear RH sensitivity observed in this experiment was 0.04 nm/%RH over a wide linear RH range of 35 – 75 %RH for an STNCS loop with a 0.198  $\mu$ m coating layer thickness of hydro-gel. The response time for both the straight STNCS and the loop STNCS was 44 seconds. However, the recovery time was found to increase with the increase in the hydro-gel coating thickness. Therefore, the RH sensitivity increased with the coating thickness of hydro-gel layer, but with the trade-off of a longer recovery time.

A novel ultrasensitive microfibre interferometer-based biosensor was also proposed, where surface modified magnetic microspheres (MMSs) and enrichment of samples were utilised to enhance sensor's sensitivity, and hCG was used as a typical sample for the demonstration of the sensing property of the sensor. An STNCS OFS with 8  $\mu$ m taper waist diameter was used as the OFS platform. The modification of fibre surface was optimized for the proposed

sensor by immobilising 16  $\mu\text{g/mL}$  of capture Ab on the fibre sensor. This modified STNCS OFS was experimentally demonstrated to be able to detect hCG in a wide range of concentrations (0.05 – 500 mIU/mL). For the lowest concentration of 0.05 mIU/mL hCG, the sensitivity observed was 3.632 nm/mIU/mL. The LOD was improved by adding anti-hCG- $\alpha$  Ab modified nano or micro particles in the hCG samples. Furthermore, the results showed that the larger the particle size, the higher is the sensitivity of the sensor. A maximum sensitivity of 27 nm/mIU/mL was observed for 0.01mIU/mL of hCG with 1  $\mu\text{m}$  diameter MMSs. Further improvement in LOD was achieved by enriching the hCG-MMS sample by immunomagnetic separation, and a maximum sensitivity of 98 nm/mIU/mL was observed for the hCG concentration of 0.01 mIU/mL. The sensor was measured to have an LOD of 0.0001 mIU/mL using an OSA with resolution of 0.01 nm. The proposed sensor has the advantage of small size and easy operation. The ultrahigh sensitivity of the developed sensor can be utilised for detecting hCG doping in athletes and tumour diagnosis, with the inherent advantage of immunity to EM interference.

Finally, an MB sol-gel-coated STNCS OFS was proposed and experimentally investigated for oxygen sensing. The taper waist diameter of the STNCS and the coating thickness of the MB sol-gel were demonstrated to improve the absorption at 993.5 nm, hence increasing the sensor's sensitivity towards oxygen concentrations. The proposed OFS showed no significant improvement in the sensitivity by reducing the taper waist diameter below 2  $\mu\text{m}$ . However, significant improvement in the sensitivity was observed by increasing the coating layer thickness, with a maximum of 0.189 dB/O<sub>2</sub>% is achieved for a STNCS with a 2  $\mu\text{m}$  diameter and a 0.86  $\mu\text{m}$  coating thickness of MB sol-gel. The sensor was measured to have a response time of 4 minutes in the steady-state environment with good selectivity towards oxygen, and presented repeatable results even after a period of 7 days from its fabrication. In comparison with the fluorescence-based optical fibre oxygen sensors, where the optical fibre acts as a waveguide to carry the fluorescence produced by the coating material, the proposed sensor used the chromogenic approach, which is useful for the detection and quantification of oxygen in environments with minimal influence from the ambient light; more specifically, where visible light is attenuated.

In a practical system, the three sensing applications demonstrated in this chapter can be implemented at a low cost by using intensity-based analysis, as discussed in summary of Chapter 2 and 3. The cost of agarose hydro-gel (~ £40) and MB (~ £30), used as a coating material for humidity and oxygen sensing respectively, is very low. Even though, the hCG-

Abs and MMSs, used for hCG detection are relatively expensive (~ £400) but they can provide record high sensitivity. Therefore, for implementing the humidity and oxygen sensor in a practical system, the approximate cost of the system could be < £300, which can be reduced significantly on bulk production. However, for implementing STNCS OFS for bio-sensing applications, the effective cost of fabricating bio-sensor is higher (~ £800), due to the high cost of functionalising material.

## CHAPTER 5: Conclusion and Future Work

### 5.1 Introduction

This thesis is mainly focused on the research work dedicated to optical fibre sensors (OFSs) based on fibre structures with multimode interference (MMI). A traditional singlemode-multimode-singlemode (SMS) fibre structure was investigated as a simple means to introduce MMI in the fibre structure in the initial part of this thesis, and forms the base of the whole research. The SMS fibre structure was also demonstrated for several novel applications such as temperature sensing, breath state monitoring of patients and phase transition monitoring of phase change materials (PCMs). However, due to the lack of light-environment interactions in traditional SMS fibre structure, it cannot be used as bio-chemical sensor. Therefore, the latter part of this thesis is dedicated to introducing (by using no-core fibre (NCF)) and improving (by tapering the NCF) the refractive index (RI) sensitivity of the SMS based OFSs, and investigating several fibre surface functionalisation techniques for the development of high sensitivity micro/nano SMS fibre sensors for bio-chemical sensing applications.

This chapter briefly summarises the output of the research reported in this thesis and draws a few specific conclusions, before finally proposing several potential research directions, into which the current work can be extended.

### 5.2 Conclusion from the research

The primary aim of this research, as stated in Chapter 1, is to

*Develop highly sensitivity OFSs for the detection and quantification of different physical parameters and biological-chemical analytes.*

This aim has been achieved, as evidenced by the developments presented in the previous chapters, specifically:

- I. Traditional SMS fibre structure for monitoring temperature, breath state and phase transition of phase change materials (PCMs)**

In this thesis, firstly a traditional SMS fibre structure was introduced theoretically, followed by its sensing application for strain and temperature in both simulations and experiments. The summary of conclusions drawn from several novel applications such as monitoring temperature, breath state and phase transition of PCMs using SMS fibre structures is as follows:

*Modified SMS fibre sensor for highly sensitive temperature monitoring*

The traditional SMS fibre sensors have a strain sensitivity of 1.77 pm/ $\mu\epsilon$ , and a temperature sensitivity of 10 pm/ $^{\circ}\text{C}$ , which are due to the low thermo-optic coefficient of silica ( $\alpha = 1.06 \times 10^{-5} /^{\circ}\text{C}$ ). A modified SMS fibre sensor was proposed and experimentally investigated using a hollow core fibre (HCF) filled with a higher thermo-optic coefficient ( $-1.83 \times 10^{-4} /^{\circ}\text{C}$ ) Norland Adhesive (NOA-84) in the middle of the SMS fibre structure. The conclusions from this research are as follows:

- The experimental investigation showed that the HCF length had significant influence on the temperature sensitivity of the sensor, where longer HCF lengths demonstrated higher sensitivities, while the length of the MMF was found to have limited influence on the temperature sensitivity.
- The maximum temperature sensitivity demonstrated was 2.15 nm/ $^{\circ}\text{C}$  for the singlemode-multimode-HCF-multimode-singlemode (SMHMS) sensor with 20 mm length of polymer-filled HCF, which is over 200 times higher than the sensitivity of the traditional SMS fibre sensor.

*SMS fibre structure for breath state monitoring*

Since the SMS fibre structure is extremely sensitive to bend applied to the multimode fibre (MMF) section, a novel breath state sensor was demonstrated based on a bent SMS fibre structure for monitoring different breathing conditions (such as regular and irregular breathing states). The conclusions from this research are as follows:

- The proposed SMS-based breath sensor is capable of monitoring human patients' breathing states and breath rate in real time.
- The SMS based breath sensor can be used in strong electromagnetic fields and radioactive environments such as those experienced during MRI and CT examinations where traditional electronic sensors could not be utilised.

### *SMS fibre structure for phase state monitoring*

Solid-liquid PCMs have been widely used in latent heat thermal storage systems for heat pumps, solar engineering and spacecraft thermal control. A novel platinum-coated (reflective) singlemode-multimode (SM) fibre structure was proposed as an optical fibre sensor to monitor the phase transitions of PCMs. The micro-bend introduced in the MMF during the phase change of PCMs is utilised to realise this application. The conclusions from this research are as follows:

- The proposed reflective SM sensor is capable of detecting the phase change point of different PCMs, including paraffin wax and two salt hydrates (S32 and S46).
- The smaller length of MMF in the reflective SM structure was demonstrated to provide better measurement accuracy.
- The sensor has the advantage of simple fabrication and low cost, and can be embedded in thermal storage systems for phase monitoring.

## **II. Extending the application of SMS fibre sensor by introducing and improving the RI sensitivity of the fibre structure**

Sensitivity towards the surrounding RI is an important requirement for OFSs, not only for RI sensing, but also for measurements of magnetic field strength and detecting bio-chemical analytes. To achieve this objective, the following two SMS-based fibre structures were investigated to measure RI and improve RI sensitivity of the fibre structure:

### *Singlemode-no-core-singlemode (SNCS) OFS for RI sensing*

The evanescent field entrapped within the cladding layer of a traditional SMS fibre structure was released by replacing the MMF section with a single-layered NCF, which allows the light-environment interaction necessary for making the OFS sensitive towards its surrounding RI changes. This SNCS OFS was theoretically and experimentally studied for RI sensing. The conclusions from this research are as follows:

- The length of NCF was found to have no influence on the RI sensitivity; however, the RI sensitivity was shown to improve significantly by reducing the NCF diameter.
- The experimentally achieved maximum RI sensitivity was  $\sim 327$  nm/RIU for an NCF with 55  $\mu\text{m}$  diameter, which agrees well with theoretical simulations.

- As opposed to the traditional method, the proposed SNCS OFS provides easily accessible evanescent field, without the need for chemically/mechanically etching the cladding layer, which not only introduces surface roughness, (making the sensors unreliable due to the resulting unstable output response) but also degrades mechanical strength of the OFS.

#### *Singlemode-tapered no-core-singlemode (STNCS) OFS for RI sensing*

To improve RI sensitivity, the NCF section in the SNCS fibre structure was tapered using a microfibre tapering setup, established as a prerequisite for this project. The RI sensitivity of the STNCS OFS was investigated both experimentally and theoretically. The conclusions from this research are as follows:

- The experimentally observed maximum RI sensitivity of the STNCS OFS with 8  $\mu\text{m}$  taper waist diameter was 26,061.77 nm/RIU for the RI range around 1.41, which was also verified theoretically through simulations.
- This RI sensitivity is higher than the previously proposed tapered SMS-based OFSs used for bio-chemical sensing. Therefore, the STNCS OFS can be considered as a suitable sensor platform for developing bio-chemical sensors.

### **III. Tapered small-core SMF (TSCSMF) OFS for magnetic field sensing**

The use of tapered microfibres for other sensing applications such as magnetic field sensing was investigated. A high sensitivity magnetic field sensor was proposed and investigated based on a TSCSMF OFS that was encapsulated in a magnetic fluid (MF) containing ferromagnetic particles (FMPs). Depending upon the strength of magnetic field, the FMPs align themselves along the magnetic field, and around the OFS. The change in concentration of FMPs changes the RI around the OFS and serves as the basis for magnetic field sensing. The conclusions from this research are as follows:

- The magnetic sensitivity of this sensor was investigated by studying the effect of the taper waist diameter of the TSCSMF and the concentration of the MF surrounding it. The magnetic sensor demonstrated reversible results, with a maximum sensitivity of 0.46 nm/mT for a TSCSMF with 10  $\mu\text{m}$  taper waist diameter, encapsulated in 1.22% FMPs in the MF.

- The effect of magnetic field orientation along X-Y, X-Z and Y-Z axis was also investigated for the sensor, which demonstrated its capability for developing a vector magnetic field sensor.

#### **IV. Investigating various functionalising techniques for the proposed OFSs to develop a robust, highly sensitive bio-chemical sensor.**

The STNCS fibre sensor was chosen as a sensing platform for achieving the final objective of developing a highly sensitive bio-chemical sensor. Different functionalisation techniques were utilised to modify the fibre surface, and were used to develop a humidity sensor, an oxygen sensor and a bio-sensor for detecting the human chorionic gonadotropin (hCG) hormone. This objective was realised as follows:

##### *STNCS OFS functionalised with agarose hydro-gel for humidity sensing*

An STNCS OFS coated with agarose hydro-gel, which changes its RI by absorbing moisture from its surrounding was proposed for relative humidity (RH) sensing. The influence of the hydro-gel coating layer thickness and the STNCS OFS taper waist diameter on sensitivity were investigated, and the conclusions from this research are as follows:

- A maximum RH sensitivity of 0.0295 nm/%RH was achieved within the linear sensing range of 35 – 75 %RH using an STNCS with a taper waist diameter of 4  $\mu\text{m}$ , coated with the hydro-gel of 0.198  $\mu\text{m}$  thickness.
- This sensitivity was further enhanced by bending the taper waist region in the STNCS to form a STNCS loop with a 4.7 cm radius of curvature.
- The maximum linear RH sensitivity observed for the STNCS loop was 0.04 nm/%RH over a wide linear RH range of 35 – 75 %RH.
- The response time for both the straight STNCS and the loop STNCS was 44 seconds. However, the recovery time was found to increase with the increase in the hydro-gel coating thickness. Therefore, the RH sensitivity increased with the coating thickness of the hydro-gel layer, but with the trade-off of increased recovery time.

##### *STNCS OFS functionalised with anti-hCG- $\beta$ antibody (Ab) for hCG detection*

A novel ultrasensitive STNCS OFS was proposed for hCG detection by immobilising 16  $\mu\text{g/mL}$  of anti-hCG- $\beta$  as capture Ab on the fibre sensor. The conclusions from this research are:

- The modified STNCS OFS was experimentally demonstrated to be able to detect hCG in a wide range of concentrations (0.05 – 500 mIU/mL). For the lowest concentration of 0.05 mIU/mL hCG, the sensitivity observed was 3.632 nm/mIU/mL.
- The sensitivity was improved by adding anti-hCG- $\alpha$  Ab modified magnetic microspheres (MMSs) in the hCG samples. The results showed that the larger the particle size, the higher the sensitivity achieved. A maximum sensitivity of 27 nm/mIU/mL was observed for 0.01mIU/mL of hCG with 1  $\mu$ m diameter MMSs.
- Further improvement in the sensitivity was achieved by enriching the hCG-MMS samples by immunomagnetic separation, and a maximum sensitivity of 98 nm/mIU/mL was observed for an hCG concentration of 0.01 mIU/mL.
- The sensor was measured to have a limit of detection (LOD) of 0.0001 mIU/mL using an OSA with a resolution of 0.01 nm.
- The proposed sensor has the advantage of small size and easy operation. The ultrahigh sensitivity of the developed sensor can be utilised for detecting hCG doping in athletes and tumour diagnosis, with the inherent advantage of immunity to EMI.

*STNCS OFS functionalised with methylene blue entrapped in sol-gel matrix (MB sol-gel) for oxygen sensing*

Finally, an MB sol-gel-coated STNCS OFS was proposed and experimentally investigated for oxygen sensing. The taper waist diameter of the STNCS and the coating thickness of the MB sol-gel were investigated for increasing the sensor's sensitivity towards oxygen concentrations. The conclusion from this research are as follows:

- The proposed OFS showed no significant improvement in the sensitivity by reducing the taper waist diameter below 2  $\mu$ m. However, significant improvement in the sensitivity was observed by increasing the coating layer thickness.
- A maximum sensitivity of 0.189 dB/O<sub>2</sub>% was experimentally achieved for an STNCS with a 2  $\mu$ m diameter and a 0.86  $\mu$ m MB sol-gel coating thickness.
- The sensor exhibited a response time of 4 minutes in the steady-state environment with good selectivity towards oxygen, and presented repeatable results even after a period of 7 days from its fabrication.
- In comparison with the fluorescence-based optical fibre oxygen sensors, the proposed sensor used the chromogenic approach, which is useful for the detection

and quantification of oxygen in environments with minimal influence from ambient light; more specifically, where visible light is attenuated.

### **5.3 Future Work**

In the future, there remains a number of challenges and research topics that could be extended further beyond the research presented in this thesis.

- **Extending the potential application of the proposed STNCS fibre sensor**

The no-core fibre used in this work (NCF-125, POFC) was observed, while tapering it, to achieve its viscoelastic state at a temperature higher than other types of MMFs. Therefore, the proposed STNCS OFS, along with exhibiting a high RI sensitivity (as demonstrated in Chapter 3), is expected to have a better mechanical strength than other tapered microfibre structures, which should be investigated in the future and is demanded for real life scenarios. Furthermore, while the proposed STNCS fibre sensor has already been demonstrated for hormone detection in Chapter 4, its utilisation should be extended in the future to demonstrate detecting much smaller biological analytes such as DNA. Furthermore, the use of MMSs as a non-fluorescent label to amplify the sensors' response towards smaller biological analytes should be used to extend the application of STNCS and other OFS operating on similar principle, for bio-chemical sensing with ultra-high sensitivity.

Coating materials are essential in the field of optical fibre-based bio-chemical sensing. In Chapter 4, an MB sol-gel-coated STNCS OFS was demonstrated with high sensitivity and good selectivity towards oxygen compared to other gases. However, with proper selection of a sensitive material and appropriate functionalisation techniques, the sol-gel coating can be made sensitive to other gases such as volatile organic compounds (VOCs). Utilising such modified sol-gel in conjunction with a highly sensitive OFS structure, can be used for developing portable and real-time devices for VOC detection and other greenhouse gases, which is currently the need of the hour.

- **New microfibre packaging techniques**

Small-diameter tapered optical microfibres are mechanically weak and are easily contaminated. Therefore, microfibre-based devices require a robust fibre packaging technique to ensure and maintain the function of the devices during experiments as well as over time, with easy ingress and egress of the target analyte. In this thesis, two microfibre

packaging techniques were explored, namely encapsulating the tapered fibre in capillary tubes for magnetic sensing (which is practically challenging), and using open micro-channels for bio-sensing (which requires larger analyte volume).

With the advancement in micro-channel fabrication techniques utilising laser beams, and 3D printing, more robust and custom-fit micro-channels can be fabricated, which not only serve to protect the tapered fibre sensor, but also could efficiently reduce the analyte volume and provide easy ingress and egress of the desired analyte. Therefore, designing efficient micro-channels and appropriate microfibre packaging techniques is needed to make the fibre sensing technology robust enough for real-world applications.

- **Bio and chemical sensing using other optical fibre structures**

An optical microfibre coupler (OMFC) consists of two identical microfibres with the entire taper waist region and part of the transition regions fused together. This OFS structure utilises the phase sensitivity approach, which involves the mode interference within a microfibre (or the light intercoupling between adjacent microfibres), and has been demonstrated with a sensitivity as high as 4,155 nm/RIU in the RI range from 1.3340 – 1.3515 [190]. In addition, light coupling between an un-tapered SMS fibre structure and a long period fibre grating [191], and between two parallel close-contact SMS fibre structures [192] has been demonstrated with a coupling efficiency of 1.66% and 5.9%, respectively. Therefore, an SMS microfibre coupler, where the MMF section of the two SMS fibre are fused together has the potential for developing highly sensitive fibre structures.

Another, suitable OFS for future application is an HCF based fibre structure, which offers a high quality (Q) factor and large extinction ratio [193]. Moreover, in comparison with tapered fibre structures, it has the advantages of a simple configuration, ease of fabrication, low cost, and a comparable (or even better) Q factor. To date, there has been a lack of in-depth investigations of an HCF-based fibre structure and its potential applications. There is thus a necessity to carry out further research on the modification and functionalisation of an HCF-based structure, for example, by functionalising its surface with different coating materials on the inner/outer surface of the HCF. Such future research could provide new directions for the development of novel cost effective, high performance photonics components, which will be beneficial to the wider research community in the fields of optical fibre communication components and sensors.

## References

- [1] K. Kao and G. A. Hockham, "Dielectric-fibre surface waveguides for optical frequencies," *Proceedings of the Institution of Electrical Engineers*, vol. 113, no. 7, pp. 1151-1158, 1966.
- [2] B. Culshaw, D. Davies, and S. Kingsley, "Acoustic sensitivity of optical-fibre waveguides," *Electronics Letters*, 1977, vol. 13, no. 25, pp. 760-761.
- [3] C. D. Butter and G. Hocker, "Fiber optics strain gauge," *Applied Optics*, vol. 17, no. 18, pp. 2867-2869, 1978.
- [4] G. Rajan, "Optical fiber sensors: advanced techniques and applications," London, CRC press, 2015, pp.1-37.
- [5] C. D. Kissinger, "Fiber optic proximity probe," US patent 3327584A, 1967.
- [6] D. Davies and S. Kingsley, "Method of phase-modulating signals in optical fibres: application to optical-telemetry systems," *Electronics Letters*, vol. 10, no. 2, pp. 21-22, 1974.
- [7] J. W. Berthold, "Historical review of microbend fiber-optic sensors," *Journal of Lightwave Technology*, vol. 13, no. 7, pp. 1193-1199, 1995.
- [8] G. Rajan, "A macro-bend fiber based wavelength demodulation system for optical fiber sensing applications," PhD, School of Electrical and Electronics Engineering, Dublin Institute of Technology, pp. 17-23, 2008.
- [9] P. Wang, G. Brambilla, Y. Semenova, *et al.*, "A simple ultrasensitive displacement sensor based on a high bend loss single-mode fibre and a ratiometric measurement system," *Journal of Optics*, vol. 13, no. 7, pp. 075402, 2011.
- [10] Y. Gong, T. Zhao, Y. Rao, *et al.*, "All-fiber curvature sensor based on multimode interference," *IEEE Photonics Technology Letters*, vol. 23, no. 11, pp. 679-681, 2011.
- [11] R. Wang, J. Zhang, Y. Weng *et al.*, "Highly sensitive curvature sensor using an in-fiber Mach-Zehnder interferometer," *IEEE Sensors Journal*, vol. 13, no. 5, pp. 1766-1770, 2013.
- [12] X. Wang, D. Chen, H. Li, *et al.*, "In-line Mach-Zehnder interferometric sensor based on a seven-core optical fiber," *IEEE Sensors Journal*, vol. 17, no. 1, pp. 100-104, 2017.
- [13] Y. Yu, Z. Zhao, Z. Zhuo, *et al.*, "Bend sensor using an embedded etched fiber Bragg grating," *Microwave and Optical Technology Letters*, vol. 43, no. 5, pp. 414-417, 2004.
- [14] Y. Li, W. Zhang, S. Wang *et al.*, "Bending vector sensor based on a pair of opposite tilted long-period fiber gratings," *IEEE Photonic Technology Letter*, vol. 29, no. 2, pp. 224-227, 2017.
- [15] C. R. Pollock, "Fundamentals of optoelectronics," Chicago, McGraw Hill, 1995.
- [16] F. Jun, Z. Sen, G. Liu, *et al.*, "D-shaped plastic optical fiber sensor for testing refractive index," *IEEE Sensors Journal*, vol. 14, no. 5, pp. 1673-1676, 2014.
- [17] C. Teng, F. Yu, N. Jing, *et al.*, "Investigation of refractive index sensors based on side-polished plastic optical fibers," *Optical Fiber Technology*, vol. 36, pp. 1-5, 2017.
- [18] J. Tang, J. Zhou, J. Guan *et al.*, "Fabrication of side-polished single mode-multimode-single mode fiber and its characteristics of refractive index sensing," *IEEE Journal of Selected Topics in Quantum Electronics*, vol. 23, no. 2, pp. 238-245, 2017.
- [19] J. Senosiain, I. Díaz, A. Gastón, *et al.*, "High sensitivity temperature sensor based on side-polished optical fiber," *IEEE Transactions on Instrumentation and Measurement*, vol. 50, no. 6, pp. 1656-1660, 2001.
- [20] K. Schroeder, W. Ecke, R. Mueller, *et al.*, "A fibre Bragg grating refractometer," *Measurement Science and Technology*, vol. 12, no. 7, pp. 757, 2001.
- [21] H. Jang, K. Park, J. Kim *et al.*, "Sensitive DNA biosensor based on a long-period grating formed on the side-polished fiber surface," *Optics Express*, vol. 17, no. 5, pp. 3855-3860, 2009.
- [22] A. Khalaf, F. Mohamad, N. Rahman *et al.*, "Room temperature ammonia sensor using side-polished optical fiber coated with graphene/polyaniline nanocomposite," *Optical Materials Express*, vol. 7, no. 6, pp. 1858-1870, 2017.

- [23] T. Birks and Y. Li, "The shape of fiber tapers," *Journal of Lightwave Technology*, vol. 10, no. 4, pp. 432-438, 1992.
- [24] G. Chen, M. Ding, T. Newson, *et al.*, "A review of microfiber and nanofiber based optical sensors," *The Open Optics Journal*, Vol. 7, pp.32-57, 2013.
- [25] T. Yadav, R. Narayanaswamy, M. Bakar, *et al.*, "Single mode tapered fiber-optic interferometer based refractive index sensor and its application to protein sensing," *Optics Express*, vol. 22, no. 19, pp. 22802-22807, 2014.
- [26] C. Bariain, I. Matias, F. Arregui, *et al.*, "Tapered optical-fiber-based pressure sensor," *Optical Engineering*, vol. 39, no. 8, pp. 2241-2248, 2000.
- [27] P. Wang, G. Brambilla, M. Ding, *et al.*, "High-sensitivity, evanescent field refractometric sensor based on a tapered, multimode fiber interference," *Optics Letters*, vol. 36, no. 12, pp. 2233-2235, 2011.
- [28] K. Li, T. Zhang, G. Liu, *et al.*, "Ultrasensitive optical microfiber coupler based sensors operating near the turning point of effective group index difference," *Applied Physics Letters*, vol. 109, no. 10, pp. 101101, 2016.
- [29] Y. Chunxia, D. Hui, D. Wei, *et al.*, "Weakly-coupled multicore optical fiber taper-based high-temperature sensor," *Sensors and Actuators A: Physical*, vol. 280, pp. 139-144, 2018.
- [30] T. Wieduwilt, S. Brückner, and H. Bartelt, "High force measurement sensitivity with fiber Bragg gratings fabricated in uniform-waist fiber tapers," *Measurement Science and Technology*, vol. 22, no. 7, p. 075201, 2011.
- [31] C. Wu, H. Fu, K. Qureshi, *et al.*, "High-pressure and high-temperature characteristics of a Fabry–Perot interferometer based on photonic crystal fiber," *Optics Letters*, vol. 36, no. 3, pp. 412-414, 2011.
- [32] J. Zhang, H. Liao, P. Lu *et al.*, "Ultrasensitive Temperature Sensor With Cascaded Fiber Optic Fabry–Perot Interferometers Based on Vernier Effect," *IEEE Photonics Journal*, vol. 10, no. 5, pp. 1-11, 2018.
- [33] S. Tripathi, A. Kumar, R. Varshney, *et al.*, "Strain and temperature sensing characteristics of single-mode–multimode–single-mode structures," *Journal of Lightwave Technology*, vol. 27, no. 13, pp. 2348-2356, 2009.
- [34] Q. Wu, Y. Semenova, J. Mathew, *et al.*, "Humidity sensor based on a single-mode hetero-core fiber structure," *Optics Letters*, vol. 36, no. 10, pp. 1752-1754, 2011.
- [35] D. Wu, T. Zhu, D. Duan *et al.*, "Refractive index sensing based on Mach–Zehnder interferometer formed by three cascaded single-mode fiber tapers," *Applied Optics*, vol. 50, no. 11, pp. 1548-1553, 2011.
- [36] J. Mathew, Y. Semenova, G. Rajan, *et al.*, "Humidity sensor based on photonic crystal fibre interferometer," *Electronics Letters*, vol. 46, no. 19, pp. 1341-1343, 2010.
- [37] S. Novais, C. Ferreira, M. Ferreira, *et al.*, "Optical fiber tip sensor for the measurement of glucose aqueous solutions," *IEEE Photonics Journal*, vol. 10, no. 5, pp. 1-9, 2018.
- [38] B. Wang, K. Ni, P. Wang, *et al.*, "A CNT-coated refractive index sensor based on Michelson interferometer with thin-core fiber," *Optical Fiber Technology*, vol. 46, pp. 302-305, 2018.
- [39] H. Fu, H. Tam, L. Shao *et al.*, "Pressure sensor realized with polarization-maintaining photonic crystal fiber-based Sagnac interferometer," *Applied Optics*, vol. 47, no. 15, pp. 2835-2839, 2008.
- [40] S. Pu, L. Luo, J. Tang, *et al.*, "Ultrasensitive refractive-index sensors based on tapered fiber coupler with Sagnac loop," *IEEE Photonics Technology Letters*, vol. 28, no. 10, pp. 1073-1076, 2016.
- [41] K. Naeem, B. Kim, B. Kim, *et al.*, "Simultaneous multi-parameter measurement using Sagnac loop hybrid interferometer based on a highly birefringent photonic crystal fiber with two asymmetric cores," *Optics Express*, vol. 23, no. 3, pp. 3589-3601, 2015.
- [42] F. Wei, A. Mallik, D. Liu, *et al.*, "Magnetic field sensor based on a combination of a microfiber coupler covered with magnetic fluid and a Sagnac loop," *Scientific Reports*, vol. 7, no. 1, pp. 4725, 2017.

- [43] Y. Rao, Z. Ran, and R. Chen, "Long-distance fiber Bragg grating sensor system with a high optical signal-to-noise ratio based on a tunable fiber ring laser configuration," *Optics Letters*, vol. 31, no. 18, pp. 2684-2686, 2006.
- [44] B. Guan, H. Tam, S. Ho, *et al.*, "Simultaneous strain and temperature measurement using a single fibre Bragg grating," *Electronics Letters*, vol. 36, no. 12, pp. 1018-1019, 2000.
- [45] M. Liang, X. Fang, G. Wu, *et al.*, "A fiber Bragg grating pressure sensor with temperature compensation based on diaphragm-cantilever structure," *Optik-International Journal for Light and Electron Optics*, vol. 145, pp. 503-512, 2017.
- [46] D. Tosi, M. Olivero, and G. Perrone, "Low-cost fiber Bragg grating vibroacoustic sensor for voice and heartbeat detection," *Applied Optics*, vol. 47, no. 28, pp. 5123-5129, 2008.
- [47] L. Mohanty, L. Koh, and S. C. Tjin, "Fiber Bragg grating microphone system," *Applied Physics Letters*, vol. 89, no. 16, pp. 161109, 2006.
- [48] X. Shu, T. Allsop, B. Gwandu, *et al.*, "High-temperature sensitivity of long-period gratings in B-Ge codoped fiber," *IEEE Photonics Technology Letters*, vol. 13, no. 8, pp. 818-820, 2001.
- [49] V. Bhatia, D. Campbell, D. Sherr *et al.*, "Temperature-insensitive and strain-insensitive long-period grating sensors for smart structures," *Optical Engineering*, vol. 36, no. 7, pp. 1872-1877, 1997.
- [50] J. Jang, S. Kim, S. Kim, *et al.*, "Temperature insensitive long-period fibre gratings," *Electronics Letters*, vol. 35, no. 24, pp. 2134-2136, 1999.
- [51] S. Khaliq, S. James, and R. Tatam, "Enhanced sensitivity fibre optic long period grating temperature sensor," *Measurement Science and Technology*, vol. 13, no. 5, pp. 792, 2002.
- [52] X. Pham, J. Si, T. Chen *et al.*, "Demodulation method for tilted fiber Bragg grating refractometer with high sensitivity," *Journal of Applied Physics*, vol. 123, no. 17, pp. 174501, 2018.
- [53] E. Chehura, S. James, and R. Tatam, "Temperature and strain discrimination using a single tilted fibre Bragg grating," *Optics Communications*, vol. 275, no. 2, pp. 344-347, 2007.
- [54] K. Grattan, R. Selli, and A. Palmer, "A Miniaturized Fluorescence Referenced Glass Absorption Thermometer," in *Optical Fiber Sensors Conference*, Tokyo, pp 12, 1986.
- [55] Z. Hale and F. Payne, "Fluorescent sensors based on tapered single-mode optical fibres," *Sensors and Actuators B: Chemical*, vol. 17, no. 3, pp. 233-240, 1994.
- [56] M. Zolkapi, S. Saharudin, S. Herman, *et al.*, "The influence of sol-gel coated length and withdrawal rate on plastic optical fiber core towards oxygen gas sensing sensitivity," *Jurnal Teknologi (Science & Engineering)*, vol. 3, pp. 87-91, 2015.
- [57] L. Mao, R. Yuan, Y. Chai, *et al.*, "A new electrochemiluminescence immunosensor based on Ru (bpy) 3<sup>2+</sup>-doped TiO<sub>2</sub> nanoparticles labeling for ultrasensitive detection of human chorionic gonadotrophin," *Sensors and Actuators B: Chemical*, vol. 149, no. 1, pp. 226-232, 2010.
- [58] T. Woliński, P. Lesiak, and A. Domański, "Polarimetric optical fiber sensors of a new generation for industrial applications," *Bulletin of the Polish Academy of Sciences, Technical Sciences*, vol. 56, no. 2, 2008.
- [59] J. Ma and A. Asundi, "Structural health monitoring using a fiber optic polarimetric sensor and a fiber optic curvature sensor-static and dynamic test," *Smart Materials and Structures*, vol. 10, no. 2, pp. 181, 2001.
- [60] M. Ramakrishnan, G. Rajan, Y. Semenova *et al.*, "Measurement of thermal elongation induced strain of a composite material using a polarization maintaining photonic crystal fiber sensor," *Sensors and Actuators A: Physical*, vol. 190, pp. 44-51, 2013.
- [61] S. Choi, S. Lee, J. Kim, *et al.*, "High Sensitivity Polarimetric Optical Fiber Pressure Sensor Based on Tapered Polarization-Maintaining and Fiber Bragg Grating," *Journal of Nanoscience and Nanotechnology*, vol. 19, no. 3, pp. 1403-1409, 2019.
- [62] K. Kihm, S. Cheon, J Park *et al.*, "Surface plasmon resonance (SPR) reflectance imaging: Far-field recognition of near-field phenomena," *Optics and Lasers in Engineering*, vol. 50, no. 1, pp. 64-73, 2012.

- [63] H. Lin, C. Huang, G. Cheng, *et al.*, "Tapered optical fiber sensor based on localized surface plasmon resonance," *Optics Express*, vol. 20, no. 19, pp. 21693-21701, 2012.
- [64] P. Arasu, A. Noor, A. Shabaneh, *et al.*, "Fiber Bragg grating assisted surface plasmon resonance sensor with graphene oxide sensing layer," *Optics Communications*, vol. 380, pp. 260-266, 2016.
- [65] K. Gasior, T. Martynkien, M. Napiorkowski, *et al.*, "A surface plasmon resonance sensor based on a single mode D-shape polymer optical fiber," *Journal of Optics*, vol. 19, no. 2, pp. 025001, 2016.
- [66] M. Ding, P. Wang, J. Wang, *et al.*, "A fiber tip refractive index sensor using FIB-milled gold-coated singlemode-multimode-singlemode structure," in *23rd International Conference on Optical Fibre Sensors, Spain*, vol. 9157, pp. 91578, 2014.
- [67] Y. Liu, X. Liu, C. Ma, *et al.*, "Micro-structured optical fiber sensor for simultaneous measurement of temperature and refractive index," *Optical Fiber Technology*, vol. 41, pp. 168-172, 2018.
- [68] Z. M. Research, "IoT Sensors Market Expected to Reach US \$27.38 billion by 2022, Globally:ZMR," 2018. [Online]. Available: <https://www.globenewswire.com/news-release/2018/08/25/1556631/0/en/IoT-Sensors-Market-Expected-to-Rreach-US-27-38-billion-by-2022-Globally-ZMR.html>. [Accessed: 29-Jan-2019]
- [69] A. Gassar and G. Yun, "Energy Saving Potential of PCMs in Buildings under Future Climate Conditions," *Applied Sciences*, vol. 7, no. 12, pp. 1219, 2017.
- [70] S. Grant and R. Glass, "A sol-gel based fiber optic sensor for local blood pH measurements," *Sensors and Actuators B: Chemical*, vol. 45, no. 1, pp. 35-42, 1997.
- [71] N. Nath, S. Jain, and S. Anand, "Evanescent wave fibre optic sensor for detection of L. donovani specific antibodies in sera of kala azar patients," *Biosensors and Bioelectronics*, vol. 12, no. 6, pp. 491-498, 1997.
- [72] L. Cao, G. Anderson, F. Ligler, *et al.*, "Detection of Yersinia pestis fraction 1 antigen with a fiber optic biosensor," *Journal of Clinical Microbiology*, vol. 33, no. 2, pp. 336-341, 1995.
- [73] NHS, "Failing to turn up for an appointment –don't be a DNA," 2017. [Online]. Available:<https://www.nhs.uk/Services/UserControls/UploadHandlers/MediaServerHandler.ashx?id=10646&t=636513194757088699>. [Accessed: 29- Jan- 2019].
- [74] Q. Wang, G. Farrell, and W. Yan, "Investigation on single-mode-multimode-single-mode fiber structure," *Journal of Lightwave Technology*, vol. 26, no. 5, pp. 512-519, 2008.
- [75] P. Wang, G. Brambilla, M. Ding, *et al.*, "Investigation of single-mode-multimode-single-mode and single-mode-tapered-multimode-single-mode fiber structures and their application for refractive index sensing," *Journal of Optical Society of America B*, vol. 28, no. 5, pp. 1180-1186, 2011.
- [76] Q. Wang, C. Du, J. Zhang, *et al.*, "Sensitivity-enhanced temperature sensor based on PDMS-coated long period fiber grating," *Optics Communications*, vol. 377, pp. 89-93, 2016.
- [77] Y. Dong, G. Ren, H. Xiao *et al.*, "Simultaneous Temperature and Strain Sensing Based on M-Shaped Single Mode Fiber," *IEEE Photonics Technology Letters*, vol. 29, no. 22, pp. 1955-1958, 2017.
- [78] W. Hua, Y. Jie, and W. Jing, "D-shaped photonic crystal fiber refractive index and temperature sensor based on surface plasmon resonance and directional coupling," *Acta Physica Sinica*, vol. 64, no. 22, pp. 224221, 2015.
- [79] C. Park, K. Joo, S. Kang, *et al.*, "A PDMS-coated optical fiber Bragg grating sensor for enhancing temperature sensitivity," *Journal of the Optical Society of Korea*, vol. 15, no. 4, pp. 329-334, 2011.
- [80] K. Sohn and G. Peng, "Mechanically formed loss-tunable long-period fiber gratings realized on the periodic arrayed metal wires," *Optics Communications*, vol. 278, no. 1, pp. 77-80, 2007.
- [81] D. Barrera, J. Hervás, I. Gasulla, *et al.*, "Enhanced accuracy sensors using multicore optical fibres based on RFBGs for temperatures up to 1000° C," in *Sixth European Workshop on Optical Fibre Sensors, Ireland*, vol. 9916, pp. 99161J, 2016.

- [82] S. Braun, "Respiratory rate and pattern - Clinical Methods: The History, Physical, and Laboratory Examinations". 3rd edition: Butterworths, pp. 226-230, 1990.
- [83] F. AL-Khalidi, R. Saatchi, D. Burke, *et al.*, "Respiration rate monitoring methods: A review," *Pediatric Pulmonology*, vol. 46, no. 6, pp. 523-529, 2011.
- [84] M. Dempsey and B. Condon, "Thermal injuries associated with MRI," *Clinical Radiology*, vol. 56, no. 6, pp. 457-465, 2001.
- [85] L. Dziuda, F. Skibniewski, M. Krej, *et al.*, "Monitoring respiration and cardiac activity using fiber Bragg grating-based sensor," *IEEE Transactions on Biomedical Engineering*, vol. 59, no. 7, pp. 1934-1942, 2012.
- [86] R. Schermer and J. Cole, "Improved bend loss formula verified for optical fiber by simulation and experiment," *IEEE Journal of Quantum Electronics*, vol. 43, no. 10, pp. 899-909, 2007.
- [87] J. Lizana, R. Chacartegui, A. Barrios-Padura, *et al.*, "Advanced low-carbon energy measures based on thermal energy storage in buildings: A review," *Renewable and Sustainable Energy Reviews*, vol. 82, pp. 3705-3749, 2018.
- [88] N. Zhu, P. Hu, L. Xu, *et al.*, "Recent research and applications of ground source heat pump integrated with thermal energy storage systems: A review," *Applied Thermal Engineering*, vol. 71, no. 1, pp. 142-151, 2014.
- [89] M. Islam and T. Morimoto, "Advances in low to medium temperature non-concentrating solar thermal technology," *Renewable and Sustainable Energy Reviews*, vol. 82, pp. 2066-2093, 2018.
- [90] C. Underwood, T. Shepherd, S. Bull, *et al.*, "Hybrid thermal storage using coil-encapsulated phase change materials," *Energy and Buildings*, vol. 159, pp. 357-369, 2018.
- [91] A. Arshad, H. Ali, S. Khushnood, *et al.*, "Experimental investigation of PCM based round pin-fin heat sinks for thermal management of electronics: effect of pin-fin diameter," *International Journal of Heat and Mass Transfer*, vol. 117, pp. 861-872, 2018.
- [92] S. Kumar, K. Agrawal, H. Khan, *et al.*, "Study of phase transition in hard microcrystalline waxes and wax blends by differential scanning calorimetry," *Petroleum Science and Technology*, vol. 22, no. 3-4, pp. 337-345, 2004.
- [93] G. Delgado, N. Sierralta, M. Quintero, *et al.*, "Synthesis, structural characterization and differential thermal analysis of the quaternary compound Ag<sub>2</sub>MnSnS<sub>4</sub>," *Revista Mexicana de Física*, vol. 64, no. 3, pp. 216-221, 2018.
- [94] Q. Wu, Y. Semenova, A. Hatta, *et al.*, "Bent SMS fibre structure for temperature measurement," *Electronics Letters*, vol. 46, no. 16, pp. 1129-1130, 2010.
- [95] F. Trausel, A. De Jong, and R. Cuyppers, "A review on the properties of salt hydrates for thermochemical storage," *Energy Procedia*, vol. 48, pp. 447-452, 2014.
- [96] L. Huang, G. Lin, M. Fu, *et al.*, "A refractive-index fiber sensor by using no-core fibers," in *IEEE International Symposium on Next-Generation Electronics (ISNE)*, Taiwan, pp. 100-102, 2013.
- [97] H. Fukano, T. Aiga, and S. Taue, "High-sensitivity fiber-optic refractive index sensor based on multimode interference using small-core single-mode fiber for biosensing," *Japanese Journal of Applied Physics*, vol. 53, no. 4S, pp. 04EL08, 2014.
- [98] L. Xia, L. Li, W. Li, *et al.*, "Novel optical fiber humidity sensor based on a no-core fiber structure," *Sensors and Actuators A: Physical*, vol. 190, pp. 1-5, 2013.
- [99] L. Ma, Z. Kang, Y. Qi, *et al.*, "Fiber-optic temperature sensor based on a thinner no-core fiber," *Optik-International Journal for Light and Electron Optics*, vol. 126, no. 9-10, pp. 1044-1046, 2015.
- [100] Y. Qi, L. Ma, Z. Kang, *et al.*, "Highly sensitive curvature sensor based on a multicladding fiber sandwiched dual no-core fibers structure," *Applied Optics*, vol. 53, no. 28, pp. 6382-6388, 2014.
- [101] Q. Wu, Y. Semenova, P. Wang, *et al.*, "A comprehensive analysis verified by experiment of a refractometer based on an SMF28–small-core singlemode fiber (SCSMF)–SMF28 fiber structure," *Journal of Optics*, vol. 13, no. 12, pp. 125401, 2011.
- [102] J. Knight, T. Birks, P. Russell, *et al.*, "All-silica single-mode optical fiber with photonic crystal cladding," *Optics Letters*, vol. 21, no. 19, pp. 1547-1549, 1996.

- [103] J. Wang and J. Tang, "Photonic crystal fiber Mach-Zehnder interferometer for refractive index sensing," *Sensors*, vol. 12, no. 3, pp. 2983-2995, 2012.
- [104] Q. Wang, L. Kong, Y. Dang *et al.*, "High sensitivity refractive index sensor based on splicing points tapered SMF-PCF-SMF structure Mach-Zehnder mode interferometer," *Sensors and Actuators B: Chemical*, vol. 225, pp. 213-220, 2016.
- [105] C. Zhang, T. Ning, J. Li, *et al.*, "Refractive index and strain sensor based on twin-core fiber with a novel T-shaped taper," *Optics & Laser Technology*, vol. 102, pp. 12-16, 2018.
- [106] N. Liu, M. Hu, H. Sun *et al.*, "A fiber-optic refractometer for humidity measurements using an in-fiber Mach-Zehnder interferometer," *Optics Communications*, vol. 367, pp. 1-5, 2016.
- [107] M. Frawley, A. Petcu-Colan, V. G. Truong, *et al.*, "Higher order mode propagation in an optical nanofiber," *Optics Communications*, vol. 285, no. 23, pp. 4648-4654, 2012.
- [108] L. Bo, "Tapered Optical Microfibre Based Structures for Sensing Applications," PhD, School of Electronics and Communication Engineering, Dublin Institute of Technology, pp. 8-29, 2015.
- [109] A. Snyder, "Coupling of modes on a tapered dielectric cylinder," *IEEE Transactions on Microwave Theory and Techniques*, vol. 18, no. 7, pp. 383-392, 1970.
- [110] S. Lacroix, F. Gonthier, and J. Bures, "All-fiber wavelength filter from successive biconical tapers," *Optics Letters*, vol. 11, no. 10, pp. 671-673, 1986.
- [111] H. MacKenzie and F. Payne, "Evanescent field amplification in a tapered single-mode optical fibre," *Electronics Letters*, vol. 26, no. 2, pp. 130-132, 1990.
- [112] T. Birks, W. Wadsworth, and P. S. J. Russell, "Supercontinuum generation in tapered fibers," *Optics Letters*, vol. 25, no. 19, pp. 1415-1417, 2000.
- [113] Z. Hale and F. Payne, "Demonstration of an optimised evanescent field optical fibre sensor," *Analytica Chimica Acta*, vol. 293, no. 1-2, pp. 49-54, 1994.
- [114] L. Bobb, P. Shankar, and H. D. Krumboltz, "Bending effects in biconically tapered single-mode fibers," *Journal of Lightwave Technology*, vol. 8, no. 7, pp. 1084-1090, 1990.
- [115] P. Moar, S. Huntington, J. Katsifolis, *et al.*, "Fabrication, modeling, and direct evanescent field measurement of tapered optical fiber sensors," *Journal of Applied Physics*, vol. 85, no. 7, pp. 3395-3398, 1999.
- [116] J. Villatoro and D. Monzón-Hernández, "Fast detection of hydrogen with nano fiber tapers coated with ultra thin palladium layers," *Optics Express*, vol. 13, no. 13, pp. 5087-5092, 2005.
- [117] Y. Zhao, L. Cai, and H. Hu, "Fiber-optic refractive index sensor based on multi-tapered SMS fiber structure," *IEEE Sensors Journal*, vol. 15, no. 11, pp. 6348-6353, 2015.
- [118] D. Liu, A. Mallik, J. Yuan *et al.*, "High sensitivity refractive index sensor based on a tapered small core single-mode fiber structure," *Optics Letters*, vol. 40, no. 17, pp. 4166-4169, 2015.
- [119] C. Zhang, T. Ning, J. Li, *et al.*, "Refractive index sensor based on tapered multicore fiber," *Optical Fiber Technology*, vol. 33, pp. 71-76, 2017.
- [120] B. Wang, Q. Wang, and C. Du, "Sensitivity-enhanced single-mode fiber-tapered hollow core fiber-single-mode fiber Mach-Zehnder interferometer for refractive index measurements," *Instrumentation Science & Technology*, vol. 46, no. 1, pp. 28-42, 2018.
- [121] F. Ahmed, V. Ahsani, L. Melo, *et al.*, "Miniaturized tapered photonic crystal fiber Mach-Zehnder interferometer for enhanced refractive index sensing," *IEEE Sensors Journal*, vol. 16, no. 24, pp. 8761-8766, 2016.
- [122] Q. Wu, Y. Semenova, P. Wang, *et al.*, "High sensitivity SMS fiber structure based refractometer-analysis and experiment," *Optics Express*, vol. 19, no. 9, pp. 7937-7944, 2011.
- [123] J. Yin, S. Ruan, T. Liu *et al.*, "All-fiber-optic vector magnetometer based on nano-magnetic fluids filled double-clad photonic crystal fiber," *Sensors and Actuators B: Chemical*, vol. 238, pp. 518-524, 2017.
- [124] P. Zu, C.C. Chang, W. Lew *et al.*, "Temperature-insensitive magnetic field sensor based on nanoparticle magnetic fluid and photonic crystal fiber," *IEEE Photonics Journal*, vol. 4, no. 2, pp. 491-498, 2012.
- [125] J. Dai, M. Yang, X. Li, *et al.*, "Magnetic field sensor based on magnetic fluid clad etched fiber Bragg grating," *Optical Fiber Technology*, vol. 17, no. 3, pp. 210-213, 2011.

- [126] J. Zheng, X. Dong, P. Zu *et al.*, "Magnetic field sensor using tilted fiber grating interacting with magnetic fluid," *Optics Express*, vol. 21, no. 15, pp. 17863-17868, 2013.
- [127] P. Zu, C. Chan, W. Lew *et al.*, "Magneto-optical fiber sensor based on magnetic fluid," *Optics Letters*, vol. 37, no. 3, pp. 398-400, 2012.
- [128] Y. Zheng, X. Dong, C. Chan, *et al.*, "Optical fiber magnetic field sensor based on magnetic fluid and microfiber mode interferometer," *Optics Communications*, vol. 336, pp. 5-8, 2015.
- [129] M. Deng, D. Liu, and D. Li, "Magnetic field sensor based on asymmetric optical fiber taper and magnetic fluid," *Sensors and Actuators A: Physical*, vol. 211, pp. 55-59, 2014.
- [130] L. Mao, S. Pu, D. Su, *et al.*, "Magnetic field sensor based on cascaded microfiber coupler with magnetic fluid," *Journal of Applied Physics*, vol. 120, no. 9, pp. 093102, 2016.
- [131] F. Shi, X. Bai, F. Wang, *et al.*, "All-fiber magnetic field sensor based on hollow optical fiber and magnetic fluid," *IEEE Sensors Journal*, vol. 17, no. 3, pp. 619-622, 2017.
- [132] F. Xu, P. Luan, K. Jia, *et al.*, "An optical fiber magnetic field sensor based on fiber spherical structure interferometer coated by magnetic fluid," *Optoelectronics Letters*, vol. 11, no. 5, pp. 379-381, 2015.
- [133] G. Violakis, N. Korakas, and S. Pissadakis, "Differential loss magnetic field sensor using a ferrofluid encapsulated D-shaped optical fiber," *Optics Letters*, vol. 43, no. 1, pp. 142-145, 2018.
- [134] Y. Cao, Y. Zhao, Z. Tong, *et al.*, "Optical fiber magnetic field sensors with peanut-shape structure cascaded with LPFG," *Optoelectronics Letters*, vol. 12, no. 5, pp. 358-360, 2016.
- [135] R. Kötitz, P. Fannin, and L. Trahms, "Time domain study of Brownian and Néel relaxation in ferrofluids," *Journal of Magnetism and Magnetic Materials*, vol. 149, no. 1-2, pp. 42-46, 1995.
- [136] S. Yang, Y. Chen, H. Horng, *et al.*, "Magnetically-modulated refractive index of magnetic fluid films," *Applied Physics Letters*, vol. 81, no. 26, pp. 4931-4933, 2002.
- [137] C. Hong, H. Horng, and S. Yang, "Tunable refractive index of magnetic fluids and its applications," *Physica Status Solidi (c)*, vol. 1, no. 7, pp. 1604-1609, 2004.
- [138] e.UK, "Ferrofluids," 2010. [Online] Available: [https://e-magnetsuk.com/magnetproducts/all\\_other\\_magnets/measurement\\_and\\_experimentation\\_tools/ferrofluid.aspx](https://e-magnetsuk.com/magnetproducts/all_other_magnets/measurement_and_experimentation_tools/ferrofluid.aspx). [Access ed 29- Jan- 2019].
- [139] Y. Chen, J. Barzier, M. Yan, *et al.*, "Evaluation of molecularly imprinted polyurethane as an optical waveguide for PAH sensing," in *Nanosensing: Materials and Devices conference*, Pennsylvania, U.S, vol. 5593, pp. 513-521, 2004.
- [140] X. Wang and O. Wolfbeis, "Optical methods for sensing and imaging oxygen: materials, spectroscopies and applications," *Chemical Society Reviews*, vol. 43, no. 10, pp. 3666-3761, 2014.
- [141] H. Kautsky, "Quenching of luminescence by oxygen," *Transactions of the Faraday Society*, vol. 35, pp. 216-219, 1939.
- [142] C. Chan, M. Chan, M. Zhang, *et al.*, "The performance of oxygen sensing films with ruthenium-adsorbed fumed silica dispersed in silicone rubber," *Analyst*, vol. 124, no. 5, pp. 691-694, 1999.
- [143] X. Wang, G. Farrell, E. Lewis, *et al.*, "A Humidity Sensor Based on a Singlemode-Side Polished Multimode-Singlemode Optical Fibre Structure Coated with Gelatin," *Journal of Lightwave Technology*, vol. 35, no. 18, pp. 4087-4094, 2017.
- [144] W. Xu, J. Shi, X. Yang *et al.*, "Relative Humidity Sensor Based on No-Core Fiber Coated by Agarose-Gel Film," *Sensors*, vol. 17, no. 10, p. 2353, 2017.
- [145] T. Li, X. Dong, C. Chan, *et al.*, "Humidity sensor with a PVA-coated photonic crystal fiber interferometer," *IEEE Sensors Journal*, vol. 13, no. 6, pp. 2214-2216, 2013.
- [146] R. Gao, D. Lu, J. Cheng, *et al.*, "Humidity sensor based on power leakage at resonance wavelengths of a hollow core fiber coated with reduced graphene oxide," *Sensors and Actuators B: Chemical*, vol. 222, pp. 618-624, 2016.
- [147] K. W. Dissanayake, W. Wu, H. Nguyen, *et al.*, "Graphene-Oxide-Coated Long-Period Grating-Based Fiber Optic Sensor for Relative Humidity and External Refractive Index," *Journal of Lightwave Technology*, vol. 36, no. 4, pp. 1145-1151, 2018.

- [148] C. Bariain, I. Matías, F. Arregui, *et al.*, "Optical fiber humidity sensor based on a tapered fiber coated with agarose gel," *Sensors and Actuators B: Chemical*, vol. 69, no. 12, pp. 127-131, 2000.
- [149] A. Gel, "Agargel," 2019. [Online] Available: <http://www.agargel.com.br/agar-tec-en.html>. [Accessed: 29- Jan- 2019].
- [150] A. Osman, J. Pundir, M. Elsherbini, *et al.*, "The effect of intrauterine HCG injection on IVF outcome: a systematic review and meta-analysis," *Reproductive Biomedicine Online*, vol. 33, no. 3, pp. 350-359, 2016.
- [151] J. Fan, M. Wang, C. Wang, *et al.*, "Advances in human chorionic gonadotropin detection technologies: a review," *Bioanalysis*, vol. 9, no. 19, pp. 1509-1529, 2017.
- [152] C. Lee, P. Chiu, L. Hautala *et al.*, "Human chorionic gonadotropin and its free  $\beta$ -subunit stimulate trophoblast invasion independent of LH/hCG receptor," *Molecular and Cellular Endocrinology*, vol. 375, no. 1-2, pp. 43-52, 2013.
- [153] K. Pocius, D. Bartz, R. Maurer, *et al.*, "Serum human chorionic gonadotropin (hCG) trend within the first few days after medical abortion: a prospective study," *Contraception*, vol. 95, no. 3, pp. 263-268, 2017.
- [154] K. Pocius, R. Maurer, J. Fortin, *et al.*, "Early serum human chorionic gonadotropin (hCG) trends after medication abortion," *Contraception*, vol. 91, no. 6, pp. 503-506, 2015.
- [155] N. Sheth, J. Saruiya, K. Ranadive, *et al.*, "Ectopic production of human chorionic gonadotrophin by human breast tumours," *British Journal of Cancer*, vol. 30, no. 6, pp. 566, 1974.
- [156] T. Shah, R. Srirajaskanthan, M. Bhogal *et al.*, " $\alpha$ -Fetoprotein and human chorionic gonadotrophin- $\beta$  as prognostic markers in neuroendocrine tumour patients," *British Journal of Cancer*, vol. 99, no. 1, pp. 72, 2008.
- [157] J. Douglas, A. Sharp, C. Chau *et al.*, "Serum total hCG $\beta$  level is an independent prognostic factor in transitional cell carcinoma of the urothelial tract," *British Journal of Cancer*, vol. 110, no. 7, p. 1759, 2014.
- [158] X. Yan, Z. Huang, M. He *et al.*, "Detection of HCG-antigen based on enhanced photoluminescence of hierarchical ZnO arrays," *Colloids and Surfaces B: Biointerfaces*, vol. 89, pp. 86-92, 2012.
- [159] P. Berger and C. Sturgeon, "Pregnancy testing with hCG—future prospects," *Trends in Endocrinology & Metabolism*, vol. 25, no. 12, pp. 637-648, 2014.
- [160] University of Rochester Medical Center, "HCG (Blood)," 2019. [Online]. Available: [www.urmc.rochester.edu/encyclopedia/content.aspx?contenttypeid=167&contentid=hcg\\_serum](http://www.urmc.rochester.edu/encyclopedia/content.aspx?contenttypeid=167&contentid=hcg_serum). [Accessed 29-Jan-2019]
- [161] S. Imamura, S. Miura, M. Ishiguro, *et al.*, "Enzyme-linked immunoassay of HCG," *Rinsho Kagaku Shimpojumu*, vol. 16, pp. 28-32, 1976.
- [162] M. Santandreu, S. Alegret, and E. Fabregas, "Determination of  $\beta$ -HCG using amperometric immunosensors based on a conducting immunocomposite," *Analytica Chimica Acta*, vol. 396, no. 2-3, pp. 181-188, 1999.
- [163] J. Wang, R. Yuan, Y. Chai *et al.*, "A novel immunosensor based on gold nanoparticles and poly-(2, 6-pyridinediamine)/multiwall carbon nanotubes composite for immunoassay of human chorionic gonadotrophin," *Biochemical Engineering Journal*, vol. 51, no. 3, pp. 95-101, 2010.
- [164] M. Piliarik, M. Bocková, and J. Homola, "Surface plasmon resonance biosensor for parallelized detection of protein biomarkers in diluted blood plasma," *Biosensors and Bioelectronics*, vol. 26, no. 4, pp. 1656-1661, 2010.
- [165] Y. Zhao, X. Li, X. Zhou, *et al.*, "Review on the graphene based optical fiber chemical and biological sensors," *Sensors and Actuators B: Chemical*, vol. 231, pp. 324-340, 2016.
- [166] M. Hassan, E. Gonzalez, V. Hitchins, *et al.*, "Detecting bacteria contamination on medical device surfaces using an integrated fiber-optic mid-infrared spectroscopy sensing method," *Sensors and Actuators B: Chemical*, vol. 231, pp. 646-654, 2016.

- [167] L. Liu, L. Marques, R. Correia *et al.*, "Highly sensitive label-free antibody detection using a long period fibre grating sensor," *Sensors and Actuators B: Chemical*, vol. 271, pp. 24-32, 2018.
- [168] M. Mustapa, M. A. Bakar, Y. Kamil, *et al.*, "Bio-Functionalized Tapered Multimode Fiber Coated With Dengue Virus NS1 Glycoprotein for Label Free Detection of Anti-Dengue Virus NS1 IgG Antibody," *IEEE Sensors Journal*, vol. 18, no. 10, pp. 4066-4072, 2018.
- [169] B. Sepúlveda, J. Del Rio, M. Moreno *et al.*, "Optical biosensor microsystems based on the integration of highly sensitive Mach-Zehnder interferometer devices," *Journal of Optics A: Pure and Applied Optics*, vol. 8, no. 7, p. S561, 2006.
- [170] B. Wang and Q. Wang, "An interferometric optical fiber biosensor with high sensitivity for IgG/anti-IgG immunosensing," *Optics Communications*, vol. 426, pp. 388-394, 2018.
- [171] J. Betancur-Ochoa, V. Minkovich, and Y. Montagut-Ferizzola, "Special Photonic Crystal Modal Interferometer for Highly Sensitive Biosensing," *Journal of Lightwave Technology*, vol. 35, no. 21, pp. 4747-4751, 2017.
- [172] K. Wysokiński, D. Budnicki, J. Fidelus *et al.*, "Dual-core all-fiber integrated immunosensor for detection of protein antigens," *Biosensors and Bioelectronics*, vol. 114, pp. 22-29, 2018.
- [173] D. Liu, R. Kumar, F. Wei *et al.*, "High sensitivity optical fiber sensors for simultaneous measurement of methanol and ethanol," *Sensors and Actuators B: Chemical*, vol. 271, pp. 1-8, 2018.
- [174] C. Soteropulos and H. Hunt, "Attaching biological probes to silica optical biosensors using silane coupling agents," *Journal of Visualized Experiments*, vol. 63, 2012.
- [175] F. Herr, N. Baal, K. Reisinger *et al.*, "HCG in the regulation of placental angiogenesis. Results of an in vitro study," *Placenta*, vol. 28, pp. S85-S93, 2007.
- [176] Q. Wang and W. Zhao, "A comprehensive review of lossy mode resonance-based fiber optic sensors," *Optics and Lasers in Engineering*, vol. 100, pp. 47-60, 2018.
- [177] R. Ramamoorthy, P. Dutta, and S. Akbar, "Oxygen sensors: materials, methods, designs and applications," *Journal of Materials Science*, vol. 38, no. 21, pp. 4271-4282, 2003.
- [178] P. Jorge, P. Caldas, C. Rosa, *et al.*, "Optical fiber probes for fluorescence based oxygen sensing," *Sensors and Actuators B: Chemical*, vol. 103, no. 1-2, pp. 290-299, 2004.
- [179] S. Bell, F. Dunand, M. Schubert, *et al.*, "Optical dissolved oxygen measurement in power plants—A comparison of amperometric and optical dissolved oxygen sensors for applications at low oxygen levels," *VGB PowerTech*, vol. 92, no. 9, pp. 119, 2012.
- [180] L. Sun, Y. Semenova, Q. Wu *et al.*, "High sensitivity ammonia gas sensor based on a silica-gel-coated microfiber coupler," *Journal of Lightwave Technology*, vol. 35, no. 14, pp. 2864-2870, 2017.
- [181] D. Liu, W. Han, A. Mallik *et al.*, "High sensitivity sol-gel silica coated optical fiber sensor for detection of ammonia in water," *Optics Express*, vol. 24, no. 21, pp. 24179-24187, 2016.
- [182] S. Ban, A. Hosoki, M. Nishiyama, A. Seki *et al.*, "Optical fiber oxygen sensor using layer-by-layer stacked porous composite membranes," in *Photonic Instrumentation Engineering III conference*, California, U.S, vol. 9754, pp. 97540F, 2016.
- [183] S. Hung, H. Chang, and I. Chang, "A Portable Array-Type Optical Fiber Sensing Instrument for Real-Time Gas Detection," *Sensors*, vol. 16, no. 12, pp. 2087, 2016.
- [184] C. Pulido and Ó. Esteban, "Tapered polymer optical fiber oxygen sensor based on fluorescence-quenching of an embedded fluorophore," *Sensors and Actuators B: Chemical*, vol. 184, pp. 64-69, 2013.
- [185] N. Pereira, M. Laranjo, J. Serra *et al.*, "Platinum (II) Ring-Fused Chlorins as Near-Infrared Emitting Oxygen Sensors and Photodynamic Agents," *ACS Medicinal Chemistry Letters*, vol. 8, no. 3, pp. 310-315, 2017.
- [186] N. Pereira, M. Laranjo, J. Pina *et al.*, "Advances on photodynamic therapy of melanoma through novel ring-fused 5, 15-diphenylchlorins," *European Journal of Medicinal Chemistry*, vol. 146, pp. 395-408, 2018.
- [187] P. Reineck and B. Gibson, "Near-Infrared Fluorescent Nanomaterials for Bioimaging and Sensing," *Advanced Optical Materials*, vol. 5, no. 2, pp. 1600446, 2017.

- [188] M. Partridge, S. James, and R. Tatam, "Dissolved oxygen sensing using an optical fiber long period grating coated with hemoglobin," *Journal of Lightwave Technology*, vol. 34, no. 19, pp. 4506-4510, 2016.
- [189] W. Cao and Y. Duan, "Optical fiber evanescent wave sensor for oxygen deficiency detection," *Sensors and Actuators B: Chemical*, vol. 119, no. 2, pp. 363-369, 2006.
- [190] L. Bo, P. Wang, Y. Semenova, *et al.*, "High sensitivity fiber refractometer based on an optical microfiber coupler," *IEEE Photonics Technology Letters*, vol. 25, no. 3, pp. 228-230, 2013.
- [191] Q. Wu, Y. Semenova, Y. Ma *et al.*, "Light coupling between a singlemode-multimode-singlemode (SMS) fiber structure and a long period fiber grating," *Journal of Lightwave Technology*, vol. 29, no. 24, pp. 3683-3688, 2011.
- [192] Q. Wu, Y. Ma, J. Yuan *et al.*, "Evanescent field coupling between two parallel close contact SMS fiber structures," *Optics Express*, vol. 20, no. 3, pp. 3098-3109, 2012.
- [193] D. Liu, Q. Wu, C. Mei *et al.*, "Hollow Core Fiber Based Interferometer for High-Temperature (1000° C) Measurement," *Journal of Lightwave Technology*, vol. 36, no. 9, pp. 1583-1590, 2018.